A COMPARISON OF PROTON AND NEUTRON IRRADIATION-INDUCED MICROSTRUCTURAL AND MICROCHEMICAL EVOLUTION IN ZIRCALOY-2

A thesis submitted to The University of Manchester

for the degree of

Doctor of Philosophy

in the

Faculty of Engineering and Physical Sciences

2015

Allan Harte

School of Materials

LIST OF CONTENTS

LIST OF FIGURES

Figure 4.1.11 The scatter in Fe/X (X = Cr,Ni) determination is displayed for the proton data in relation to the effective radius of the whole SPP, $r = (A/\pi)^{0.5}$, where A is the area of the (rarely circular) SPP. The figure shows the Fe/Cr at a) 0 and 2.3 dpa, b) 4.7 and 7.0 dpa, and for Fe/Ni at c) 0 and 2.3 dpa and d) 4.7 and 7.0 dpa.

Figure 4.1.12 The HAADF image is given in a) for a typical grain boundary in non-irradiated Zircaloy-2, tilted such that the boundary plane is parallel to the beam direction. Chemical maps are displayed in raw counts, each individually scaled, for b) Zr c) Sn, d) Fe, e) Cr and f) Ni. All 10 boundaries studied in this manner exhibited both Fe and Ni segregation to the boundary.

Figure 4.1.13 The HAADF image is given in a) for a grain boundary in Zircaloy-2 proton-irradiated to 7.0 dpa, tilted such that the boundary plane is parallel to the beam direction. Chemical maps are displayed in raw counts, each individually scaled, for b) Zr c) Sn, d) Fe, e) Cr and f) Ni. All boundaries exhibit Sn segregation and Fe, Ni depletion.

Figure 4.1.14 The HAADF image is given in a) for a grain boundary in Zircaloy-2 clad neutron-irradiated in a BWR to 9.5 x10^{25} n m^{-2} ~15.8 dpa, tilted such that the boundary plane is parallel to the beam direction. Chemical maps are displayed in raw counts, each individually scaled, for b) Zr c) Sn, d) Fe, e) Cr and f) Ni. All boundaries exhibit Sn segregation and Fe, Ni depletion.

Figure 4.1.15 The line scans shown in a), b) and c) correspond to a horizontal profile across Figure 13, Figure 12 and Figure 14, respectively. The line scans are quantified in terms of atomic per cent (at.%) to provide a graphical representation of the spatial distribution of elements.

MANUSCRIPT 2: A COMPARISON OF PROTON AND NEUTRON IRRADIATION-INDUCED DISLOCATION LOOP EVOLUTION AND ASSOCIATED MICROCHEMICAL CHANGES IN ZIRCALOY-2

Figure 4.2.1 a)-c) give the pole figures for the {0001}, **and** planes from the normal direction (ND) of the non-irradiated Zircaloy-2 plate. The transverse direction (TD) and rolling direction (RD) are in the horizontal and vertical direction, respectively. The split basal shown in {0001} is typical of recrystallised Zr alloys and is an important feature as the grains are both proton-irradiated and examined by S/TEM from the ND.

Figure 4.2.2 a) and b) show BF TEM and STEM images for the same grain at the same orientation and magnification after proton irradiation to 2.3 dpa. The inset in a) is a selected area diffraction pattern, indexing the zone axis at the centre of the bend contours as the . The bend contours are greatly reduced in b) due to the convergence of the scanning probe. The BF STEM image of irradiation-induced dislocations in c) is from the region highlighted by the red square in b) at an orientation close to the zone axis.

Figure 4.2.3 BF STEM images obtained after proton irradiation to 2.3 dpa. a) and b) were obtained from parallel to the g = and systematic rows, respectively, ~9° from the and zone axes, respectively. Part c) shows a BF STEM image of the same region with the crystal parallel to the g = 0002 systematic row. The insets in each image are the fast Fourier transforms of the high resolution BF STEM image at that orientation. The large particle at the top of the image is a surface oxide and acts as a fiducial marker. The visibility of defects in a) and not b) and c) confirms the defects to be a-loops with Burgers vector -type. The long defect to the bottom left of c) is invisible in a) and b), and, as such, is a dislocation of Burgers vector <0001>-type.

Figure 4.2.4 BF STEM images are obtained in material proton-irradiated to 2.3 dpa in the same region from a) and c) the zone axis and b) and d) the zone axis. Images c) and d) are taken from the very central region of images a) and b), respectively. As such, the axes in the upper right of a) and b) are the same for c) and d), respectfully, and the fast Fourier transform insets in c) and d) are applicable to a) and b), respectfully.

Figure 4.2.5 BF STEM images of a-loops are displayed from the zone axis after proton irradiation to 2.3, 4.7 and 7.0 dpa in a)-c), respectfully. a-loops become smaller and more organised between 2.3 and 4.7 dpa, aligning parallel to the trace of the basal plane.

Figure 4.2.6 BF STEM images are displayed obtained from parallel to the g = 0002 systematic row in a) and b) after proton irradiation to 4.7 and 7.0 dpa, respectfully, with SPPs highlighted by black arrows in a). An image at this orientation for the 2.3 dpa material is shown in Figure 3 c). No c-loops (Burgers vector <2-203>-type) are observed at 2.3 dpa, some are observed at 4.7 dpa and a higher number density is observed at 7.0 dpa. After 7.0 dpa, c-loops may be observed in c) from the <0001> zone axis (inset FFT of high resolution BF STEM image); white arrows indicate the presence of circular c-loops.

Figure 4.2.7 In Zircaloy-2 proton-irradiated to 7.0 dpa, BF STEM images are taken on-axis parallel to in a) and 4° from along the g = 0002 systematic row in b). As such, a) shows both a- and c-loops whereas b) shows only c-loops. The SPP in the upper right corner acts as a fiducial marker. The annotation shows that where there are a-loops in a) there are no c-loops in b). Likewise, where there are no a-loops n a) there is a c-loop in b). Additionally, if one looks closely, defects tilted ~15° from <0001> (vertical) can be seen above the 'No c-loops' annotation in part b).

Figure 4.2.8 Representative images of a- and c-loops in the neutron-irradiated material are given in a) and b), respectively, for Zircaloy-2 irradiated in a BWR to a fluence of 9/5 x1025 n m-2 ~15.8 dpa. a-loops are imaged in BF and parallel to g **=** , c-loops in BF and parallel to g = 0002. In c), c-loops are imaged in Zircaloy-2 cladding at a neutron fluence 14.7 x10^{25} n m^{-2} ~24.5 dpa.

Figure 4.2.9 Quantification of dislocation number density and size. The *x*-axes in each part of the figure are on both the irradiation dose scales of displacements per atom (dpa) for the proton- and neutron-irradiated material and in neutron fluence at the top for the neutron-irradiated material. In a) and b) the a-loop number density and shape parameters are plotted, where length and width indicate the long and short axes, respectively, of the elliptical loops. The c-loop number density and diameter variation with irradiation dose is plotted in c) and d), with the latter measured as projected from parallel to the g = 0002 systematic row.

Figure 4.2.10 The variation in a- and c-loop line density is plotted as a function of irradiation dose for both proton- and neutron-irradiated Zircaloy-2, together with the total line density, a-loops + c-loops. Such data is a combination of the dislocation number density and size given in Figure 9.

Figure 4.2.11 The BF STEM image in a) was obtained in Zircaloy-2 from the orientation after proton irradiation to 2.3 dpa. The Zr, Sn, Fe, Cr and Ni maps are displayed in b)-f), respectively.

Figure 4.2.12 The BF STEM image in a) was obtained in Zircaloy-2 from the orientation after proton irradiation to 4.7 dpa. The Zr, Sn, Fe, Cr and Ni maps are displayed in b)-f), respectively.

Figure 4.2.13 The BF STEM image in a) was obtained in Zircaloy-2 cladding from the orientation after neutron irradiation in a BWR to a fluence of 9.5 x10^{25} n m^{-2} ~15.8 dpa. The Zr, Sn, Fe, Cr and Ni maps are displayed in b)-f), respectively. The region highlighted by a red square in a) is the position of the =higher magnification map displayed in Figure 14.

Figure 4.2.14 The BF STEM image in a) and Zr, Sn, Fe, Cr and Ni chemical maps in b)-f), respectively, were obtained from the region highlighted by a red square in Figure 13 a) from the orientation after neutron irradiation in a BWR to a fluence of 9.5 x10^{25} n m^{-2} ~15.8 dpa. Discontinuous segregation of Fe and Cr to c-loop positions is evident. Possible discontinuity in Sn segregation between c-loop positions is shown in c).

Figure 4.2.15 BF STEM images at the orientation and the corresponding EDS line scans are given in a) and b) after 2.3 dpa proton irradiation, in c) and d) after 4.7 dpa proton irradiation and in e) and f) after neutron irradiation in a BWR to a fluence of 9.5 x10^{25} n m^{-2} ~15.8 dpa. The line scans are taken from the black arrows in the BF STEM images and averaged over the area in red perpendicular to the arrow. Minima in the BF STEM intensity are denoted in the line scan by vertical black dotted lines.

Figure 4.2.16 a-loop line density as a function of irradiation dose (dpa) for p, proton irradiation and n, neutron irradiation after ' * ' the present work, a (Griffiths et al. 1996), b (Northwood et al. 1979), c

A COMPARISON OF PROTON AND NEUTRON IRRADIATION-INDUCED MICROSTRUCTURAL AND MICROCHEMICAL EVOLUTION IN ZIRCALOY-2

A thesis submitted to The University of Manchester for the degree of Doctor of Philosophy in the Faculty of Engineering and Physical Sciences

2015

Allan Harte

School of Materials

ABSTRACT

This work was performed as part of an EPSRC Leadership Fellowship [EP/I005420/1] for the study of irradiation damage in Zr alloys, and is supported heavily by industrial contributors and especially by Westinghouse, Studsvik and Rolls-Royce plc. for the investigation of mechanisms relating to irradiation-induced growth (IIG). This thesis is an analysis of the microchemical and microstructural evolution of Zircaloy-2 under both proton and neutron irradiation. Comparisons are made between the effects of the different irradiative species through the use of scanning transmission electron microscopy (STEM) and energy dispersive X-ray spectroscopy (EDS). The work takes advantage of advances in EDS capability with large solid angles of collection 0.7 srad coupled with an aberration-corrected FEI Titan ChemiSTEM^{TM} with a high brightness X-FEG electron source.

2 MeV proton irradiation experiments were performed to doses of 2.3, 4.7 and 7.0 displacements per atom (dpa) at a dose rate of ~6.7 x10^{-6} dpa s^{-1} and at 350 °C. Electropolished TEM foils from Zircaloy-2 cladding and channel components of a BWR were supplied by Westinghouse in the fluence range 8.7 to 14.7 x10^{25} n m^{-2} ~14.5 to 24.5 dpa. Comparisons have been made in relation to SPP chemical composition, grain boundary chemistry, dislocation density, correlations between dislocation evolution and microchemical segregations and the nature of irradiation-induced precipitates.

Proton irradiation-induced dissolution was observed for both $Zr(Fe,Cr)_2$ and $Zr_2(Fe,Ni)$ SPPs, the depletion of Fe was preferentially from the edge region in the former SPP and from throughout the whole SPP in the latter. While no proton-induced amorphisation was observed for the $Zr(Fe,Cr)_2$, the compositional changes in all SPPs agreed well with the reports of other authors. All grain boundaries display Fe and Ni segregation prior to irradiation, which disperses into the matrix after both proton and neutron irradiation, while Sn segregates to the boundary. Sn and the light transition elements Fe, Cr and Ni have shown contrasting behaviour in the matrix also. After irradiation by both protons and neutrons, a-component dislocation loops (a-loops) align parallel to the basal plane and Fe, Cr and Ni segregate to the a-loop positions. Sn, conversely, segregates to between a-loop positions parallel to the basal trace. The threshold dose in c-component dislocation loop (c-loop) nucleation under proton irradiation (~4.5 dpa) is shown as similar to that due to neutron irradiation (~5 dpa). We observe that a-loop density decreases at the onset of c-loop nucleation and that the position of c-loops are in alignment with the a-loops but that they are anticorrelated in position along the basal trace. We therefore propose that chemical ordering promotes the alignment of a-loops, which then provides the conditions necessary for c-loop nucleation. Nanoprecipitation is evident in the matrix after both proton and neutron irradiation. After proton irradiation to ~2 dpa, parallel atom probe tomography and STEM-EDS investigations have shown the nano-rods to be of composition $Zr_4(Fe_{0.67}Cr_{0.33})$, tending towards $Zr_3(Fe_{0.69}Cr_{0.31})$ as the rod volume increases. The rods are higher in density than the a-loops by a factor of ~3 and so are likely to be a significant influence on mechanical properties and IIG phenomena.

DECLARATION

No portion of the work referred to in the thesis has been submitted in support of an application for another degree or qualification of this or any other university or other institute of learning.

COPYRIGHT STATEMENT

...and all ye need to know

- J. K., 1819

ACKNOWLEDGEMENTS

The work presented here would have been impossible were it not for the support of friends and family, and especially of my parents, Noel and Helen Harte for their unwavering encouragement and their dry, practical sense of humour that has kept me grounded and, frankly, sane.

A significant amount of the work presented here is a group effort, and sincere acknowledgement goes to the academic and student members of the zirconium irradiation group, who's particular brand of meticulous questioning has kept me on the correct path and has highlighted some of my more risky interpretations of results. The guidance of Michael Preuss, Philipp Frankel and Christopher Race has been essential to the completion of this work. In-depth discussions with actively involved fellow Ph.D students have kept my interest alive, and Matthew Topping is primarily responsible for that, as well as being the glue that keeps the zirconium group together and the agony aunt of us all. Thomas Seymour's parallel investigations by bulk analysis techniques has been essential to the interpretation of many of the results presented here and his critical viewpoint on many a proposition, both academic and otherwise, has kept my mind both analytically-orientated and entertained during experiments at unsociable hours. A wide net of thanks must be cast for the other members of the zirconium group, not least Al Garner, Elisabeth Francis, (honorary) David Bowden, Christopher Daniels, Chi Toan-Nguyen, Felicity Baxter, and especially Maria Yankova, who's patience and enthusiasm with MATLAB knows no bounds. I would like to thank Prasath Revathy for his expert knowledge in the field of Indian cuisine and for putting this into practise on location when travel for experiments results in the odd dining perk. Prasath's experience in atom probe tomography has been essential to the work described here and he is invaluable to the zirconium group.

The LEAP team at The University of Oxford, namely Charles Hirst, Tomas Martin and Michael Moody, have been very accommodating and I hope to work much more closely with them in the future. Likewise, Ovidiu Toader and Gary Was at the Michigan Ion Beam Laboratory have been instrumental in the performance of the proton irradiation experiments and have made 24 hour experiments feel like a breeze. I would like to thank Malcolm Griffiths for essential discussions and advice, in addition to vital deliberations with Mhairi Gass, Sarah Haigh, Ted Darby, Aidan Cole-Baker, Daniel Jädernäs, Lars Hallstadius and Robert Comstock. The work here is funded by an EPSRC Leadership Fellowship [EP/I005420/1] for the study of irradiation damage in zirconium alloys, and is supported heavily by industrial contributors and especially Westinghouse, Studsvik and Rolls-Royce plc. in terms of material acquisition, top up funding and useful discussions.

PUBLICATIONS AND PRESENTATIONS

The following two manuscripts have been published peer-reviewed journals:

A. Harte, T. Seymour, E.M. Francis, P. Frankel, S. P. Thompson, D. Jädernäs, J. Romero, L. Hallstadius, M.Preuss, 2014, *Advances in Synchrotron X-Ray Diffraction and Transmission Electron Microscopy Techniques for the Investigation of Microstructure Evolution in Proton- and Neutron-Irradiated Zirconium Alloys*, Journal of Materials Research, Focus Issue: Nuclear Materials, 1349-1365

E. Francis, A. Harte, P. Frankel, S.J. Haigh, D. Jädernäs, J. Romero, L. Hallstadius, M.Preuss, 2013, *Iron redistribution in a zirconium alloy after neutron and proton irradiation studied by energy-dispersive X-ray spectroscopy (EDX) using an aberration-corrected (scanning) transmission electron microscope*, Journal of Nuclear Materials, 454, **1-3**, pp. 387-397

These published manuscripts are not included in the present work. The manuscripts presented here have not yet been submitted for peer-reviewed publication, although work has been presented at a number of conferences and meetings, including:

Jun 2015	Oral presentation to the Manchester Microscopy and Microanalysis group, The University of Manchester, UK. *Thickness Measurements by Convergent Beam Electron Diffraction in the TEM*.
Apr 2015	Oral presentation, Zr Fellowship Progress to industrial collaborators, Imperial Collage London, UK.
Mar 2015	Oral presentation, Rolls Royce University Technology Centre, The University of Manchester, UK.
Dec 2014	Oral presentation, Rolls Royce University Technology Centre, Managers Meeting, The University of Manchester, UK.
Nov 2014	Oral presentation, Rolls Royce Nuclear Materials Reseach Conference, Derby, UK

Oct 2014 Oral presentation at NuMat2014, Clearwater, FL, USA. *The Influence of Neutron- and Proton-Irradiation on Microchemical Segregation in Zr Alloys*.

May 2014 Oral presentation, Zr Fellowship Progress to industrial collaborators, EDF Energy, Fontainebleau, France.

Feb 2014 Oral presentation at TMS2014, San Diego, CA, USA. *Advanced TEM Techniques for Characterisation of Proton Irradiation Damage in Zr Alloy Zircaloy-2*.

Dec 2013 Oral presentation, Zr Fellowship Progress to industrial collaborators, The University of Oxford, UK.

Aug 2013 Oral presentation, Zirconium Experts Meeting, Westinghouse Electric Company, Nuclear, Västerås, Sweden.

1 INTRODUCTION

1.1 AIMS OF THE PROJECT

The work presented in this thesis was performed as part of an EPSRC Leadership Fellowship [EP/I005420/1] for the study of irradiation damage in zirconium (Zr) alloys, and is supported heavily by industrial contributors and especially by Westinghouse, Studsvik and Rolls-Royce plc. in terms of material acquisition, top up funding and frequent meetings for useful discussion. Zr alloys are used widely in the nuclear industry, and so the effects of irradiation damage on alloy properties is an essential field of study. The broad aim of this work is to assess the extent to which proton irradiation may be used to emulate the effects of neutron irradiation in terms of the irradiation-induced microstructural and microchemical evolution in Zr alloys. Proton irradiation experiments are systematic and performed under a narrow range of experimental variation, they are quick to perform and the resulting material is of low radioactivity. As such, proton irradiation experiments are an attractive method of study. However, a detailed understanding of the differences between proton and neutron irradiation with respect to Zr alloys is lacking in the literature. The electron microscopy capability in the School of Materials at The University of Manchester is world-leading, and its application to a an intricate study such as this is ideal. The use of aberration-corrected scanning transmission electron microscopy (STEM) and energy-dispersive X-ray spectroscopy (EDS) correlated to observations made by way of atom probe tomography (APT) has been central to the present work and has revealed not only similarities and differences between Zr alloys irradiated with protons or neutrons, but has also been used to improve the mechanistic understanding of the defect evolution that follows such ballistic processes.

This thesis contains three manuscripts for publication, for which the primary focus is in Zr alloy Zircaloy-2. To put the manuscripts into context, much of the literature review is devoted to a description of the Zr-Sn-based family of alloys

and their behavior under irradiation, although Zr-Nb- and Zr-Sn-Nb-based families are also referenced where appropriate. The section following the literature review concerns the experimental methods employed for the completion of this work. The proton irradiation experiments and sample preparation methods for analysis by scanning electron microscopy (SEM), S/TEM and APT are described, followed by details of microscopic analysis, such as examination by EDS and measurements of dislocation density. The three manuscripts are then presented, followed by a summary of the various outcomes of the work as a whole. This final section aims to formulate a coherent picture of the behavior of Zircaloy-2 under irradiation and to highlight the novel contribution of the present work.

1.2 ENGINEERING AND ACADEMIC CONTEXT

Zr alloys are used extensively in pressurised water reactors (PWRs), boiling water reactors (BWRs), the Russian high power channel-type reactors (RBMKs) and water-water energetic reactors (VVERs), and the heavy water reactors such as pressurised heavy water reactors (PHWRs) and the Canada deuterium uranium reactors (CANDUs). The Zr components are generally the channel material and the cladding used to house the uranium fuel, as shown in Figure 1-1, but may also be used for the structural components, guide tubes and control blades. During reactor operation, Zr cladding components elongate in a process known as irradiation-induced growth (Buckley 1961), which is accounted for in the reactor core by allowing space for growth at either end of the cladding tube. However, extensive growth results in distortion of the fuel rod elements and buckling of the cladding, Figure 1-2, which limits the insertion of control rods and hence the operational lifetime of the fuel pile.

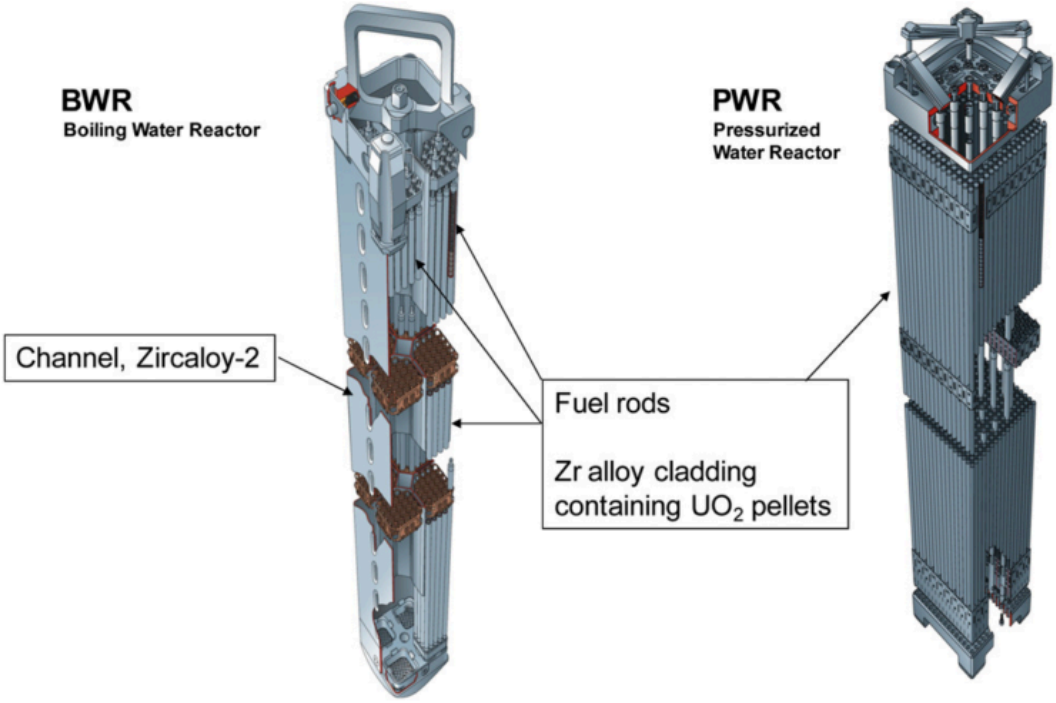

Figure 1-1 Diagram of reactors BWR and PWR, highlighting the uses of Zr alloys (Hallstadius et al. 2012).

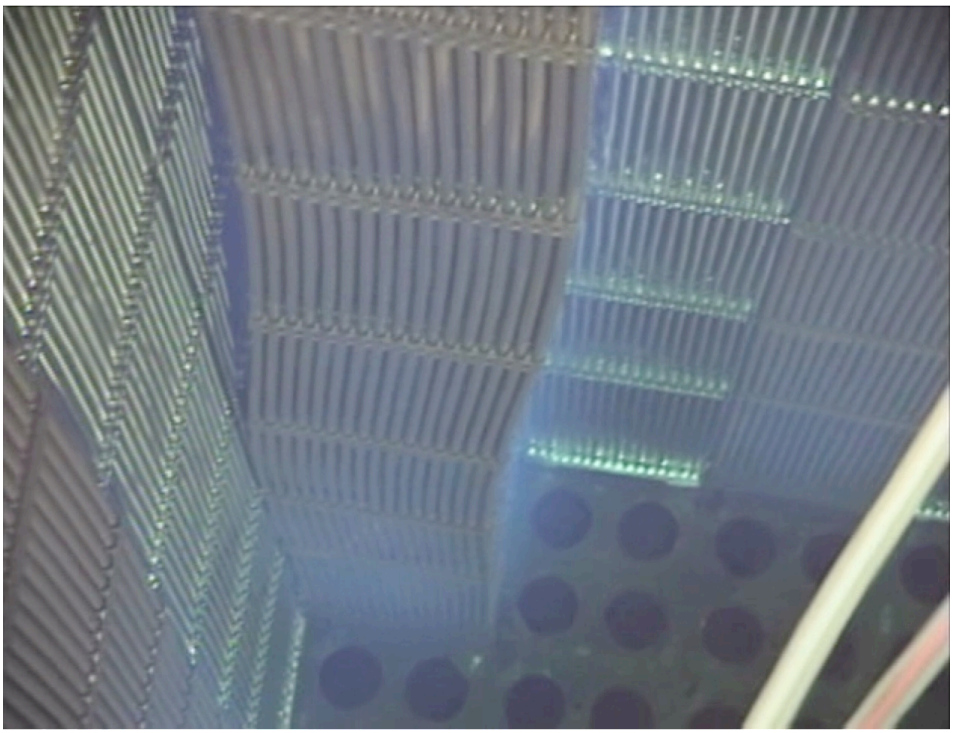

Figure 1-2 Cladding buckling in a fuel assembly. The length of the cladding tube is ~4 m.

As the extension of Generation II power reactor lifetimes has been increased from the originally planned 30-40 years to ~50-60 years, research into damage mechanisms has become an important area of research. Further, the world population is set to increase from it's current (2015) 7.3 bn to an estimated 9.7 bn by 2050 (UN 2015) and the European Commission has recently committed to 'at least' 40% reduction in greenhouse gas emissions by 2030 (EU 2015). As such, nuclear energy is a viable alternative to fossil fuels and has seen a boost in research efforts. The number of academic publications per year since 1960 is displayed in Figure 1-3 for those papers with the topic *Zirconium* and *Nuclear*, showing a dramatic increase in the number of papers published the past 25 years. The ASTM International group oversees the *Zirconium in the Nuclear Industry* symposia, which publishes the single largest collection of peer-reviewed papers dedicated to Zr research in the nuclear sphere. The collection of work spans basic metallurgy, accidental conditions, fabrication, creep, growth, corrosion and hydrogen embrittlement, and contains ~ 40 papers that are collected after the single session symposium that is held every two years. This invaluable source of collective knowledge has been essential to the present work. The *Journal of Nuclear Materials* has likely made the largest academic contribution to the field and also deserves considerable recognition, especially in regard to the early work of the 1980's and '90's that form the basis of much of this thesis.

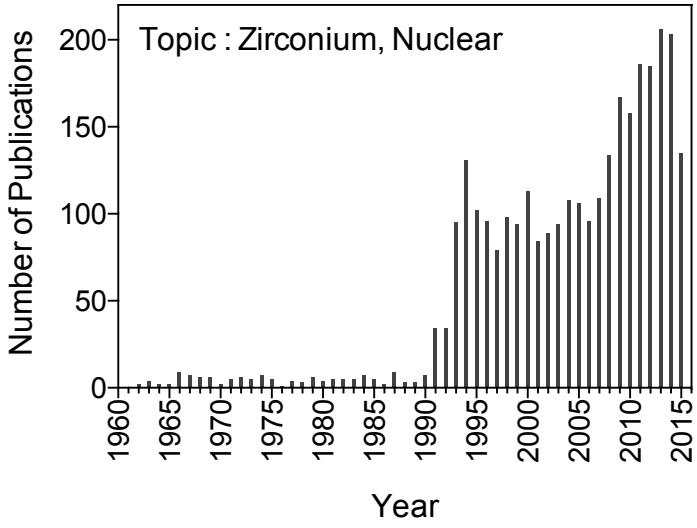

Figure 1-3 The number of publications per year since 1960 with the topic *Zirconium* and *Nuclear*. Data obtained from Web of science, September 2015.

1.3 REFERENCES

Buckley, S.N., 1961. Properties of Reactor Materials and the Effects of Irradiation Damage. In London: Butterworths, p. 443.

EU, 2015. Energy Union : secure, sustainable, competitive, affordable energy for every European. *Euopean Commission - Press Release*, (February).

Hallstadius, L., Johnson, S. & Lahoda, E., 2012. Cladding for high performance fuel. *Progress in Nuclear Energy*, 57, pp.71–76.

UN, 2015. World population prospects: Key findings & advice tables. *United Nations*.

2 LITERATURE REVIEW

The following is an examination of the current literature regarding the effect of microstructural evolution on irradiation-induced growth (IIG) phenomena in Zr and its alloys, highlighting the attempts at a mechanistic understanding. The survey begins by describing the alloy systems and their design with respect to mechanical and corrosion properties. Following this, the effects of irradiation will be described in relation to the alloys relevant to this work, starting with point defect evolution following the initial damage cascade event. The effect of the anisotropic hcp crystal system will be assessed, its effect on the diffusion of point defects and the resulting explanations of macroscopic IIG that shape the current understanding in the field. Subsequently, a description will be given of observable defect evolution, especially that of dislocation loops and second phase particles (SPPs), in order to support the mechanistic understanding of IIG and to highlight its controversies. Both neutron- and proton-irradiation effects will be assessed throughout, as well as references to heavy-ion and electron irradiation where possible. The focus of the review will be on transmission electron microscopy (TEM) investigation, although other methodologies will be referred to where appropriate and necessary.

A note on units: the literature is varied in its use of units, between mole fraction, weight per cent, atomic per cent, and both weight and atomic parts per million. Atomic and weight per cent are most common and so are given where possible, commonly by the author's own conversion. Neutron irradiation dose is frequently given in neutron fluence, n m^{-2}, and is converted to displacements per atom (dpa) after Ref. (Shishov et al. 2005)

2.1 THE ALLOYING OF ZIRCONIUM

Pure zirconium (Zr) may take two crystal structures: the α-phase at temperatures less than the β transus ~863 °C (Okamoto 2010), a hexagonal close-packed (hcp) structure that is stabilised by the elements Sn, O, N, Be, Pb, Hf and Cd (Benjamin 1979); and the β-phase at higher temperatures, a body-centred cubic (bcc)

structure that is stabilised by the elements Fe, Cr, Ni, Nb, Mo, Cu, Ta, Th, U, W, Ti, Mn, Co and Ag (Benjamin 1979). The α-phase is, therefore, the phase present under light water reactor operating conditions of water temperatures ~300-330 °C (Hallstadius et al. 2012), although both α- and β-stabilisers are common alloying additions to commercial Zr alloys. Figure 2-1 gives the hcp structure and some important planes for slip in α-Zr (Tenckhoff 2005). The a and c parameters of pure α-Zr at 27 °C were obtained by Goldak et al. using X-ray diffraction from single crystals in different orientations as 0.323312 and 0.514905 nm for the a and c parameters, respectively (Goldak et al. 1966), resulting in a c/a ratio of 1.5926, which is less than the ideal (ideal $\sqrt{(8/3)}$ = 1.6330 based on the hard sphere model). From single crystal measurements, the coefficient of thermal expansion of hcp Zr in the $<11\bar{2}0>$ and <0001> directions is 5.2 x10^{-6} and 10.4 x10^{-6} K^{-1}, respectively, with an average of 6.7 x10^{-6} K^{-1} (IAEA-TECDOC-966 1998).

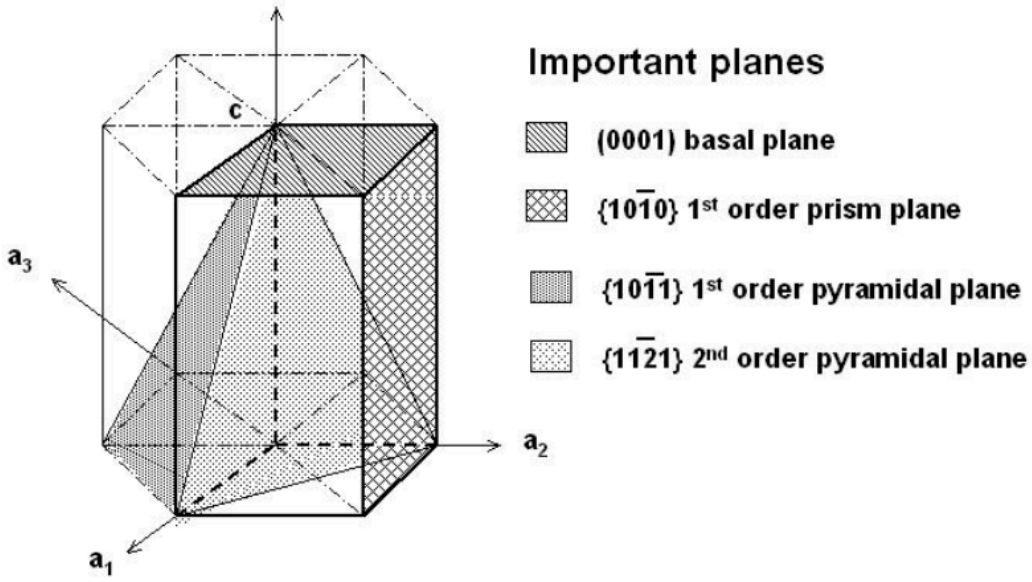

Figure 2-1 The hcp unit cell and important planes, from (Tenckhoff 2005).

In addition to temperature, the use of alloying elements changes the α-Zr lattice parameters depending on the alloying element's solubility in the matrix and its propensity for anisotropic diffusion, properties that are important in the evolution of microstructure during irradiation (Woo & Göslel 1983; Perez et al. 2003; Christensen et al. 2014; M Christensen et al. 2015). The common alloying elements

of Zr are Sn, Nb, Fe, Cr and Ni, some properties of which are displayed in Table 1 at the end of this review and are discussed in the following.

The ratio of the metallic radii of element *i* to that of Zr, r_i/r_{Zr}, is thought to give an indication of the position of alloying element *i* in the α-Zr lattice; *i* being substitutional if $r_i/r_{Zr} > 0.83$ and interstitial otherwise (Tendler & Abriata 1987). This general rule has recently been supported by ab initio DFT calculations of common alloying elements in α-Zr, in which 1 wt.% of element *i* were used to replace Zr atoms in substitutional sites, homogeneously dispersed, and the percentage volume change in the structure was calculated (Christensen et al. 2014). A summary of these two observations is shown in Figure 2-2, in which the diffusion coefficients of Zr, Sn, Nb, Fe, Cr and Ni are plotted as a function of atomic radii on the x axis, after Ref. (Perez et al. 2003), and the percentage volumetric change for 1 wt.% of element i, after Ref. (Christensen et al. 2014) plotted in the same figure.

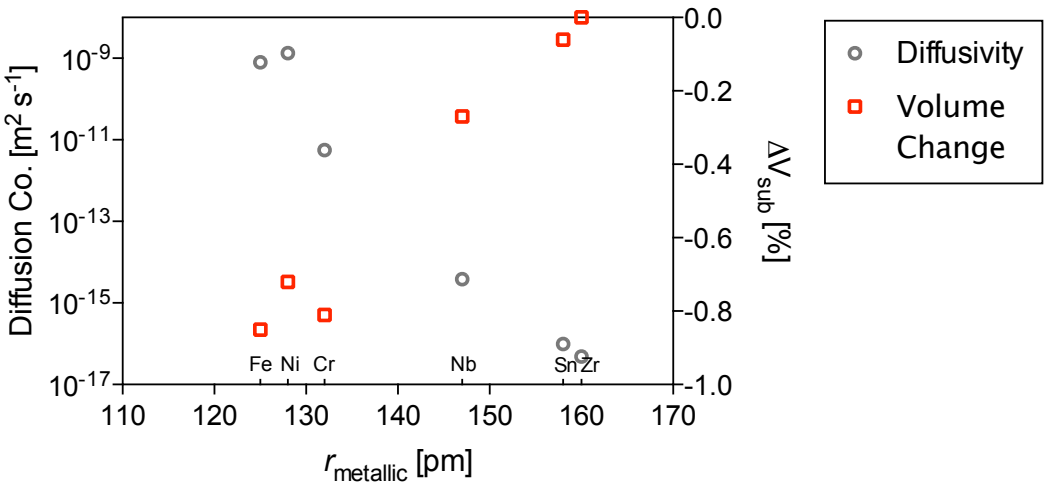

Figure 2-2 Diffusion coefficient (Perez et al. 2003) and volumetric change of substitutional Zr, Sn, Nb, Fe, Cr and Ni (Christensen et al. 2014) in α-Zr.

As might be expected, the volume of the system changed more (approaching -1%) with decreasing atomic radii, suggesting that elements of smaller radii induce more strain in substitutional positions and are therefore more likely to be interstitial, although it was found that Ni, Nb and Sn are quite stable at the substitutional site, remaining close to the centre of the vacancy after geometry optimisation (Christensen et al. 2014). The diffusivity of the elements is shown to increase with decreasing radii, the small transition elements believed to be interstitial in nature (Pasianot & Pérez 2013), Fe especially as diffusing between octahedral sites (Pasianot et al. 2009). Plotted on the same figure, the data from the two studies demonstrate that elements that are likely to be interstitials, i.e. those of a large change in volume in substitutional sites and agreeing with the principle that interstitials occur if $r_i/r_{Zr} < 0.83$, are correlated with higher rates of diffusivity. Such diffusers, Fe, Cr and Ni, prefer diffusion in the <0001> direction (Christensen et al. 2014), whereas Zr self-interstitials (SIAs) prefer diffusion in the basal plane (Christensen et al. 2014). Interestingly, Fe has been shown to enhance Zr self-interstitial atom (SIA) diffusion due to the low migration energy of the Fe-vacancy pair (King et al. 1991) and the tendency of substitutional Fe, Cr and Ni atoms to swap with Zr SIAs (Hood 1977; Christensen et al. 2014), making Fe, Cr or Ni interstitial and recovering the α-Zr lattice. Conversely, substitutional elements Sn and Nb hinder Zr SIA diffusion in both a and c directions, this effect increasing with decreasing temperature (Christensen et al. 2014). The interaction of alloying elements results in precipitation, especially between Fe and other species. Being fast diffusers, Fe, Ni and Cr are likely to precipitate as second phases under thermal equilibrium, the most common of which in commercial alloys are listed in Table 2 at the end of this review and will be discussed in §2.8.2.

2.2 COMMERCIAL ZIRCONIUM ALLOYS

A short summary of seven commercial alloys is given in Table 2, namely Zircaloy-2, Zircaloy-4, Zr-1Nb, Zr-2.5Nb, E635, ZIRLO™ and M5™. The table details the dominant second phase particles (SPPs) and not the minor less frequently observed. These alloys have been selected as representative of not only the current and future alloys used in reactor operation but also of historical significance. For

instance, the Zr-Sn(-Fe,CrNi) and the Zr-Nb families preceded the Zr-Sn-Nb(-Fe,Cr), in which the Russian E635 was the basis of development for ZIRLO™ and M5™. A selection of these alloys is used in various reactors around the planet, comprising the structural cladding and channel components, as well as pressure and calandria tubes. The following is an account of why each alloying addition is made and a description of the phases precipitated in each alloy in addition to the α-Zr matrix.

The addition of Sn stabilises the α-phase in supersaturated solid solution and its solubility in α-Zr, along with that of Nb, Fe, Cr and Ni, is detailed in Table 1, Sn having the highest solubility of all of the elements listed at 3-6.5 at.% depending on temperature (Okamoto 2010; Jerlerud Pérez et al. 2008). Sn is commercially alloyed with Zr in Sn concentrations <1.3 at.% (~1.7 wt.%) (Hallstadius et al. 2012) for better creep resistance (Adamson et al. 2009) and better mechanical properties in terms of increased strength and hardness; the addition of Sn hinders prismatic slip (Crépin et al. 1995; Mani Krishna et al. 2015), the preferred slip mode in Zr (Tenckhoff 2005). Sn was historically added to improve corrosion resistance if the N impurity content in the material exceeded 30-60 ppm (Sabol 2005), although ~0.4 at.% (~0.5 wt.%) was determined as optimal and so higher additions contribute to solid solution strengthening at the expense of corrosion resistance.

Fe, Cr and Ni are primarily added to Zr-Sn-based alloys for improved corrosion properties, but in small amounts such that a (Fe+Cr+Ni) total is < 0.7 at.% (~0.45 wt.%) in the alloy (Hallstadius et al. 2012). The solubility of the small transition elements Fe, Cr and Ni in α-Zr is low, as detailed in Table 1, even at high temperatures close to the β-transus; a study by Charquet et al. demonstrated the maximum solubility of (Fe+Cr) in the Zr- 1.4wt.%Sn- Fe-Cr system as 150 wppm (0.025 at.%, i.e. 0.016 at.% Fe and 0.009 at.% Cr) at 810 °C (Charquet et al. 1988). Due to the their low solubility, Fe, Cr and Ni precipitate as intermetallics known as second phase particles (SPPs), which have a size in the 30-200 nm diameter range (Gros & Wadier 1990; Rudling 2000; Tagtstrom et al. 2002; Valizadeh et al. 2014), although SPPs up to 500 nm in diameter have been reported (Gilbert et al. 1985). Indeed, the SPP size and volume fraction changes with thermomechanical

processing parameters, increasing in size and volume fraction with longer times at higher temperatures during the post-quench annealing stage of recrystallisation (Motta et al. 2002). The most common SPPs in commercial alloys are detailed in Table 2. In commercial Zircaloy-2, the Laves phase $Zr(Fe,Cr)_2$ (hcp, Fe/Cr ratio 0.82 (Chemelle et al. 1983) or 0.7-1.1 (Valizadeh et al. 2014)) and the $Zr_2(Fe,Ni)$ phase (bct, Fe/Ni ratio 1.6-2.1 (Valizadeh et al. 2014)) are present. The $Zr_2(Fe,Ni)$ phase is absent in Zircaloy-4, resulting in Laves phases of a higher Fe/Cr ratio of 2.5 (Van der Sande & Bement 1974) but with almost identical lattice parameters (Motta et al. 2002), likely suggesting that Fe and Cr easily replace one another at lattice sites.

The addition of Nb to Zr alloys takes two forms; that added to Zr-Sn systems and that alloyed alone with Zr in binary form. Due to the similarity in atomic mass with Zr, the solubility of Nb in the α-Zr matrix is higher than that of Fe, Cr and Ni, but the value varies between publications (Sabol 2005; Barberis et al. 2004; Kim et al. 2005; Woo & Griffiths 2009). Common values stated are 0.3 and 0.6 wt.%, although it is thought to be lower in a 'true' binary alloy (Woo & Griffiths 2009). In the binary systems, the most common commercial Zr alloys are those alloyed with 1 or 2.5 wt.% Nb, in which there may exist β-Zr and/or β-Nb precipitates, depending on the processing parameters (Shishov et al. 2005). Such alloys are noted to have improved corrosion resistance with respect to the Zircaloys (Sabol 2005). However, the mechanical and in-reactor deformation properties are improved by adding the solid solution strengthener Sn to form Zr-Nb-Sn-based systems as done in the Zircaloys.

In the Zr-Sn-Nb-Fe(-Cr) system, ≤1 wt.% (~1 at.%) Nb is added in the commercial ZIRLO™, M5™ and the Russian E635 alloys, varying primarily in their Sn and Fe contributions. The excess of Nb above its solubility limit in α-Zr results in, most notably in the alloys mentioned, the Laves phase $Zr(Fe,Nb)_2$ (hcp, Fe/Nb = 0.38-1 (Shishov et al. 2010; Sabol et al. 1994)) and the β-Nb (bcc) phase. In E635, there has also been report of the T-phase $(Zr,Nb)_2Fe$ (Zr/Nb ~6) (Shishov et al. 2011). More recent developments in ZIRLO™ have been made to reduce the Sn content in order to improve corrosion properties (Yueh et al. 2005).

The response of various alloys to irradiation will be the subject of the remainder of this review. The alloys Zircaloy-2, -4 are the most relevant to this work and so will be assessed in detail. Other alloy systems will be referenced where appropriate but will not be considered explicitly. Point defects will start the discussion, their clustering and collapse into dislocation loops, and also the evolution of second phase particles, the resulting irradiation-induced precipitation and the evolution of grain boundaries.

2.3 INITIAL DAMAGE DUE TO DIFFERENT IRRADIATIVE SPECIES

The following is an overview of the primary interaction of a Zr atom with a neutron or high energy electron, proton or heavy ion, which lends itself to initial defect formation after the cooling phase and, ultimately, observable defect formation in the form of dislocation loops.

The interaction of thermal neutrons (energy 25.30 meV and wavelength 0.1798 nm) with Zr and its alloying elements are summarised in the final two columns of Table 1, in which the absorption cross section, σ_{abs}, and the scattering cross section, σ_{sct}, are given (Sears 1992). The low σ_{abs} of Zr makes it suitable as the cladding material such that neutrons are allowed to pass through it and not hinder the fission reaction nor become too radioactive itself. By comparison, σ_{abs}(U) = 545 x10^{-28} m^2 (fission), 100 x10^{-28} m^2 (capture) >> σ_{abs}(Zr) 0.2 x10^{-28} m^2. σ_{abs}(Fe) is 13 times that of σ_{abs}(Zr), and so Zr replaced much stainless steel cladding 50 years ago, the steel being favoured over Zr only for its excellent corrosion resistance and correspondingly low amounts of hydrogen formation (Hallstadius et al. 2012). A comparison of the scattering cross sections for Zr under neutron and proton irradiation at various energies is given in Figure 2-3, which demonstrates that the damage due to protons at 1 MeV or 2 MeV is significantly higher than that due to neutrons at 25 meV or 1 MeV. The displacement of a Zr atom from its lattice site by an incident neutron is called a primary knock-on atom (PKA), which itself can remove further atoms from their lattice sites, resulting in a cascade of displacements.

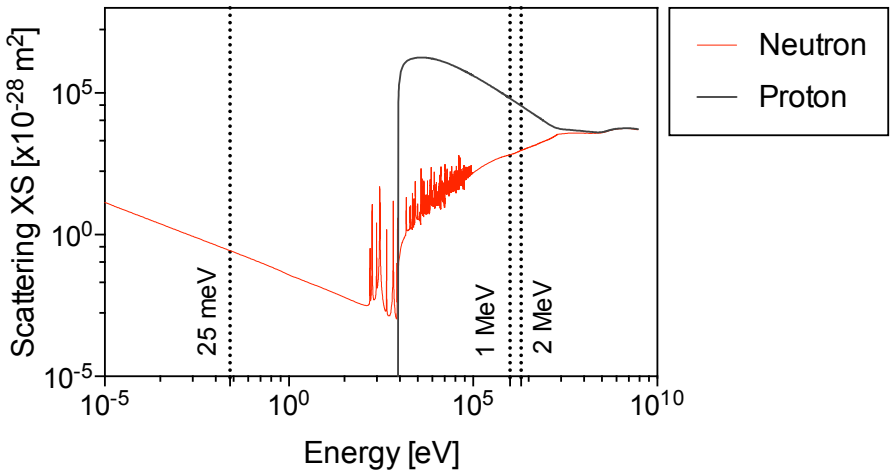

Figure 2-3 The scattering cross section for Zr for neutron (red) and proton (grey) irradiation at energy ranging 10-5 to 1010 eV. Thermal neutrons in a reactor core are at 25 meV, and fast neutrons 1 MeV. Proton irradiation are carried out at 2 MeV. Data calculated from NRT model, assuming displacement energy 40 eV, and was obtained from https://www-nds.iaea.org/exfor/endf.htm Sep 2015.

The modified Kinchin and Pease or the Norgett-Robinson-Torrens (NRT) model are the industry standard for calculating the damage in irradiated material, which state that the number of displaced atoms within the initial cascade, N_{NRT}

$$N_{NRT} = 0.4\overline{T} / E_d \quad \textbf{(2-1)}$$

from Ref. (Norgett et al. 1975), where $\overline{T}$ is the mean energy transferred to the PKA ~ 22 keV for a Zr PKA after collision with a fast 1 MeV neutron (Onimus & Bechade 2012), and E_d is the displacement energy for Zr from its lattice site ~ 40 eV (Was 2007). This simple calculation therefore predicts 220 atomic displacements per cascade event in Zr. However, recent molecular dynamics calculations have shown that, considering the thermal spike caused by the cascade and the interstitial-vacancy recombinations of both mono-defects and their clusters, the actual number of defects per cascade is ~20-25% of this value (Wooding et al. 1998; Gao et al. 2001), with more mono-vacancies than SIAs at a given temperature and more clustering of SIAs with respect to vacancies, as shown in Figure 2-4. The effect of

an increased lattice temperature from -127 to 327 °C is a decrease in the total number of defects (Gao et al. 2001).

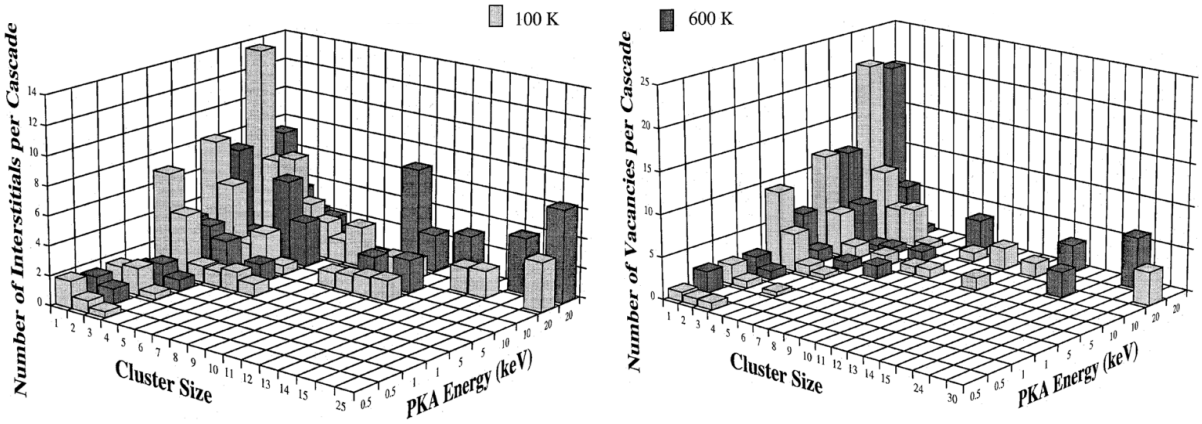

Figure 2-4 Interstitial (left) and vacancy (right) cluster numbers and sizes as a function of Zr PKA energy for 100 (light grey) and 600 K (dark grey). Adapted from (Gao et al. 2001).

The graphics in Figure 2-4 show that the energy transferred from the irradiative species to the PKA, $\overline{T}$, is significant in determining the final number of displaced atoms. Indeed, the early NRT model given in Equation (2-1) shows a directly proportional dependency of N_{NRT} on $\overline{T}$. Thermal neutrons have energy of ~25 meV and so will impart a much reduced $\overline{T}$ in comparison to that produced by the interaction with a fast neutron. A schematic by Was is given in Figure 2-5, in which the size of the damage cascade is directly related to the PKA energy and is given for different 1 MeV irradiative species incident on Ni (Was 2000); electrons produce single Frankel pairs (a mono-vacancy and -interstitial in close proximity), protons small damage clusters, heavy ions larger cascades and neutrons the largest size of cascade. The energy transferred to the PKA is given as $\overline{T}_e$, $\overline{T}_p$, $\overline{T}_i$, and $\overline{T}_n$, respectively, in increasing magnitude. The final rate of damage is also dependent on the particle flux and for Zr has been calculated as follows (format: species, damage rate (Ref.)): 1 MeV electrons, 7 x10^{-3} dpa s^{-1} (de Carlan et al. 1996); 2 MeV protons, 10^{-5} dpa s^{-1} (Zu et al. 2005); 1 MeV Kr^{+} heavy ions, 10^{-3} dpa s^{-1} (Idrees, Yao,

Kirk, et al. 2013); 600 keV Ne^{+} heavy ions, 10^{-3} dpa s^{-1} (Zu et al. 2005); and neutrons (LWR conditions), 0.7-1 $x10^{-7}$ dpa s^{-1} (Shishov et al. 2005; Adamson 2014). Therefore, electrons and heavy ions may give similar damage rates but different damage morphologies, and while the damage morphology of heavy ions is similar to that of neutrons, the damage rate of the former is much higher. High energy electrons have high damage rates because of the production of isolated Frenkel pairs. These single vacancy-interstitial pairs are widely spaced from the next Frenkel pair and so have less chance of interaction and annihilation. In contrast, the neutron-, proton and heavy ion-induced cascade and thermal spike induce some thermal recombination but create larger defect clusters. Additionally, the experimenter's choice of current, i.e. particle flux, is directly proportional to the damage rate and so explains the higher damage rate due to heavy ions in comparison to neutrons. Unfortunately, current densities and particle flux are not always reported in publications, which makes meaningful comparisons difficult. It should be noted that the dpa rates given for neutrons and other species are determined by the NRT model and the Kinchin Pease model (Stoller et al. 2013), respectively, and do not take thermal recombination and clustering directly into account.

2.4 POINT DEFECTS AND THEIR DIFFUSION

In a similar manner to cubic systems, the fundamental form of irradiation-induced damage takes the form of single self-interstitials (SIAs) and vacancies. Their configuration and diffusion within Zr are therefore essential to the explanation of microstructure evolution. The anisotropy of the hcp crystal ensures that irradiation-induced defects diffuse and accumulate under different reaction kinetics to the isotropic cubic case. In a review of computer models by Bacon (Bacon 1988), it is concluded that vacancy migration is only weakly anisotropic while Zr self-interstitial (SIA) diffusion is more so and that SIAs may exist in many different configurations within the hcp lattice.

Domain and Legris (2005) have more recently studied the SIA configurations shown in Figure 2-6 (Domain & Legris 2005), and found the most stable to be the octahedral (O), the basal octahedral (Bo) and the basal crowdion (Bc), with energies of formation E^f_o = 2.84, E^f_{bo} = 2.88 and E^f_{bc} = 2.95 eV. Further, the two-defect basal dumbbell (D_B) is one of the most stable (Woo 2000), although absolute values of E^f vary between publications (Vérité et al. 2013; Peng et al. 2014; Domain & Legris 2005). Indeed, polymorphism is expected and transition barriers between

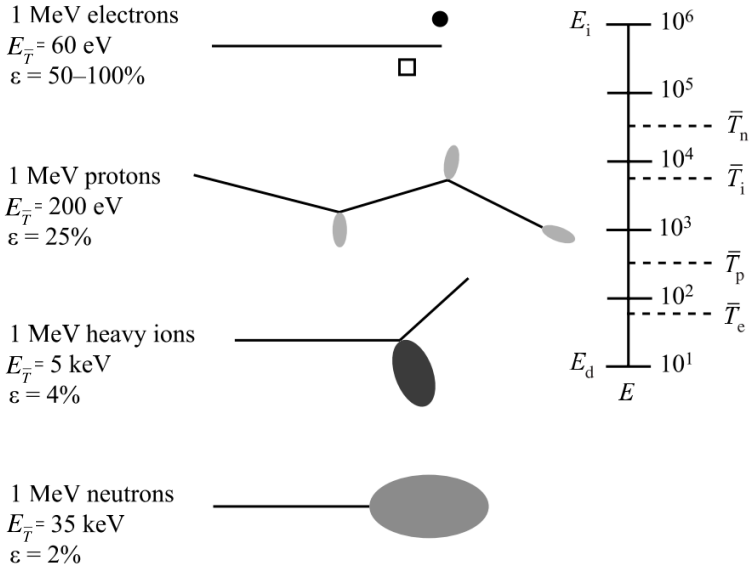

Figure 2-5 Schematic of 1 MeV electron, proton, heavy ion and neutron irradiation-induced damage morphology, PKA energy $E_{\bar{T}}$, the displacement efficiency, ε, and the energy transferred to the PKA, $\bar{\boldsymbol{T}}$ ($= \boldsymbol{E_{\bar{T}}}$) for different incident 1 MeV energetic particles in Ni. Adapted from (Was 2000).

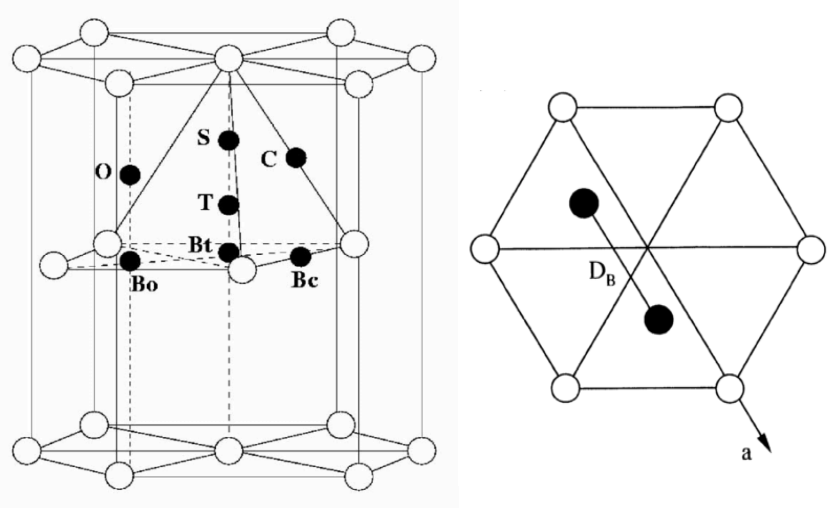

Figure 2-6 SIA configurations in the hcp Zr unit cell (Domain & Legris 2005), showing tetrahedral (T), octahedral (O), basal tetrahedral (Bt), basal octahedral (Bo), basal crowdion (Bc), non-basal crowdion (C).

configurations are easily accessible by thermal agitation (Bacon 1988). The stability of the various configurations depends on the *c/a* ratio. For Zr alloys, *c/a* < ideal, and so basal configurations have a lower formation energy and are preferred (Woo 2000). However, recent ab initio calculations by Vérité et al. (2013) demonstrated the stability of low-symmetry configurations within 0.4 eV of the basal octahedral. In addition, it has been shown that pressure effects can change the preference of one configuration over another (Peng et al. 2014).

The migration of the SIA takes place via jumps between configurations. There are two types of jumps: in-plane jumps between configurations such as Bo, Bt, or Bc; and out-of-plane jumps between configurations such as T, O or C. A difference in the energetics of the two types of jumps results in the anisotropy of SIA diffusion. The jump energetics depend on the *c/a* ratio, and are thought to be most isotropic as the *c/a* ratio approaches the ideal (Woo 2000). The diffusion coefficients for Zr SIAs and vacancies as calculated by Christensen et al. are as follows:

(2-2)
$$D_{SIA}^{av} = 5.5 \times 10^{-8} e^{-9.4/(RT)}$$

(2-3) $$D_{SIA}^{axial} = 3.4 \times 10^{-9} e^{-7/(RT)}$$

(2-4) $$D_{SIA}^{basal} = 4.44 \times 10^{-9} e^{-3/(RT)}$$

(2-5) $$D_{V}^{axial} = 9.87 \times 10^{-6} e^{-73/(RT)}$$

(2-6) $$D_{V}^{basal} = 8.62 \times 10^{-6} e^{-69/(RT)}$$

Equation (2-2), (2-5) and (2-6) are from (M. Christensen et al. 2015) and Equation (2-3) and (2-4) are from (Christensen et al. 2014), where each diffusion coefficient is in units of m^2 s^{-1} and each activation energy (Q in the exponential term $e^{-Q/(RT)}$) is given in units of kJ mol^{-1}. It should be noted that Equation (2-3) and (2-4) were derived after Figure 6 of Ref. (Christensen et al. 2014) and so are approximations of the present author's, although the values of Q are those given by Christensen to the nearest kJ mol^{-1}. Additionally, the diffusion of vacancies in Equation (2-5) and (2-6) was calculated by ab initio quantum mechanical methods and that of SIA diffusion in Equations (2-2) - (2-4) by molecular dynamics, making the accuracy of the former better than the latter. Indeed, the average SIA diffusivity, D and Q, given in (2-2) is greater than that of either the axial or basal given in (2-3) and (2-4), respectively, which is a little confusing. A graphical description of Equations (2-3) - (2-6) is given in Figure 2-7, in which it can be seen that that the diffusion rate of Zr SIA basal > SIA axial > vacancy basal > vacancy axial, the anisotropy of SIAs being much greater than that of vacancies. As a useful example, at 300 °C after 1 hr, the Zr vacancy will have diffused ~0.1 mm and the interstitial 5-10 times this distance (M. Christensen et al. 2015), assuming no recombination.

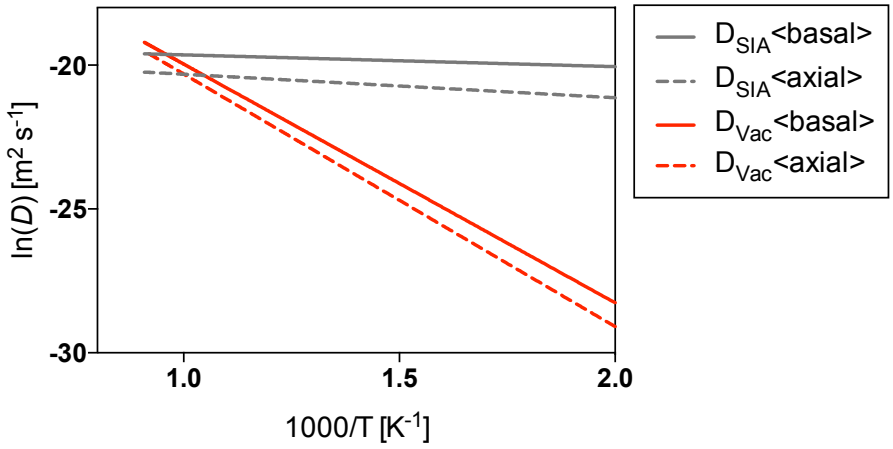

Figure 2-7 Natural log of diffusivity (*D*) in the basal plane, <basal>, and axial direction, <axial>, of Zr self-interstitials (SIA) and vacancy (Vac) defects in α-Zr as a function of temperature.

The work of Christensen is thorough and expands that described here to the diffusivities of H and O, and while the magnitudes and trends of diffusivities are similar to those calculated by other methods (Woo & Liu 2007) the diffusion coefficient values of SIAs and vacancies by Christensen are several orders of magnitude higher than that expected from experimental data (Hood et al. 1995; Perez et al. 2003), putting the diffusivity of Zr SIAs in the same regime as that of the notoriously fast diffusers, interstitial Fe and Ni (Hood 1988). This may arise from a difficulty in experimentally separating interstitial and vacancy diffusion or a difficulty in theoretical cells large and diverse enough to simulate real systems. However, Zr self-diffusion has been shown as higher than that of Fe, Ni at high temperatures close to the β-transus (Perez et al. 2003) and the presence of interstitials, especially of Fe (King et al. 1991; Pérez & Weissmann 2008), have been shown to increase the diffusivity of Zr within α-Zr by the low energetic barrier to migration of the Fe-vacancy pair. The presence of substitutional atoms, such as Sn and Nb, causes a decrease in self-diffusion rates (Christensen et al. 2014). As such, experimental determinations of SIA diffusivity will be affected by impurities in addition to other factors affecting diffusion, such as temperature and local stress. Calculations to include stress contributors have shown that changes in the external pressure causes different configurations to be preferred (Peng et al.

2014) and changes in local *c/a* ratio cause a change in diffusional anisotropy; calculated as decreasing from SIA diffusional anisotropy at no strain, D_{basal}/D_{axial} = 195 at 278 °C, to D_{basal}/D_{axial} = 5 with an increase in the *c/a* ratio of 0.5% and D_{basal}/D_{axial} < 1 for an increase in *c/a* of 0.5-0.75% (M Christensen et al. 2015). Using radiotracers, Hood (Hood et al. 1995) showed experimentally that in high purity α-Zr, SIA D_{basal}/D_{axial} = 1.89 at 838 °C, which is very different in magnitude with respect to that calculated in Ref. (M Christensen et al. 2015), but still shows a preference for basal diffusion. However, when Fe impurities are present then the anisotropy D_{basal}/D_{axial} = 1 at 835 °C and 0.32 at 596 °C, indicating that the encouragement of Zr self-diffusion by Fe may cause a preference of Zr diffusion in the <c> direction, although this has not been confirmed by simulations.

While Zr is generally thought of as preferentially diffusing in the basal plane, Fe, Ni and Cr are believed to be anisotropic with a strong preference for diffusion in the <0001> direction (Perez et al. 2003; Christensen et al. 2014), the diffusivity of Fe and Ni being much higher than that of Cr, which is conventionally explained by a metallic radii effect (Perez et al. 2003). The preferable configurations of atomically dispersed Fe, Ni and Cr have been computationally assessed (Christensen et al. 2014) and are predominantly thought of interstitial or of taking off-site substitutional positions. Christensen showed that substitutional Fe, Ni, Cr will swap with a neighbouring Zr SIA (Christensen et al. 2014), restoring the Zr lattice and creating an Fe, Ni, Cr interstitial, a mechanism initially proposed by Hood (Hood 1977). However, the consideration of interstitials such as Fe as atomically dispersed may be inconsequential, as clusters form quickly (Burr et al. 2015) with short Zr-Fe bond distances that are possibly the precursors of intermetallic phases such as Zr_3Fe (Yoshida et al. 1990; Perez et al. 2003; Pérez & Weissmann 2008) and the Zr-(Fe,Cr,Ni) types (Christensen et al. 2014).

2.5 DEFECT CLUSTERS, THEIR DIFFUSION AND EARLY DISLOCATION LOOP FORMATION

As briefly discussed in §2.3, molecular dynamics simulations of cascade events have demonstrated the formation of both mono-defects and their clusters after the

cooling phase (Wooding et al. 1998; Gao et al. 2001; Was 2000). Small interstitial clusters with the number of mono-defects n ≤ 30 were studied by de Diego et al. and shown to be most stable on $\{11\bar{2}0\}$ planes (de Diego et al. 2002). The most stable four-SIA cluster was considered to be the building block of larger clusters (de Diego et al. 2002; de Diego et al. 2008) and is shown in Figure 2-8 as four $[\bar{1}2\bar{1}0]$ crowdions in adjacent $(\bar{1}2\bar{1}0)$ planes. Larger SIA rectangular clusters have also been shown to habit the $\{11\bar{2}0\}$ planes (de Diego et al. 2008) with little effect of the rectangular orientation (long axis in <0001> or (0001)) on the formation and binding energies but a higher degree of perfection of the lattice in the centre of the cluster for those that have their long axis in the <0001> direction. Between publications, the Burgers vector is consistently $\frac{1}{3}<11\bar{2}0>$ for SIA clusters (de Diego et al. 2002; de Diego et al. 2008; Gao et al. 2001; Wooding et al. 1998) with increasing perfection of the lattice in the centre of the cluster for larger clusters (de Diego et al. 2008).

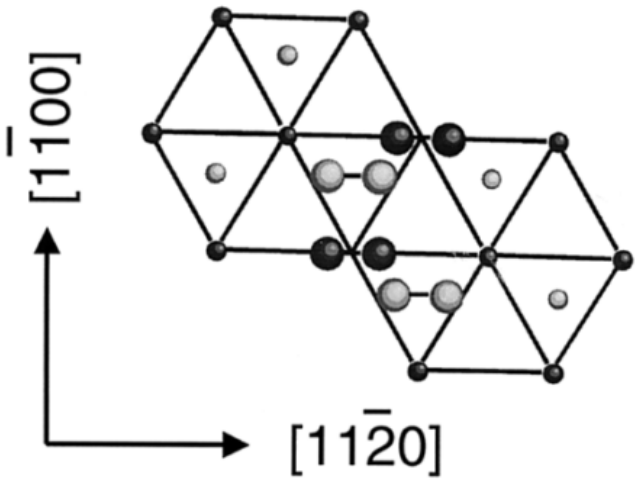

Figure 2-8 The most stable four-SIA cluster; four closely-packed $[11\bar{2}0]$ crowdions in two adjacent $(\bar{1}2\bar{1}0)$ planes.

Varvenne et al. studied small vacancy clusters in Zr by both ab initio DFT and hybrid empirical approaches to show that the binding energy, and therefore the stability, of clusters increases with n up to n = 7, with the most stable configurations as 3D clusters, i.e. voids (Varvenne et al. 2014). For planar clusters, i.e. the precursors to dislocation loops, the prismatic $\{10\bar{1}0\}$ plane was found to be more stable than the basal for clusters of $n \geq 5$, with clusters displaying dislocation characteristics such as a Burgers vector $\frac{1}{2}<1\bar{1}00>$ or $\frac{1}{3}<11\bar{2}0>$, depending on cluster size. For clusters of $n < 150$ (radius r ~2 nm) the $\frac{1}{2}<1\bar{1}00>$ Burgers vector is preferred, for $150 < n < 250$ (r ~2-2.7 nm) both $\frac{1}{2}<1\bar{1}00>$ and $\frac{1}{3}<11\bar{2}0>$ are observed, and for $n > 250$ (r ~2.7 nm) the $\frac{1}{3}<11\bar{2}0>$ Burgers vector is preferred (Varvenne et al. 2014). Like Varvenne et al., de Diego et al. used empirical potentials in simulations to show that the most stable clusters for $n \leq 10$ are 3-dimensional (de Diego et al. 2011), which is also supported by the calculations of Kulikov and Hou (Kulikov & Hou 2005). Similarly, both groups showed that next nearest neighbour defects are the most thermodynamically stable for the di-vacancy. However, the differences in results obtained when using different empirical potentials becomes apparent as Varvenne et al., showed that the next nearest neighbour is stable when on adjacent basal planes and de Diego et al. showed that that same configuration is unstable with respect to dissociation. Varvenne et al. compared their empirical potential results to agreeing ab initio DFT calculations to solidify their position on the matter, although there were differences between the absolute binding energies obtained by the different methods; the empirical methods used overestimated the stability of vacancies due to the neglected interatomic angular dependence on stability (Varvenne et al. 2014). Additionally, de Diego et al. showed that, for $n \leq 10$ vacancy platelets, those in the $\{11\bar{2}0\}$ planes are more stable than those in the $\{10\bar{1}0\}$ and for $40 < n < 120$ the most stable are in the basal planes, which does not agree with either Varvenne et al.'s larger cluster data or experimental observations of the exclusively prismatic habit planes of a-component dislocation loops (a-loops) in irradiated Zr (A. Jostsons et al. 1977; A Jostsons et al. 1977; Griffiths 1988). This criticism is based on the assumption that the clusters are precursors to a-loops; clusters on the basal plane as precursors to c-component dislocation loops (c-loops) would be more

fitting to the results, although the Burgers vector expected from experiment, namely $\frac{1}{6}<20\bar{2}3>$, was not observed. de Diego et al. has noted that clusters showing Burgers vector $\frac{1}{6}<20\bar{2}3>$ character would need to be larger in size than previously studied (de Diego et al. 2008).

More detailed work on vacancy clustering by de Diego et al. showed that rectangular clusters on prismatic planes showed that there was little effect of the rectangle dimensions on stability (de Diego et al. 2008). Indeed, for cluster sizes n < 150 there was little effect of configuration on stability. Interestingly, all vacancy and SIA clusters had dislocation-like character in their Burgers vector $\frac{1}{3}<11\bar{2}0>$ and the habit plane of the clusters were shown to incline slightly to the $\{11\bar{2}2\}$ plane after picosecond time-scale annealing. However, the fixed boundary conditions used in this work were not well justified; indeed, work by Woo and Liu has shown that satisfactory convergence was difficult to obtain in systems with less than 10^4 atoms surrounding a single point defect (Woo & Liu 2007). While de Diego et al. used between 1.5 x10^4 and 1 x10^5 atoms 'depending on the defect size and shape' (de Diego et al. 2008), little information was given by the authors regarding any investigation into the suitability of this for defects that are large relative to Woo and Liu's mono-interstitial and vacancy simulations.

Both interstitial and vacancy clusters exceeding *n* > 25-30 are rarely observed in MD calculations of cascades and have shown to collapse into both vacancy and interstitial dislocation loops on the $\{10\bar{1}0\}$ planes with Burgers vector $\frac{1}{3}<11\bar{2}0>$ (Gao et al. 2001) although vacancy loops on the same habit plane but with Burgers vector $\frac{1}{2}<10\bar{1}0>$ have been suggested for the smallest of loops (Varvenne et al. 2014; Wooding et al. 1998). The formation energy of vacancy and interstitial clusters/loops of similar sizes and shapes are similar but the binding energy of the former is lower than the latter (de Diego et al. 2008), suggesting a lower stability of vacancy clusters. SIA clusters are not sessile as previously assumed (Holt et al. 1993), but have been shown for clusters of all sizes to glide along the Burgers vector direction $<11\bar{2}0>$ (de Diego et al. 2002; de Diego et al. 2008). For small SIA

clusters, mobility is highly dependent on geometry, the configuration given in Figure 2-8 being the most mobile four-SIA cluster at 328 °C with other four-SIA clusters collapsing into this stable geometry at this temperature (de Diego et al. 2002). Perfection of the lattice at the core of the SIA cluster has been shown as an important factor in cluster glide, with clusters as small as 24 SIAs having 'almost perfect' cores (de Diego et al. 2008). While the most stable configuration of clusters is the basal crowdion (de Diego et al. 2011), diffusion of this di-SIA cluster in the <0001> direction in a helical motion has only be discussed by Vérité et al. in a thorough ab initio DFT investigation into non-symmetric sites of SIA occupation in the hcp Zr lattice (Vérité et al. 2013). While the $<11\bar{2}0>$ crowdion is the basis of the SIA cluster structure, its Burgers vector and its glide plane, the mobility of vacancy clusters is less well reported in the literature, which is reflected in the fast diffusion of mono-SIAs with respect to vacancies and hence the proposed importance of the former (M. Christensen et al. 2015).

The interaction of point defects with pre-existing dislocation loops or larger clusters is of interest to the nucleation and growth of dislocation loops, which are essential observations that are believed to contribute to irradiation-induced growth. In 1983, Woo and Savino demonstrated in cubic-based Cu and Fe that the nature of a dislocation loop, vacancy or interstitial, and the orientation anisotropy of its strain field will affect the saddle point energies of interactions with point defects (Woo & Savino 1983). More recently, Kulikov and Hou have demonstrated that a single SIA will interact differently with a basal vacancy loop depending on the orientation of the loop with respect to the point defect (Kulikov & Hou 2005). For instance, it was shown that an SIA will diffuse in the basal plane until it is aligned with the mis-coordinated region of the vacancy loop, at which point it will diffuse along <0001> to the mis-orientated region. However, if an SIA is located in the plane of the loop then the SIA either will or will not migrate along the basal plane to the region of misorientation for recombination, depending on the position of the SIA in that plane. This is a demonstration of how defects of opposite nature may habit the same plane. The interaction of larger clusters and dislocation loops is of course computationally demanding, although there is no doubt that such studies will be the focus of future work.

2.6 IRRADIATION-INDUCED GROWTH PHENOMENA

The following is an account of macroscopic irradiation-induced growth (IIG) deformation processes and how they relate to various alloy parameters, such as grain size, temperature, degree of prior mechanical deformation and alloy type. While much of IIG is explained through the diffusion of point defects (Woo & Göslel 1983), such phenomena are not resolvable by microscopic techniques. The effect of point defects will be considered in §2.7, and microstructural contributions to macroscopic phenomena will be referenced throughout but will be given specific consideration in §2.8.

Zr alloys exhibit IIG, which is independent of an applied stress and is characterised by a volume-conservative shape change. Pilgered, recrystallised, single phase α-Zr alloy tube has a texture corresponding to grain <0001> axes orientated to ±20-40° in the radial direction (Mahmood et al. 2000; Tenckhoff 2005). As such, the majority of <c> axes are radially aligned and the majority {0001} basal planes are aligned parallel to the axial direction of the tube. Irradiation-induced changes in individual grain morphology is anisotropic along <c> and <a> directions will therefore contribute to macroscopic deformation along the corresponding textured tube axes. In power reactors, Zr alloy cladding tube grows in the axial direction and contracts in the radial, which Buckley first attributed to dislocation loops of interstitial and vacancy nature on prism and basal planes, respectively (Buckley 1961). The current framework for describing IIG includes Buckley's postulations, adding to it the implications of an anisotropic diffusion of point defects in the hcp lattice (Woo & Göslel 1983; Woo 1987; Woo 1988). The role of small defect clusters is becoming an important aspect to include in Woo's diffusional anisotropy difference model, as well as the concept of a bias in the production of defects themselves (Woo & Singh 1992; Holt et al. 1993). An analysis of such mechanistic understanding will be given in §2.7; the current section will describe observed phenomena.

The relationship between IIG strain and the dose received by the alloy is complex. The pre-existing microstructure, determined by the thermomechanical history of the material, the orientation relationship between grains, grain size and shape, the

irradiation temperature and flux, the type of irradiating species and the microstructural evolution of the alloy during irradiation all contribute to the IIG behaviour.

2.6.1 IIG: MACROSCOPIC PHENOMENA

The macroscopic IIG behaviour of recrystallised (RX) material is reflected in the experimental axial IIG curve for Zircaloy-2 shown in Figure 2-9. The RX IIG curve is characterised by three stages. The first stage is the initial transient, in which there is a rapid increase in IIG strain with respect to increasing neutron fluence. This high rate of growth plateaus after low irradiation fluences of < 0.5-1 $x10^{25}$ n m^{-2} (Rogerson 1988; Fidleris et al. 1987) ~0.8-1.6 dpa. The second stage is a steady-state such that the growth strain is constant with increasing fluence up to ~3-5 $x10^{25}$ n m^{-2} (Holt 1988) ~5-8.3 dpa, after which the final stage is accelerated growth or 'breakaway', in which the growth rate increases rapidly. To briefly touch on the related microscopic phenomena, small dislocation loops up to 30 nm in diameter of both vacancy and interstitial nature are observed throughout the irradiation. Such loops are termed a-loops due to their <a>-component Burgers vector $\frac{1}{3}<11\bar{2}0>$ and habit planes $\{10\bar{1}0\}$ (A Jostsons et al. 1977; Griffiths 1988). There is a delay in the nucleation of c-loops, <c>-component dislocation loops of Burgers vector $\frac{1}{6}<20\bar{2}3>$ that order parallel to basal planes, which increase rapidly in size and number density during the breakaway regime (A. Jostsons et al. 1977; Griffiths 1988; Griffiths et al. 1989).

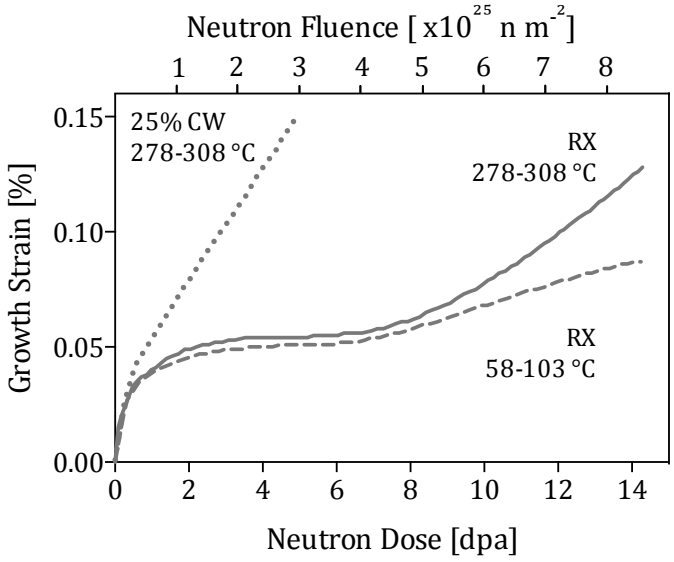

Figure 2-9 IIG curve for Zircaloy-2 in condition RX at 278-308 °C, RX at 58-103 °C, and 25% CW at 278-208 °C, adapted from (Griffiths 1988; Griffiths et al. 1989).

2.6.2 THE EFFECT OF GRAIN BOUNDARIES

Single crystal pure Zr demonstrates <a>-axis expansion and <c>-axis contraction although no saturation stage is observed (Rogerson & Zee 1987). The role of grain boundaries in accelerating the mechanisms of IIG is demonstrated by the higher saturation growth strain of polycrystalline pure Zr in comparison to that of the single crystal (Carpenter et al. 1988). Polycrystalline, pure Zr shows no breakaway regime at 280 °C and even less IIG strain at 80 °C (Rogerson 1988), although there is evidence for accelerated growth at higher temperatures (Holt 1988). Therefore, as might be expected, the effect of grain size on IIG strain is inversely proportional (Fidleris 1988), with small-grained Zr (~5 μm) experiencing higher growth strains than large-grained Zr (~40 and up to 225 μm), this effect increasing with temperature (Griffiths et al. 1989). The study of grain boundary area as a sink for point defects and their clusters is uncommon in the literature, although the orientation of a grain boundary with respect to a defect's preferred diffusion path is included in current theories of IIG mechanisms (Woo 2000). However texture, local orientation relationships and grain boundary structure is not.

2.6.3 THE EFFECT OF TEMPERATURE

The effect of an increase/decrease in temperature is to increase/decrease the IIG kinetics in terms of both saturation strain and breakaway strain, even shortening/delaying the onset of the breakaway regime. This effect can be observed in Figure 2-9 in the IIG behaviour of Zircaloy-2 at temperature ranges 58-103 °C and 278-308 °C as dashed and continuous lines, respectively. This direct relationship between temperature and growth rate is observed for many single phase α-Zr alloy systems (Holt 1988). Holt studied higher temperature growth rates in the 350-425 °C temperature range (Holt et al. 1993). As a high density of vacancy c-loops are observed to correlate with the breakaway regime of growth (Griffiths 1988), Holt postulated that the higher growth rates at higher temperatures were due an increase in the nucleation and growth of vacancy c-loops on basal planes. As an extension of the production bias model (Woo & Singh 1992), Holt argued that higher temperatures cause the evaporation of vacancies from vacancy clusters, which results in a higher density of mono-vacancies that are faster diffusing than their clusters. Subsequently, mono-vacancies are able to diffuse to dislocations, increasing their size and/or number density and hence increasing growth strain. Of course, a similar argument could be made for self-interstitials (SIAs) and their clusters. However, recent ab initio studies into defect clusters show that SIAs are only mobile along their Burgers vector (Osetsky et al. 2000; de Diego et al. 2002; de Diego et al. 2011) and this must be included in future models of IIG (Golubov et al. 2015). The relationship between temperature and IIG strain ends at temperatures of ~500 °C, above which decreasing IIG strain is observed as defect annihilation processes become dominant (Fidleris 1988).

2.6.4 THE EFFECT OF COLD WORK

From Figure 2-9 it can be also seen that cold work (25% CW, dotted line) causes an increase in the IIG rate from the very start of irradiation, with no saturation stage. This suggests that the dislocation networks and the reduced grain sizes associated with deformation aid the kinetics by which IIG operates. An increase in cold work, the corresponding increase in dislocation density and increase in IIG strain is well known (Fidleris 1988; Fidleris et al. 1987; Rogerson 1988; Griffiths 1988). The c-

component network dislocations produced by cold work are thought to be the dominant vacancy sinks in such materials. Interestingly, the vacancy c-loops that are normally associated with breakaway growth are not observed in cold-worked materials at temperatures ≤ ~310 °C (Griffiths 1988), most likely due to the relatively high sink strength of the network dislocations.

2.6.5 IIG PHENOMENA IN DIFFERENT ALLOY SYSTEMS

The reason for the steady-state delay of the accelerated growth regime in recrystallised (RX) material remains under discussion, as does the mechanism of c-loop nucleation and growth. It is difficult to report at exactly what dose level an alloy undergoes breakaway, as the transition point and the post-breakaway growth rate depends on irradiation temperature, dose rate, the pre-existing microstructure and second-phase particle (SPP) microchemistry and the evolution of all microstructural parameters during irradiation. Therefore, within an alloy family, there is some variation in the dose to acceleration. While most fall within a few dpa of each other, the damage rate in light water reactors is typically ~3.2 dpa yr^{-1} (Shishov et al. 2005; Adamson 2014), and so differences between alloys and under varying conditions is essential to understand.

The irradiation-induced growth (IIG) behaviour of Zircaloy-2 can be seen in Figure 2-9 and has been discussed in §2.6.1. Although there is much literature providing irradiation-induced growth (IIG) data for Zircaloy-2 under various metallurgical and irradiation conditions (Griffiths et al. 1989), there is comparably less information available regarding the IIG behaviour of Zircaloy-4. The development of Zircaloy-4 over -2 was motivated by a decrease in the hydrogen (denoted H, although its atomic nature is questionable) absorption of the former by half with respect to Zircaloy-2, while retaining similar oxide growth properties (Whitmarsh 1962). However, while an increase in IIG strain has been correlated with an increase in H uptake (Valizadeh et al. 2014), the IIG behaviour of Zircaloy-2 and -4 are thought of as very similar (Holt 1988) with accelerated growth occurring at neutron fluence 3-4 $x10^{25}$ n m^{-2} at 280-297 °C (Griffiths et al. 1995). This is surprising given that the nominal composition of Zircaloy-4 replaces the 0.03-0.08

wt.% Ni in Zircaloy-2 with Fe (Hallstadius et al. 2012), and, as a result, the microstructures of the two alloys are quite different with respect to SPP type and number density. Several different conclusions may be drawn from such observations, but it is possible that Ni and Ni-containing SPPs trap H, increasing H uptake during oxidation. This has recently been shown to be true for the bct Zr_2Ni phase in DFT calculations concerning the accommodation of H within various Zr-containing phases (Burr et al. 2013), although the authors suggested that the presence of Fe in $Zr_2(Fe,Ni)$ would reduce the SPP's affinity for H. Additionally, ignoring any differences in texture and grain size, it is either the case that Fe, Ni and H all act in a similar manner with respect to IIG in Zr-Sn-based systems or that they all contribute very little to IIG behaviour, resulting in the similar IIG characteristic of Zircaloy-2 and -4. The former of these postulations is most likely given that the microstructure evolution, correlated with macroscopic phenomena, has been demonstrated as dependent on microchemical changes (Griffiths 1988; de Carlan et al. 1996). Further, the diffusivities of Fe and Ni are known to be similar (Hood 1988) and Christensen et al. have recently shown that the anisotropic <c>-preference for diffusion and the interstitial/substitutional behaviour of Fe and Ni in α-Zr are similar (Christensen et al. 2014). As such, the interaction of Fe and Ni with defects that contribute to IIG, such as vacancy dislocation loops and grain boundaries, may be comparable. With respect to H, Christensen found that its diffusivity is slower than that of Fe and Ni, but as the rate of damage in the reactor core is typically ~3.2 dpa yr^{-1} (Shishov et al. 2005; Adamson 2014), small differences in diffusivity may be inconsequential.

The role of Sn in IIG is not clearly defined. The IIG characteristics of Zr-Sn binary alloys have been utilised to some extent to determine the effect of Sn in comparison to commercial alloy systems. At an irradiation temperature of 80 °C, the IIG strain of pure Zr ~ Zr0.1Sn > Zr-1.5Sn (wt.%) ~ Zircaloy-2, whereas at temperature 280 C, the IIG strain of pure Zr ~ Zircaloy-2 ~ Zr0.1Sn < Zr1.5 Sn (wt.%) (Zee et al. 1984; Rogerson & Zee 1988). This is explained by the authors as the trapping of vacancies (such that they cannot contribute to IIG strain) by Sn at low temperatures, which is 'ineffective' at higher temperatures (Zee et al. 1984; Rogerson & Zee 1988). While this cannot account for the changes in Zircaloy-2

behaviour observed, there is evidence for the trapping of vacancies by Sn at these low temperatures by positron annihilation spectroscopy measurements (Hood 1977; Hood 1988) and recent calculations have shown that Sn may repel Zr self interstitial atoms (Christensen et al. 2014). Further, there is evidence to suggest that, at intermediate temperatures, Sn acts as a barrier to the diffusion of defects (Gilbert et al. 1979). Unfortunately there is a significant lack of investigation in the literature in regards to the effect of Sn on IIG, which is surprising due to its addition to many alloys for the purpose of solid solution strengthening (Sabol 2005) and α-phase stability (Okamoto 2010).

In the Nb-containing families of Zr alloys, it is the more complex alloys containing transition metal elements that have the most IIG resistance. The Russian E110 and E125, binary alloys containing 1 and 2.5 wt% Nb, respectively, have quite low IIG resistance, both alloys experiencing accelerated growth kinetics at 10-15 dpa (Shishov et al. 2005). However, E110 (RX) has such a high rate of IIG that its growth strains at high doses are higher than that of many other alloys, including Zy-2 and -4 (RX, CW, SR), E125 (RX) and E635 (RX, SR) (Shishov et al. 2005). Interestingly, the addition of 0.04-0.10 wt% Fe and ≤0.15 wt% O to E110 causes the onset of breakaway growth to delay to a higher dose of > ~15 dpa. The addition of alloying elements to the composition found in E635 causes a dramatic decrease in the IIG kinetics, to the extent that breakaway growth is not observed in the E635 alloy in any metallurgical condition under neutron irradiation to very high doses of 30 dpa (Shishov et al. 2005). In the same study, E635-type alloys with various Fe contents were neutron-irradiated to show that acceleration in IIG was found for low Fe contents (0.15 wt%), but at higher Fe contents (0.35 and 0.65 wt%), acceleration was not observed. This demonstrates that Fe is necessary in Nb-containing alloys for the delay of breakaway growth. Conversely, in Zy-4 alloys doped with various amounts of Fe, it was found that the density of <c>-component dislocation loops under electron-irradiation increases with increasing Fe content (de Carlan et al. 1996). As a higher c-loop density is correlated with higher growth strains (Holt & Gilbert 1986), a higher Fe content in Zr-Sn-based alloys may be expected to increase growth strain. The discrepancy in the behaviour of Fe between these two types of alloys demonstrates that Fe does not act alone in its

role in IIG, but that there is a complex interplay between alloying elements and the structure-phase state that they create in their respective alloys. Microstructural and microchemical evolution under irradiation is therefore a highly significant topic of study with respect to IIG phenomena in Zr alloys, and shall be the subject of the remainder of this review.

2.7 FUNDAMENTAL EXPLANATIONS OF IRRADIATION-INDUCED GROWTH

Originally suggested by Buckley in 1961 (Buckley 1961), the underlying explanation for the irradiation-induced <a>-expansion and <c>-contraction, IIG, is the formation of interstitial dislocation loops on prismatic planes and that of vacancy loops on basal planes. Buckley's explanation is valid at higher irradiation doses where vacancy c-loops, aligning parallel to the trace of the basal plane, are effective vacancy sinks, first observed by Jostsons et al. in 1977 (A. Jostsons et al. 1977). However, in the pre-breakaway regime of IIG interstitial and vacancy a-loops coexist on prismatic planes (Griffiths 1988). Given such observations and their suspected contribution to IIG, the formation of dislocation loops has been a topic of much study, as has the diffusion of mono-defect Zr self interstitials (SIAs), vacancies and their clusters (de Diego et al. 2011; de Diego et al. 2002; de Diego et al. 2008; M Christensen et al. 2015; Hood 1988; Hood 1977; Hood et al. 1995).

In 1988, a review of the mechanistic understanding of IIG was published by Holt (Holt 1988), the most persuasive arguments being those proposed by Woo and Gösele in 1983 (Woo & Göslel 1983; Woo 1987; Woo 1988). Woo's diffusion anisotropy difference (DAD) model suggested that vacancy diffusion is isotropic and interstitial diffusion anisotropic with a preference for basal diffusion, and so the expansion in the <a>-direction contraction in the <c> is readily explained; SIAs diffusing in the basal plane expand <a> and net vacancy diffusion in the perpendicular direction contract <c>. Other observations, such as a-loop spatial ordering and their ellipticity can also be explained by DAD theory, as well as sink bias and the dependence of sink strength on the geometrical orientation of the sink with respect to the crystal lattice (Woo 2000). For instance, grain boundaries and dislocation lines lying perpendicular to the direction of net point defect diffusion would act as effective sinks for those defects.

The question of the coexistence of both interstitial and vacancy a-loops on prismatic habit planes has been addressed by Woo as the relative neutrality of loop nature as a sink (Woo 1988). Experimentally, interstitial and vacancy a-loop coexistence has been explained by their spatial ordering; vacancy a-loops have been shown as aligning in rows parallel to the trace of the basal plane and interstitial a-loops lying in between these rows (Griffiths 1988; A Jostsons et al. 1977). Different capture volumes for vacancy and interstitial a-loops has been determined for circular loops using non-linear elasticity theory (Wolfer & Si-Ahmed 1980), with the capture efficiency of interstitial a-loops greater than that of vacancy up to a loop radius of ~50 nm. Indeed, a-loops have a maximum radius of ~30 nm in neutron-irradiated pure Zr (A Jostsons et al. 1977), the loops decreasing in size upon alloying (Griffiths 1988). In explanation of the different capture volumes of interstitial and vacancy a-loops (Wolfer & Si-Ahmed 1980), anisotropic configurations of point defects in their saddle points before capture has been suggested as a source of bias between vacancy and interstitial loops (Woo 1982), although the effect of loop size was unclear in this work. Alternatively, numerical calculations of loop sink strengths have demonstrated that loop size is an important factor in capture efficiency (Dubinko et al. 2005; Rouchette et al. 2015; Bullough et al. 1979), and can account for a net flow of vacancies to large loops and SIAs to smaller loops, consistent with the large size of vacancy c-loops in comparison to interstitial a-loops at high irradiation doses (Cockeram et al. 2011).

One of the criticisms of DAD theory is its focus on the diffusion of point defects and the neglect of defect clusters. The production bias model (PBM) was developed by Woo and Singh in cubic systems for predicting SIA and vacancy cluster behaviour due to the cascade event (Woo & Singh 1992). The primary focus in the PBM is that there is a difference in the net production of point defects due to the cascade event, its thermal spike and the energies of formation of various defect types. Additionally, the mobility of the generated point defects are also different in terms of energetic barriers to migration, and most importantly the mobility of various sinks, such as un/faulted dislocation loops and networks, have a bias in terms of

their ability to climb and/or glide. The interaction of moving sinks and point mono-defects with clusters is the basis of PBM and Holt et al. demonstrated its suitability in predicting the increase in IIG rates at high temperatures > 400 °C (Holt et al. 1993). However, its application to hcp systems, and in particular to Zr by Holt (Holt et al. 1993), assumed the clusters to be immobile, which, as has been discussed in §2.5, is not the case; small clusters have been calculated as mobile in three dimensions and larger clusters in one dimension along the cluster's Burgers vector (de Diego et al. 2008; de Diego et al. 2011). In response to this exclusion of cluster mobility and the questionable assumption of a-loop glide without an externally-applied stress, Golubov at al. (2005) employed the exclusive use of the PBM for an explanation of all stages of IIG in Zr (Golubov et al. 2015). As an interesting concept, the authors showed that the coexistence of interstitial and vacancy a-loops could be explained by an anisotropic distribution of a-Burgers vectors with respect to the three-fold multiplicity of $\frac{1}{3}<11\bar{2}0>$. However, the authors claim that this is not explainable by DAD theory, which, as discussed earlier, is not completely true (Woo 1988). Further, it is unclear as to why there would be an anisotropic distribution of a- Burgers vectors. Additionally, Golubov et al. explicitly neglect the DAD between vacancy and Zr SIA point defects, which is well accepted within the community and has much computational and experimental evidence (M. Christensen et al. 2015; Christensen et al. 2014; Bacon 1988; Holt 1988; Hood et al. 1995). Importantly, the authors neglect the anisotropy of point defect saddle points upon their interaction with dislocations, which has been described by Woo in detail (Woo & Savino 1983).

A combination of both DAD theory and the PBM has been successful in describing IIG phenomena under various temperature conditions and metallurgical thermomechanical histories (Woo & Liu 2007). However, the different approaches are used under different conditions without a full explanation as to why. An all-encompassing theory that includes the established DAD of mono-defects and the new data concerning cluster mobility remains elusive, but the approach is far from phenomenological and is useful in its predictions of IIG under a wide variety of conditions. Lastly, a discussion of a-loop mobility is lacking in the literature. While perfect a-loops are thought of as glissile and faulted c-loops sessile, a driving force

for their mobility is questionable and much of the PBM with respect to Zr is dependent on such an assumption (Holt et al. 1993; Woo & Liu 2007).

2.8 MICROSTRUCTURAL AND MICROCHEMICAL EVOLUTION OBSERVATIONS

The behaviour of material on the microstructural scale has been the topic of much investigation in regards to explaining macroscopic irradiation-induced growth phenomena. The following section is an assessment of the literature to date in regards to the evolution of dislocations and second phase particles under irradiation, the resulting irradiation-induced precipitation in the matrix and phenomena relating to grain boundary evolution.

2.8.1 DISLOCATION LOOPS

In Zr and its alloys there are two dominating types of dislocation loops that form during neutron irradiation, known as a-loops and c-loops. The images in Figure 2-10 exemplify a- and c-loops in part a and b, respectively, the former in pure Zr irradiated to a low fluence at high temperature and the latter in Zircaloy-2 at a higher fluence and a temperature closer to normal power reactor operating temperatures. a-loops are the primary observable form of damage and are so-called due to their Burgers vector $\frac{1}{3}<11\bar{2}0>$ and their $\{10\bar{1}0\}$ prism habit planes (A Jostsons et al. 1977; Griffiths 1988). c-loops form after a delay to higher fluence levels (~5 dpa) and are of interest due to their correlation with increased growth strain (Holt & Gilbert 1986). c-loops have Burgers vector $\frac{1}{6}<20\bar{2}3>$ and are observed to form in rows parallel to (0001) basal planes (A. Jostsons et al. 1977; Griffiths 1988; Holt & Gilbert 1986). The variation in dislocation size and density between different alloys under different metallurgical and irradiation conditions will be the subject of the following discussion. All work referenced obtained data by transmission electron microscopy (TEM) imaging techniques unless otherwise stated.

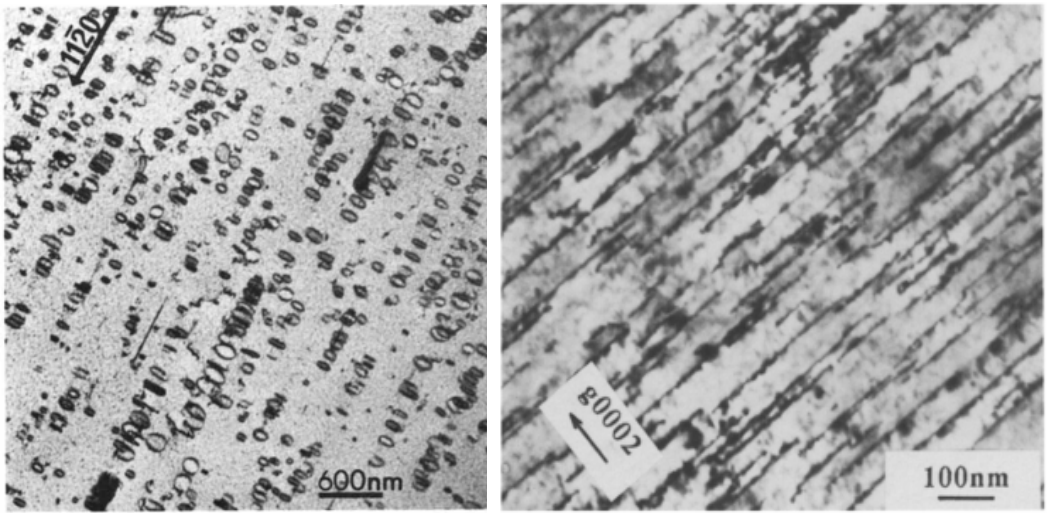

Figure 2-10 a-loops in pure Zr irradiated to 0.064 x10^{25} n m^{-2} at 395 °C (A Jostsons et al. 1977) and c-loops in Zircaloy-2 irradiated to 'high fluences' at 277 °C (Holt 1988).

2.8.1.1 A-LOOPS

First, a note on the data available in the literature. In power reactors, a-loops nucleate at low fluences and c-loops at higher fluences, the latter correlated with increased growth strain (Holt & Gilbert 1986). As the high fluence data is of more interest from a material performance perspective, there is naturally less data available from low fluence material. Indeed, removing and destructively testing the structural and cladding components from nuclear cores after a few months of operation would be inefficient for power generation. As such, much of the low fluence dislocation data available in the literature is either from scientific neutron irradiation studies, using test reactors at higher fluxes and temperatures with respect to power reactors, or from the odd sample from a power reactor but with no systematic approach to the investigation. As such, there is large scatter when comparing data from different laboratories, especially when one considers human error and a non-standardised way of determining densities from TEM foils. However, different research groups decide on wide differences in experimental parameters and this can be useful in suggesting mechanistic processes.

In an extensive study of a-loops in pure Zr, Jostsons et al. observed a-loops at fluences as low as 0.038 x10^{25} n m^{-2} at 300 °C (NB: all fluences will be in terms of

10^{25} n m^{-2} for ease of comparison) ~0.01 dpa (A Jostsons et al. 1977). Likewise, in Zircaloy-2, Carpenter and Northwood estimated the onset of a-loop nucleation as 0.02-0.03 x10^{25} n m^{-2} at 300 °C (Carpenter & Northwood 1975). At such low fluences, a similar a-loop nucleation onset in pure Zr and Zircaloy-2 suggests that the Sn in supersaturated solution of the latter has little effect on this threshold neutron dose. With an increase in fluence, both Jostsons et al. and Carpenter and Northwood demonstrated that, in both pure Zr and Zircaloy-2, the elliptical a-loop size increases from an average diameter of 5-6 nm at < 0.2 dpa to exceeding 7 nm at ~20 dpa (A Jostsons et al. 1977; Carpenter & Northwood 1975). Additionally, the a-loop number density, after an initial increase in number density, decreases gradually (A Jostsons et al. 1977; Carpenter & Northwood 1975), resulting in a gradual decrease in line density as exemplified, along with a-loop line densities from other studies, in Figure 2-12 and Figure 2-12, Figure 2-12 being a re-scaled version of Figure 2-12 to reveal details of the lower a-loop line densities. In contrast to Carpenter and Northwood, Griffiths has reported that, in Zircaloy-4, while a-loop sizes are 10-20 nm at 0.5 x10^{25} n m^{-2} (~0.8 dpa) they decrease in size at a higher fluence of 8 x10^{25} n m^{-2} (~13 dpa) (Griffiths 1988), although the exact size at the higher fluence was not given. More recently, Cockeram et al. have demonstrated that there is little change in loop size with increasing neutron dose for both Zircaloy-2 and Zircaloy-4, and that the a-loop size difference between the two alloys is also minimal at both 300 and 400 °C (Cockeram et al. 2011; Cockeram et al. 2014).

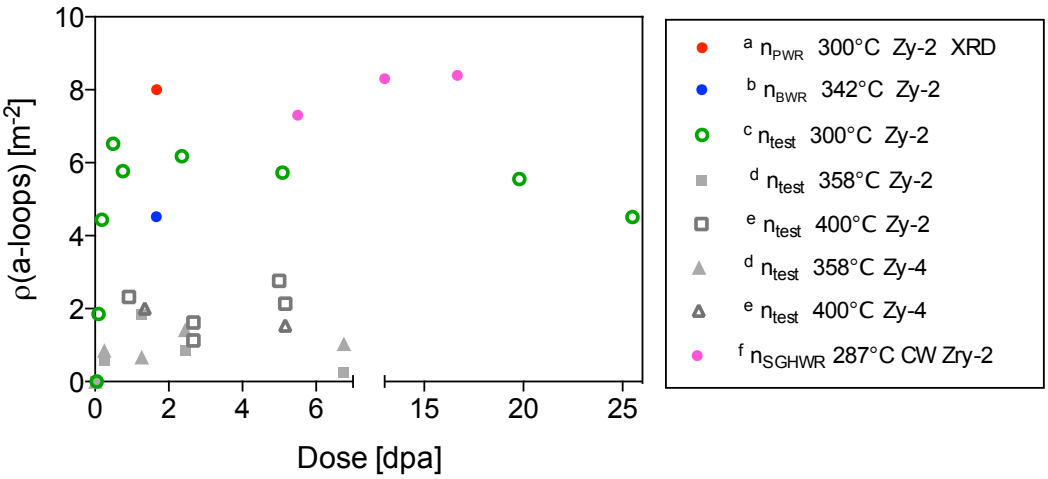

Figure 2-12 Line density of a-loops after neutron irradiation at various temperatures and in various reactors. References: a (Griffiths et al. 1996); b (Northwood et al. 1979); c (Carpenter & Northwood 1975); d (Cockeram et al. 2011); e (Cockeram et al. 2014); f (Holt et al. 1996).

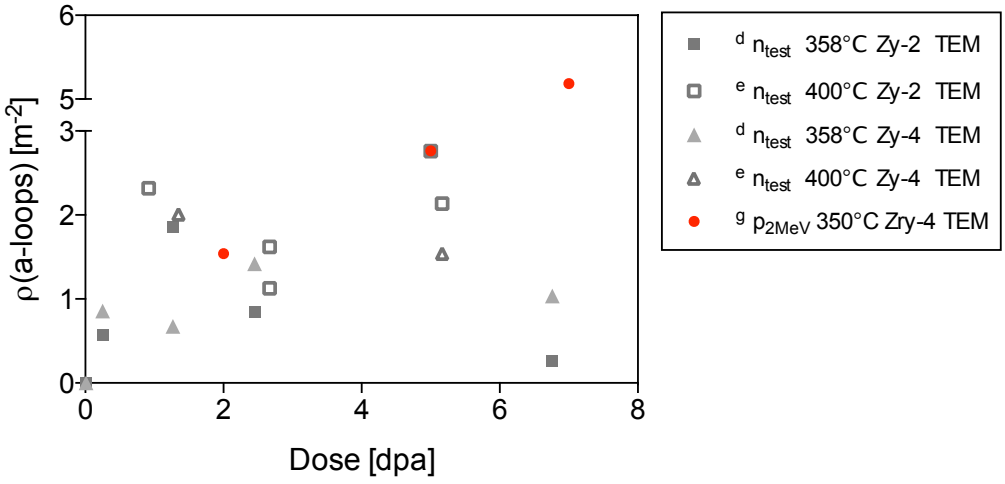

Figure 2-12 Line density of a-loops after neutron and proton irradiation at various temperatures and in various reactors. References: d (Cockeram et al. 2011); e (Cockeram et al. 2014); g (Zu et al. 2005).

A saturation in a-loop number density is commonly quoted by authors but has not been demonstrated very frequently. Some discussion of a-loop saturation at fluences > 1 x10^{25} n m^{-2} is given by Adamson (Adamson 2000), although the most convincing argument comes from Griffiths et al. in 1996 by analysis of line broadening in X-ray diffraction profiles of neutron-irradiated Zircaloy-4 (Griffiths et al. 1996). Griffiths et al. argued that the saturation in broadening of prism reflections in Zircaloy-4 was evidence of a saturation in a-loop density. However, it is technically a saturation in strain that is likely originating from loop line length, and so it is the dislocation line density that must be addressed: if we consider Griffiths et al. to be correct in that the line density saturates, and if it is true that Zircaloy-4 a-loop sizes decrease with increasing fluence (Griffiths 1988), then for a saturation in line density the number density must increase with fluence; conversely, if a-loop sizes increase with fluence, as is suggested in Zr and Zircaloy-2 by some authors (A Jostsons et al. 1977; Carpenter & Northwood 1975), then the dislocation number density must decrease as the prism reflection broadening saturates. Cockeram et al. has shown that, at ~350 °C, the number and line density of a-loops saturates for Zircaloy-4 but decreases for Zircaloy-2, and that at ~400 °C it is Zircaloy-4 that decreases in number and line density and Zircaloy-2 that saturates (Cockeram et al. 2011; Cockeram et al. 2014). However, such trends are difficult to rely upon when few and scattered data points are considered. Indeed, the authors fit a curve within their data as a basis for discussion but the data points do not fit the curves well.

In comparing pure Zr and Zircaloy-2, Gilbert et al. demonstrated that at 300 °C and at a fluence of 1.2 x10^{25} n m^{-2}, the a-loop size was 0.5 times that of pure Zr and the number density 4 times higher (Gilbert et al. 1979). Conversely, keeping the same fluence but increasing the temperature to 400 °C showed that the a-loop size was roughly the same between Zircaloy-2 and pure Zr but that the number density was lower by a factor of 2. Therefore, we may conclude that alloying with Zircaloy-2 components and irradiating at 300 °C causes an increase in the dislocation line density by a factor of ~2, but at 400 °C by a factor of ~0.5. While not considered by the authors of the 1979 paper by Gilbert et al., the Sn in solution of Zircaloy-2 may act as a barrier to diffusion of point defects and their clusters, causing higher

dislocation line densities as dislocations become the dominant sink with respect to α-Zr grain boundaries and second phase particle interfacial boundaries that require more long-range diffusion. At the higher temperature, this Sn diffusion barrier may be overcome and a different sink may become favourable for point defects and their clusters, causing the observed dislocation density to decrease. Indeed, Sn has been suggested as a trap for vacancies by several groups, as discussed by Hood (Hood 1988), although the size of Sn relative to Zr is thought to be very similar in the a-Zr matrix (Perez et al. 2003) and so any elastic interaction with point defects and clusters may be minimal.

The effect of increasing temperature has been shown in several independent studies to increase the a-loop size and decrease the number density (A Jostsons et al. 1977; Gilbert et al. 1979; Northwood et al. 1979; Griffiths 1988). Although Gilbert et al. did not allude as to why, when increasing the irradiation temperature from 300 to 400 °C the overall decrease in line density is ~3 times more severe for Zircaloy-2 than for pure Zr, suggesting a role of Sn in point defect and cluster trapping or as a general barrier to diffusion at lower doses. However, the effects of texture and grain size have not been taken into account here which have been shown to affect growth strain (Fidleris 1988) and are therefore likely to affect the resulting dislocation structure (Holt & Gilbert 1986).

More recent studies by Cockeram et al. have shown something quite different. A comparison of the work published by the same authors in 2011 and 2014 shows that, for both Zircaloy-2 and -4, an increase in temperature from ~358 °C (2011) to ~400 °C (2014) causes an decrease in a-loop size and an increase in number density and an overall increase in the a-loop line density (Cockeram et al. 2011; Cockeram et al. 2014). This is an inconsistency with the literature that was not addressed by the authors in the later paper. The experiments were performed in the different types of test reactor and the 400 °C experiment at a neutron flux ~3 times lower than that in the 358 °C experiment, which may of course be a source of discrepancy when comparing the works. Indeed, one may expect a higher flux to cause a higher number density of smaller defects, as Allen et al. has demonstrated that higher neutron fluxes cause a higher density of smaller voids to nucleate in

austenitic stainless steels (Allen et al. 2006). Therefore, a decrease in flux from ~3 x10^{18} n m^{-2} s^{-1} (2011, ~358 °C) to 0.1-0.8 x10^{18} n m^{-2} s^{-1} (2014, ~400 °C) may have a stronger effect on a-loop structure than that of increasing the temperature by ~40 °C in this temperature range. Conversely, Carpenter and Northwood analysed Zircaloy-2 from test reactors at fluxes ~3 times that of power reactors but at similar temperatures (Carpenter & Northwood 1975). This gave similar line densities to those observed in power reactors (Griffiths et al. 1996; Northwood et al. 1979) and so temperature may be more important than flux in the ~300 °C temperature range. In recommendation, if one were to use test reactors, the neutron flux may not have much of an effect in terms of differing dislocation structure as long as the temperature is controlled well; for representation of power reactors, one would irradiate at ~300 °C at any flux up to ~3 times that of power reactors. In support of this small effect of flux on dislocation structure, irradiation-induced hardening in Zr alloys, which is conventionally thought to arise from a-loop dislocation evolution, is relatively independent of neutron flux at a given fluence and temperature (Adamson & Cox 2005). However, with reference to the recent studies by Cockeram et al., flux may have more of an effect at higher irradiation temperatures ~350-400 °C. At irradiation temperatures exceeding 450-500 °C, no individual dislocation loops are observed (A Jostsons et al. 1977), although some dislocation tangles have been reported (Gilbert et al. 1979).

While qualitative trends in a-loop size and number density are frequently discussed in the literature, quantitative measurements are more difficult to find. A compilation of data from some of the publications already discussed regarding a-loop line density in Zircaloy-2 and Zircaloy-4 is given in Figure 2-12 and Figure 2-12, for which Figure 2-12 also includes proton irradiation data on a-loop line density. A clear trend is difficult to discern in published number density data, although there may be a decreasing number density from 2-3 dpa towards 7 dpa. The line density data is more revealing and is simply obtained by multiplying the published number density by the published a-loop diameter, multiplied by π to account for the circumference of an assumedly (but rarely) circular loop. This accomplishes two things; to some extent it normalises the number densities provided by different groups and it also provides an idea of total strain arising

from loop line length. From Figure 2-12, the a-loop line densities provided by Carpenter and Northwood more closely resemble the line densities in PWR and BWR material than any of the other studies. This may be due to the power reactor temperature used at ~300 °C (Carpenter & Northwood 1975), as all other neutron irradiation studies in Figure 2-12 were conduced at higher temperatures and give lower line densities. In Figure 2-12, the scale is changed to remove the data from Carpenter and Northwood. A general increasing yet saturating line density is observed in Figure 2-12, supporting the saturation of prism reflection broadening observed in XRD profiles by Griffiths et al. (Griffiths et al. 1996). While Griffiths et al. gave dislocation densities by XRD in the correct range obtained from TEM investigations, Holt et al. has used the same method and provided higher a-loop densities in Zircaloy-2 in comparison to the TEM-determined densities by Carpenter and Northwood in Zircaloy-2 at similar fluences (Holt et al. 1996; Carpenter & Northwood 1975), all of which are displayed in Figure 2-12. As such, great care must be taken when analysing and interpreting XRD profiles.

In relation to proton, electron and heavy ion irradiation, there is even less data available in the literature than for a-loops arising from low dose neutron irradiation. Zircaloy-4 a-loop line densities arising from 2 MeV proton irradiations at 350 °C are included in red in Figure 2-12 after Zu et al., which show a clear increasing trend in line density (Zu et al. 2005), arising from a saturation an a-loop diameter (5 to 11 nm) and an increase in number density. While the absolute density values from Zu et al. seem to be in the correct range, the increasing trend is rather different from neutron irradiation experiments that demonstrate a gradual decrease at higher fluences. Unfortunately, the exact method by which Zu et al. conducted the TEM analysis is not given and the images of a-loops provided in the publication are bright-field TEM images that are of relative low magnification in relation to the size of the a-loops. Indeed, the authors count black-spot damage without reference to any orientation or diffraction properties of the dislocation loops. Concerning electron and heavy ion irradiation, many groups use such high damage rate methods to obtain high irradiation doses, and as such it is c-loops that are quantified and not a-loops. However, Onimus et al. have performed Zr ion irradiation at 0.6-1 MeV and 350 °C for post-irradiation strain experiments and

have given a-loop line densities after 1.3 dpa at ~4.7 x10^{14} m^{-2} (Onimus et al. 2012). While this is in the correct range of neutron irradiations at 300 °C provided by Carpenter and Northwood (Carpenter & Northwood 1975), and are therefore more representative of power reactor line densities than any other test reactor neutron or proton irradiation experiment described thus far (Northwood et al. 1979; Griffiths et al. 1996), the a-loop structure after heavy ion irradiation is different in that the line density is composed of a very high number density of small loops (~50 x10^{21} m^{-3}, mean diameter 3 nm). Additionally, Onimus et al. simply assumed the thickness of the TEM foil for their a-loop quantifications as 150 nm without any actual thickness measurement, and as such there may be significant errors associated with such a measurement.

The nature of a-loops in Zr and its alloys may take both interstitial and vacancy forms and are known to have the same Burgers vector and habit the same plane ((A Jostsons et al. 1977; Griffiths 1988; Woo 1988)), unlike in cubic systems where irradiation-induced interstitial dislocation loops are more stable than their vacancy counterparts (Osetsky et al. 2000). It is generally believed that at normal power reactor operating temperatures ~300 °C, there are an equal number of interstitial and vacancy loops at low fluences < ~ 5 x10^{25} n m^{-2} ~8.3 dpa, and that the ratio of vacancy to interstitial (v/i) loops increases with irradiation temperature (Griffiths 1988) to ~2.3 at ~370 °C and decreases with increasing alloy additions, i.e. irradiation at 427 °C in the test reactor ERB-II to a fluence of 1.1 x10^{25} n m^{-2} ~2.8 dpa results in a-loop v/i ~1 for Zircaloy-2 and ~1.5 for crystal-bar Zr (Griffiths, R.W. Gilbert, et al. 1987). However, it is important to note two points: first, much work done on a-loop nature has been performed on pure Zr at elevated irradiation temperatures, and such loops are large which allow the determination of their nature by inside-outside contrast; and second that Jostsons highlights that the v/i ratio is significantly different from grain to grain and so it is difficult to obtain a representative picture of the distribution of loop nature by TEM methods (A Jostsons et al. 1977). There are several TEM methods for a-loop nature determination but that most frequently used is that of 'inside-outside' contrast close to the $<1\bar{1}23>$ zone axis. Details for this method may be found in Jostsons (A Jostsons et al. 1977), but the premise is simply that the strain fields of vacancy and

interstitial loops are opposite and can be differentiated by the selection of appropriate diffracting vectors.

The following is a consideration of the a-loop size necessary to determine a-loop nature using the inside-outside method from the 'safe' $<11\bar{2}3>$ orientation. First one may assume that all loops being considered are elliptical and lie on the $\{10\bar{1}0\}$ habit plane with the loop long axis (length) in the [0001] direction and the short axis (width) in the $[11\bar{2}0]$ direction, and that Griffiths is correct in that the nature of loops < 5 nm in diameter are difficult to determine (Griffiths 1988). Therefore we may assume that an a-loop requires a projected width of 6 x 6 nm from the $<11\bar{2}3>$ orientation in order to be successful in its nature determination. As such, we may calculate the real loop size necessary for loop nature determination when observed from the habit plane normal, $<10\bar{1}0>$, by simple trigonometry. The $[11\bar{2}3]$ zone axis is at an angle 67.8° from the $[10\bar{1}0]$ assuming that the c/a ratio of the Zr hcp lattice is equal to 1.59 (Goldak et al. 1966). Therefore, in the TEM, one would need to tilt 67.8° from the habit plane normal to the safe $[11\bar{2}3]$ orientation for a-loop nature determination. Of course, this is not actually possible in the TEM due to the limiting geometry of the stage and the thin foil, but as a thought experiment it is useful to imagine such a procedure. This tilt may be achieved by first tilting from the $[10\bar{1}0]$ orientation along the $(1\bar{2}10)$ Kikuchi band toward the [0001] direction by 59.4° to the $[10\bar{1}2]$ zone axis, which would change the projected length of the loop by a factor of 0.51. The foil must then be tilted 10.1° in the perpendicular direction from the $[10\bar{1}2]$ zone axis to the $[11\bar{2}3]$ along the $(10\bar{1}1)$ Kikuchi band. This is the orientation suitable for inside-outside analysis and the projected width of the loop would change by a factor of 0.98. Therefore, for an a-loop to retain dimensions length x width of 6 x 6 nm when projected from the $[11\bar{2}3]$ orientation, its actual size must be ~12 x 7 nm when projected from its habit plane normal, which is greater in dimensions than a-loops observed in commercial alloys after neutron, proton and heavy-ion irradiation at temperatures 300-400 °C (Carpenter & Northwood 1975; Griffiths et al. 1996; Northwood et al. 1979; Cockeram et al. 2011; Zu et al. 2005; Onimus et al. 2012). Determination of

a-loop nature has not, therefore, been reported for commercial alloys at any operating temperature or under any irradiation conditions other than a qualitative description of Zircaloy-2 by Griffiths (Griffiths, R.W. Gilbert, et al. 1987), and, as such, leaves a large gap in the knowledge base of the field. Computational analysis of TEM micrographs that highlight slight changes in contrast may allow the nature determination for smaller loops, especially when in combination with better imaging by use of higher resolution CCD cameras or by STEM detectors and convergent scanning beams, which reduce matrix strain contrast and provide clearer images of dislocation lines. However, to the author's knowledge, this has not been attempted in irradiated Zr alloys to date. In pure Zr and at elevated temperatures, Jostsons et al. reported that interstitial a-loops are predominantly circular and vacancy a-loops elliptical (A Jostsons et al. 1977; Griffiths 1988), but Northwood et al. has demonstrated large variability in shape between loops of differing nature (Northwood et al. 1979) and so a shape analysis for the determination of a-loop nature may prove untrustworthy.

2.8.1.2 C-LOOPS

c-component dislocation loops (c-loops) of Burgers vector $\frac{1}{6}<20\bar{2}3>$ are generally thought of as sessile due to their faulted nature but have been observed to climb over SPPs in Zircaloy-2 when irradiated at higher temperatures ~437 °C (Griffiths, R.W. Gilbert, et al. 1987). Although these 'basal' loops are known to habit the (0001) planes, non-basal c-loops have been observed in Zircaloy-2 after irradiation in test reactor EBR-II at ~370 °C and a fluence of 0.59 x10^{25} n m^{-2} (Griffiths, R.W. Gilbert, et al. 1987). These loops were shown to habit $\{11\bar{2}3\}$ planes and to possibly have solute segregation. Interestingly, such loops were not observed in Zircaloy-4 to any fluences, suggesting that the segregation to the loops in Zircaloy-2 may be Ni (Griffiths, R.W. Gilbert, et al. 1987). Further, after electron irradiation, vacancy <c>-loops with Burgers vector ½<0001> have been observed, as have interstitial <c+a>-loops with Burgers vector $\frac{1}{3}<11\bar{2}3>$ on $\{10\bar{1}1\}$ planes (Griffiths 1988). The majority of the following discussion will focus on the more commonly reported basal $\frac{1}{6}<20\bar{2}3>$ c-loops, unless otherwise stated.

The delayed onset of basal c-loop nucleation and growth is interesting predominantly in its correlation with accelerated irradiation-induced growth strain; the coincidence of vacancy c-loops and accelerated growth strains in Zircaloy-4 at fluences > 3 $x10^{25}$ n m^{-2} ~5 dpa was demonstrated by Holt and Gilbert at ~297 °C (Holt & Gilbert 1986) and from the linear behaviour of c-loop density increase observed by Mahmood, one may deduce c-loop nucleation in Zircaloy-2 PWR control blades at ~290 °C to occur at ~3 $x10^{25}$ n m^{-2} ~5dpa (Mahmood et al. 2000). This agreement between c-loop nucleation fluences in Zircaloy-2 and -4 is consistent with their similarity in breakaway growth fluences; 3-4 $x10^{25}$ n m^{-2} at 280-297 °C (Griffiths et al. 1995). A summary of data concerning c-loop line density derived from the number density and size of c-loops reported by several studies is given in Figure 2-14 and Figure 2-14, from which it may be seen that the combination of the majority of neutron-irradiation experiments provides an almost linear increase in c-loop line density with fluence. The study of neutron-irradiated Zircaloy-2 at 290 °C by Mahmood et al., for, that of Griffiths et al. for Zircaloy-2 at 297 °C and that of Bossis et al. for Zircaloy-4 at 315 °C agree well (Mahmood et al. 2000; Griffiths et al. 1996; Bossis et al. 2011). Mahmood demonstrated by TEM investigations that, post-breakaway, c-loop line density increases linearly with neutron luence at a rate of ~7.5 $x10^{-13}$ n^{-1} at 290 °C in Zircaloy-2 (Mahmood et al. 2000). By X-ray diffraction line broadening analysis, Griffiths et al. measured the rate of increase to be ~5 $x10^{-3}$ n^{-1} at 293 °C (Griffiths et al. 1996). While both studies show a linear increase in c-loop density, the discrepancy in the rates of line density increase may simply be due scatter and Mahmood et al. measuring to much higher fluences than Griffiths et al. at up to 32 $x10^{25}$ n m^{-2} ~ 53 dpa versus Griffiths et al.'s maximum of 12 $x10^{25}$ n m^{-2} ~20 dpa. Holt et al. have predicted that when the density of c-loops equals that of a-loops there will be a saturation in growth strain and even a decrease in strain if c-loop density increases to rise (Holt et al. 1996). However, Griffiths et al. have demonstrated that c-loops regenerate by unfaulting when their density is large enough for high degrees of loop overlap, which in turn may cause growth strain not to saturate (Griffiths, R.W. Gilbert, et al. 1987). Importantly, Mahmood has shown linear increases in growth and c-loop density up to high fluences of 32 $x10^{25}$ n m^{-2} ~53 dpa with no saturation in growth strain or c-loop density, even

though the c-loop density is above that considered for a-loops at such high fluences. Of course, a-loop density could also be increasing at such high fluences, although this has not been demonstrated experimentally to date.

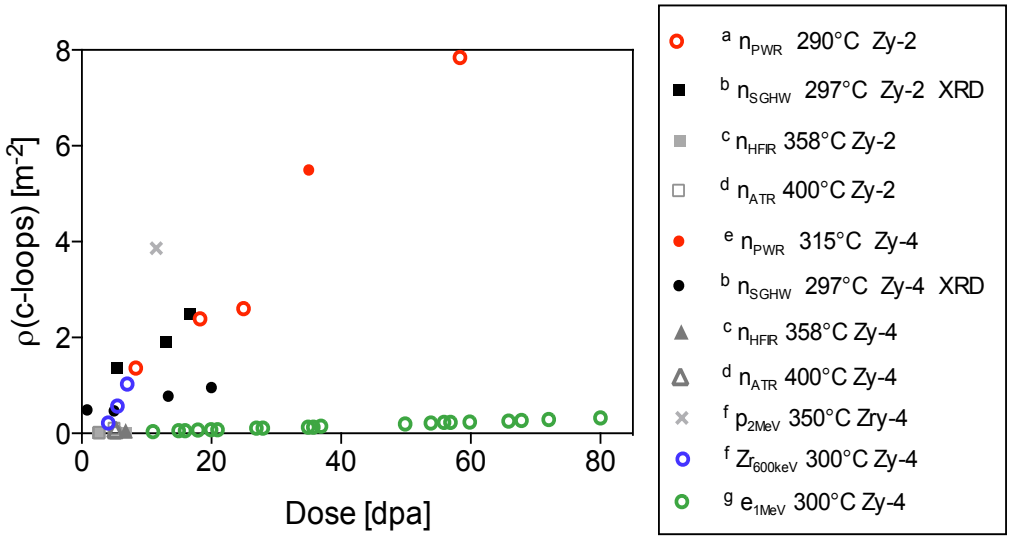

Figure 2-14 c-loop line densities. References: a (Mahmood et al. 2000); b (Griffiths et al. 1995); c (Cockeram et al. 2011); d (Cockeram et al. 2014); e (Bossis et al. 2011); f (Tournadre et al. 2012); g (de Carlan et al. 1996).

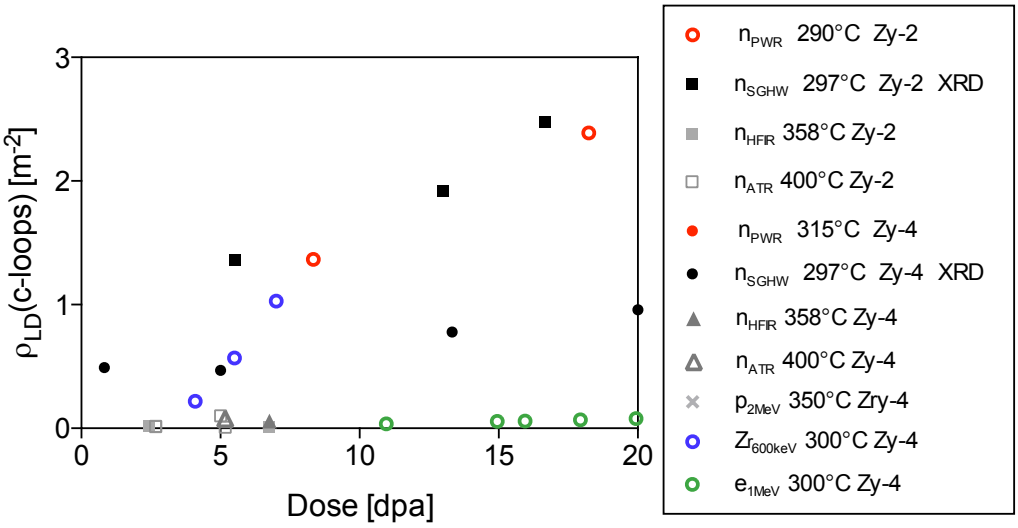

Figure 2-14 c-loop line densities. References: a (Mahmood et al. 2000); b (Griffiths et al. 1995); c (Cockeram et al. 2011); d (Cockeram et al. 2014); f (Tournadre et al. 2012); g (de Carlan et al. 1996).

No c-loops are observed low irradiation temperatures ~77 °C up to high fluences of 25 x10^{25} n m^{-2} ~42 dpa (Griffiths et al. 1996), whereas in Zircaloy-4 at a neutron irradiation temperature of ~370 °C, c-loops have been observed at fluences as low as 0.1 x10^{25} n m^{-2} ~0.2 dpa (Griffiths et al. 1989). An increase in c-loop density with increasing temperature and a correlating increase in irradiation-induced growth strain has been demonstrated for high temperature neutron irradiations at 450-425 °C by Holt et al., who revealed the importance of including defect clusters and their mobility when assessing micro- and macroscopic phenomena (Holt et al. 1993). In the high temperature range 427-437 °C, Griffiths et al. showed very high c-loop densities in Zircaloy-2 irradiated in test reactor EBR-II (Griffiths et al. 1989). In comparing two recent studies by Cockeram et al., a change in temperature from ~358 to ~400 °C caused no significant change in c-loop number density or size, apart from one extraneously high data point at 400 °C and 3 x10^{25} n m^{-2}, which was not explained by the authors (Cockeram et al. 2011; Cockeram et al. 2014). Conversely, Zircaloy-4 at the same irradiation temperatures 300 and 400 °C demonstrated an increase in number density at 400 °C and higher fluences (Cockeram et al. 2011; Cockeram et al. 2014). Likewise, Griffiths et al. has shown that Zircaloy-4 has both higher c-loop density and growth strain and in the 367-467 °C temperature range in comparison to Zircaloy-2 (Griffiths et al. 1995).

While the Zircaloy-2 c-loop density data in Figure 2-14 (Mahmood et al. 2000; Griffiths et al. 1995) are similar to that of Zircaloy-4 in the temperature range 290-315 °C (Bossis et al. 2011), Griffiths et al. has used X-ray diffraction line broadening to demonstrate that Zircaloy-2 has a higher c-loop line density than Zircaloy-4 by a factor of ~3 at 298 °C, seen in Figure 2-14 and Figure 2-14 as solid black circles. Conversely, Cockeram et al. has shown that, at 358 °C, Zircaloy-2 experiences c-loop nucleation at a lower fluence than Zircaloy-4 but has a lower c-loop line density than Zircaloy-4 at higher fluences; at 2.93 x10^{25} n m^{-2} ~6.8 dpa the line density of Zircaloy-4 is higher than that of Zircaloy-2 by a factor of ~5 (Cockeram et al. 2011). However, the c-loop line densities given by Cockeram et al. are lower than the power reactor densities given by other studies by a factor of at least 6, an inconsistency that is not addressed by the authors but is may be due to

an influence of higher flux at higher irradiation temperatures (Cockeram et al. 2011; Cockeram et al. 2014).

Different irradiative species are able to induce c-loop formation in Zr and its alloys, some of which are detailed in Figure 2-14 and Figure 2-14. Tournadre et al. have demonstrated c-loops in both proton- and Zr heavy-ion irradiated Zircaloy-4 (Tournadre et al. 2012). While Tournadre et al. concluded that 2 MeV proton irradiations at 350 °C were more representative than 600 keV Zr heavy ion irradiations at 300 °C, due to the larger c-loop size of the former and the slower proton irradiation damage rate, the trend in in Figure 2-14 and Figure 2-14 show that c-loop line density fits better for the Zr heavy-ion irradiations than for the proton with respect to neutron irradiation studies. Indeed, the Zircaloy-4 c-loop line density by Tournadre after proton irradiation to 11.5 dpa is higher than that in neutron-irradiated Zircaloy-2 by Griffiths et al. by a factor of ~2 (Griffiths et al. 1995) and higher than Zircaloy-4 by a factor of ~5 (Griffiths et al. 1995) at similar dose levels but at 300 °C in comparison to Tournadre et al.'s 350 °C. However, the assumption of a 150 nm thick TEM foil without a thickness measurement makes comparing quantitative measurements questionable. While Zu et al. made no mention of c-loops in Zircaloy-4 after proton irradiation to 7 dpa at 350 °C, the authors did not claim that they were looked for (Zu et al. 2005). Therefore, while the incubation dose for 2 MeV protons at 350 °C in Zircaloy-4 may be between 7 and 11.5 dpa, a more thorough investigation is required, especially as this is a high dose in comparison to the onset of c-loop nucleation that is expected from neutron irradiations at a fluence of ~3 x10^{25} n m^{-2} ~5 dpa (Holt & Gilbert 1986; Mahmood et al. 2000). The 600 keV Zr heavy-ion irradiation of Tournadre et al. gave appropriate line densities, but in a similar manner to the production of a-loops by heavy ions, the c-loops were small and in high density (Tournadre et al. 2012). Further, as c-loops are much larger than a-loops and the Zr ions only penetrate 300 nm into the Zr matrix, c-loops are more likely to be hindered by the physical constraint of the non-irradiated remainder of the grain and the sink strength of this region and the free surface 300 nm above it. In regards to electron irradiation, Griffiths et al. have shown that both basal vacancy c-loops of Burgers vector $\frac{1}{6}<20\bar{2}3>$ that habit (0001) planes and non-basal interstitial c+a-loops of Burgers

vector $\frac{1}{3}<11\bar{2}3>$ that habit $\{10\bar{1}1\}$ planes can be induced in pure Zr (Griffiths et al. 1983), also observed after electron irradiation of Zircaloy-2 and -4 (Griffiths et al. 1993). Basal c-loops have been observed by de Carlan et al. after electron irradiation at various temperatures (de Carlan et al. 1996), but have shown a much lower line density than those produced by neutron irradiation, exemplified in Figure 2-14 and Figure 2-14 for de Carlan et al.'s electron irradiations at 300 °C. This may be explained by the presence of cavities at this temperature, which act as an alternative vacancy sink. No cavities and higher c-loop densities were observed at higher electron irradiation temperatures ~350 °C, but the data was not provided by the authors and so could not be included in this analysis.

Cavities are an alternative vacancy sink to vacancy c-loops, but are usually only observed in electron-irradiated pure Zr (Griffiths et al. 1993) or electron-irradiated commercial alloys at medium-to-low temperatures ≤ 300 °C (de Carlan et al. 1996). However, cavities faceted on crystallographic planes have been reported in neutron-irradiated pure Zr and Zircaloy-2 at ~400 °C and at relatively low fluences of 1.2 $x10^{25}$ n m^{-2}, and also in Zr - 2.5wt.% Nb at 650 °C and 0.7 $x10^{25}$ n m^{-2} (Gilbert et al. 1979). Their nucleation is therefore considered as related to both a lack in matrix solute content and high damage rates and are often observed to nucleate in rows parallel to the trace of the basal plane (Griffiths 1988). De Carlan et al. showed clearly that an increase in Fe implantation in Zircaloy-2 was related to an increase in c-loop density and a decrease in cavity formation (de Carlan et al. 1996), and Griffiths et al. has shown that both c-loops and cavities are associated with regions of high Fe content (Griffiths, R.W. Gilbert, et al. 1987). Griffiths et al. have observed both a high density of c-loops and some cavities in Zircaloy-2 irradiated at high temperatures and fluences (Griffiths, R.W. Gilbert, et al. 1987), possibly suggesting a saturation in c-loop density as a vacancy sink and the necessity for an alternative. The effect of matrix chemistry on c-loop formation has been shown as important by increasing alloying and impurity additions to increase c-lop density (Griffiths, R.W. Gilbert, et al. 1987) and the effect of Sn in the matrix is to decrease the onset fluence at which c-loops form (Griffiths, R.W. Gilbert, et al. 1987; Griffiths & Gilbert 1987), as at relatively high temperatures and low neutron fluences, where little SPP dissolution has taken place, Zircaloy-2 and -

4 demonstrate c-loop nucleation and no cavities whereas pure Zr demonstrates cavities and sparse evidence of c-loop nucleation. Although Griffiths and Gilbert have demonstrated that Sn precipitates from solution during irradiation, the authors also discussed that the strain this would induce in the matrix is small in comparison to that required to induce a change of loop habit plane, i.e. for vacancy $\{10\bar{1}0\}$ a-loops to transform into vacancy (0001) c-loops due to this change in Sn environment (Griffiths & Gilbert 1987).

The delay in c-loop nucleation may be causally related to a-loops. Griffiths and Gilbert noted that, in impure Zr, the number density of a-loops decreases as c-loops increases at higher fluences (Griffiths & Gilbert 1987). Griffiths et al. have explained c-loop growth at the expense of a-loops as the difficulty in climb of the latter once c-loops provide a physical barrier in rows parallel to the basal plane (Griffiths, R.W. Gilbert, et al. 1987). However, recent molecular dynamics calculations by Di et al. demonstrate that vacancy a-loops may nucleate vacancy c-loops directly by interaction with a cascade event (Di et al. n.d.). This is interesting because such an event may require a-loop alignment parallel to the basal plane, which is a common feature of irradiated zirconium alloys (A Jostsons et al. 1977; Griffiths 1988) but which may take time to develop, accounting for the delay in observable c-loop nucleation and the spacing between c-loops in the <0001> direction. The work by Di et al. is, however, rather preliminary as the a-loop modelled habits the $\{11\bar{2}0\}$ plane as opposed to the $\{10\bar{1}0\}$ and so further work is required to solidify the results as representative. The formation of c-loops is predominantly dependent on temperature and fluence and hence barriers to diffusion, as it has been shown that for different fluxes there is little difference in c-loop density or growth strain for a given fluence and temperature (Griffiths, R.W. Gilbert, et al. 1987).

2.8.2 SECOND PHASE PARTICLES

The types of second phase particles (SPPs) in Zr alloys have already been introduced and are summarised in Table 2. The following is a more in-depth assessment of SPPs, their structure and how they evolve during irradiation.

Further, the effect of SPP evolution on matrix chemistry and the implications for irradiation-induced growth will be discussed.

2.8.2.1 NON-IRRADIATED STRUCTURE AND COMPOSITION

The limited solubility of the light transition elements in α-annealed α-zirconium induces the precipitation of thermodynamically stable second phases (β-quenched systems will contain smaller SPPs (Kuwae et al. 1983) and metastable precipitates (Kuwae et al. 1983; Yang et al. 1986)). The evolution of such phases under irradiation is important to the system as a whole, as mechanical behaviour and corrosion properties are intrinsically dependent on microstructural features. A comparison of irradiation-induced growth strain at a given fluence in the binary system Zr-1.5Sn (wt.%) at 280 °C (Zee et al. 1984) as compared with that of Zircaloy-2 (nominally Zr-1.5Sn-1.4Fe-0.1Cr-0.06Ni (Hallstadius et al. 2012)) at ~290 °C (Holt & Gilbert 1986) shows that the latter, in which the dominant microstructural difference is the presence of second phase particles (SPPs), demonstrates a reduced growth strain in comparison to the Zr-1.5Sn (wt.%) binary system. As such, the behaviour of such phases under irradiation in different alloy systems is of interest, as are scientific studies that make use of electron, proton or ion irradiation to understand the mechanisms of SPP evolution.

The most well studied SPPs of the Zircaloys are the Zr-Fe-Cr and Zr-Fe-Ni intermetallics, stoichiometrically $Zr(Fe,Cr)_2$ and $Zr_2(Fe,Ni)$, respectively. As the Zr/(Fe+X) and the Fe/X (X = Cr, Ni) stoichiometry are variable after irradiation at elevated temperatures, the phases will be referred to as Fe-Cr and Fe-Ni hereafter when irradiation effects are under discussion. Zircaloy-2 is known to contain both the Fe-Cr and Fe-Ni type SPPs and Zircaloy-4 only the Fe-Cr, with size ranges 30-650 nm for Fe-Ni SPPs and 20-170 nm for Fe-Cr SPPs (Goll & Ray 2002). While Zr-Fe binary SPP intermetallics are observed in Zircaloy-4 when the alloy composition Fe/Cr > 4 (Charquet et al. 1988) and zirconium silicides, phosphides and zirconium copper sulphides have been observed in Zircaloy-2 (Yang et al. 1986; Meng & Northwood 1989), their number densities are low by comparison to the Fe-Cr and Fe-Ni SPP types and so will not be considered explicitly here. Large

Fe-Ni SPPs in Zircaloy-2 may act as nucleation sites for smaller Fe-Cr SPPs, resulting in small SPP clusters with the orientation relationship $(1\bar{1}0)_{Fe-Ni} \| (10\bar{1}1)_{Fe-Cr}$ and $(002)_{Fe-Ni} \| (\bar{2}110)_{Fe-Cr}$ (Chemelle et al. 1983), although such clusters may be expected to behave under irradiation as the sum of their parts if we assume no internal SPP defect diffusion anisotropy. This, of course, may not be the case (Moura et al. 2001), and will be discussed in the following section.

The $Zr(Fe,Cr)_2$ SPP is of a Laves AB_2 structure with the smaller, more abundant element (Fe, Cr) forming a sublattice of tetrahedra that allow higher average coordination numbers than would be possible if the size of A = B (Smallman & Bishop 1999). Laves phases observe three crystal structures, the cubic C15 ($MgCu_2$) type, the hexagonal C14 ($MgZn_2$) or the hexagonal C36 ($MgNi_2$) type. The C14 is the most commonly quoted in the literature for the Fe-Cr phase in the Zircaloys, and indeed it has been explicitly stated the there is a lack of cubic C15 in such materials (Yang et al. 1986; Vizcaíno et al. 2008; Van der Sande & Bement 1974). X-ray diffraction studies of bulk $Zr(Fe_xCr_{x-1})_2$ alloys show that the stable phase is cubic when x = 0 or 1 and is hexagonal in the range x = 0.25-0.8 (Shaltiel et al. 1977). Additionally, if hexagonal structures do form when x = 1, they are metastable and transform to cubic upon heat treatments (Burany & Northwood 1991). The cubic structure of $ZrFe_2$ and $ZrCr_2$ (x = 0 and 1, respectively) are reflected in the Zr-Fe and Zr-Cr binary phase diagrams (Okamoto 2006; Arias & Abriata 1986), with $ZrFe_2$ cubic stability arising from its high magnetism (Chen, Wolf, Podloucky, Rogl, et al. 2005). However, it is the $ZrCr_2$ phase that displays a temperature-dependent polymorphism: hexagonal C14 at 1622 - 1673 °C, hexagonal C36 at 1562 - 1622 °C and cubic C15 at < 1592 °C. We might conclude that Fe stabilises the hcp C14 $ZrCr_2$ structure, which is usually only stable at temperatures close to the melting point at 1673 °C (Arias & Abriata 1986). It should be noted that although both C14 and C15 have been reported in both Zircaloy-2 and -4 (Pêcheur et al. 1993), especially after specific thermomechanical heat treatments (Meng & Northwood 1985a), it has been noted by Meng and Northwood that multiple electron diffraction patterns are required to correctly distinguish between the C14 and C15 structures (Meng & Northwood 1985b).

Unfortunately, such practise is not common in the literature and the structure is assumed from limited reflections in a limited number of diffraction patterns.

While $ZrCr_2$ and, to some extent, $Zr(Fe,Cr)_2$ exhibit structural polymorphism, Zr_2Fe, Zr_2Ni and $Zr_2(Fe,Ni)$ do not; all are of the bct crystal structure (Lucuta et al. 1981). The Zr_2Ni phase has an exact stoichiometry with reference to the Zr-Ni phase diagram (Okamoto 2007) whereas that of $ZrCr_2$ is variable in the 65-68 at.% Cr range (Arias & Abriata 1986), implying a resistance of the latter to structural change with respect to slight alterations in stoichiometry. While it has been reported that the space group of $Zr_2(Fe,Ni)$ (I4/mmm) is different from Zr_2Ni (I4/mcm) due to the distortion of Fe in partial replacement of Ni (Meng & Northwood 1989), the lattice parameters of Zr_2Ni and $Zr_2(Fe,Ni)$ are essentially the same within an error of ~1% (Lucuta et al. 1981; Chemelle et al. 1983). This is also the case for a comparison between C14 $ZrCr_2$ and $Zr(Fe,Cr)_2$ lattice parameters (Chemelle et al. 1983). As such, Fe and Ni are thought to replace one another's lattice positions in the Fe-Ni SPPs, as are Cr and Fe in the Fe-Cr SPPs. Furthermore, Fe has been shown to replace both Zr and Cr in the Fe-Cr Laves phase, resulting in compositions such as $Zr_{0.86}(Fe,Cr)_{0.14}(Fe,Cr)_2$ (Sinha et al. 1985), an unlikely occurrence in the Zr-Ni system due to the strict stoichiometry of Zr_2Ni.

The Fe/X (X = Cr, Ni) ratio of the SPPs is more flexible than the ratio Zr/(Fe+X), and is usually measured by energy-dispersive X-ray spectroscopy (EDS) in a transmission electron microscope (TEM) and, more recently, by atom probe tomography (Sawabe et al. 2013; Cockeram et al. 2013). In Zircaloy-2, the Fe/Cr ratio in the hcp C14 Laves phase varies only slightly between most reports in the approximate range 0.7-0.85 (Chemelle et al. 1983; Meng & Northwood 1989; Pêcheur et al. 1993; Huang et al. 1996) although slightly higher or lower ratios have been reported (Etoh & Shimada 1993; Sawabe et al. 2013; Cockeram et al. 2013; Goll & Ray 2002). The range in the Fe/Ni of $Zr_2(Fe,Ni)$ SPPs is generally considered to be larger, and has been demonstrated as 0.6-1.-5 (Meng & Northwood 1989; Sawabe et al. 2013; Cockeram et al. 2013; Goll & Ray 2002; Chemelle et al. 1983; Pêcheur et al. 1993) but has been reported as high as 2 or 4 (Valizadeh et al. 2014). In Zircaloy-4, which has no Ni above impurity ppm

concentration, the Fe/Cr ratio in the Laves Fe-Cr phase is consistently higher than that of Zircaloy-2 Fe-Cr SPPs at 1.5-2.5 (Gilbert et al. 1985; Van der Sande & Bement 1974; Kuwae et al. 1983; Pêcheur et al. 1993; Yang et al. 1986). While a comparison between different studies can be troublesome due to different methods of calculating elemental concentrations and changes in opinion on best practise throughout the past 40 years, general agreement in trends is often found. The use of standards is painstaking in TEM and is rarely chosen over more immediate methods such as the Cliff-Lorimer integral ratio and k-factor approach, where methods of background subtraction and the decision of whether to account for thickness and characteristic X-ray absorption, particularly by the low energy Sn L_{α} peak at 3.443 keV, will make 'quantitative' results variable between different laboratories. To obtain a more representative picture and better sampling statistics, the use of scanning electron microscopy (SEM) to observe surface SPPs and their chemistry has been shown to give Fe/Ni ratios in Fe-Ni SPPs of Zircaloy-2 that are similar to that obtained in the TEM (Goll & Ray 2002). However, the concentrations obtained are in the 1-2 wt.,% range and so the matrix contribution to such measurements remains large. Brighter electron sources, finer probe sizes and larger, more efficient detectors will pave the way for quick and thorough analysis in the SEM.

The tendency toward $ZrFe_2$ as Fe/Cr increases in $Zr(Fe,Cr)_2$ will increase long-range magnetic ordering when Fe/Cr > 2.3 (Coaquira & Rechenberg 2001), which is responsible for the stability of the cubic C14 phase in $ZrFe_2$ (Chen, Wolf, Podloucky, Rogl, et al. 2005). No such behaviour is observed in $Zr_2(Fe,Ni)$ as both Zr_2Fe and Zr_2Ni have the bct structure and neither contain enough Fe for appreciable magnetic ordering (Poynor et al. 2001). As such, the increased range of the Fe/X ratio in the Fe-Ni SPP is unsurprising. Interestingly, Yang reported that aging Zircaloy-2 in the high α-phase temperature range caused an increase in the Fe/Ni of Fe-Ni SPPs from 0.9 to ~1.1, but did not cause any change in the Fe/Cr ratio of the Laves Fe-Cr phase, suggesting more flexibility in the Fe/X stoichiometry of the former.

The bonding in the Fe-Cr and Fe-Ni phases of the Zircaloys is not widely reported. In 1987, Griffiths, Gilbert and Carpenter referred to the Zr_2(Fe,Ni) SPP as 'Zintl' phase (Griffiths, R W Gilbert, et al. 1987), a name that has been used since by many researchers in reference to the 1987 paper. Strictly, a Zintl phase is one that obeys certain valence rules, or the rules observed to be the case at the time of definition in Laves' obituary on the life's work of Eduard Zintl (Laves 1941), and, as such, comprise compounds of a Group 1 or Group 2 element with those from Groups 13-17 in varying stoichiometry. The Zr_2(Fe,Ni) SPP fits into the Zintl format in the type of bonding expected for such phases. An analysis by Schäfer suggested a wider definition concerning the partial sublattice formed by the less abundant element and the anionic nature of the bonding within that sublattice (Schäfer et al. 1973). While the electronic localisation in Zr_2(Fe,Ni) has not been explored fully, density of states (DOS) calculations by Visnov et al. have shown that Zr_2Ni contains an electron density that 'converge(s) towards the atomic Ni' (Visnov et al. 1982), suggesting some degree of ionicity. In support of this, Kuri et al. have used EXAFS and XANES to probe the local coordination environment in Zr_2(Fe,Ni) and have calculated a Zr-Ni bond distance (0.277 nm) significantly smaller than the sum of Zr and Ni elemental radii (Kuri et al. 2010). This is in line with Visnov's charge transfer from the Zr *4d* orbital to the *3d* state of Ni and therefore supports the idea of some degree of ionic character. As such, the Zr_2(Fe,Ni) phase may be referred to as Zintl-like, but it is not strictly a Zintl phase. While there is a valley at the Fermi level in the DOS for Zr_2(Fe,Ni) (Kuri et al. 2010), there is a larger valley at the Fermi level for Laves phase hexagonal C14 $ZrCr_2$ (Sun & Jiang 2004; Chen, Wolf, Podloucky & Rogl 2005), suggesting more covalent character in the *d-d* bonding of the latter. However, it should be noted that Sun and Jiang calculate the Poisson's ratio to be high for $ZrCr_2$, suggesting that any directionality in bonding is weak (Sun & Jiang 2004). If one is to roughly calculate ionicity, as do Naguib and Kelly (Naguib & Kelly 1975), by use of Pauling's equation

(2-7) $$i = 1 - E^{-0.25(X_A - X_B)^2}$$

where i is the ionicity and X_A and X_B are the electronegativities of element A and B, respectively, then the ionicity of the Zr-Ni, Zr-Fe and Zr-Cr bonds can be calculated as 0.06, 0.04 and 0.01, respectively, so that we may describe the ionic nature of the bond Zr-Ni > Zr-Fe > Zr-Cr. Such rough calculations are of course weakly convincing given the more metallic nature of bonding of such systems. There is a wide gap in the literature in terms of understanding the fundamental local electronic structures of SPPs in zirconium alloys from both a theoretical and an experimental standpoint. Importantly, the nature of bonding is to have a direct consequence in all properties of a phase, and, in particular, the differences observed in SPP behaviour in terms of defect creation and the resulting solubility and mobility of defects that have such a profound effect on phase evolution under irradiation (Brimhall et al. 1983). In the interim, observed phenomena are reported and conclusions may be drawn. The following is an analysis of the literature in regards to such irradiation-induced phenomena.

2.8.2.2 BEHAVIOUR UNDER IRRADIATION

Gilbert, Griffiths and Carpenter were the first to report the crystalline-to-amorphous transformation of the Laves phase $Zr(Fe,Cr)_2$ (i.e. Fe-Cr) in Zircaloy-2 and -4 after neutron irradiation (Gilbert et al. 1985). It was shown that more amorphisation occurred at lower irradiation temperatures (~80 °C) than at higher temperatures (~290 °C). Partial amorphisation of SPPs at fluences of 1 $x10^{25}$ n m^{-2} (~1.7 dpa) took the form of a crystalline core and an amorphous rim of ~10 nm width. Further, the amorphous rim was shown as depleted in Fe (Zircaloy-4 SPP Fe/Cr = 0.6) relative to the crystalline core (Fe/Cr = 1.7). The Fe-Cr phase has since been shown to experience several types of irradiation-induced transformation, including amorphisation, Fe-depletion, dissolution and/or growth depending on SPP size, irradiation temperature and neutron flux (Garzarolli et al. 1996; Bajaj et al. 2002). The following discussion will assess the most relevant of these trends.

Under neutron irradiation, the rate of SPP amorphisation has been shown as independent of fluence. In Zircaloy-4, the rate of increase in the width of the amorphous rim of Fe-Cr SPPs is ~10-13 nm fl^{-1} under reactor operating conditions

(Griffiths, R W Gilbert, et al. 1987; Griffiths 1990; Gilbon & Simonot 1994), where fl denotes a neutron 'fluence' of 1 $x10^{25}$ n m^{-2}. Of course, 'reactor operating conditions' is a broad term when considering the temperature and neutron flux profiles within a single reactor and the variation in such profiles between different reactors. In a comprehensive study of the effect of temperature, flux and fluence on SPPs in Zircaloy-4, Bajaj et al. have demonstrated rates of amorphous rim ingress as 7.6-25 nm fl^{-1} when operating at 310 °C and 1.2 $x10^{18}$ n m^{-2} s^{-1} (Bajaj et al. 2002), a range that agrees with the values given by Griffiths and by Gilbon and Simonot (Griffiths, R W Gilbert, et al. 1987; Griffiths 1990; Gilbon & Simonot 1994) but may lean towards a higher rate due to the higher flux than expected from power reactors at 0.7-1 $x10^{18}$ n m^{-2} s^{-1} (Shishov et al. 2005; Adamson 2014). Indeed, Bajaj et al. demonstrated that the amorphisation rate increases with neutron flux, and that no amorphisation of the Fe-Cr phase is observed at 310 °C and a low neutron flux 0.6 $x10^{18}$ n m^{-2} s^{-1}.

The tendency toward an amorphous transformation increases at higher neutron fluxes but decreases at higher temperatures (Gilbert et al. 1985; Bajaj et al. 2002), and the Laves Fe-Cr phase in Zircaloy-4 has been shown to remain fully crystalline after neutron irradiation at 400 °C (Gilbon & Simonot 1994). In the seminal work by Griffiths, Gilbert and Carpenter, different SPPs in Zircaloy-2 were shown to behave differently in different temperature regimes; at $T \leq 77$ °C all SPPs became amorphous, at $247 \leq T \leq 327$ °C the Fe-Cr SPP became partially amorphous and the Fe-Ni remained fully crystalline, and at $367 \leq T \leq 427$ °C all SPPs retained crystallinity but underwent dissolution, which resulted in re-precipitation in the matrix and at grain boundaries (Griffiths, R W Gilbert, et al. 1987). In the same publication, Griffiths et al. suggested that the rate of amorphisation in Zircaloy-2 Fe-Cr SPPs (20 nm fl^{-1}, fl = 10^{25} n m^{-2}) is twice that of Zircaloy-4 Fe-Cr SPPs (10 nm fl^{-1}) at similar temperatures of 280 and 287 °C for Zircaloy-2 and -4, respectively (Griffiths, R W Gilbert, et al. 1987). However, the Zircaloy-4 observations were in material from a BWR and the Zircaloy-2 from experimental reactor DIDO at a flux up to 17 times that of a BWR. This higher flux effect is reflected in the nature of the amorphisation process in Zircaloy-2 under high flux; no amorphous rim was observed but the core gradually accumulated an increasing number of amorphous

microstates (Griffiths, R W Gilbert, et al. 1987), suggesting different mechanisms at higher flux or, conversely, at low temperatures. Indeed, an Fe-Cr SPP amorphisation rate in Zircaloy-2 irradiated in a BWR has been shown to agree with Griffiths et al.'s 1987 Zircaloy-4 in a BWR, both at ~10 nm fl^{-1} (Huang et al. 1996).

The opposing effects of flux and temperature on SPP evolution has lead to the concept of a critical temperature for amorphisation, T_{crit}, below which amorphisation occurs and above which it does not. T_{crit} is described by Motta as the temperature at which the rate of damage equals the rate of annealing (Motta 1997), such that thermal recovery mechanisms can annihilate the irradiation damage. In a review of irradiation damage mechanisms in intermetallic systems, Motta makes the argument for the need of a system to retain short-range order at the expense of the long-range order that is destroyed under ballistic collisions, creating more microstates that eventually lead to a loss of crystallinity (Motta 1997). The electronic structure of a phase and its influence on self-solubility and allowable range of stoichiometry was discussed by Brimhall et al. (Brimhall et al. 1983), who built on the work of Naguib and Kelly, observing that a phase was likely to undergo amorphisation if the amorphous phase recrystallised at a temperature > 30% its melting temperature (Naguib & Kelly 1975). This suggests that an amorphous phase is stable if a temperature higher than $0.3T_{melt}$ is required to induce crystallisation. While Naguib and Kelly studied non-metallic systems, their correlation of an increased tendency toward amorphisation for systems of more covalent character may be relevant to the $Zr(Fe,Cr)_2$ and $Zr_2(Fe,Ni)$ phases if the former is considered to have more covalent character in its bonding (Sun & Jiang 2004; Chen, Wolf, Podloucky & Rogl 2005) and the latter more ionic (Visnov et al. 1982; Kuri et al. 2010). Alternatively, Brimhall et al. showed that ionicity had little significance in tendency toward amorphisation for a range of intermetallic systems (Brimhall et al. 1983), although the Zr_2Ni and $ZrCr_2$ phases were not studied explicitly. While Motta explains the onset of amorphisation at an SPP's interfacial region by ballistic mixing and resulting dissolution into the α-Zr matrix (Motta & Lemaignan 1992; Motta 1997), amorphisation at lower neutron fluxes where no dissolution takes place (Bajaj et al. 2002) cannot be accounted for in this model.

To fully describe SPP evolution under irradiation, we must also consider irradiation-induced dissolution. Increased chemical disorder within an SPP is a necessary requirement for amorphisation, exemplified by the lack of amorphisation in relatively pure or solid solution phases, such as the α-Zr matrix or the bcc β-Nb phase found in the Zr-Nb-based alloy systems (Shishov et al. 2011). Under irradiation, the stoichiometry ratio Fe/X (X = Cr, Ni) can be measured for the SPPs in the Zircaloys and correlations can be made with respect to irradiation parameters or the spatial distribution of the crystalline and amorphous regions of the phase. As already mentioned, Gilbert, Griffiths and Carpenter were the first to demonstrate a lower Fe/Cr ratio in the amorphous rim of the Fe-Cr SPP (Gilbert et al. 1985) with respect to the SPP core, suggesting depletion of Fe as the cause for amorphisation. This agrees with Motta's model for amorphisation, as Fe diffuses faster than Cr in the α-Zr matrix (Perez et al. 2003) and so ballistic mixing at the SPP interfacial region would result in faster Fe diffusion with respect to Cr, decreasing Fe/Cr. However, there are two main issues with this explanation. First, it does not explain amorphisation at low temperature without Fe depletion (Griffiths, R W Gilbert, et al. 1987; Bajaj et al. 2002). Second, such a model cannot explain how a decrease in the Fe/Ni ratio is observed in Fe-Ni SPPs at intermediate temperatures where Fe-Cr SPPs become amorphous, but the Fe-Ni SPPs retain their crystallinity (Griffiths, R W Gilbert, et al. 1987; Etoh & Shimada 1993). Importantly, the stoichiometric range of $ZrCr_2$ > Zr_2Ni (Arias & Abriata 1986; Okamoto 2007), and so Fe depletion, resulting in an increase in Zr/(Fe+X), should be more severe for the stability of the Fe-Ni phase, but it is not. This must be due to an increased ability for the Fe-Ni phase to compensate for the irradiation damage.

A compilation of data from several studies demonstrates trends in the Fe/X ratio and can be seen in Figure 2-15a for X = Cr and Figure 2-15b for X = Ni. All data points are from Zircaloy-2 irradiated in a BWR at nominally ~300 °C with the exception of those from Cockeram 2013, which were irradiated in neutron test reactor HFIR at ~358 °C. From Figure 2-15, the wider range in non-irradiated Fe/Ni as compared to Fe/Cr can be seen, a broad stoichiometry being a condition for better resistance to irradiation damage as discussed by Brimhall et al. (Brimhall et al. 1983). Additionally it seems that, in the early stages of irradiation <

8 dpa ~5 x10^{25} n m^{-2}, the decrease in Fe/Cr is faster than that of Fe/Ni, the former mirroring the decrease in SPP number density proposed by Goll and Ray (Goll & Ray 2002). As both types of SPP have been shown to dissolve under irradiation (Etoh & Shimada 1993; Huang et al. 1996), the SPPs must be sinks for Zr self interstitials (SIAs) and SIA clusters that are generated in the initial cascade event. Griffiths has reflected that vacancies cannot be the cause for irradiation-induced dissolution, as the SPPs are thermally stable at elevated temperatures where vacancy concentration is high (Griffiths, R W Gilbert, et al. 1987). Directional irradiation-induced dissolution of the Fe-Cr SPP along the trace of the (0001) basal plane of the α-Zr matrix has been shown quite beautifully by Yang, Figure 2-16. As such, there are two mechanisms thought to govern dissolution; Fe-depletion from the defective phase, resulting in amorphisation, and the influx of Zr SIAs along the basal plane towards the SPPs resulting in the reverse-flux of alloying elements from the SPPs along the basal plane (Griffiths, R W Gilbert, et al. 1987; Yang et al. 1986; Griffiths 1990; Huang et al. 1996). This theory has its root in the diffusional anisotropy of Zr SIAs and vacancies (Woo & Göslel 1983; M Christensen et al. 2015).

Directional dissolution along the (0001) is supported by increased Cr content detected parallel to the basal plane trace close to dissolving Fe-Cr SPPs (Griffiths, R W Gilbert, et al. 1987; Valizadeh et al. 2014), which is likely due to the basal diffusion of Zr SIAs as predicted by Woo and Göslel and the theory of diffusional anisotropy in hcp systems (Woo & Göslel 1983). This is especially convincing given that recent calculations show Fe, Cr and Ni to prefer diffusion in the [0001] direction, perpendicular to the (0001) basal plane (Christensen et al. 2014). As such, the detection of such alloying elements parallel to the basal plane must be an effect of Zr SIA diffusion towards the SPP. Interestingly, Griffiths et al. reported that 20% cold-worked Zircaloy-2 showed little evidence of SPP dissolution in comparison to recrystallised material (Griffiths, R W Gilbert, et al. 1987). This behaviour was attributed to network dislocations hindering outward diffusion,. However, it may be that the network dislocations become the dominant sinks for SIAs and SIA clusters, which is a crucial point as it is evidence for SPPs as SIA sinks in fully recrystallised systems. The detection of Fe in the matrix surrounding a

dissolving SPP seems more uniform than the basal segregation of Cr (Yang et al. 1986; Griffiths, R W Gilbert, et al. 1987). Huang et al. has noted that the Fe/Ni ratio remains constant for longer than the Fe/Cr in the early stages of neutron irradiation at ~290 °C. This means that either the Fe-Ni resists dissolution for longer or that Fe and Ni are dissolving at the same rate (Huang et al. 1996). To distinguish which, it is possible to consider the SPP morphology at its periphery; Etoh and Shimada et al. have noted the more irregular morphology of dissolving Fe-Ni SPPs in comparison to the Fe-Cr, as have other authors (Etoh & Shimada 1993; Mahmood et al. 2000; Goll & Ray 2002; Valizadeh et al. 2014). However, the fluence onset of this morphological irregularity has not been reported.

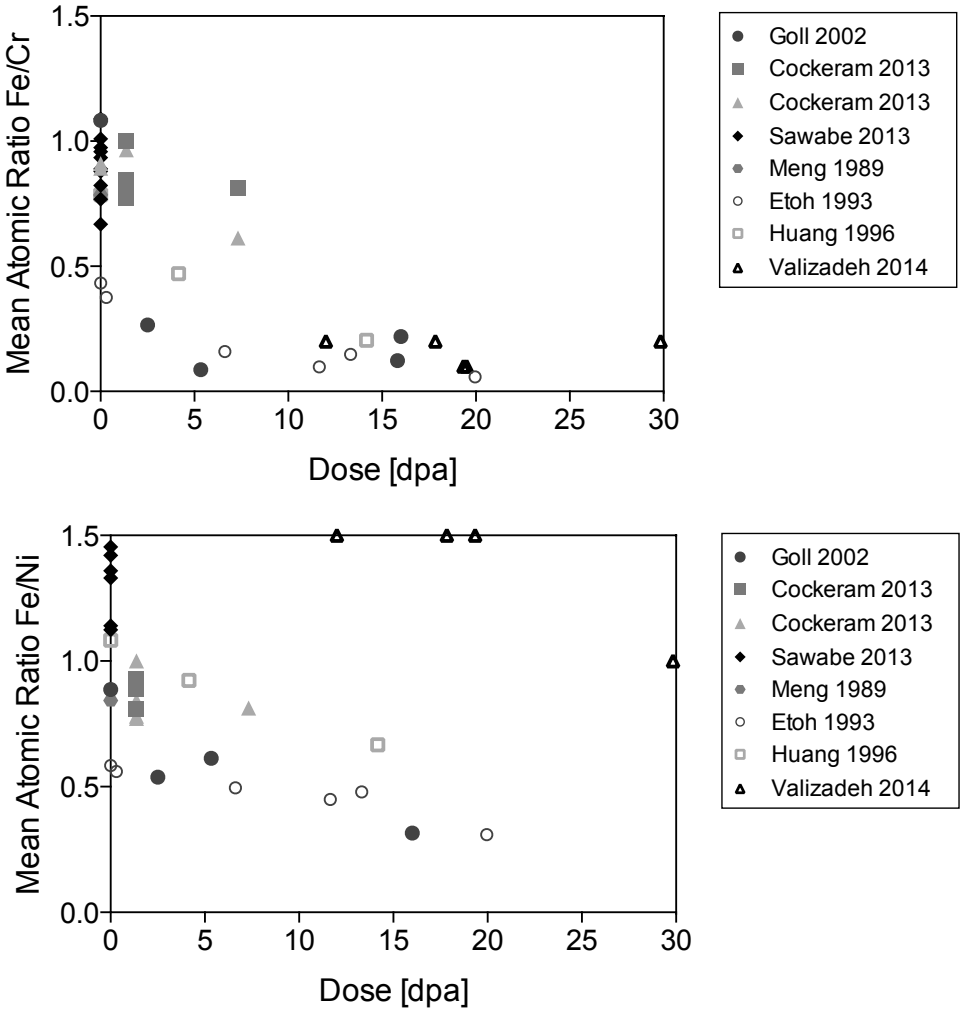

Figure 2-15 SPP Fe/X with neutron dose, (top) X = Cr, and (bottom) X = Ni. References are given in the legend. Most comprise BWR irradiation apart from one in which HFIR test reactors at 358 C were employed (Cockeram et al. 2013).

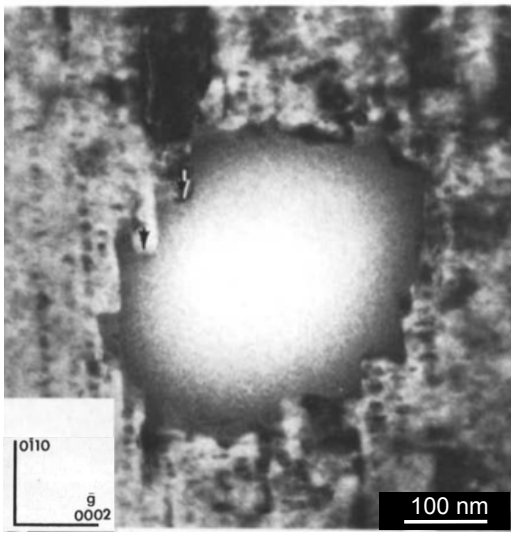

Figure 2-16 A fully amorphous Fe-Cr SPP, 14.7 x10^{25} n m^{-2}, 288 °C, BWR. Directional dissolution observed parallel to the (0001) basal plane trace (Yang 1988).

The relative diffusivities of the small transition elements in α-Zr are Fe > Ni >> Cr, Fe and Ni having similar diffusion coefficients (Perez et al. 2003). This trend in diffusivity is generally assumed to apply to the internal diffusion within the Fe-Cr and Fe-Ni phases, which may account for the better recovery properties and resulting resistance to irradiation-induced structural changes of the latter. However, little work has been done on the subject and the relative diffusivities in α-Zr are often quoted as the reason for the amorphisation the Fe-Cr phase and the lack of any structural change in the Fe-Ni. This assumption, while possibly true, has not been accounted for in the literature and an examination of diffusivity within the SPP structure is required. Recent calculations have given the point defect energies in the C14 hcp $ZrCr_2$ and the C16 bct Zr_2Ni systems (Chen, Wolf, Podloucky & Rogl 2005; Moura et al. 2001). In the $ZrCr_2$ system, the vacancy-type defects are the least energetically favourable and antisite defects, where Zr substitutes onto a Cr site (Zr^{Cr}) or Cr onto a Zr site (Cr^{Zr}) are more likely, such that a defective state may be made up of more chemical disorder than of vacancies and interstitials. In the Zr_2Ni system, the vacancy and antisite defects are on average lower in formation energy than in the $ZrCr_2$ system (Chen, Wolf, Podloucky & Rogl 2005), suggesting that if both systems had an equal number of such defects then the Zr_2Ni would be in a lower free energy state. Although this could account for

why the Fe-Ni SPPs recover irradiation damage more effectively than the Fe-Cr, arguments towards free energy are not strictly valid when one considers the dynamic and localised nature of ballistic collision cascades (Motta 1997). Interestingly, vacancy migration in the Zr_2Ni system was determined to be anisotropic with a preference in the [001] direction (Moura et al. 2001), which will have a profound effect on point defect interactions and larger, extended defects and their evolution. The Fe-Ni system does indeed become defective under neutron irradiation, as Kuri et al. have demonstrated by comparing the EXAFS and XANES with and without neutron irradiation in a BWR (Kuri et al. 2010). The degree of disorder is, however, difficult to discern and although Kuri et al. described a lack in post-irradiation long-range order, the spectra show signs of local order that may exceed that of an amorphous system. Of course, verification by TEM would be beneficial, but such fine detail is not always possible in the microscope when stoichiometry is variable, even in the non-irradiated state. Calculations regarding defect interactions have not yet been performed for either the defective $Zr_2(Fe,Ni)$ or $Zr(Fe,Cr)_2$ systems, but are certainly required if we are to have a full understanding of defect evolution within SPPs. Etoh et al. has experimentally calculated Fe diffusivities in defective Fe-Cr SPPs after neutron irradiation in a BWR by assuming that Fe dissolves from the SPP by the shortest path and relating this to the change in the Fe/Cr ratio of that SPP with respect to the non-irradiated mean (Etoh & Shimada 1993). While the Fe/Cr ratio was shown to decrease with increasing fluence, there was no significant trend towards Fe diffusivity with fluence. However, a convincing trend was observed in regards to neutron flux, suggesting that a higher flux induces a more defective structure that increases Fe diffusivity, but that under constant flux there exists a steady-state of defect generation. However, it has been demonstrated that amorphisation of Fe-Cr SPPs may occur with no dissolution at the highest neutron fluxes (Griffiths, R W Gilbert, et al. 1987; Bajaj et al. 2002). The damage rates induced by different irradiative species may be even higher than under neutron irradiation, and this effect on SPP evolution will be discussed in the following section.

2.8.2.3 SPP EVOLUTION UNDER DIFFERENT IRRADIATIVE SPECIES

The critical temperature for amorphisation, T_{crit}, above which no amorphisation occurs, has been defined earlier as the temperature at which the rate of damage production is equal to the rate of defect annealing (Motta 1997). This definition implies that higher damage rates require higher irradiation temperatures for defect annealing, and, as such, the T_{crit} under high damage rates will be higher. This is true for neutron irradiation and has been demonstrated well by Bajaj et al. (Bajaj et al. 2002). A point of interest arises when one considers the effect of different irradiative species, such as that of electrons, protons and heavy ions, as the damage rate is conventionally higher than under neutron irradiation to make experiments feasible. Under neutron irradiation, the damage rate in the α-Zr matrix is ~0.7-1 x10^{-7} dpa s^{-1} (Shishov et al. 2005; Adamson 2014), under proton irradiation it is higher by a factor of ~10^{2} at ~10^{-5} dpa s^{-1} (Zu et al. 2005), under heavy ion irradiation it is higher by a factor of ~10^{4} to ~10^{-3} dpa s^{-1} (Idrees, Yao, Kirk, et al. 2013; Zu et al. 2005) and under electron irradiation it is higher by a factor of ~10^{5} at ~7 x10^{-3} dpa s^{-1} (de Carlan et al. 1996). As such, the damage rate of electron irradiation > heavy ion irradiation > proton > neutron. One may therefore expect the T_{crit} of the $Zr(Fe,Cr)_2$ phase to follow the same trend, but it does not. In fact, T_{crit} of the Fe-Cr SPP for electron irradiation is ~27 °C (Pêcheur et al. 1993), for Ar irradiation it is ~380-577 °C (Motta et al. 1994; Pêcheur et al. 1993), for proton irradiation it is 310-350 °C (Zu et al. 2005) and for neutron irradiation T_{crit} ~330-360 °C (Griffiths, R W Gilbert, et al. 1987; Motta et al. 1991). Therefore, for different irradiative species, T_{crit} of Fe-Cr SPPs under irradiation by heavy ions > protons ~ neutrons >> electrons. This trend can be explained when one considers both the dose rate and the nature of the damage created.

With reference to Figure 2-5, the size of the damage cascade for neutrons > heavy ions > protons, and electrons produce only isolated Frankel pairs (Woo & Singh 1992), which constitutes a single vacancy and an interstitial that remains close to its ejection point. The thermal energy required to annihilate a Frankel pair is therefore low, but the damage rate is high because a relatively large distance separates one Frankel pair from the next. As such, T_{crit} for electron irradiation is low and the dpa rate high. Heavy ion irradiation creates relatively large damage

cascades and is operated under a high flux with a large displacement cross section. This means that the dpa rate is high, creating defects and clusters that require more thermal energy to recover, and so T_{crit} is high. In between, proton irradiation results in a T_{crit} only slightly higher than that of neutrons, given its small defect cascades and high damage rate. As such, proton irradiation may be the most suitable emulation of neutron irradiation in regards to amorphisation of the Fe-Cr phase. However, the measurement of irradiation dose, i.e. dpa, is clearly a poor measure of the damage as it does not consider thermal effects within cascades, resulting recombinations and the types of defects that form after the cascade's cooling phase. Although beyond the scope of the present work, there is a need in the community to model defect cascades due to protons and heavy ions in order to understand the defect evolution under such conditions more thoroughly.

The benefit of electron, proton and heavy ion irradiations is in their controllability and, on occasion, their suitability to be monitored in situ TEM. Motta has demonstrated amorphisation in both $Zr(Fe,Cr)_2$ and $Zr_2(Fe,Ni)$ SPPs, noting no preferred nucleation site for the transformation and a larger dependence on the dose to amorphisation for the Fe-Ni type SPP (Motta et al. 1991). The amorphous rim observed in neutron-irradiated Fe-Cr SPPs (Gilbert et al. 1985) has not therefore been replicated by electron irradiation (Motta et al. 1991), although a higher density of stacking faults within $ZrFe_2$ SPPs have been correlated to a lower T_{crit} for that system (Motta et al. 1996). Pêcheur has shown that the dose to amorphisation of Fe-Cr SPPs in Zircaloy-4 increases exponentially with increasing temperature under heavy ion irradiations (He, Ar and Kr ions) (Pêcheur et al. 1993), although the relative susceptibility towards amorphisation between different SPPs was shown to vary under different temperatures and irradiative species. For instance, under Ar irradiation at 60 °C the Fe-Cr SPP required a lower dose for amorphisation onset than the Fe-Ni, whereas under He ion irradiation at -150 °C the reverse was true (Pêcheur et al. 1993). The authors suggested that at lower temperatures it is chemical disorder that is rate determining, and as the stoichiometry range for the $ZrCr_2$ is larger than that of Zr_2Ni (Arias & Abriata 1986; Okamoto 2007), the $Zr(Fe,Cr)_2$ SPP is more stable at lower irradiation temperatures. At higher irradiation temperatures, the authors suggested that

defect mobility is rate controlling, and the similar diffusivities of Fe and Ni in comparison to that between Fe and Cr account for better thermal recovery of the Fe-Ni system, reversing the order of SPP stability. However, such an argument cannot account for the generally wide Fe/Ni atomic fraction stoichiometry in comparison to that of Fe/Cr (See Figure 2-15), nor the high cost to free energy of defects in the $ZrCr_2$ system in comparison to that in the Zr_2Ni (Chen, Wolf, Podloucky & Rogl 2005; Moura et al. 2001). A theoretical approach to this problem and the relative diffusivities of defects and their clusters within a defective SPP structure must be investigated in order to understand these experimentally observed phenomena more thoroughly.

While heavy ion irradiations often result in the complete amorphisation of SPPs with no change in global stoichiometry (Motta et al. 1994), 2 MeV proton irradiations of Zircaloy-4 at 310 °C have demonstrated the amorphous rim in Fe-Cr SPPs so often observed in neutron-irradiated material (Zu et al. 2005). As Zu et al. observed an amorphous rim of size 5-10 nm after a dose of 7 dpa, one might assume a linear rate of amorphous rim ingress of 0.7-1.4 nm dpa^{-1}. If we consider a rate of conversion from neutron fluence to dpa as 0.6 $x10^{25}$ n m^{-2} dpa^{-1} (Shishov et al. 2005), then this would correspond to an amorphisation rate of 1.2-2.3 nm fl^{-1} (fl = 1 $x10^{25}$ n m^{-2}), which is a slower rate of ingress by a factor of ~4 in comparison to that given by others under neutron irradiation in reactor conditions (Griffiths, R W Gilbert, et al. 1987; Griffiths 1990; Gilbon & Simonot 1994; Bajaj et al. 2002). Zu et al. also demonstrated no amorphisation of Fe-Cr phases after proton irradiation at 350 °C and complete amorphisation when under Ne ion irradiation at the same temperature at a dose of 1.2 dpa (Zu et al. 2005). While some diffraction analysis took place to observe amorphisation, high resolution TEM (HRTEM) was used to image a lack of lattice planes in the amorphous zone for the proton irradiations at 310 °C. One should be careful when assessing the extent of amorphous zones by HRTEM, as through-focal series must be obtained to demonstrate that the lack in lattice plane contrast is not due to a defocus artefact. This is especially important for interfaces, as the electropolishing sample preparation process may preferentially attack interfaces due to the different internal potentials of different phases making one anodic with respect to the other. While Zu et al. did not

correlate the amorphous rim with any Fe-depletion, as is observed in the neutron case, Fe segregation to the interfacial region of Fe-Cr and binary Zr-Fe SPPs was reported (Zu et al. 2005). Such segregation seems unlikely given the dissolution of SPPs under neutron irradiation, and the SPP in question was located at a grain boundary, which, although not considered by the authors, may provide a pathway for solute diffusion. Additionally, the segregation of Fe to the '$ZrFe_2$' precipitate shown must be considered with care, as the Zr contribution from the matrix is large to suggest a stoichiometry and one must be considerably careful when such Fe segregation is observed; zirconium silicides are known to be coated in Fe and Ni, segregated to their interface with the matrix after neutron irradiation (Griffiths et al. 1992). Impurity elements such as Si may be easily overlooked in chemical analyses.

In an in situ TEM Ne ion irradiation experiment at 350 °C, Shen et al. demonstrated the amorphisation of the Fe-Cr phase in Zircaloy-4 by 2.3 dpa and further irradiation to recrystallise the phase by 7 dpa (H.-H. Shen et al. 2014). This observation is inconsistent with Motta's observations of many amorphisation processes under many different types of irradiation, in which the amorphous phase is stable under irradiation (Motta 1997). The recrystallisation of the amorphous phase under irradiation by Shen et al. demonstrates similarities to post-irradiation annealing of neutron-irradiated material, which show recrystallisation in amorphous Fe-Cr SPPs as the precipitation of nanocrystalline clusters < 60 nm in diameter (Griffiths, R W Gilbert, et al. 1987; Yang 1988). Griffiths demonstrated that the recrystallisation temperature varied with the initial irradiation conditions, flux and temperature, although no clear trend was observed (Griffiths, R W Gilbert, et al. 1987). Yang demonstrated the back-diffusion of Fe into the recrystallising precipitates after post-irradiation anneals of at 750 °C and that such a phase transformation did not occur at temperatures of 560 °C, preferring precipitation at grain boundaries (Yang 1988). Likewise, synchrotron X-ray diffraction has been used to study neutron-irradiated material and post-irradiation annealing at 600 °C and demonstrates the appearance of broad peaks that may indicate the recrystallisation of the Fe-Cr phase (Vizcaíno et al. 2008). However, the authors do noted that the structure is difficult to determine and that

the cubic C15 structure may be involved, as opposed to the hexagonal C14 structure usually reported. Of course, X-ray diffraction gives a bulk description and so nano-precipitation in the matrix, at grain boundaries or at amorphous SPP sites, cannot be distinguished. Further, unusual XRD reflection behaviour, such as peaks moving or disappearing with time at temperature, may be due to several effects such as phase transformations, element redistribution and/or texture effects, making results difficult to interpret without parallel TEM investigation of the microstructure. In Shen et al.'s in situ Ne ion irradiations, it is reported that the Fe-Cr-type nanoprecipitates within the recrystallised pre-amorphous Fe-Cr SPPs are of the same structure as the initial hexagonal (presumably C14) structure (H.-H. Shen et al. 2014). This is probable as the amorphisation rate is high enough to expect little solute redistribution, although no semi-quantitative analyses of chemistry were performed. A radial integration of the nanocrystalline diffraction patterns obtained and their comparison to the expected C14 and C15 reflections would have proven a useful comparison to the work of Vizcaíno et al. (Vizcaíno et al. 2008).

While amorphisation of SPPs in Zr-Sn-Nb-Fe-Cr alloys has been observed by both Ne ions at 310 °C (H.H. Shen et al. 2014) and protons at 360 °C (H H Shen et al. 2014), it is the latter that displayed partial amorphisation of the 'hcp $Zr(Fe,Cr,Nb)_2$' phase by the inwardly-progressing amorphous rim observed in neutron-irradiated Fe-Cr SPPs. This is in contrast to the $Zr(Fe,Cr)_2$ SPPs in Zircaloy-4 proton-irradiated at 350 °C that exhibit no amorphisation (Zu et al. 2005), suggesting that the addition of Nb to the SPP creates a higher tendency toward chemical disorder. Shen et al. claimed that the two different SPPs, $Zr(Fe,Cr,Nb)_2$ and $Zr(Fe,Cr)_2$, had the same structure (H H Shen et al. 2014), but the elemental radius of Nb is closer to Zr and much larger than that of Fe and Cr (Perez et al. 2003). As such, antisite defects may be considered as more energetically costly with respect to the $Zr(Fe,Cr)_2$ Laves phase. Although the reported Fe depletion from the amorphous zone in the Zr-Fe-Cr-Nb SPP was clear at higher proton doses, the correlation of this to fluence may be inappropriate. The authors created their samples by extraction of focused ion beam lamella foils at various depths from the surface of a single proton-irradiated bulk specimen. As such, due to the non-linear proton

damage profile, the different samples studied had not only different proton fluences but also different flux given the same time at temperature. This adds an element of complication to the interpretation of results. For example, Shen et al. show an almost linear increase in amorphous rim size between 3.9 and 7 dpa protons (and so a rate of ~2.8 nm dpa^{-1}) but complete amorphisation at 8 dpa as opposed to the ~23 nm rim expected. The authors did not consider that the highest dose sample at 8 dpa also received the highest dose rate at twice the rate of the sample at 3.9 dpa. As has been discussed previously, neutron-irradiation flux and therefore dose rate is known to have a significant effect on both element redistribution and amorphisation within intermetallic SPPs (Griffiths, R W Gilbert, et al. 1987; Etoh & Shimada 1993; Bajaj et al. 2002).

2.8.2.4 THE INFLUENCE OF SPP EVOLUTION ON DISLOCATIONS AND IRRADIATION-INDUCED GROWTH

A higher local density of c-loops have been observed in the vicinity of second phase particles in neutron-irradiated Zircaloy-4 in the temperature range ~290-310 °C and proton-irradiated Zircaloy-4 at 350 °C (Griffiths & Gilbert 1987; Tournadre et al. 2012; de Carlan et al. 1996). This is exemplified in Figure 2-17, suggesting an effect of either a change in chemistry or strain in the surrounding matrix. While de Carlan et al. noted that preferential c-loop nucleation was only observed after Fe-Cr SPP amorphisation, the authors also demonstrated an increase in Fe concentration at c-loop positions by energy-dispersive X-ray spectroscopy line scans (de Carlan et al. 1996), suggesting that changes in chemistry are responsible for nucleation. This was also demonstrated in neutron-irradiated Zircaloy-4 by Griffiths et al. and more recently in Zircaloy-2 by Valizadeh et al., who both highlighted segregation of Cr to c-loops surrounding irradiation-induced dissolving Fe-Cr Laves phase (Griffiths et al. 1995; Valizadeh et al. 2014). Importantly, Griffiths et al. have demonstrated that amorphisation without Fe-depletion of Zircaloy-4 Fe-Cr SPPs at the lower irradiation temperature of 280 °C does not induce preferential c-loop nucleation at the interfacial region of the SPP (Griffiths et al. 1996) and de Carlan et al. noted that there are no bending contours surrounding SPPs that would suggest strain in the matrix. As such, a change in

local matrix chemistry is believed to be the cause of preferential c-loop nucleation at the SPP interfacial regions.

Figure 2-17 SPPs nucleating in the vicinity of Fe-Cr SPPs in Zy-4 after neutron-irradiation at 312 °C to 10 dpa in a PWR ~6 x10^{25} n m^{-2}.

As higher c-loop densities are correlated to higher growth strain in the Zircaloys (Holt & Gilbert 1986) and as increased Fe content in the Zircaloys are known to increase c-loop density (de Carlan et al. 1996), one could assume that an increased Fe content in the matrix would increase irradiation-induced growth. However, the growth strain of Zircaloy-2 (Holt & Gilbert 1986) is less than that of Zr-1.5Sn (wt.%) at similar temperatures (Zee et al. 1984). The main difference between the two alloy systems is the presence of SPPs containing Fe, Cr and Ni in the former. It may of course be the case that c-loops do not induce anisotropic growth but relax the strain caused by growth, which may also extend to c-loops acting to relax the strain induced in the matrix upon supersaturation with solute atoms from a partially-dissolved SPP. The nature and morphology of second phases have been shown to be the predominant factor affecting in-reactor corrosion of the Zircaloys

(Garzarolli et al. 1994). Better corrosion resistance and hence reduced hydrogen ingress has recently been shown to correlate with a decreased growth strain (Valizadeh et al. 2014), and, although beyond the scope of the present work, may have a significant impact on dislocation evolution (Christensen et al. 2014; M. Christensen et al. 2015). Whether the SPPs have a direct or indirect impact on growth strain, their evolution with neutron fluence and the mechanisms for their dissolution are a necessary field of investigation, as is the possibility of emulating the effects of neutrons with other irradiative species.

2.8.3 IRRADIATION-INDUCED PRECIPITATION

The irradiation-induced dissolution of second phase particles (SPPs) has likely consequences in precipitation elsewhere in the matrix due to the low solid solubility of Fe, Cr and Ni in the α-Zr matrix (Stupel et al. 1985; Charquet et al. 1988; Zou et al. 1995). While the solubility of the light transition elements is likely to increase under the irradiation-induced defective state and at power reactor operating temperatures, irradiation-induced precipitation (IIP) is observed throughout the matrix after irradiation at intermediate to high temperatures 280-600 °C (Griffiths, R W Gilbert, et al. 1987; Woo & Carpenter 1988), the higher temperatures being used for higher flux irradiations in neutron test reactors such as EBR-II. The following is a description of the types of IIP reported in the literature.

While it has been suggested that irradiation-induced Sn precipitates are a electropolishing-induced artefacts arising from redeposition (Yang et al. 1986), such artefacts should be distinguishable from true Sn precipitates by electron diffraction techniques. Hexagonal-shaped Zr-Sn type precipitates faceted by (0001) and close to $\{21\bar{3}0\}$ planes have been observed only after neutron irradiation at high fluxes, high temperatures and to high fluences (Griffiths, R W Gilbert, et al. 1987; Gilbon & Simonot 1994). Such IIPs are thought to form due to irradiation-enhanced diffusion, have been shown as stabilised by relatively low concentrations of Fe (Sn/Fe ~5) (Griffiths, R W Gilbert, et al. 1987; Woo & Carpenter 1988) and are stoichiometrically Zr_5Sn_3 with an epitaxial relationship

with the matrix (Woo & Carpenter 1988). Such IIPs are not reported in the non-irradiated material, but Zr_4Sn SPPs in non-irradiated Zircaloy-4 have been demonstrated (Van der Sande & Bement 1974), as have their nucleation after proton irradiation at 350 °C to 1 dpa (Kai et al. 1990). However, Mössbauer spectra of Zr alloys ZIRLO™, Excel, Zircaloy-2 and -4 have demonstrated no obvious change in Sn environment after neutron irradiation at the high temperatures and flux that should create Sn-containing IIPs (Sawicki 1999). Bulk, non-destructive analytical techniques such as Mössbauer spectroscopy and X-ray diffraction are of course desirable for obtaining global information, but they are limited in the detection of small precipitates of low volume fraction. As such, parallel microscopy investigations are desirable to corroborate findings, but research groups generally specialise in either bulk or microscopic techniques. The stability of IIPs may be assessed by post-irradiation annealing experiments, which have shown no change in Zr_5Sn IIPs after 1 hr at 600 °C (Griffiths, R W Gilbert, et al. 1987) but complete dissolution after 27 days at 590 °C (Woo & Carpenter 1988).

Rod-shaped IIPs rich in Fe and Cr have been observed in Zircaloy-2 and -4 after neutron irradiation at intermediate to high temperatures (Griffiths, R W Gilbert, et al. 1987; Woo & Carpenter 1988). Such rods are predominantly observed after high flux irradiations, are long in the <0001> direction and have been shown to align in the (0001) basal plane (Griffiths, R W Gilbert, et al. 1987) with a large range in length but an average of ~150 nm (Woo & Carpenter 1988). Such features have been shown in higher density close to partially-dissolved $Zr(Fe,Cr)_2$ SPPs (Griffiths 1988) and have been reported to have either Fe/Cr ~1 (Griffiths, R W Gilbert, et al. 1987) or Fe > Cr (Woo & Carpenter 1988). Basal-aligned IIP of rods or platelets rich in Fe and Ni have also been show as having their length inclined to the <0001> direction after fast-flux neutron irradiation at ~420 °C (Griffiths 1988). Post-irradiation annealing has demonstrated the instability of the Fe-Cr and Fe-Ni SPPs discussed thus far (Griffiths, R W Gilbert, et al. 1987; Woo & Carpenter 1988), which suggests that their formation is induced by the irradiation process. IIPs close to partially-dissolved SPPs have been shown to diffract according to the precipitate reflection after post-irradiation annealing at 600 °C for 1 hr (Griffiths & Gilbert 1987). This may suggest that the irradiation-induced precipitates are most

stable when they more closely reflect the chemistry of the parent $Zr(Fe,Cr)_2$ SPP. However, the chemical content of these features has not been studied extensively with respect to matrix position or under different irradiation conditions and to various fluences. Interestingly, while no rods are observed under irradiation at 300 °C, they are after post-irradiation annealing at 600 °C (Griffiths, R W Gilbert, et al. 1987). As such, small rods or solute clusters in the matrix may be present at power rector operating temperatures and may act as nucleation sites for rod growth during post-irradiation annealing. Matrix supersaturation with solute has been shown to be important in this regard, as β-quenched Zircaloy-4-type material has been shown to contain more IIP rods than fully recrystallised material irradiated under the same conditions (Gilbon & Simonot 1994). Such an observation may raise the question of whether the matrix surrounding an SPP, and for that matter elsewhere in the matrix, is simply supersaturated in solute, which then precipitates upon cooling and, as such, does not occur in the dynamic irradiation environment. To date, this has not been assessed in the literature.

In addition to Zr-Fe-Cr or Zr-Fe-Ni IIPs, the nucleation of binary Zr-Fe precipitates, either during irradiation or after a post-irradiation annealing treatment, is reasonably well documented in the literature. While Yang et al. reported no evidence of IIP after neutron irradiation at 288 °C, post-irradiation annealing at 560 C for 10 minutes resulted in the precipitation of Zr-Fe precipitates at grain boundaries (Yang 1988). The nucleation of Zr-Fe phases with stoichiometry Zr_3Fe has been reported in Zircaloy-4-type alloys under PWR conditions (Garzarolli et al. 1996) and in Zircaloy-2 under BWR conditions (Goll & Ray 2002). Zr-Fe phases are found in the non-irradiated state if the Fe/Cr > 4 (wt.%) in the total alloy composition (Charquet et al. 1988), resulting in the nucleation of either Zr_3Fe or Zr_2Fe, the preference for which possibly depending on cooling rates (Charquet et al. 1988). This is supported by the relative stability of phases in the binary Fe-Zr phase diagram; Zr_2Fe is stable at higher temperatures and Zr_3Fe at lower temperatures (Stein et al. 2002; Okamoto 2006). The Zr_3Fe phase has been shown as stable under neutron irradiation at ~315-350 °C in regards to both changes in chemistry and structure (Shishov et al. 1996; Garzarolli et al. 1996), although its amorphisation behaviour under electron irradiation is well known (Motta et al.

1993; Motta 1997). Such stability may be predicted if one considers the low melting point of the Zr_3Fe phase (885 °C) in comparison to other phases (e.g. $Zr(Fe,Cr)_2$ T_{melt} = 1630 °C (Motta & Lemaignan 1992). As such, for a given irradiation temperature, the Zr_3Fe SPP might be better able to recover the damage incurred by thermal annealing effects in comparison to high T_{melt} SPPs. It should be noted that while irradiation-induced precipitation of Zr_3Fe is sometimes observed after the dissolution of $Zr(Fe,Cr)_2$ SPPs, IIP of $Zr(Fe,Cr)_2$ is also thought to occur, depending on the irradiation temperature (Garzarolli et al. 1996). However, Garzarolli et al. have demonstrated that the growth rate of SPPs in Zircaloy-4-type alloys prior to irradiation is in the order Zr_3Fe > $Zr(Fe,Cr)_2$ > $ZrCr_2$ > $Zr_2(Fe,Si)$ (Garzarolli et al. 1996). This was determined simply by measuring SPP size as a function of annealing parameter, and may suggest that Zr_3Fe is commonly reported as the main form of IIP because it grows quickly at the expense of other types of phase. Further, while Garzarolli et al. reported no observed epitaxial relationships between Zr_3Fe and the α-Zr matrix, multiple epitaxial relationships have been reported elsewhere (Barberis et al. 2005). It has therefore been suggested that Zr_3Fe has a low anisotropy with respect to interfacial energy and, as such, the interfacial energy is not thought to be a dominating influence in the formation and stabilisation of the phase (Barberis et al. 2005), adding to its ability to nucleate and grow at the expense of other phases. Lastly, the $Zr_4(Fe,Cr)$ phase has been reported as present after quenching from the α+β- or β-phase region, and is known to dissolve quickly at low fluences (Yang et al. 1986; Cheng et al. 1994). While some have referred to the existence of this phase as 'questionable' (Barberis et al. 2005) as it is not present in the Zr-Fe phase diagram (Stein et al. 2002; Okamoto 2006), its metastability may be important to consider in the redistribution of solute and nucleation of new phases during irradiation.

While the irradiation-induced precipitates described thus far have been observable in the TEM due to their diffraction contrast, smaller clusters < 10 nm in diameter may not diffract sufficiently to provide contrast against the defective matrix background. Atom probe tomography (APT) is well suited for such an application and has been used recently to demonstrate clusters containing predominantly Fe and Cr (Ni to a much lesser extent) in Zircaloy-2 cladding

material after irradiation in a BWR (Sundell et al. n.d.). While the cluster composition was highly variable in the 1-5 nm diameter clusters, and, as such, the structure likely non-crystallographic, Sundell et al. reported a high number density of the clusters as high at 8 ±2 x10^{23} m^{-3} and clearly demonstrated that the clusters were aligned in planar arrays separated by a distance of ~10 nm (Sundell et al. n.d.). These planes were assumed to be basal (0001) planes due to their uniqueness, but orientation information was not available from the APT data sets. The tendency of Fe and Cr to cluster in a defective Zr lattice has recently been investigated by Burr et al., who have shown by way of ab initio DFT calculations that clusters of Fe, Cr or Fe+Cr around a Zr vacancy induces less lattice strain than an isolated interstitial defect (Burr et al. 2015). Burr et al. do not only provide evidence for cluster growth but also suggest that larger Zr vacancy clusters (Varvenne et al. 2014) would provide a significant sink for dispersed Fe, Cr solute that this interaction may be a driving force for SPP dissolution. While this does not take into account the dissolution of SPPs by its sink strength for Zr self-interstitials with mobility in the basal plane (Griffiths 1990), the vacancy sink of IIP clusters may act as a cooperative mechanism and indeed there is suggestion that Fe, Cr clusters, while 3-dimensional in nature, form predominantly in the basal plane (Burr et al. 2015). It should be noted that APT of non-irradiated Zircaloy-4 has revealed a relatively low density of Fe-Cr clusters (Dong et al. 2013) but without the planar segregation observed by Sundell et al.

While not strictly precipitation, Fe and Cr segregation to c-loop positions have been reported by way of EDS line scans (Griffiths et al. 1995; de Carlan et al. 1996; Valizadeh et al. 2014) and Fe and/or Ni segregation suggested at pyramidal defect positions (Griffiths, R.W. Gilbert, et al. 1987). Sundell et al. were the first to directly observe segregation of Fe and Sn in a clear loop-type formation (Sundell et al. n.d.). Chemical segregation to dislocation loops has been discussed as likely to change the loop bias for point defects and clusters, and, as such, is thought to be important in the stability, shape and evolution of dislocation structures (Griffiths 1988). The dependence of c-loop formation on matrix solute content has been well-studied (Griffiths & Gilbert 1987), as has the nucleation of c-loops in the vicinity of partially-dissolved SPPs (Griffiths & Gilbert 1987; Tournadre et al. 2012; de Carlan

et al. 1996). Further, the effect of variable solute segregation to dislocations in different alloys and at different irradiation doses has been suggested as a source of variation in both a-loop size and in irradiation-induced hardening measurements in Zircaloy-2 and -4 (Cockeram et al. 2011; Cockeram et al. 2013; Cockeram et al. 2014). As dislocation loops are thought to be intrinsically related to macroscopic irradiation-induced growth strain, their interaction with dispersed solute and its clustering is worthy of further investigation.

2.8.4 GRAIN BOUNDARIES

Both Fe-Cr and Fe-Ni type second phase particles (SPPs) are commonly observed both in the matrix and at the grain boundaries in the Zircaloys (Kuwae et al. 1983; Yang et al. 1986; Griffiths, R.W. Gilbert, et al. 1987; Zou et al. 1994). In Zircaloy-4 that is heat treated in the α+β- or β-phase temperature range, followed by quenching, metastable Zr_4(Fe,Cr) SPPs form at grain boundaries which dissolve under neutron irradiation (Yang et al. 1986). Grain boundary precipitates with elongated morphology along the grain boundary precipitate by annealing in the α+β-phase temperature range (Griffiths, R.W. Gilbert, et al. 1987). Therefore, chemical segregation to grain boundaries is evident prior to irradiation. Further, post-irradiation annealing experiments of neutron-irradiated Zircaloy-4 at 560 °C for 1 hour demonstrate the precipitation of Zr-Fe binary phases at grain boundaries, but, interestingly, not at higher annealing temperatures of 750 °C (Yang 1988). Likewise, irradiation at temperatures 370-440 °C results in the irradiation-induced precipitation of Fe-, Cr- and Ni-rich SPPs at grain boundaries (Griffiths, R.W. Gilbert, et al. 1987).

While such behaviour has been known for some time, the direct detection of segregation to grain boundaries has not been reported until more recently, aided especially by the development of atom probe tomography (APT). The first report of segregation to grain boundaries in a Zr alloy was of Fe and Nb segregation in ZIRLO™ (Hudson & Smith 2009), detected by APT as continuous along the boundary. The segregation was explained by the authors as due to a mismatch in the elemental size of the segregated element with respect to Zr. Discontinuous

grain boundary segregation has been observed by APT for Zr-0.8Fe and Zr-0.15Cr (wt.%) β-quenched binary alloys (Gault et al. 2013). In the Zr-0.8Fe alloy, the average grain boundary composition contained ~2.5 at.% Fe but the individual nano-precipitates or clusters contained either up to 50 at.% Fe or had the composition Zr_3Fe, depending on the shape (lath or spheroid, respectively). In the Zr-0.15Cr alloy, the average Cr concentration at the boundary was 0.5-0.8 at.% and the spheroidal nano-clusters of average composition 35 at.% Cr. APT studies of pure Zr (crystal bar) show Fe segregation to grain boundaries at ~2.5 at.% and in a test alloy Zr-0.4Fe-0.2Cr (wt.%) at ~2.7 at.% (Dong et al. 2013). In the same study, segregation to grain boundaries in Zircaloy-4 consisted of both Fe and Sn with Fe > Sn and the former at ~1.5 at.%. The concentration of Sn at the boundary was not provided, likely due to the enhanced diffusion of Sn at surfaces and interfacial regions during atomisation, which makes quantification of Sn difficult by APT (Sundell et al. 2015). When a line scan was extracted along such a boundary, a depletion in Sn was observed either side of the boundary, which was not discussed by the authors (Dong et al. 2013). Such depletion next to the grain boundary in conjunction with the known diffusive behaviour of Sn may make such an observation questionable and supporting STEM-EDS evidence would be ideal. Interestingly, no Cr segregation was observed at any grain boundary in crystal bar Zr, the Zr-0.4Fe-0.2Cr alloy or Zircaloy-4 (Dong et al. 2013). There is little in the literature regarding chemical segregation to grain boundaries in Zircaloy-2. However, 'significant' Fe segregation to some (but not all) grain boundaries has been observed in Zircaloy-2 cladding after neutron irradiation in a BWR and no segregation of Cr, Sn or Ni (Sundell et al. n.d.). However, grain boundaries were not the main focus of that particular work and as such the number of grain boundaries studied was, although not stated explicitly, likely few.

Grain boundary segregation in steels has predominantly been studied by STEM-EDS (Vatter & Titchmarsh 1989; Simonen et al. 1995; Allen et al. 1997; Jiao & Was 2011a; Jiao & Was 2011b; Wharry et al. 2011; Wharry et al. 2012), Auger electron spectroscopy (AES) (Damcott et al. 1995; Allen et al. 1997) and more recently by electron energy loss spectroscopy (EELS) (Marquis, Lozano-Perez, et al. 2011) and especially by atom probe tomography (APT) (Etienne et al. 2010; Marquis, Hu, et

al. 2011; Jiao & Was 2011a; Marquis, Lozano-Perez, et al. 2011; Jiao & Was 2011b; Kuksenko et al. 2012; Hu et al. 2012). In STEM-EDS this is a tedious task due to the limiting geometry of the sample stage and the EDS detector; the one-detector system requires the sample to be tilted towards it and grain boundaries require tilting such that the boundary plane is parallel to the beam direction. These two conditions can be difficult to satisfy simultaneously. Although not a comprehensive study, no segregation to grain boundaries has been observed in neutron-irradiated Zircaloy-2 BWR cladding (Valizadeh et al. 2014). In a recent study of neutron irradiation in a HFIR test reactor at ~358 °C, EDS line scans over grain boundaries has demonstrated some segregation in both Zircaloy-2 and -4 (Cockeram et al. 2013). In the Zircaloy-4 observations by Cockeram et al., no segregation to boundaries was observed at 0.11 and 0.55 $x10^{25}$ n m^{-2} but both Fe and Sn segregation after irradiation to 2.93 $x10^{25}$ n m^{-2}. Likewise, in Zircaloy-2, segregation of Fe, Sn, Ni and/or Cr was detected at some grain boundaries after irradiation to 2.93 $x10^{25}$ n m^{-2} but not for all boundaries. In conclusion, the authors suggested that segregation to grain boundaries occurs after a threshold neutron dose that may be related to the onset of irradiation-induced second phase particle dissolution (Cockeram et al. 2013). However, the difference in segregation between different grain boundaries was large, few grain boundaries were studied and no boundaries were studied in the non-irradiated material. Further, a clear boundary line is not evident from many of the images shown, and, as such, some of the boundaries studied may not have been tilted such that the boundary plane was exactly parallel to the beam direction, thereby diluting any segregation signal with that of the matrix.

The relevance of grain boundary evolution is not only in SPP observations but also in that of dislocations. A grain boundary-adjacent zone of ~200 nm in width has been shown as denuded in a-loops for Zircaloy-2, neutron-irradiated in the test ORR reactor at 400 °C and relatively low neutron fluences, 0.7-1.2 $x10^{25}$ n m^{-2} (Gilbert et al. 1979). In recent in situ TEM irradiation studies with 1 MeV Kr ions, a depletion in c-loop density was observed in the region close to grain boundaries for both pure Zr after 1 dpa at irradiation temperatures of 400 and 500 °C (Idrees, Yao, Kirk, et al. 2013) and for Zr alloy Excel (Zr-3.56Sn-0.87Mo-0.84Nb-0.13Fe

(wt.%)) after 10 dpa at an irradiation temperature of 100 °C (Idrees, Yao, Sattari, et al. 2013). Interestingly, neutron irradiation at 400 °C results in a-loop denuded zone (Gilbert et al. 1979) and Kr ion irradiation at the same temperature results in a c-loop denuded zone but no such zone for a-loops (Idrees, Yao, Kirk, et al. 2013). While the dpa range is similar for the two irradiation experiments (low dose ~1 dpa), the type and rate of damage is different, as is the alloy (Zircaloy-2 under neutron and pure Zr under Kr ion irradiation). For the Excel alloy, the authors correlated the 80 nm wide c-loop denuded zone with a decrease in characteristic Fe X-ray signal and, as such, the authors suggest that a lack in Fe close to the boundary prevents c-loop formation (Idrees, Yao, Kirk, et al. 2013). Fe has been demonstrated to segregate to c-loop positions in electron-irradiated Zircaloy-4 (de Carlan et al. 1996) and a higher density of c-loops are commonly observed in the vicinity of partially dissolved SPPs (Griffiths & Gilbert 1987; Tournadre et al. 2012; de Carlan et al. 1996). As such, Fe is generally thought to have an effect of stabilising the nucleation of invariably vacancy c-loops, likely through an elastic interstitial (Fe) -vacancy interaction or through stable, crystallographic Fe-vacancy pairing (de Carlan et al. 1996).

While Idrees et al. use this knowledge base to suggest that the grain boundary-adjacent region in Kr ion-irradiated Excel has a depletion in Fe that results in a c-loop denuded zone, no explanation is proposed as to why this Fe depletion may occur. Fe depletion from the boundary is suggested by the authors (Idrees, Yao, Sattari, et al. 2013), which has been discussed as occurring by one of two mechanisms in irradiated steel (Bruemmer et al. 1999): an inverse Kirkendall mechanism that supposes that vacancy diffusion to a boundary encourages fast disusing elements to deplete from the boundary and slow diffusing elements to segregate to the boundary; and an interstitial association mechanism by which self interstitials migrate to the boundary and bring with them elements of a large misfit. As such, the inverse Kirkendall mechanism would result in irradiation-induced depletion of Fe, Ni, Cr at the boundary and an increased segregation of Sn. However, it would not explain the depletion adjacent to the grain boundary that is observed by Idrees et al. (Idrees, Yao, Sattari, et al. 2013), which can be explained by irradiation-induced segregation of Fe to the boundary by the interstitial

association mechanism. While not suggested by the authors, this is in support of the proposed irradiation-induced segregation of Fe to boundaries in Zircaloy-2 and -4 after neutron irradiation in test reactor HFIR at ~358 °C (Cockeram et al. 2013).

The question of a mechanism for grain boundary segregation in Zr and its alloys, i.e. either an inverse Kirkendall by vacancy migration to the boundary or an interstitial association by SIA migration to the boundary, may be assessed to some extent by a consideration of anisotropic diffusion. The proposal that vacancies and SIAs have a difference in anisotropic diffusion (DAD) within the hcp lattice, i.e. that vacancies are almost isotropic and that SIAs have a preference for diffusion in the basal plane (Woo & Göslel 1983), has been demonstrated experimentally with respect to the nucleation of cavities in the vicinity of grain boundaries. One consequence of DAD theory is that grain boundaries will receive a net influx of vacancies or interstitials depending on their orientation with respect to the crystal; boundaries parallel to the <0001> direction will receive a net flux of SIAs from the basal plane and those parallel to the basal plane will receive a net flux of vacancies from the <0001> direction (Woo & Göslel 1983). As such, one may expect cavities (vacancy agglomerations) to preferentially form close to grain boundaries that have a line perpendicular to the basal plane, i.e. one that receives a net flux of interstitials, causing cavities close to the boundary. This has indeed been shown in pure Zr (crystal bar and sponge), neutron-irradiated in test reactor EBR-II at ~430 °C (Griffiths et al. 1988) and is demonstrated in Figure 2-18. Further, it was reported in the same study that grain boundaries parallel to the basal plane have a smaller interstitial a-loop denuded zone and that interstitial a-loop denuded zones were consistently larger than vacancy a-loop denuded zones, independent of grain boundary orientation (Griffiths et al. 1988). While Griffiths et al. noted that this anisotropic effect may not necessarily hold true for alloyed Zr as some cavities were observed in Zircaloy-2 at grain boundary lines parallel to the basal plane (Griffiths et al. 1988), it is important to consider the effect of anisotropic diffusion and grain boundary orientation when assessing segregation to a boundary and defective structures (or lack thereof) in the surrounding zone. As such, an inverse Kirkendall mechanism may be expected at boundaries that receive a net flux of vacancies parallel to the basal plane, and an interstitial association mechanism

may be expected to occur at grain boundaries that receive a net flux of interstitials perpendicular to the basal plane. Recent calculations by Christensen et al. have demonstrated that Fe, Ni and Cr have an anisotropic diffusion in hcp Zr with a preference in the <0001> direction (Christensen et al. 2014), which may affect segregation or depletion at boundaries orientated differently. Such a concept, theoretical or experimental, has not to date been investigated. However, the lack in irradiation-induced Cr segregation to grain boundaries (Cockeram et al. 2013) can not therefore be explained by diffusivity alone and may be due to irradiation-induced precipitation before reaching the boundary.

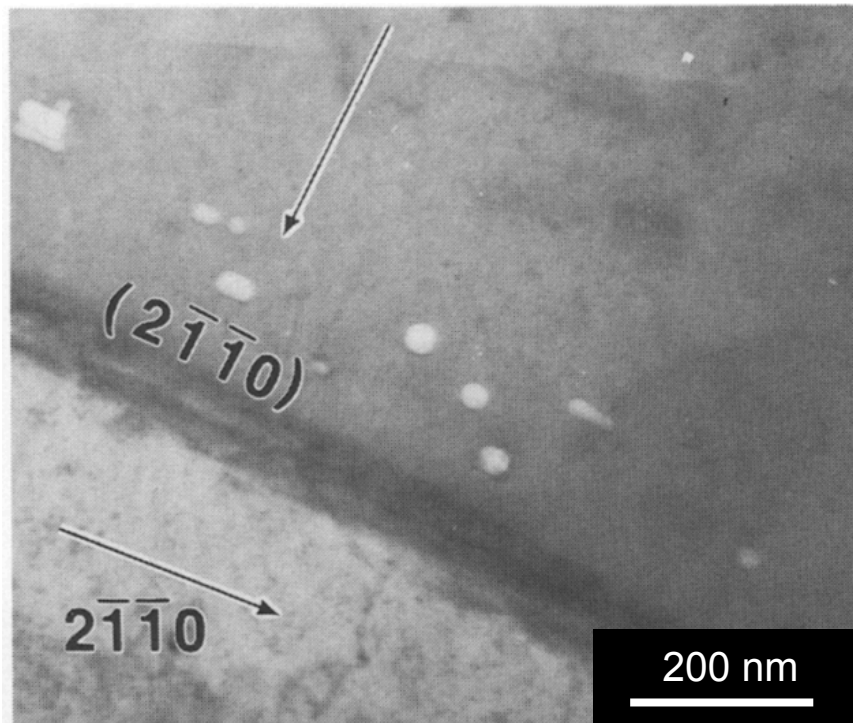

Figure 2-18 Cavities are observe to nucleate at grain boundaries orientated with their line perpendicular to the basal plane (top grain) and not parallel (bottom grain) after neutron irradiation in test reactor EBR-II of crystal bar Zr at ~430 °C and to a fluence of 15 x10^{25} n m^{-2}.

2.9 TABLES

Table 1 Zr, it's common alloying elements and some of their physical properties

Element	[a]$r_{metallic}$ [pm]	r/r_{Zr}	Position matrix	[a]D_{av} in α-Zr [m^2 s^{-1}]	[n]ΔVol_{sub} [%]	Max solubility in α-Zr [at.%]	[b]σ^n_{abs} [x10^{-28} m^{-2}]	[b]σ^n_{sct} [x10^{-28} m^{-2}]
Zr	160	1	Substitutional	4.8601e^{-17}	0	-	0.185	6.46
Sn	158	0.988	Substitutional	9.9375e^{-17}	-0.06	[m]3%, 50 °C; [h,i]5.1-6.5%, 943-953 °C	0.626	4.892
Nb	147	0.919	Substitutional	3.8292e^{-15}	-0.27	[c-g]0.3-0.6%, up to 620 °C	1.15	6.255
Fe	128	0.800	Interstitial	1.3346e^{-09}	-0.72	[j]0.005%, 400 °C; [k]0.020%, 820 °C	2.56	11.62
Cr	132	0.825	Interstitial	5.6322e^{-12}	-0.81	[k]0.035%, 860 °C	3.05	3.49
Ni	125	0.781	Interstitial	7.9533e^{-10}	-0.85	[l]0.0014%, rtp, anneal 96hr 837 °C	4.49	18.5

[a]Metallic radii, $r_{metallic}$, and diffusion coefficients averaged over all crystallographic directions, D_{av}, (Perez et al. 2003). An atom is considered to be substitutional if $r/r_{Zr} > 0.83$ (Tendler & Abriata 1987)

[b]Absorption and displacement cross sections, σ^n_{abs} and σ^n_{scat}, respectively, for 25.30 meV thermal neutrons, wavelength 0.1798 nm, velocity 2200 m s^{-1} (Sears 1992)

[j](Stupel et al. 1985)

[k](Charquet et al. 1988), NB: values are in Zr- 1.4wt.% Sn solid solutions

[c-g](Sabol 2005; Barberis et al. 2004; Kim et al. 2005; Woo & Griffiths 2009; Abriata & Bolcich 1982)

[h,i](Jerlerud Pérez et al. 2008; Okamoto 2010)

[m](Okamoto 2010)

[l](Zou et al. 1995)

[n](Christensen et al. 2014)

Table 2 Alloy compositions and their SPPs.

Alloy	Composition					SPP Properties			
	Sn	Nb	Fe	Cr	Ni	Type	Chemistry	Structure, Lattice Parameters [nm]	T_m(SPP) [°C]
^Zircaloy-2	1.20-1.70	-	0.07-0.20	0.05-0.15	0.03-0.08	$Zr(Fe,Cr)_2$	Fe/Cr = $^{\$}$0.82, $^{+}$0.7-1.1, ^{b}0.7	*hcp C14 *a* = 0.500 *c* = 0.820, §SG *P63/mmc*	^{a}1627
						$Zr_2(Fe,Ni)$	Fe/Ni = $^{+}$1.6-2.1, ^{b}1	*bct C16 *a* = 0.648 *c* = 0.526, ^{T}SG *I4/mcm*	^{b}1137
^Zircaloy-4	1.20-1.70	-	0.18-0.24	0.07-0.13	-	$Zr(Fe,Cr)_2$	Fe/Cr = $^{\pm}$2.5, ^{b}1.7	*hcp C14 *a* = 0.501 *c* = 0.821, §SG *P63/mmc*	^{a}1627
						$^{x}Zr_3Fe$	Stoichiometric	^{o}Orthorhombic *a* = 0.33, *b* = 1.1, *c* = 0.55	^{c}885
Zr-1Nb	-	1.0	-	-	-	β-Nb	^{Y}10-15 wt.% Zr	^{n}bcc *a* = 0.32970, SG = *Im-3m*	
Zr-2.5Nb	-	2.5	-	-	-	β-Nb	^{f,g}5% Zr	^{n}bcc *a* = 0.32970, SG = *Im-3m*	
^{Y}E635	1.2	1	0.35	-	-	$Zr(Fe,Nb)_2$	^{i}Fe/Nb = 0.38	^{Y}hcp C14 *a* = 0.53-0.55 *c* = 0.85-0.87	^{d}≤750
						$(Zr,Nb)_2Fe$		^{Y}fcc *a* = 1.21	
						$(Zr,Nb)_2(Fe,Nb)$		^{Y}fcc *a* = 1.21	
^ZIRLO™	1.0	1.0	0.1	-	-	$Zr(Fe,Nb)_2$	^{j}Fe/Nb = 0.67-1	*hcp C14 *a* = 0.53 *c* = 0.875	^{d}≤750
						β-Nb		^{n}bcc *a* = 0.32970, SG = *Im-3m*	^{e}<2230
M5™	<30 wppm	0.97	237 wppm	32 wppm	-	β-Nb	^{h}10-15 wt.% Zr	^{n}bcc *a* = 0.32970, SG = *Im-3m*	^{e}<2230

^(Hallstadius et al. 2012)
*SXRD (Motta et al. 2002)
§SG = space group, (Coaquira et al. 1999)
$Fe/Cr ratio (Chemelle et al. 1983)
+Fe/X (X = Cr, Ni) ratio (Valizadeh et al. 2014)
xZr_3Fe SPPs occur when the alloy composition Fe/Cr > 4 (Garzarolli et al. 1996)
±Fe/Cr ratio (Van der Sande & Bement 1974)
TSG = space group, (Havinga et al. 1971)
a(Motta & Lemaignan 1992)
b(Pêcheur et al. 1993)
Y(Shishov et al. 2005)
n(Arakcheeva et al. 2002)
c(Garzarolli et al. 1996)
d(Shishov et al. 2011)
eT_m(bcc Nb), decreasing with increasing Zr content (Ashkenazi et al. 1978)
f(Abriata & Bolcich 1982)
g(Cheadle et al. 2010)
h(Mardon et al. 2000)
i(Shishov et al. 2010)
j(Sabol et al. 1994)

2.10 THE PRESENT WORK

Much of the preceding literature review highlights the lack in a systematic approach to the study of irradiation damage in Zr and its alloys. While the range of experimental conditions chosen in the literature is wide, and so variables may be assessed when comparing the work of different groups, uncertainty arises from a lack in a methodical and clear way of providing results that are directly comparable. For instance, the temperature and flux profiles within power reactors make comparisons to tightly controlled experiments almost impossible, and indeed there are significant discrepancies between power- and test-reactor experiments that seek to quantify dislocation density, Figure 2-12. Importantly, a mechanistic understanding of phenomena is lacking due to this lack in a systematic approach. With advancements in experimental techniques such as atom probe tomography (APT), the detection of chemical segregation on the smallest of scales is possible (Hudson & Smith 2009; Sundell et al. n.d.), but a simultaneous crystallographic analysis is difficult in such data sets.

It is the objective of the present work to utilise high spatial resolution scanning transmission electron microscopy (STEM) together with energy dispersive X-ray spectroscopy (EDS) of a large solid angle and detection efficiency for the systematic study of irradiation defects and microchemical changes with variable irradiation dose. Both proton and neutron irradiation is assessed in order to quantify the degree to which the systematic former may emulate the frequently variable latter. Importantly, the relationship between the evolution of microchemistry in the matrix and dislocation arrangement is studied in order to probe the mechanisms by which dislocations interact and how this affects the microscopic phenomena that are so frequently attributed to irradiation-induced growth. For instance, the alignment in basal planes of a-loops (A Jostsons et al. 1977; Griffiths 1988), c-loops (A. Jostsons et al. 1977; Holt & Gilbert 1986; Griffiths 1988) and nano-clusters (Sundell et al. n.d.) suggests inter-relatedness, but this has not been studied explicitly to date. The present work attempts to combine such observations in a cohesive study of Zircaloy-2. In order to obtain a detailed picture

on the nano-scale, we utilise both APT and STEM-EDS in order to obtain a more complete picture of the crystallographic-dependent nano-precipitation that was reported more than 25 years previously (Griffiths, R W Gilbert, et al. 1987; Woo & Carpenter 1988).

Aside from the technical objectives of the present work, it is hoped that a detailed study of irradiation damage under proton irradiation may inspire other research groups to do the same. The development that such a technique could bring to the field of nuclear materials is almost infinite, and widespread academic access to such facilities will promote a global response to the global crisis that is energy resource.

2.11 REFERENCES

Abriata, J.P. & Bolcich, J.C., 1982. The Nb-Zr (niobium-zirconium) system. *Bulletin of Alloy Phase Diagrams*, 3(1), pp.34–44.

Adamson, R., 2014. *Charged particle bombardment of zirconium alloys: A review*, Sweden.

Adamson, R. & Cox, B., 2005. ZIRAT-10 Special Topics Report: Impact of Irradiation on Material Performance: Impact of irradiation on material performance.

Adamson, R., Garzarolli, F. & Patterson, C., 2009. *In-Reactor creep of zirconium alloys*,

Adamson, R.B., 2000. Effects of Neutron Irradiation on Microstructure and Properties of Zircaloy. *Zirconium in the Nuclear Industry: Twelfth International Symposium, ASTM STP 1354*, pp.15–31.

Allen, T.R. et al., 2006. The effect of dose rate on the response of austenitic stainless steels to neutron radiation. *Journal of Nuclear Materials*, 348(1-2), pp.148–164.

Allen, T.R., Was, G.S. & Kenik, E. a., 1997. The effect of alloy composition on radiation-induced segregation in Fe-Cr-Ni alloys. *Journal of Nuclear Materials*, 244(3), pp.278–294.

Arakcheeva, a. V. et al., 2002. Structure studies of solid solutions of oxygen in electrolytic niobium. *Crystallography Reports*, 47(2), pp.237–244.

Arias, D. & Abriata, J.P., 1986. The Cr-Zr (Chromium-Zirconium) system. *Bulletin of Alloy Phase Diagrams*, 7(3), pp.237–244.

Ashkenazi, J. et al., 1978. Elastic constants in Nb-Zr alloys from zero temperature to the melting point: Experiment and theory. *Physical Review B*, 18(8), pp.4120–4131.

Bacon, D.J., 1988. A review of computer models of point defects in hcp metals. *Journal of Nuclear Materials*, 159, pp.176–189.

Bajaj, R., Kammenzind, B.F. & Farkas, D, M., 2002. Effects of Neutron Irradiation on the Microstructure of Alpha-Annealed Zircaloy-4. *Zirconium in the Nuclear Industry: Thirteenth International Symposium, ASTM STP 1423*, pp.400–406.

Barberis, P. et al., 2005. Microstructure and Phase Control in Zr-Fe-Cr-Ni Alloys: Thermodynamic and Kinetic Aspects. *Journal of ASTM International*, 2(5), pp.129–156.

Barberis, P., Charquet, D. & Rebeyrolle, V., 2004. Ternary Zr-Nb-Fe(O) system:

Phase diagram at 853 K and corrosion behaviour in the domain Nb < 0.8%. *Journal of Nuclear Materials*, 326(2-3), pp.163–174.

Benjamin, D., 1979. *Metals handbook. Properties and selection: Nonferrous alloys and pure metals* 9th Ed., V., Metals Park, Ohio: American Society for Materials.

Bossis, P. et al., 2011. In PWR comprehensive study of high burn-up corrosion and growth behaviour of M5 and Recrystallized low-tin Zircaloy-4. *Journal of ASTM International*, 6(2), pp.430–4565.

Brimhall, J.L., Kissinger, H.E. & Charlot, L. a., 1983. Amorphous phase formation in irradiated intermetallic compounds. *Radiation Effects*, 77, pp.273–293.

Bruemmer, S.M. et al., 1999. Radiation-induced material changes and susceptibility to intergranular failure of light-water-reactor core internals. *Journal of Nuclear Materials*, 274(3), pp.299–314.

Buckley, S.N., 1961. Properties of Reactor Materials and the Effects of Irradiation Damage. In London: Butterworths, p. 443.

Bullough, R., Hayns, M.R. & Woo, C.H., 1979. The sink strength of dislocation loops and their growth in irradiated materials. *Journal of Nuclear Materials*, 84, pp.93–100.

Burany, X.M. & Northwood, D.O., 1991. Polytypic structures in close-packed Zr(FeCr)2 Laves phases. *Journal of the Less Common Metals*, 170, pp.27–35.

Burr, P. a et al., 2015. From solid solution to cluster formation of Fe and Cr in α-Zr. *Submitted to Acta Materiallia*.

Burr, P.A. et al., 2013. Hydrogen solubility in zirconium intermetallic second phase particles. *Journal of Nuclear Materials*.

de Carlan, Y. et al., 1996. Influence of Iron in the Nucleation of <c> Component Dislocation Loops in Irradiated Zircaloy-4. *Zirconium in the Nuclear Industry: Eleventh International Symposium, ASTM STP 1295*, pp.638–653.

Carpenter, G.J.C. & Northwood, D.O., 1975. The contribution of dislocation loops to radiation growth and creep of Zircaloy-2. *Journal of Nuclear Materials*, 56, pp.260–266.

Carpenter, G.J.C., Zee, R.H. & Rogerson, A., 1988. Irradiation growth of zirconium single crystals: A review. *Journal of Nuclear Materials*, 159, pp.86–100.

Charquet, D. et al., 1988. Solubility limits and formation of intermetallic precipitates in ZrSnFeCr alloys. *Zirconium in the Nuclear Industry: Eighth International Symposium*, pp.405–422.

Cheadle, B. a., Barberis, P. & Dean, S.W., 2010. The development of Zr-2.5Nb

pressure tubes for CANDU reactors. *Journal of ASTM International*, 7(8), pp.67–87.

Chemelle, P. et al., 1983. Morphology and composition of second phase particles in Zircaloy-2. *Journal of Nuclear Materials*, 113, pp.58–64.

Chen, X.-Q., Wolf, W., Podloucky, R. & Rogl, P., 2005. Ab initio study of ground-state properties of the Laves phase compounds TiCr2, ZrCr2, and HfCr2. *Physical Review B*, 71(174101), pp.1–11.

Chen, X.-Q., Wolf, W., Podloucky, R., Rogl, P., et al., 2005. Ab initio study of ground-state properties of the Laves-phase compound ZrMn2. *Physical Review B*, 72(054440), pp.1–11.

Cheng, B.-C., Kruger, R.M. & Adamson, R.B., 1994. Corrosion Behavior of Irradiated Zircaloy. *Zirconium in the Nuclear Industry: Tenth International Symposium, ASTM STP 1245*.

Christensen, M. et al., 2015. Diffusion of point defects , nucleation of dislocation loops , and effect of hydrogen in hcp-Zr : Ab initio and classical simulations. *Journal of Nuclear Materials*, 460, pp.82–96.

Christensen, M. et al., 2014. Effect of alloying elements on the properties of Zr and the Zr–H system. *Journal of Nuclear Materials*, 445(1-3), pp.241–250.

Christensen, M. et al., 2015. Effect of hydrogen on dimensional changes of zirconium and the influence of alloying elements: First-principles and classical simulations of point defects, dislocation loops, and hydrides. *Zirconium in the Nuclear Industry: 17th Volume*, pp.55–92.

Coaquira, J.A.H. & Rechenberg, H.R., 2001. Magnetic Properties of hexagonal Laves-phase Zr(Cr1-xFex)2 compounds. *Journal of Physics: Condensed Matter*, 13, pp.8415–8434. Available at: http://jpsj.ipap.jp/link?JPSJ/52/3163/.

Coaquira, J.A.H., Rechenberg, H.R. & Mestnik Filho, J., 1999. Structural and Mossbauer spectroscopic study of hexagonal Laves-phase Zr(FexCr1-x)2 alloiys and their hydrides. *Journal of Alloys and Compounds*, 288, pp.42–49.

Cockeram, B. V. et al., 2011. Development of microstructure and irradiation hardening of Zircaloy during low dose neutron irradiation at nominally 358 C. *Journal of Nuclear Materials*, 418, pp.46–61.

Cockeram, B. V. et al., 2014. Development of microstructure and irradiation hardening of Zircaloy during low dose neutron irradiation at nominally 377-440 C. *Journal of Nuclear Materials*, 449, pp.69–87.

Cockeram, B.V. et al., 2013. The use of a laser-assisted Local Electrode Atom Probe and TEM to examine the microstructure of Zircaloy and precipitate structure

following low dose neutron irradiation at nominally 358°C. *Journal of Nuclear Materials*, 433(1-3), pp.460–478.

Crépin, J., Bretheau, T. & Caldemaison, D., 1995. Plastic deformation mechanisms in β-treated zirconium. *Acta Metallurgica*, 43(10), pp.3709–3719.

Damcott, D.L., Allen, T.R. & Was, G.S., 1995. Dependence of radiation-induced segregation on dose, temperature and alloy composition in austenitic alloys. *Journal of Nuclear Materials*, 225, pp.97–107.

Di, S. et al., <c> Component Dislocation Loop Nucleation in Zirconium under Irradiation: Atomic-level Simulations. *Unpublished*.

de Diego, N. et al., 2011. On the structure and mobility of point defect clusters in alpha-zirconium: a comparison for two interatomic potential models. *Modelling and Simulation in Materials Science and Engineering*, 19, p.35003.

de Diego, N., Osetsky, Y.N. & Bacon, D.J., 2002. Mobility of interstitial clusters in alpha-zirconium. *Metallurgical and Materials Transactions A*, 33(13), pp.783–789.

de Diego, N., Osetsky, Y.N. & Bacon, D.J., 2008. Structure and properties of vacancy and interstitial clusters in α-zirconium. *Journal of Nuclear Materials*, 374, pp.87–94.

Domain, C. & Legris, A., 2005. Ab initio atomic-scale determination of point-defect structure in hcp zirconium. *Philosophical Magazine*, 85(4-7), pp.569–575.

Dong, Y., Motta, A.T. & Marquis, E. a., 2013. Atom probe tomography study of alloying element distributions in Zr alloys and their oxides. *Journal of Nuclear Materials*, 442(1-3), pp.270–281.

Dubinko, V.I., Abyzov, a. S. & Turkin, a. a., 2005. Numerical evaluation of the dislocation loop bias. *Journal of Nuclear Materials*, 336, pp.11–21.

Etienne, A. et al., 2010. Atomic scale investigation of radiation-induced segregation in austenitic stainless steels. *Journal of Nuclear Materials*, 406(2), pp.244–250.

Etoh, Y. & Shimada, S., 1993. Neutron irradiation effects on intermetallic precipitates in Zircaloy as a function of fluence. *Journal of Nuclear Materials*, 200, pp.59–69.

Fidleris, V., 1988. The irradiation creep and growth phenomena. *Journal of Nuclear Materials*, 159, pp.22–42.

Fidleris, V., Tucker, R.P. & Adamson, R.B., 1987. An Overview of Microstructural and Experimental Factors Tliat Affect the Irradiation Growth Behavior of Zirconium Alloys. *Zirconium in the Nuclear Industry: Seventh International*

Symposium, ASTM STP 939, pp.49–85.

Gao, F. et al., 2001. Temperature-dependence of defect creation and clustering by displacement cascades in a-zirconium. *Journal of Nuclear Materials*, 294, pp.288–298.

Garzarolli, F. et al., 1996. Effect of In-PWR Irradiation on Size , Structure , and Composition of Intermetallic Precipitates of Zr Alloys. *Zirconium in the Nuclear Industry: Eleventh International Symposium, ASTM STP 1295*, pp.541–556.

Garzarolli, F., Schumann, R. & Steinberg, E., 1994. Corrosion optimized Zircaloy for boiling water reactor (BWR) fuel elements. *Zirconium in the Nuclear Industry: Tenth International Symposium, ASTM STP 1245*, pp.709–723.

Gault, B. et al., 2013. Atom probe microscopy characterization of as quenched Zr–0.8wt% Fe and Zr–0.15wt% Cr binary alloys. *Materials Letters*, 91, pp.63–66.

Gilbert, R.W., Farrell, K. & Coleman, C.E., 1979. Damage structure in zirconium alloys neutron irradiated at 573 to 923 K. *Journal of Nuclear Materials*, 84, pp.137–148.

Gilbert, R.W., Griffiths, M. & Carpenter, G.J.C., 1985. Amorphous intermetallics in neutron irradiated Zircaloys after hIgh fluences. *Journal of Nuclear Materials*, 135, pp.265–268.

Gilbon, D. & Simonot, C., 1994. Effect of Irradiation on the Microstructure of Zircaloy-4. *Zirconium in the Nuclear Industry: Tenth International Symposium, ASTM STP 1245*, pp.521–548.

Goldak, J., Lloyd, L.T. & Barrett, C.S., 1966. Lattice parameters, thermal expansions, and Gruneisen coefficients of zirconium, 4.2 ton 1130K. *Physical Review*, 144(2), pp.478–484.

Goll, W. & Ray, I., 2002. The Behavior of Intermetallic Precipitates in Highly Irradiated BWR LTP Cladding. *Zirconium in the Nuclear Industry: Thirteenth International Symposium, ASTM STP 1423*, pp.80–95.

Golubov, S.I. et al., 2015. Breakthrough in Understanding Radiation Growth of Zirconium. *Zirconium in the Nuclear Industry: 17th International Symposium*, pp.729–758.

Griffiths, M., 1988. A review of microstructure evolution in zirconium alloys during irradiation. *Journal of Nuclear Materials*, 159, pp.190–218.

Griffiths, M., 1990. Comments on precipitate stability in neutron-irradiated Zircaloy-4. *Journal of Nuclear Materials*, 170, pp.294–300.

Griffiths, M. et al., 1992. *Evolution of microstructure in zirconium allo core components of nuclear reactors during service*, Ontario K0J 1J0.

Griffiths, M. et al., 1993. HVEM study of the effects of alloying elements and impurities on radiation damage in Zr-alloys. *Journal of Nuclear Materials*, 205, pp.273–283.

Griffiths, M., Gilbert, R.W., et al., 1987. Neutron damage in zirconium alloys irradiated at 644 to 710 K. *Journal of Nuclear Materials*, 150(2), pp.159–168.

Griffiths, M. & Gilbert, R.W., 1987. The Formation of c-component defects in zirconium alloys during neutron irradiation. *Journal of Nuclear Materials*, 150, pp.169–181.

Griffiths, M., Gilbert, R.W. & Carpenter, G.J.C., 1987. Phase instability, decomposition and resdistribution of intermetallic precipitates in Zircaloy-2 and -4 during neutron irradiation. *Journal of Nuclear Materials*, 150, pp.53–66.

Griffiths, M., Gilbert, R.W. & Coleman, C.E., 1988. Grain boundary sinks in neutron-irradiated Zr and Zr-alloys. *Journal of Nuclear Materials*, 159, pp.405–416.

Griffiths, M., Gilbert, R.W. & Fidleris, V., 1989. Accelerated irradiation growth of zirconium alloys. *Zirconium in the Nuclear Industry: Eighth International Symposium*, pp.658–677.

Griffiths, M., Holt, R.A. & Rogerson, A., 1995. Microstructural aspects of accelerated deformation of Zircaloy nuclear reactor components during service. *Journal of Nuclear Materials*, 225, pp.245–258.

Griffiths, M., Loretto, M.H. & Smallman, R.E., 1983. Electron Damage in Zirconium II . Nucleation and growth of c-component loops. *Journal of Nuclear Materials*, 115, pp.323–330.

Griffiths, M., Mecke, J.F. & Winegar, J.E., 1996. Evolution of Microstructure in Zirconium Alloys During Irradiation. *Zirconium in the Nuclear Industry: Eleventh International Symposium, ASTM STP 1295*, pp.580–602.

Gros, J.P. & Wadier, J.F., 1990. Precipitate growth kinetics in Zircaloy-4. *Journal of Nuclear Materials*, 172, pp.85–96.

Hallstadius, L., Johnson, S. & Lahoda, E., 2012. Cladding for high performance fuel. *Progress in Nuclear Energy*, 57, pp.71–76.

Havinga, E.E., Damsma, H. & Hokkeling, P., 1971. Compounds and pseudo-binary alloys with the CuAl2 (C16)-type structure. I. Preparation and x-ray results. *Journal of the Less Common Metals*, 27(1972), pp.169–186.

Holt, R. a. & Gilbert, R.W., 1986. c-component dislocations in annealed Zircaloy

irradiated at about 570 K. *Journal of Nuclear Materials*, 137(3), pp.185–189.

Holt, R. a., Woo, C.H. & Chow, C.K., 1993. Production bias — A potential driving force for irradiation growth. *Journal of Nuclear Materials*, 205, pp.293–300.

Holt, R.A., 1988. Mechanisms of irradiation growth of alpha-zirconium alloys. *Journal of Nuclear Materials*, 159, pp.310–338.

Holt, R.A. et al., 1996. Non-Linear Irradiation Growth of Cold-Worked Zircaloy-2. *Zirconium in the Nuclear Industry: Eleventh International Symposium, ASTM STP 1295*, pp.623–637.

Hood, G.M. et al., 1995. alpha-Zr Self-diffusion anisotropy. *Journal of Nuclear Materials*, 223, pp.122–125.

Hood, G.M., 1988. Point defect diffusion in a-Zr. *Journal of Nuclear Materials*, 159, pp.149–175.

Hood, G.M., 1977. *Point defect properties of α-Zr and their influence on irradiation behaviour of Zr alloys*, Chalk River National Laboratories, Chalk River, Ontario, Canada.

Hu, R., Smith, G.D.W. & Marquis, E.A., 2012. Atom probe study of radiation induced grain boundary segregation/depletion in a Fe-12%Cr alloy. *Progress in Nuclear Energy*, 57, pp.14–19.

Huang, P.Y., Mahmood, S.T. & Adamson, R.B., 1996. Effects of thermomechanical processing on in-reactor corrosion and post-irradiation mechanical properties of Zircaloy-2. *Zirconium in the Nuclear Industry: Eleventh International Symposium, ASTM STP 1295*, pp.726–757.

Hudson, D. & Smith, G.D.W., 2009. Initial observation of grain boundary solute segregation in a zirconium alloy (ZIRLO) by three-dimensional atom probe. *Scripta Materialia*, 61(4), pp.411–414.

IAEA-TECDOC-966, 1998. *Waterside corrosion of zirconium alloys in nuclear power plants*, Vienna.

Idrees, Y., Yao, Z., Kirk, M. a., et al., 2013. In situ study of defect accumulation in zirconium under heavy ion irradiation. *Journal of Nuclear Materials*, 433(1-3), pp.95–107.

Idrees, Y., Yao, Z., Sattari, M., et al., 2013. Irradiation -nduced microstructural changes in Zr-Excel alloy. *Journal of Nuclear Materials*, 441, pp.138–151.

Jerlerud Pérez, R. et al., 2008. The Zr-Sn binary system: New experimental results and thermodynamic assessment. *Computer Coupling of Phase Diagrams and Thermochemistry*, 32, pp.593–601.

Jiao, Z. & Was, G.S., 2011a. Novel features of radiation-induced segregation and radiation-induced precipitation in austenitic stainless steels. *Acta Materialia*, 59(3), pp.1220–1238.

Jiao, Z. & Was, G.S., 2011b. Segregation behavior in proton- and heavy-ion-irradiated ferritic-martensitic alloys. *Acta Materialia*, 59(11), pp.4467–4481.

Jostsons, A. et al., 1977. Faulted loops in neutron-irradiated zirconium. *Journal of Nuclear Materials*, 68, pp.267–276.

Jostsons, A., Kelly, P.M. & G, B.R., 1977. The Nature of Dislocation Loops in Neutron Irradiated Zirconium. *Journal of Nuclear Materials*, 66, pp.236–256.

Kai, J.J., Huang, W.I. & Chou, H.Y., 1990. The microstructural evolution of Zircaloy-4 subjected to proton irradiation. *Journal of Nuclear Materials*, 170, pp.193–209.

Kim, H.G., Park, J.Y. & Jeong, Y.H., 2005. Phase boundary of the Zr-rich region in commercial grade Zr-Nb alloys. *Journal of Nuclear Materials*, 347(1-2), pp.140–150.

King, A.D., Hood, G.M. & Holt, R.A., 1991. Fe-enhancement of self-diffusion in ar-Zr. *Journal of Nuclear Materials*, 185, pp.174–181.

Kuksenko, V., Pareige, C. & Pareige, P., 2012. Intra granular precipitation and grain boundary segregation under neutron irradiation in a low purity Fe-Cr based alloy. *Journal of Nuclear Materials*, 425(1-3), pp.125–129.

Kulikov, D. & Hou, M., 2005. Vacancy dislocation loops in zirconium and their interaction with self-interstitial atoms. *Journal of Nuclear Materials*, 342, pp.131–140.

Kuri, G. et al., 2010. Micro-focussed XAFS spectroscopy to study Ni-bearing precipitates in the metal of corroded Zircaloy-2. *Applied Physics A: Materials Science and Processing*, 98, pp.625–633.

Kuwae, R. et al., 1983. Mechanism of Zircaloy nodular corrosion. *Journal of Nuclear Materials*, 119, pp.229–239.

Laves, F., 1941. Eduard Zintl's work on chemistry and structure of alloys. *Naturwissenschaften*, 29, pp.244–255 (German).

Lucuta, P.G., Patru, I. & Vasiliu, F., 1981. Microstructural features of hot pressure bonding between stainless steel type AISI-304 L and Zircaloy-2. *Journal of Nuclear Materials*, 99, pp.154–164.

Mahmood, S.T. et al., 2000. Post-Irradiation Characterization of ultra-high fluence zircaloy-2. *Zirconium in the Nuclear Industry: Twelfth International Symposium, ASTM STP 1354*, pp.139–169.

Mani Krishna, K. V. et al., 2015. Influence of Sn on deformation mechanisms during room temperature compression of binary Zr–Sn alloys. *Zirconium in the Nuclear Industry: 17th International Symposium, STP 1543*, pp.138–158.

Mardon, J.P., Charquet, D. & Senevat, J., 2000. Influence of composition and frabication process of out-of-pile and in-pile M5 alloy. *Zirconium in the Nuclear Industry: Twelfth International Symposium, ASTM STP 1354*, pp.505–524.

Marquis, E.A., Hu, R. & Rousseau, T., 2011. A systematic approach for the study of radiation-induced segregation/depletion at grain boundaries in steels. *Journal of Nuclear Materials*, 413(1), pp.1–4.

Marquis, E.A., Lozano-Perez, S. & Castro, V. De, 2011. Effects of heavy-ion irradiation on the grain boundary chemistry of an oxide-dispersion strengthened Fe-12 wt.% Cr alloy. *Journal of Nuclear Materials*, 417(1-3), pp.257–261.

Meng, X. & Northwood, D., 1989. Second phases in Zircaloy-2. *Journal of Nuclear Materials*, 168, pp.125–136.

Meng, X.Y. & Northwood, D.O., 1985a. A TEM study of the C15 type Zr(CrFe)2 Laves phase in Zircaloy-4. *Journal of Nuclear Materials*, 136, pp.83–90.

Meng, X.Y. & Northwood, D.O., 1985b. Intermetallic precipitates in Zircaloy-4. *Journal of Nuclear Materials*, 132, pp.80–87.

Motta, A.T., 1997. Amorphization of intermetallic compounds under irradiation — A review. *Journal of Nuclear Materials*, 244, pp.227–250.

Motta, A.T. et al., 1996. In Situ Studies of Phase Transformations in Zirconium Alloys and Compounds Under Irradiation. *Zirconium in the Nuclear Industry: Eleventh International Symposium, ASTM STP 1295*, pp.557–579.

Motta, A.T. et al., 2002. Synchrotron Radiation Study of Second- Phase Particles and Alloying Elements in Zirconium Alloys. *Zirconium in the Nuclear Industry: Thirteenth International Symposium, ASTM STP 1423*, pp.59–79.

Motta, A.T., Howe, L.M. & Okamoto, P.R., 1994. *Amorphization Kinetics of Zr(Fe,Cr)2 under ion irradiation*,

Motta, A.T., Howe, L.M. & Okamoto, P.R., 1993. Amorphization kinetics of Zr3Fe under electron irradiation. *Journal of Nuclear Materials*, 205, pp.258–266.

Motta, A.T., Lefebvre, F. & Lemaignan, C., 1991. Amorphization of Precipitates in Zircaloy under Neutron and Charged-Particle Irradiation. *Zirconium in the Nuclear Industry: Ninth International Symposium, ASTM STP 1132*, pp.718–739.

Motta, A.T. & Lemaignan, C., 1992. A ballistic mixing model for the amorphization of precipitates in Zircaloy under neutron irradiation. *Journal of Nuclear Materials*, 195, pp.277–285.

Moura, C.S. et al., 2001. Point defect energetics in the ZrNi and Zr2Ni intermetallics. *Nuclear Instruments and Methods in Physics Research B*, 175(177), pp.526–531.

Naguib, H.M. & Kelly, R., 1975. Criteria for bombardment-induced structural changes in non-metallic solids. *Radiation Effects*, 25, pp.1–12.

Norgett, M.I., Robinson, M.T. & Torrens, I.M., 1975. A proposed method of calculating displacement dose rates. *Nuclear Engineering and Design*, 33, pp.50–54.

Northwood, D.O. et al., 1979. Characterization of neutron irradiation damage in zirconium alloys - an international "round-robin" experiment. *Journal of Nuclear Materials*, 79, pp.379–394.

Okamoto, H., 2006. Fe-Zr (iron-zirconium). *Journal of Phase Equilibria & Diffusion*, 27(5), pp.543–544.

Okamoto, H., 2007. Ni-Zr (nickel-zirconium). *Journal of Phase Equilibria and Diffusion*, 28(4), p.409.

Okamoto, H., 2010. Sn-Zr (Tin-zirconium). *Journal of Phase Equilibria and Diffusion*, 31(4), pp.411–412.

Onimus, F. & Bechade, J.-L., 2012. Radiation effects in zirconium alloys. *Comprehensive Nulcar Materials*, 4, pp.1–31.

Onimus, F., Dupuy, L. & Mompiou, F., 2012. In situ TEM observation of interactions between gliding dislocations and prismatic loops in Zr-ion irradiated zirconium alloys. *Progress in Nuclear Energy*, 57, pp.77–85.

Osetsky, Y.N. et al., 2000. Stability and mobility of defect clusters and dislocation loops in metals. *Journal of Nuclear Materials*, 276(1), pp.65–77.

Pasianot, R.C. et al., 2009. Ab initio approach to the effect of Fe on the diffusion in hcp Zr II: The energy barriers. *Journal of Nuclear Materials*, 392(1), pp.100–104.

Pasianot, R.C. & Pérez, R. a., 2013. First-principles appraisal of solute ultra-fast diffusion in hcp Zr and Ti. *Journal of Nuclear Materials*, 434, pp.158–161.

Pêcheur, D. et al., 1993. Effect of irradiation on the precipitate stability in Zr alloys. *Journal of Nuclear Materials*, 205, pp.445–451.

Peng, Q. et al., 2014. Pressure effect on stabilities of self-Interstitials in HCP-

Zirconium. *Scientific Reports*, 4, pp.1–7.

Perez, R.A., Nakajima, H. & Dyment, F., 2003. Diffusion in alpha-Ti and Zr. *Materials Transactions*, 44(1), pp.2–13.

Pérez, R.A. & Weissmann, M., 2008. Ab-initio approach to the effect of Fe on the diffusion in hcp Zr. *Journal of Nuclear Materials*, 374(1-2), pp.95–100.

Poynor, A.N. et al., 2001. Hyperfine interactions of 181 Ta in Zr2Ni observed using PAC spectroscopy. *Hyperfine Interactions*, 136(137), pp.549–553.

Rogerson, A., 1988. Irradiation growth in zirconium and its alloys. *Journal of Nuclear Materials*, 159, pp.43–61.

Rogerson, A. & Zee, R.H., 1987. High fluence irradiation growth in single crystal zirconium at 553 K. *Journal of Nuclear Materials*, 151, pp.81–83.

Rogerson, A. & Zee, R.H., 1988. Irradiation growth in zirconium-tin alloys at 353 and 553 K. *Journal of Nuclear Materials*, 152, pp.220–224.

Rouchette, H. et al., 2015. Numerical evaluation of dislocation loop sink strengths : A phase-field approach. *Nuclear Instruments and Methods in Physics Research B*, 352, pp.31–35.

Rudling, P., 2000. Zr-2 Corrosion and Hydriding Performance. *Zirconium in the Nuclear Industry: Twelfth International Symposium, ASTM STP 1354*, pp.678–706.

Sabol, G. p et al., 1994. In-reactor corrosion performance of ZIRLOTM and Zircaloy-4. *Zirconium in the Nuclear Industry: Tenth International Symposium, ASTM STP 1245*, pp.724–744.

Sabol, G.P., 2005. ZIRLO – An alloy development success. *Zirconium in the Nuclear Industry: 14th Symposium*, 2(2), pp.3–24.

Van der Sande, J.B. & Bement, A.L., 1974. An investigation of second phase particles in Zircaloy-4 alloys. *Journal of Nuclear Materials*, 52, pp.115–118.

Sawabe, T. et al., 2013. Analysis of atomic distribution in as-fabricated Zircaloy-2 claddings by atom probe tomography under high-energy pulsed laser. *Journal of Nuclear Materials*, 442, pp.168–174.

Sawicki, J. a., 1999. Mössbauer spectroscopy of tin in unirradiated and neutron irradiated Zircaloys. *Journal of Nuclear Materials*, 264, pp.169–179.

Schäfer, H., Eisenmann, B. & Müller, W., 1973. Zintl phases : transitions between metallic and ionic bonding. *Angewandte Chemie International Edition*, 12(9), pp.694–712.

Sears, V.F., 1992. Neutron scattering lengths and cross sections. *Neutron News*,

3(3), pp.26–37.

Shaltiel, D., Jacob, I. & Davidov, D., 1977. Hydrogen absorption and desorption properties of AB2 Laves-phase pseudobinary compounds. *Journal of the Less Common Metals*, 53, pp.117–131.

Shen, H.-H. et al., 2014. Microstructure evolution of Zircaloy-4 during Ne ion irradiation and annealing: An in situ TEM investigation. *Chinese Physics B*, 23(3), pp.036102–1–5.

Shen, H.H. et al., 2014. In situ TEM investigation of amorphisation and recrystallization of Zr(Fe,Cr,Nb)2 precipitates under Ne ion irradiation. *Vacuum*, 110, pp.24–29.

Shen, H.H. et al., 2014. Proton irradiation effects on the precipitate in a Zr- 1.6Sn– 0.6Nb– 0.2Fe– 0.1Cr alloy. *Journal of Nuclear Materials*, 452, pp.335–342.

Shishov, V.N. et al., 1996. Influence of Neutron Irradiation on Dislocation Structure and Phase Composition of Zr-Base Alloys. *Zirconium in the Nuclear Industry: Eleventh International Symposium, ASTM STP 1295*, pp.603–622.

Shishov, V.N. et al., 2005. Influence of structure-phase state of Nb containing Zr alloys on irradiation-induced growth. *Zirconium in the Nuclear Industry: 14th Symposium*, 2(8), pp.666–685.

Shishov, V.N. et al., 2011. Structure-phase state, corrosion and irradiation properties of Zr-Nb-Fe-Sn system alloys. *Zirconium in the Nuclear Industry: 15th Symposium*, 5(3), pp.724–743.

Shishov, V.N., Barberis, P. & Dean, S.W., 2010. The evolution of microstructure and deformation stability in Zr–Nb–(Sn,Fe) alloys under neutron irradiation. *Journal of ASTM International*, 7(7), p.103005.

Simonen, E.P., Chariot, L.A. & Bruemmer, S.M., 1995. Quantification of defect-solute coupling from inverse-Kirkendall segregation. *Journal of Nuclear Materials*, 225, pp.117–122.

Sinha, V.K., Yu, G.Y. & Wallace, W.E., 1985. Hydrogen storage in some ternary and quaternary zirconium-based alloys with the C14 structure. *Journal of the Less Common Metals*, 106, pp.67–77.

Smallman, R.E. & Bishop, R.J., 1999. *Modern Physical Metallurgy & Materials Engineering* 6th ed.,

Stein, F., Sauthoff, G. & Palm, M., 2002. Experimental determination of intermetallic phases, phase equilibria, and invariant reaction temperatures in the Fe-Zr system. *Journal of Phase Equilibria*, 23(6), pp.480–494.

Stoller, R.E. et al., 2013. On the use of SRIM for computing radiation damage exposure. *Nuclear Instruments and Methods in Physics Research B*, 310, pp.75–80.

Stupel, M.M., Bamberger, M. & WEiss, B.Z., 1985. Determination of Fe solubility in αZr by Mössbauer spectroscopy. *Scripta Metallurgica*, 19, pp.739–740.

Sun, J. & Jiang, B., 2004. Ab initio calculation of the phase stability, mechanical properties and electronic structure of ZrCr2 Laves phase compounds. *Philosophical Magazine*, 84(29), pp.3133–3144.

Sundell, G. et al., Redistribution of alloying elements in Zircaloy-2 after in-reactor exposure. *Journal of Nuclear Materials*.

Sundell, G., Thuvander, M. & Andrén, H., 2015. Tin clustering and precipitation in the oxide during autoclave corrosion of Zircaloy-2. *Journal of Nuclear Materials*, 456, pp.409–414.

Tagtstrom, P. et al., 2002. Effects of hydrogen pickup and second-phase particle dissolution on the in-reactor corrosion performance of BWR claddings. *Zirconium in the Nuclear Industry: Thirteenth International Symposium, ASTM STP 1423*, pp.96–118.

Tenckhoff, E., 2005. Review of deformation mechanisms, texture, and mechanical anisotropy in zirconium and zirconium base alloys. *Zirconium in the Nuclear Industry: 14th Symposium*, 2(4), pp.25–50.

Tendler, R. & Abriata, J.P., 1987. Atomic size and fast diffusion of metallic impurities in zirconium. *Journal of Nuclear Materials*, 150, pp.251–258.

Tournadre, L. et al., 2012. Experimental study of the nucleation and growth of c-component loops under charged particle irradiations of recrystallized Zircaloy-4. *Journal of Nuclear Materials*, 425(1-3), pp.76–82.

Valizadeh, S. et al., 2014. Effects of Secondary Phase Particle Dissolution on the In-Reactor Performance of BWR Cladding. *Journal of ASTM International*, 8(2), pp.729–753.

Varvenne, C., Mackain, O. & Clouet, E., 2014. Vacancy clustering in zirconium: An atomic-scale study. *Acta Materialia*, 78, pp.65–77.

Vatter, I.A. & Titchmarsh, J.M., 1989. measurement of grain boundary segregation by STEM-EDX analysis. *Ultramicroscopy*, 28, pp.236–239.

Vérité, G. et al., 2013. Self-interstitial defects in hexagonal close packed metals revisited: Evidence for low-symmetry configurations in Ti, Zr, and Hf. *Physical Review B*, 87, p.134108.

Visnov, R., Ducastelle, F. & Treglia, G., 1982. Electronic structure of NiZr2 C16 compound. *Journal of Physics F: Metal Physics*, 12, pp.441–447.

Vizcaíno, P., Banchik, a. D. & Abriata, J.P., 2008. Synchrotron X-ray diffraction evidences of the amorphization/dissolution of the second phase particles (SPPs) in neutron irradiated Zircaloy-4. *Materials Letters*, 62(3), pp.491–493.

Was, G.S., 2007. Fundamentals of Radiation Materials Science. In *Fundamentals of Radiation Materials Science*. Springer Berlin Heidelberg New York, p. 83.

Was, G.S., 2000. The damage cascade. In *Fundamentals of Radiation Materials Science*. Springer Berlin Heidelberg New York, pp. 125–154.

Wharry, J.P. et al., 2011. Radiation-induced segregation and phase stability in ferritic-martensitic alloy T 91. *Journal of Nuclear Materials*, 417(1-3), pp.140–144.

Wharry, J.P., Jiao, Z. & Was, G.S., 2012. Application of the inverse Kirkendall model of radiation-induced segregation to ferritic-martensitic alloys. *Journal of Nuclear Materials*, 425(1-3), pp.117–124.

Whitmarsh, C.L., 1962. *Review of Zircaloy-2 and Zircaloy-4 properties relevent to N. S. Savannah deactor design*,

Wolfer, W.G. & Si-Ahmed, A., 1980. The effect of nonlinear elasticity on the capture efficiency of dislocation loops. *Physics Letters*, 76A(3, 4), pp.341–343.

Woo, C.., 2000. Defect accumulation behaviour in hcp metals and alloys. *Journal of Nuclear Materials*, 276(1-3), pp.90–103.

Woo, C.H., 1987. Effects of Anisotropic Diffusion on Irradiation Deformation. In *Radiation-Induced Changes in Microstructre: 13th International Symposium (PART I), ASTM STP 955*. pp. 70–89.

Woo, C.H., 1982. Intrinsic bias differential between vacancy loops and interstitial loops. *Journal of Nuclear Materials*, 107, pp.20–30.

Woo, C.H., 1988. Theory of irradiation deformation in non-cubic metals: effects of anisotropic diffusion. *Journal of Nuclear Materials*, 159, pp.237–256.

Woo, C.H. & Göslel, U., 1983. Dislocation bias in an anisotropic diffusive medium and irradiation growth. *Journal of Nuclear Materials*, 119, pp.219–228.

Woo, C.H. & Liu, X., 2007. Atomistic calculation of point-defect diffusion anisotropy and irradiation growth in α-zirconium. *Philosophical Magazine*, 87(16), pp.2355–2369.

Woo, C.H. & Savino, E.J., 1983. Stress-induced preferred absorption due to saddle-point anisotropy: The case of an infinitesimal dislocation loop. *Journal of*

Nuclear Materials, 116, pp.17–28.

Woo, C.H. & Singh, B.N., 1992. Production bias due to clustering of point defects in irradiation-induced cascades. *Philosophical Magazine A*, 65(4), pp.889–912.

Woo, O.T. & Carpenter, G.J.C., 1988. Radiation-induced precipitation in Zircaloy-2. *Journal of Nuclear Materials*, 159, pp.397–404.

Woo, O.T. & Griffiths, M., 2009. The role of Fe on the solubility of Nb in ??-Zr. *Journal of Nuclear Materials*, 384(1), pp.77–80.

Wooding, S.J. et al., 1998. A molecular dynamics study of high-energy displacement cascades in α-zirconium. *Journal of Nuclear Materials*, 254, pp.191–204. Available at: http://www.sciencedirect.com/science/article/pii/S0022311597003656.

Yang, W.J.S., 1988. Precipitate stability in neutron-irradiated Zircaloy-4. *Journal of Nuclear Materials*, 158, pp.71–80.

Yang, W.J.S., Tucker, R.P. & Adamson, R.B., 1986. Precipitates in Zircaloy: Identification and the Effects of Irradiation and Thermal Treatment. *Journal of Nuclear Materials*, 138, pp.185–195.

Yoshida, Y. et al., 1990. Local atomic-jump processes of iron in α-Zr. *Physical Review Letters*, 61(2), pp.195–198.

Yueh, H. et al., 2005. Improved ZIRLOTM cladding performance through chemistry and process modifications. *Journal of ASTM International*, 2(6), pp.330–346.

Zee, R.H. et al., 1984. Effect of tin on the irradiation growth of polycrystalline zirconium. *Journal of Nuclear Materials*, 120, pp.223–229.

Zou, H. et al., 1994. Solute distribution in annealed Zircaloy-2 and Zr-2.5Nb. *Journal of Nuclear Materials*, 208, pp.159–165.

Zou, H. et al., 1995. The solid solubility of Ni and Co in α-Zr: a secondary ion mass spectrometry study. *Journal of Nuclear Materials*, 223, pp.186–188.

Zu, X.T. et al., 2005. Effect of proton and Ne irradiation on the microstructure of Zircaloy 4. *Philosophical Magazine*, 85(4-7), pp.649–659.

3 EXPERIMENTAL METHODS

The following is a description and analysis of the experimental methods used in the present work. It should be noted that while all sample preparation and electron microscopy was performed by the present author, the atom probe tomography and reconstruction of tomograms was performed by collaborators at The University of Oxford, namely Charles Hirst, Tomas Martin and Michael Moody. As such, a description of the principles of APT is provided but a full analysis of the technique is not given.

3.1 MATERIALS

The material under investigation in the present work is Zircaloy-2, nominally Zr-1.5Sn-1.4Fe-0.1Cr-0.06Ni (wt.%) (Hallstadius et al. 2012). The ~3 mm thick plate was provided by Westinghouse Electric Company and served as both the non-irradiated baseline and the material for proton irradiation experiments. All alloys were studied in the fully recrystallised condition.

The neutron-irradiated BWR cladding and channel material was provided by Westinghouse Electric Company. The material was delivered as prepared electropolished foils after exposure to various neutron fluences ranging between 8.7 and 14.7 $x10^{21}$ n m^{-2}.

3.2 SAMPLE PREPARATION AND PROTON IRRADIATIONS

The following is a description of sample preparation processes for microscopic analysis. Mechanical polishing was performed for optical microscopy, electron backscatter diffraction (EBSD) analysis in the scanning electron microscope (SEM) and for proton irradiation experiments. A flat surface is required for proton irradiation such that the penetration depth of the protons is uniform. Likewise, a flat surface is required to observe grain structure in the optical microscope and EBSD signal will not be detected from the grooves of a rough surface. For analysis in the transmission electron microscope (TEM) and scanning TEM (STEM), thin

foils were prepared by twin-jet electropolishing until perforation. For atom probe tomography (APT) analyses, the focussed ion beam (FIB) was used to create needles with an end radius ~50 nm.

3.2.1 METALLOGRAPHIC PREPARATION FOR OPTICAL MICROSCOPY, EBSD AND PROTON IRRADIATION EXPERIMENTS

Zircaloy-2 plate was sectioned with a SiC cutting wheel in a Struers Accutom 5 cutting machine under water cooling at a feed rate of 0.8 mm min^{-1} to dimensions of 2 x 2 x 20 mm, were set in Bakelite in the normal direction (ND) and mechanically polished from the ND to a quality such that the grains are visible under polarised light. The proton irradiation experiments, all optical microscopy, EDSB analysis and APT needle sample preparation was performed from this sample direction on such matchstick samples. The mechanical polishing was performed under abrasive cloths of successively smaller grit size, i.e SiC paper was used at P800 grit size, followed by diamond polishing of particle size 6 μm, and then briefly 1 μm. After each step the surface scratches became smaller, until they are barely noticeable after the 1 μm diamond polishing step. The surface was then etched in a similar manner to that of hcp Ti alloys (Gammon et al. 2004) in a solution of 45% H_2O 45% HNO_3 and 10% HF for a fraction of a second, before final polishing with colloidal silica of particle size 0.06 μm. The etchant is used to create an even, brittle surface which is easily removed by the colloidal silica after polishing for ~10 minutes. After this final stage, the grain structure should be visible under polarised light, such as that in **Figure 3-1**.

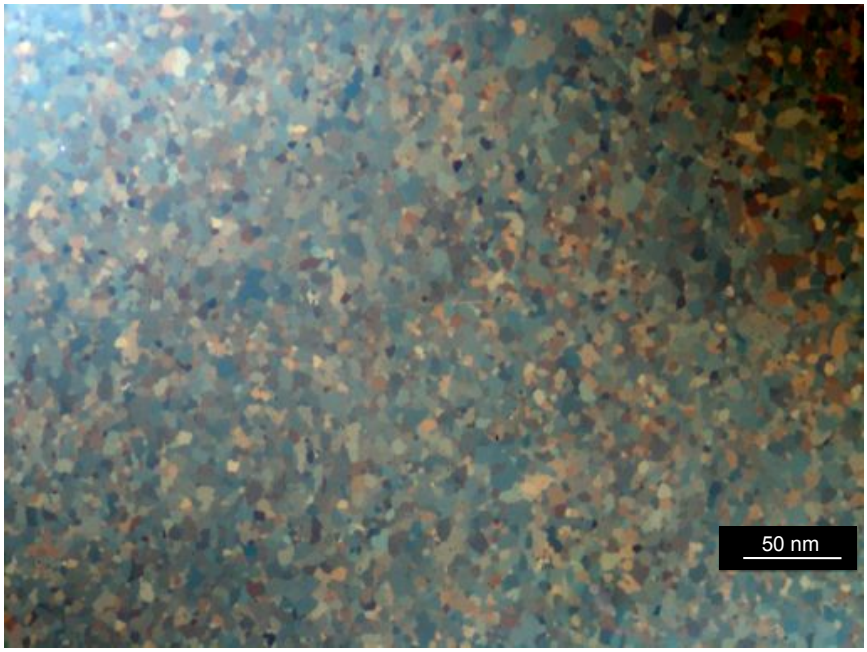

Figure 3-1 Grains are observable after mechanical polishing. This micrograph was obtained from Zircaloy-2 plate from the normal direction on a Zeiss Axio (Scope.A1) microscope with differential interference contrast and a cross polarised light filter.

3.2.2 PROTON IRRADIATION EXPERIMENTS

The matchstick bars (§3.2.1) were irradiated with 2 MeV protons at the Michigan Ion Beam Laboratory's 1.7 MeV Tandertron accelerator facility at 2 MeV and 350 ±9 °C to doses of 2.3, 4.7 and 7.0 displacements per atom (dpa) at a current of ~0.2 μA mm^{-2}, resulting in a damage rate ~6.7 $x10^{-6}$ dpa s^{-1}. A schematic of the irradiation stage in cross section is shown in **Figure 3-2**, in which it can be seen that a copper block is heated internally from the rear. Air cooling is required to control the heating and provide a constant temperature. A shim is placed on top of the copper block to provide a platform for the samples, which are arranged on top of the shim. Indium foils is placed between the samples and the copper block, which melts upon heating to > 180 °C and provides complete thermal contact between the samples and the heat source. The samples are held in place by hold-down bars. A photograph of this set up is shown in **Figure 3-3**a.

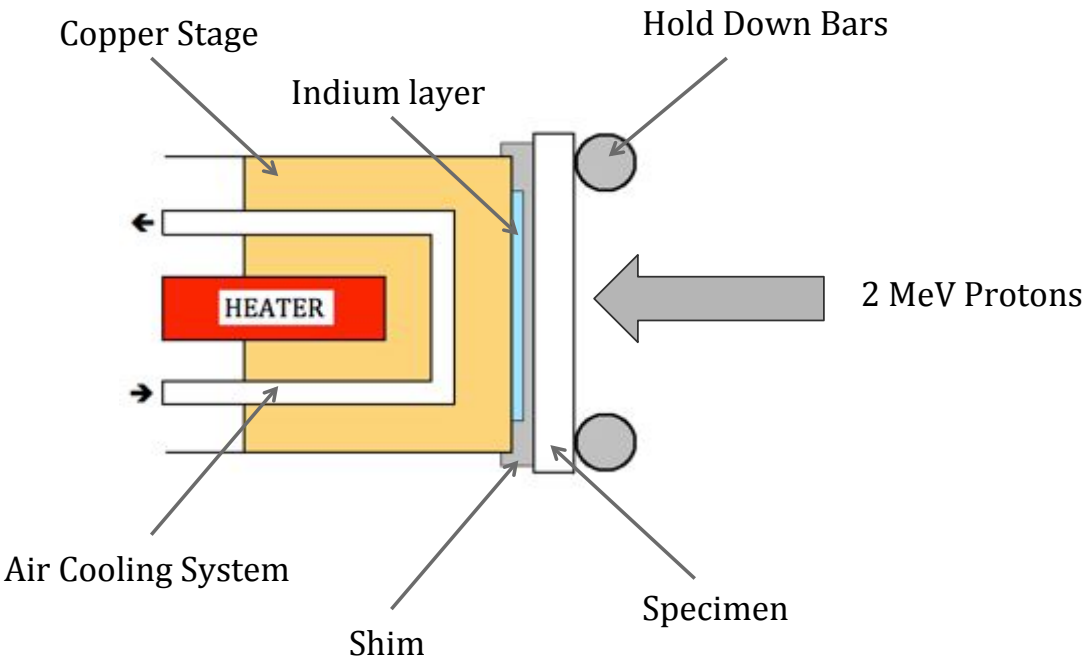

Figure 3-2 Schematic of the proton irradiation stage.

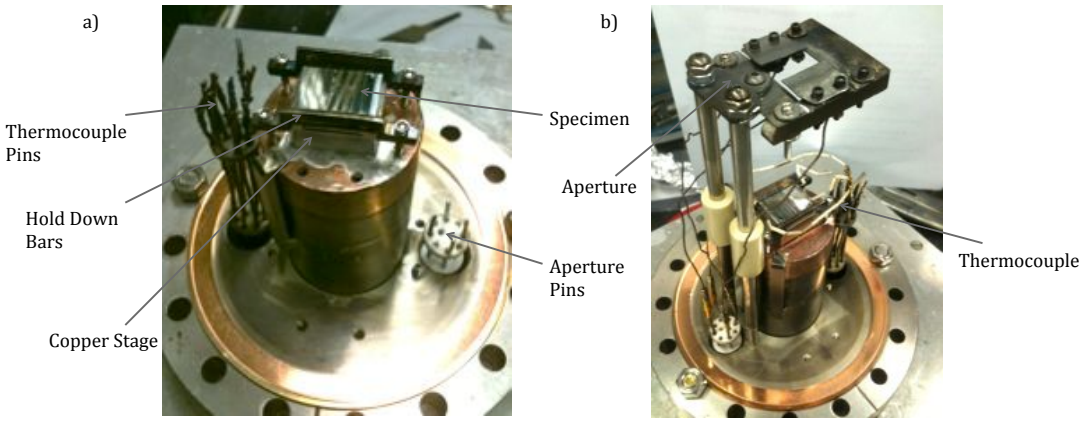

Figure 3-3 Photos of the irradiation stage a) before and b) after spot welding of thermocouples and attachment of the aperture.

In **Figure 3-3**b, it can be seen that four thermocouples have been spot-welded to the sample surface. Before irradiation, the stage is heated to the irradiation temperature 350 °C and this is measured by the thermocouples. When the stage in in the beamline, the stage is heated again and the thermocouples register the temperature. In this condition, a thermal imaging camera is calibrated to 350 °C. Then the sample is cooled to ~180 °C and the proton beam switched on. This renders the thermocouples useless, but the temperature is monitored by the calibrated thermal imaging camera, and so can be monitored throughout the experiment.

A tantalum aperture is also attached to the stage such that the irradiation area can be clearly defined. This aperture has electrical connections such that the proton irradiation current on the aperture may be recorded. As such, any change in the aperture current is an indication of beam drift and may be manually corrected for by steering the beam back onto the sample.

The proton irradiation dose (in displacements per atom, dpa) level was calculated at 60% of the maximum proton penetration depth (max 29 μm), calculated by the quick Kinchin-Pease calculation in SRIM (freeware from www.SRIM.org) as recommended by Stoller *et al.* (Stoller et al. 2013). A *guide to SRIM* may be found in Appendix I. 60% penetration depth is chosen because the damage profile due to the protons is relatively flat in this region. The results of this calculation for irradiation under the present conditions for 96 hr is shown in **Figure 3-4**, together with the depths at which the APT and TEM samples were extracted; ~0.5 and ~12 μm, respectively, resulting in a dose level of ~1.5 and ~2.3 dpa, respectfully.

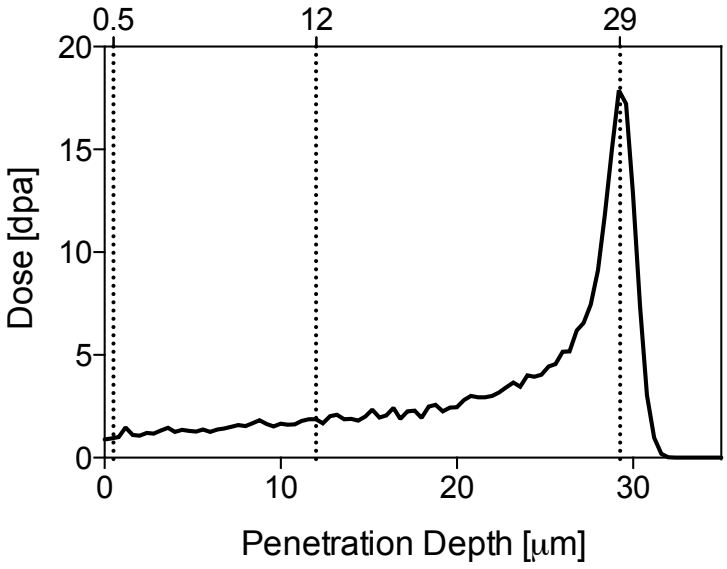

Figure 3-4 SRIM dpa profile after 96 hr at ~0.2 uA mm^{-2}. The depths highlighted indicate the APT sample position and the TEM sample positions, corresponding to ~1.5 and ~2.3 dpa, respectively.

3.2.3 ELECTROPOLISHING FOR TEM AND STEM

The proton-irradiated TEM foils were prepared by carefully grinding from the non-irradiated face with P800 SiC abrasive paper to a thickness of ~160 μm and punching samples with a 3mm disk punch. The irradiated bars were in the form of 2 x 2 x 2 mm matchsticks, and so the resulting samples were 3 x 2 mm in dimensions. The samples were then mounted in a twin-jet Tenupol-5 electropolisher together with a Julabo FP50 cooling unit. An electrolyte of 10% perchloric acid and 20% 2-butoxyethanol in ethanol (Tournadre et al. 2012) was used at 0 °C to electropolish ~12-15 μm from both the irradiated and non-irradiated faces. The amount of material removed as a function of time was monitored ex situ using a Keyence VK-X200K 3D Laser Scanning Microscope, which was used to provide topographical information. Then, Elektron Technology's acid-resistant Lacomit varnish was used to protect the irradiated face while electropolishing to perforation for the non-irradiated face. The non-irradiated bulk material was prepared by the same method.

3.2.4 FOCUSED ION BEAM FOR APT

The needles for atom probe tomography (APT) were prepared on a FEI Novalab 660 gallium focused ion beam (FIB) microscope, equipped with an electron beam for imaging. The procedure for sample preparation (Thompson et al. 2007) consisted of cutting and lifting out a long wedge with a cross section shape of an isosceles triangle. Snapshots of the procedure are shown in **Figure 3-5**. First, a rectangular Pt layer of ~1 μm thickness and ~40 μm in length was deposited to protect the sample surface from the Ga beam. This Pt layer was initially electron-deposited to avoid Ga damage. Next, two trenches were cut either side of the bar at relatively high ion beam current, 30° to the sample surface such that the isosceles triangle cross section was created, shown in **Figure 3-5**a. Then, the wedge was cut such that one side became free and the other remained attached by a small region close to the bulk sample surface, **Figure 3-5**b. The micromanipulator was then placed at the Pt surface of the free end of the wedge and attached with Pt. The attached end of the wedge was then cut and the wedge removed from the bulk material, **Figure 3-5**c and retracted. Next, an array of Si posts was placed in the microscope chamber, **Figure 3-5**d, the micromanipulator was used to place the wedge on top of a Si post and the wedge attached with Pt. The wedge was then cut and the micromanipulator retracted, leaving the sample on the Si post, **Figure 3-5**f. A top-down view of the mounted sample is given in **Figure 3-5**g, which was then milled by use of an annular milling mask such as that shown in **Figure 3-5**h. The sample was milled from the top-down direction with progressively smaller inner diameters of the annular mask and progressively smaller Ga ion beam currents (1 nA-0.1 nA) to make the needle increasingly sharp, **Figure 3-5**i-l.

The final step involved a low kV clean to remove the surface layer damaged in Ga. APT analysis of Ga content of different needles with various low kV cleaning steps showed that the least amount of Ga implantation was observed after a 5 kV polish with a subsequent 2 kV polish. Without such steps, the Ga implantation was found to be higher by a factor of 10.

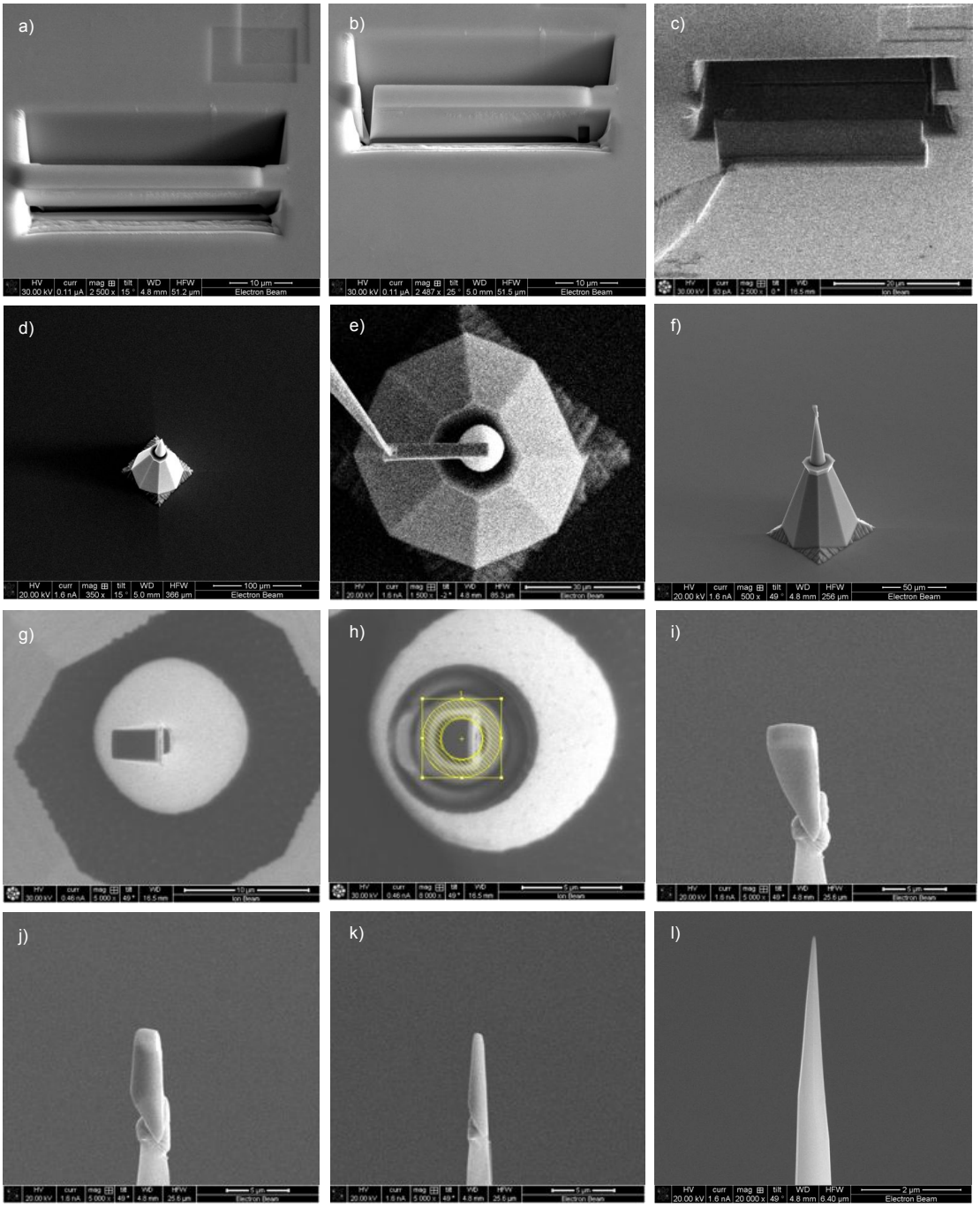

Figure 3-5 Electron and ion beam images of various stages throughout the APT needle preparation process.

3.3 THE ELECTRON MICROSCOPE: SEM TEM AND STEM

The scanning electron microscope (SEM), transmission electron microscope (TEM) and scanning TEM (STEM) are similar in that they contain an electron source and accelerate electrons towards a target of interest. The electrons interact with the

material and several types of signal are produced, detected and analysed. Simplified schematics for the three types of microscope are shown in **Figure 3-6**a, b and c for the SEM, TEM and STEM, respectively. All of the microscopes are similar in that they contain an electron source and condenser lens (CL) systems for the manipulation of the electrons accelerated from the source. The CL may manipulate the electrons in various ways. In the TEM, the CL system is used to provide a parallel beam of electrons for imaging. In the SEM and STEM, the CL system is used in conjunction with the objective lens (OL) to produce a highly convergent probe on the sample, which is then moved laterally by the scan coils. As such, the SEM and STEM give information as a function of position and the TEM gives parallel information of the whole illuminated area. The OL of the TEM is used to form the diffraction pattern in the back focal plane and is the strongest lens, creating the largest magnification. The TEM also has extra lenses (intermediate and projector) for increased magnification and projection onto the viewing screen. In the SEM and STEM, a 'magnified' image is obtained simply by scanning a smaller area. While the condenser and objective lenses perform different functions in the TEM and STEM, modern microscopes are equipped with a combined condenser-objective lens that may perform both functions. As such, the user is able to switch between TEM and STEM modes without having to change the polepiece.

The surface of a bulk sample is studied in the SEM. In the TEM and STEM, samples ~100 nm in thickness are studied such that the electrons are transmitted. Therefore, the interaction volume is lower in TEM and STEM, improving resolution. Further, the energy of the electrons in the TEM and STEM is higher than in the SEM by up to a factor of 10, and so the resolution is correspondingly better due to the Plank-Einstein relation. The resolution in SEMs and STEMs is governed by the size of the convergent electron probe. The probe forming lenses, i.e. the CL, control the probe size and so it is aberrations in the CL system that limits STEM resolution. In TEM, the spatial resolution is limited by aberrations in the OL, as this is the lens that produces the greatest magnification. In both TEM and STEM, the largest contributor to aberration is spherical aberration, which may be corrected for in modern TEMs and STEMs by an extra set of lenses.

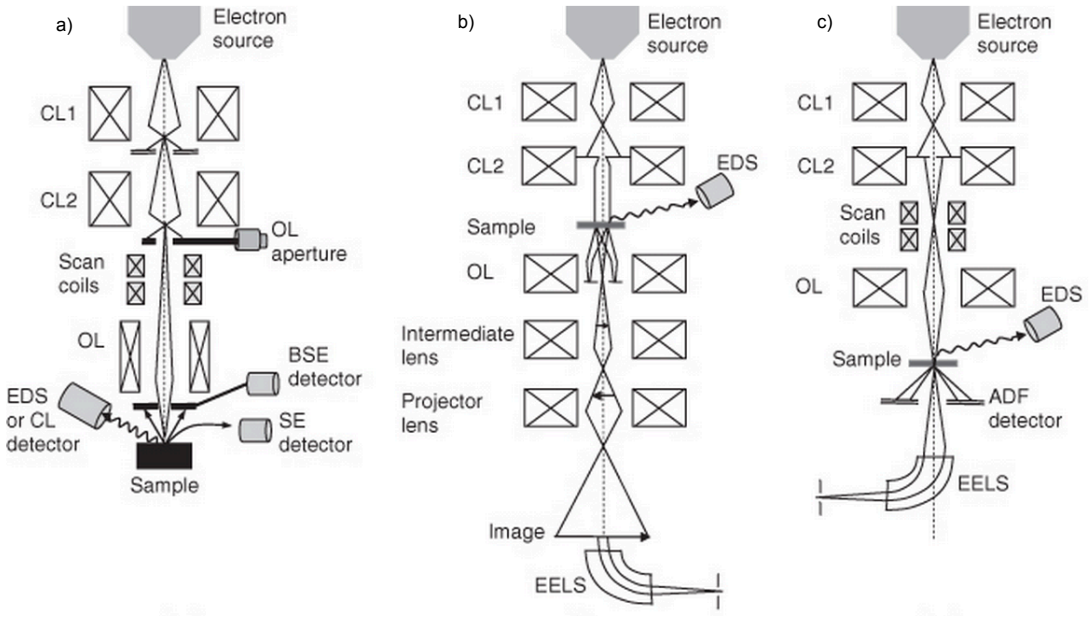

Figure 3-6 Schematics of the configurations of the SEM, TEM and STEM in a, b and c, respectively. Adapted from (Bell & Erdman 2013).

All analytical investigations in the present work were conduced on a spherical-aberration probe-corrected FEI Titan microscope, operating at 200 kV in STEM mode. The aberration-corrector allows for a high current in a sub-angstrom sized probe ~0.4 nm in diameter. The Titan is equipped with FEI's ChemiSTEM™ system, which comprises four energy-dispersive X-ray spectroscopy (EDS) detectors in close proximity to the sample, coupled with a high brightness X-FEG source. The detectors are windowless Si drift detectors and result in a maximum total collection angle of 0.7 srad at 0° specimen tilt and zero shadowing. As such, X-ray detection is possible at all specimen tilts, although care should be taken to individually turn off shadowed detectors when large specimen tilts are used.

3.3.1 ELECTRON-MATERIAL INTERACTION AND SIGNAL GENERATION

The interaction of an electron with material may be used to obtain information specific to that material. Some of the electron-atom interaction process and the resulting signals that may be detected are shown in **Figure 3-7**.

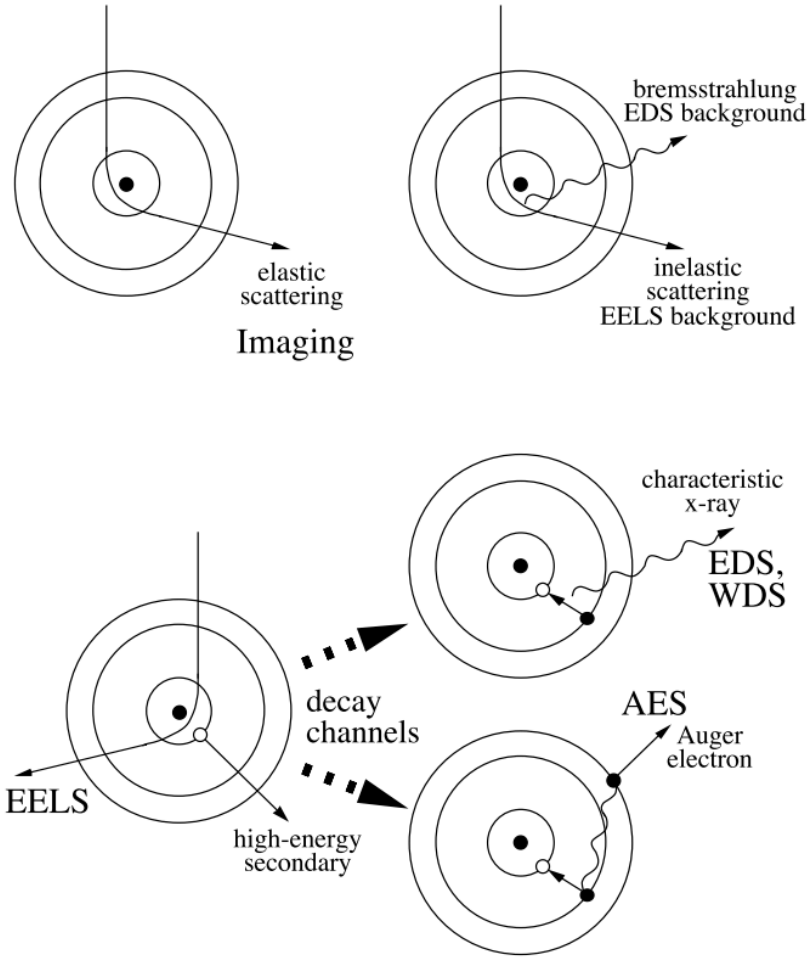

Figure 3-7 The creation of various detectable signals, arising from the interaction of an electron with an atom in a solid, adapted from (Fultz & Howe 2008).

The elastic scattering of electrons occurs due to the interaction of the electron wave front with the periodic potential of the crystalline atomic structure. As such, the electrons are deflected from the optic axis by an angle $\pm\theta_B$, the Bragg angle, which is defined by

$$\sin\theta_B = \frac{n\lambda}{2d} \qquad (3\text{-}1)$$

where λ is the electron wavelength, constructive when *n* is an integer, and *d* is the interplanar spacing between 2-dimensional planes of atoms. The Bragg angle is therefore is a measure of the arrangement of atoms between atomic planes. With

respect to the direction of electron travel, the atomic potential changes depending on the orientation of the crystal structure, As a result, the degree of deflection will change depending on the crystal orientation in a process known as diffraction. This is the basis for most imaging techniques in the TEM and STEM, as diffracted electrons may be either selected for imaging or prevented from contributing to the image, resulting in contrast referred to as dark-field and bright-field, respectively.

The inelastic scattering of electrons gives rise to secondary signals that provide information pertaining to chemical composition. Transmitted electrons may transfer sufficient energy to an electron such that it is displaced from its orbital, ionizing the atom and creating a hole in the core states. Subsequently, an outer electron may drop into the hole and release excess energy through the emission of an X-ray. This X-ray energy is equal to the difference between the energy of the two electron states. As such, the X-ray energy is characteristic of this specific transition and so may be used to identify the type of atom from which it originated. Alternatively, an electron may be ejected from an outer shell to compensate for the electron transition. Such an electron is termed an Auger electron and is also be detected as characteristic of a specific transition and atom type. Auger electron spectroscopy (AES) is beyond the scope of the present work and so will not be considered further.

The bremsstrahlung occurs if the incoming electron interacts with the atomic nucleus to induce a significant change in electron momentum. The change in momentum results in the emission of an X-ray, which is absorbed by the material at low bremsstrahlung energies but that is detected by the energy dispersive X-ray detector at energies > ~ 2 keV (Williams & Carter 2009a). This results in a background in intensity proportional to the average atomic number of the material, which must be removed before it is possible to quantify chemical content by analysis of characteristic X-rays.

The inelastic electron-atom interaction reduces the energy of the transmitted electron, which may be recorded in an electron energy loss spectrum (EELS). While EELS is beyond the scope of the present work, the EELS signal may be

collected in parallel to the X-ray signal to provide complimentary information. Further, EELS may provide sample thickness measurements and quantitative information regarding chemical environment and binding on the atomic scale. As such, theoretical EELS profiles must be generated and standards used in order for accurate analyses. While such an approach is also appropriate for EDS, there is a multitude of commercial software available for EDS analysis and a standardless approach.

3.3.2 ELECTRON BACKSCATTER DIFFRACTION

Electron backscatter diffraction (EBSD) was used to characterise the non-irradiated bulk Zircaloy-2 plate in terms of the relative orientation of grains. Fist observed by Nishikawa and Kikuchi in 1928 (Nishikawa & Kikuchi 1928), Kikuchi patterns form as a result of a two-stage process. First, electrons incident on the sample are inelastically scattered in all directions. Second, many of these diffusely scattered electrons will be at the Bragg angle with respect to various atomic planes in the sample, and so these electrons diffract according to Bragg's law in Equation (3-1). As the incident beam is convergent on the sample surface, Kikuchi diffraction takes the physical form of a cone of diffracting electrons, which project on the viewing screen as 2-dimensional lines. Kikuchi patterns may be obtained in the SEM, TEM and STEM, but are used in the SEM for EBSD data collection. As the beam scans the sample surface, the Kikuchi patterns are collected as a function of position, indexed by comparison to simulated patters, and orientation information for tens of thousands of grains may be obtained over a period of time.

Such a procedure was performed in the present work on a FEI Quanta 650 FEG SEM, operating at 20 kV, a spot size of 4.5 and a working distance of ~11 μm. The grain size as determined by optical microscopy (§3.2.1) was 5-15 μm and so a step size of 4 μm was used for data collection. The analysis of orientation information was performed using the CHANNEL5 HKL software package to produce pole figures in Mambo.

3.3.3 THE INTERACTION OF STEM ELECTRONS WITH THE SAMPLE

During a head-on collision of an incident electron of energy E_0 with an atom, the maximum kinetic energy transferred to that atom, T_m, is described by Oen (Oen 1965) as

$$T_m(eV) = \frac{2147.66E_0(E_0 + 1.0220)}{A} \quad (3\text{-}2)$$

where E_0 is in MeV and A is the atomic weight in g mol^{-1}. **Figure 3-8** shows the variation in T_m with E_0 in keV for the common alloying elements of Zr alloys. It can be seen in **Figure 3-8** that T_m increases with E_0 and decreases with atomic weight, Cr to Sn. The relationship between T_m and A is demonstrated more clearly in **Figure 3-9**, simply a re-arrangement of Equation (3-2) at the two common operating electron energies, E_0 = 200, 300 kV. The markers on the x-axis and associated dotted lines indicate the atomic masses of the elements in **Figure 3-8**, i.e. that of Cr = 52.0, Fe = 55.875, Ni = 58.69, Zr = 91.22, Nb = 92.91 and Sn = 118.71 g mol^{-1}.

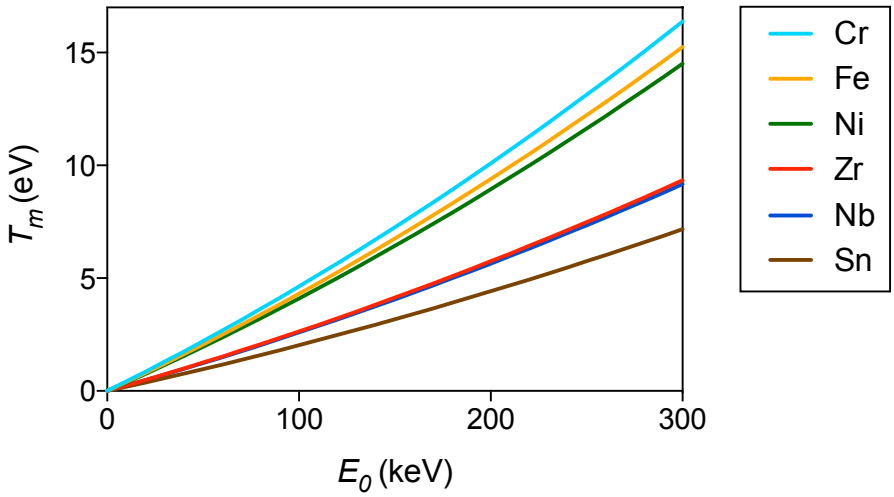

Figure 3-8 The variation in the maximum kinetic energy transferred to an atom in a head-on collision (T_m) is shown to increase with the incident electron energy (E_0) and to decrease with atomic mass (Cr to Sn).

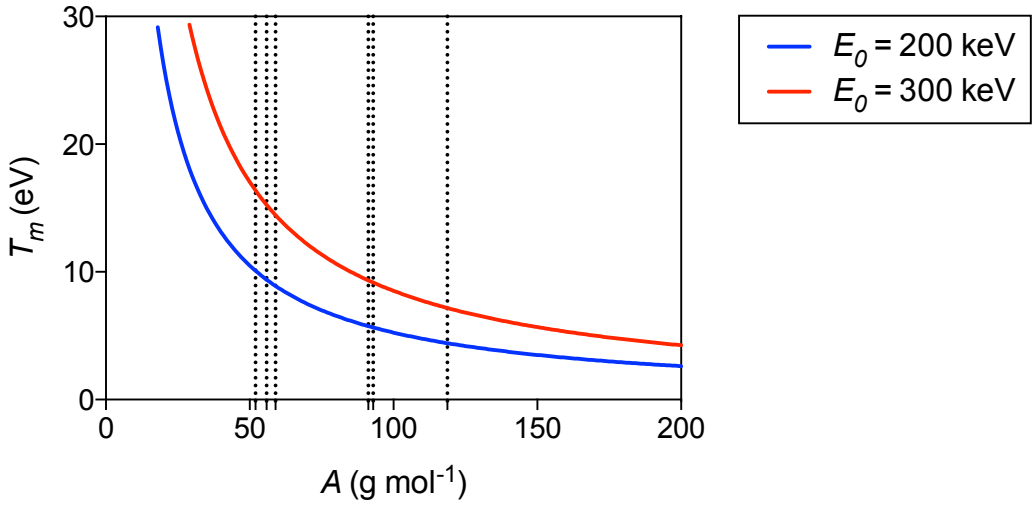

Figure 3-9 The variation in the maximum kinetic energy transferred to an atom in a head-on collision (T_m) is shown to decrease with atomic weight (A) and increase with incident electron energy (E_0) for 200 and 300 keV electrons. The common alloying elements are noted by markers and dotted lines at Cr = 52.0, Fe = 55.875, Ni = 58.69, Zr = 91.22, Nb = 92.91 and Sn = 118.71 g mol^{-1}.

Woo considers the displacement energy of Zr by electrons as 24 eV to be reasonable in comparison to neutrons at 40 eV (Woo et al. 2000) when considering that the damage efficiency for electrons and neutrons are 80% and 20%, respectively. In the study by Woo, high electron energies of 10 MeV were used to cause irradiation damage in Zr-2.5Nb (wt.%) and Zircaloy-2. Under the normal TEM operating electron energies of 200 and 300 keV, however, the cross section for displacement is much lower for Zr and other heavy elements (Oen 1965). In **Figure 3-10** the displacement energy, E_d, is plotted as a function of atomic weight, A, using values from Williams and Carter (Williams & Carter 2009d). E_d is observed to increase with atomic weight, as might be expected, and the suggestion by Woo of 24 eV for Zr agrees well with the data in **Figure 3-10** at A = 91.22 g mol^{-1}.

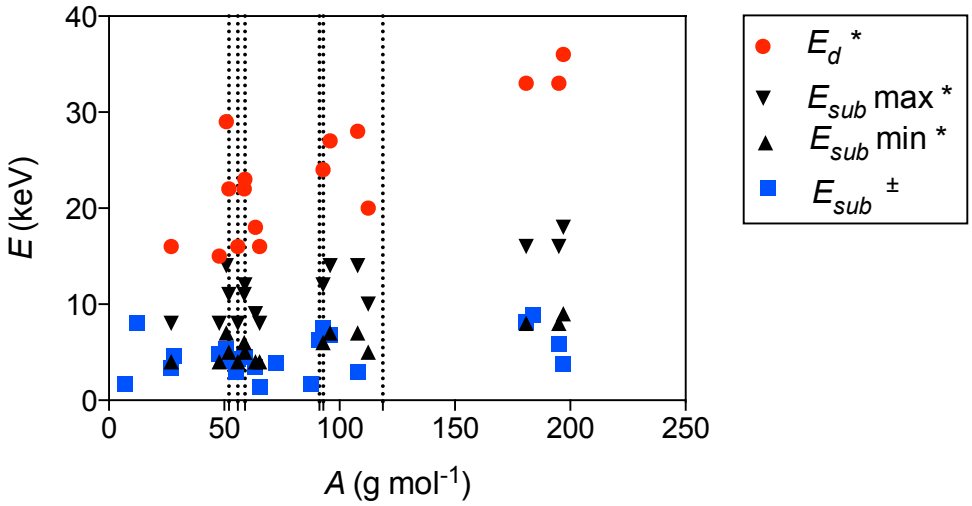

Figure 3-10 The variation in displacement (E_d) and sublimation energy (E_{sub}) is shown to increase with atomic weight (A). The legend shows values from *Williams and Carter (Williams & Carter 2009d), in which a range is given for E_{sub}, and ±Egerton (Egerton et al. 2010). The common alloying elements are noted by markers and dotted lines at Cr = 52.0, Fe = 55.875, Ni = 58.69, Zr = 91.22, Nb = 92.91 and Sn = 118.71 g mol^{-1}.

The T_m at incident electron energies of 200 and 300 keV and the E_d for Zr and its common alloying elements is summarised in **Table 3-1**. It is immediately clear from this table that $E_d > T_{m,\,300\text{ keV}} > T_{m,\,200\text{ keV}}$ and so bulk displacement of the atoms in Zr alloys under normal TEM operating might be considered unlikely. However, the threshold energy for bulk displacement, E_t, is a function of both E_d and atomic weight, A, and has been calculated for Zr and its alloying elements and is also included in **Table 3-1**. According to Williams and Carter (Williams & Carter 2009d),

(3-3)
$$E_t = \frac{\left(\frac{100 + AE_d}{5}\right)^{\frac{1}{2}} - 10}{20}$$

where A and E_d have already been defined. From **Table 3-1**, it can be seen that $E_t >$ 200 keV for all of the elements and so bulk displacement is unlikely when using this incident electron energy. It should be noted, however that E_t (Fe) = 205 keV

which is very close to E_0 = 200 keV. At E_0 = 300 keV, however, E_t (Cr, Ni) < 300 keV and so bulk displacement may occur. This may be mitigated in Zr alloys if a small (with respect to the TEM foil thickness) second-phase particle (SPP) containing high a concentration of Fe and/or Cr is protected by a Zr-Sn or Zr-Nb matrix above the SPP. In this case, the SPP should be resistant to irradiation with 300 keV electrons, although an assessment of displacement as a function of penetration depth has not been considered explicitly.

Table 3-1 Zr and its common alloying elements are listed in order of increasing atomic weight (A) and details of the maximum transferable energy between an electron and the element is given at an incident electron energy of 200 keV ($T_{m,\,200\,\mathrm{keV}}$) and 300 keV ($T_{m,\,300\,\mathrm{keV}}$). The bulk displacement energy (E_d), obtained, and in the case of Sn, estimated from * Williams and carter (Williams & Carter 2009d), the threshold energy for displacement (E_t) calculated using Equation (3-3), and the sublimation energy (E_{sub}), obtained, and, in the case of Sn, estimated from ±Egerton (Egerton et al. 2010) are also given.

Element	A (g mol^{-1})	$T_{m,\,200\,\mathrm{keV}}$ (eV)	$T_{m,\,300\,\mathrm{keV}}$ (eV)	E_d (eV) *	E_t (keV)	E_{sub} (eV) ±	E_t^{sp} (eV) ±
Cr	52.0	10.09	16.38	22	289	4.10	89
Fe	55.85	9.40	15.25	16	205	4.29	100
Ni	58.98	8.94	14.51	22	334	4.52	109
Zr	91.22	5.75	9.34	24	570	6.26	215
Nb	92.91	5.65	9.16	24	579	7.50	254
Sn	118.71	4.42	7.18	26	762	8	271

If an SPP is located at the top surface of the TEM foil then spluttering may occur. Egerton (Egerton et al. 2010) used the energy of sublimation, E_{sub}, detailed in **Table 3-1**, to calculate the threshold energy for spluttering from a surface, E_t^{sp}, the values for which are shown in **Figure 3-11** as a function of atomic weight and are detailed in **Table 3-1** for Zr and its common alloying elements. The values in **Table 3-1** are the minimum values of E_t^{sp}, calculated by assuming that the displacement energy is equal to that of the sublimation energy. The data in **Figure 3-11** demonstrates this minimum in blue squares but also the case for the displacement energy of surface atoms equalling $^5/_3$ that of the sublimation energy. It can be seen from the values for E_t^{sp} that Cr, Fe and Ni have threshold energies below 200 keV, meaning that they are likely to be spluttered away from the surface

when operating with E_0 = 200 keV. At E_0 = 300 keV, all of the elements, including the heavier Zr, Nb and Sn atoms, are likely to be spluttered from the surface.

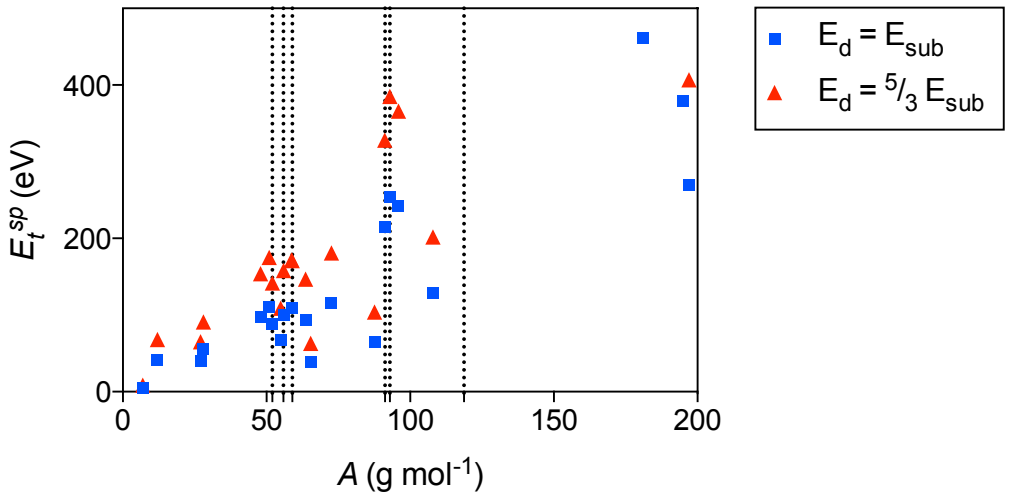

Figure 3-11 The variation in the threshold energy required to splutter atoms from the surface (E_t^{sp}) is shown to increase with atomic weight (A). The displacement energy used for this calculation is assumed to be either the energy of sublimation (E_{sub}), blue squares, or five thirds that of the sublimation energy ($^5/_3E_{sub}$), red triangles. The common alloying elements are noted by markers and dotted lines at Cr = 52.0, Fe = 55.875, Ni = 58.69, Zr = 91.22, Nb = 92.91 and Sn = 118.71 g mol^{-1}.

With regard to the techniques utilised in the present work, the FEI Titan microscope is operated at E_0 = 200 keV for chemical analysis and so is not likely to cause any splutter damage to the sample unless an SPP or other Cr, Fe and/or Ni segregation is located at the top surface of the foil. Although thin regions are preferred in order to obtain good spatial resolution and analytic sensitivity, this should not be an issue in the majority of features studied, which are consistently in the range 5-60 nm in diameter.

The spherical aberration-corrected probe of the Titan microscope results in the ability to contain high current in a sub-angstrom probe. While this is beneficial for the detection of greater number of characteristic X-rays per unit time, a high current can cause damage. Experimentally, it was determined that a probe current of 0.6 and 1.2 nA resulted in no observable damage, whereas a current of 2 nA

resulted in observable spluttering. While it may have been possible to use 1.2 nA, 0.6 nA was used as counting times for reliable data remained < 30 minutes, which was deemed appropriate while avoiding any enhanced diffusion of the fast-diffusing Fe, Cr and Ni elements (Perez et al. 2003; Pasianot & Pérez 2013).

3.3.4 STEM IMAGING TECHNIQUES

The majority of STEM imaging in the present work made use of the bright-field (BF) detector aligned with the optic axis of the microscope. A schematic of BF-STEM data collection is given in **Figure 3-12**. Transmitted electrons that have not diffracted (but which may or may not have interacted inelastically with the sample) travel along the optic axis, or at very slight angles to it, and are detected by the on-axis BF detector. The camera length is adjusted such that only the central BF disk falls onto the detector, which contains partial overlap from diffracted disks. Contrast in the BF image therefore arises from diffraction and the resulting intensity variation in the BF disk as a function of scan position.

In addition to the BF detector, annular dark-field detectors collect diffracting electrons at an angle from the optic axis that is defined by the inner radius of the ADF detector and the camera length used. High-angle ADF (HAADF) detectors have large inner angles and collect electrons arising from Rutherford scattering, providing atomic number contrast.

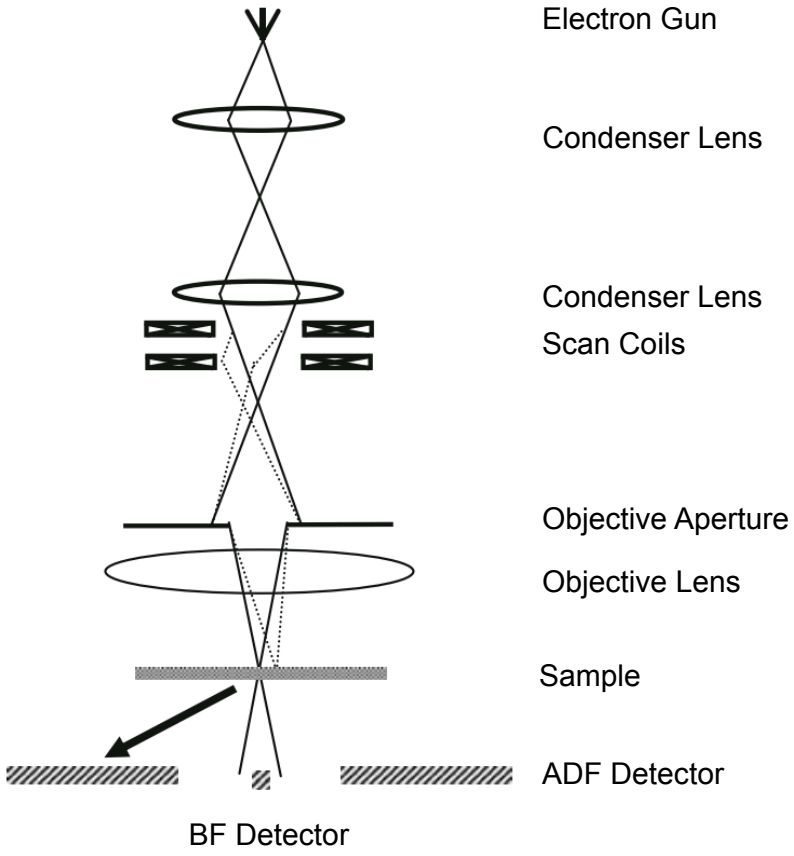

Figure 3-12 STEM schematic demonstrating the parallel recording of BF and ADF signals, adapted from (Nellist 2011).

3.3.5 ENERGY-DISPERSIVE X-RAY SPECTROSCOPY ANALYSIS

A central aspect of the present work is in the determination of composition of second phase particles (SPPs) within the Zr matrix. As such, the following is an example of how this was achieved. It should be noted that an absolute quantification of chemical composition has not been attempted, as SPPs are embedded within the Zr matrix and so matrix contribution is obtained both above and below the SPP of interest. As a result of this limitation, Fe/X atomic fractions (X = Cr, Ni) are often sought due to the low solubility of Fe, Cr and Ni in the Zr matrix (Stupel et al. 1985; Charquet et al. 1988; Zou et al. 1995), even after irradiation. As an overview, the Cliff-Lorimer approach was used assuming no absorption, no fluorescence and no detector effects. An assessment of the suitability of these assumptions and its implication for the determination of

chemical content is to follow, and results in describing data from such an approach as semi-quantitative. All data analysis was performed within the Bruker Quantax Esprit software and selected data sets were plotted using MATLAB code.

A BF STEM image of a typical Fe-Cr type SPP in Zircaloy-2 is shown in **Figure 3-13**a, in which the green square is the area to be scanned for mapping and consists of 700 x 700 pixels, resulting in a pixel size of 0.275 nm. The pixel size is therefore small in regards to the approximate size of the probe (~0.4 nm), but later quantification will require the binning of pixels 4 x 4 which will increase the average pixel size to 1.1 nm. The average X-ray spectrum from all 700 x 700 pixels in the energy range collected, 0-20 keV, is displayed in **Figure 3-13**b and the region of greatest interest is displayed in **Figure 3-13**c between ~3.5-16 keV. In this region of interest, the peaks used for the semi-quantification do not overlap and are the following: Sn L_α at 3.4 keV; Cr K_α at 5.4 keV; Fe K_α at 6.4 keV; Ni K_α at 7.5 keV; and Zr K_α at 15.8 keV. In addition to these peaks of interest there is signal from Cu and Pb, which arise from the microscope itself and the sample holder. A plot of the intensity of these peaks of interest as a function of position results in a map of raw counts, which is shown for these elements in **Figure 3-14**, each individually scaled to reveal details and with a smoothing factor applied to reduce the grainy appearance. The instrumental signals of Pb and Cu are plotted in a similar manner and are shown in **Figure 3-15**a and b, respectively, in raw counts, each individually scaled with the same smoothing factor applied. The uniformity of the maps demonstrate that there is no Pb or Cu in the material. Further, the lack of a Au Lα signal at 9.7 keV in **Figure 3-13**c is evidence that there is no Au in the material. Au was therefore used to ensure that there were no observed segregation due to thickness effects and a resulting larger Bremsstrahlung. This is done simply by mapping with the Au signal, which provides no variation in contrast in regions of constant thickness, displayed in **Figure 3-15**c. Such a qualitative analysis was performed for all spectral images acquired.

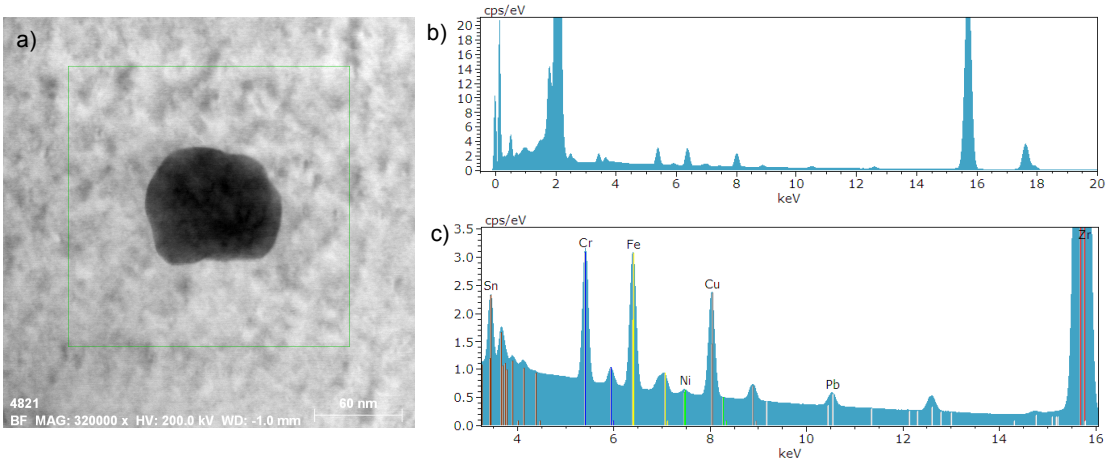

Figure 3-13 A typical Zr(Fe,Cr)2 SPP is shown in a) the BF STEM image. The spectrum in b) is the average of every 700 x 700 pixel in the area defined by the green square in a). The spectrum in c) is the region of interest in b), containing all of the peaks of interest for the Cliff-Lorimer quantification.

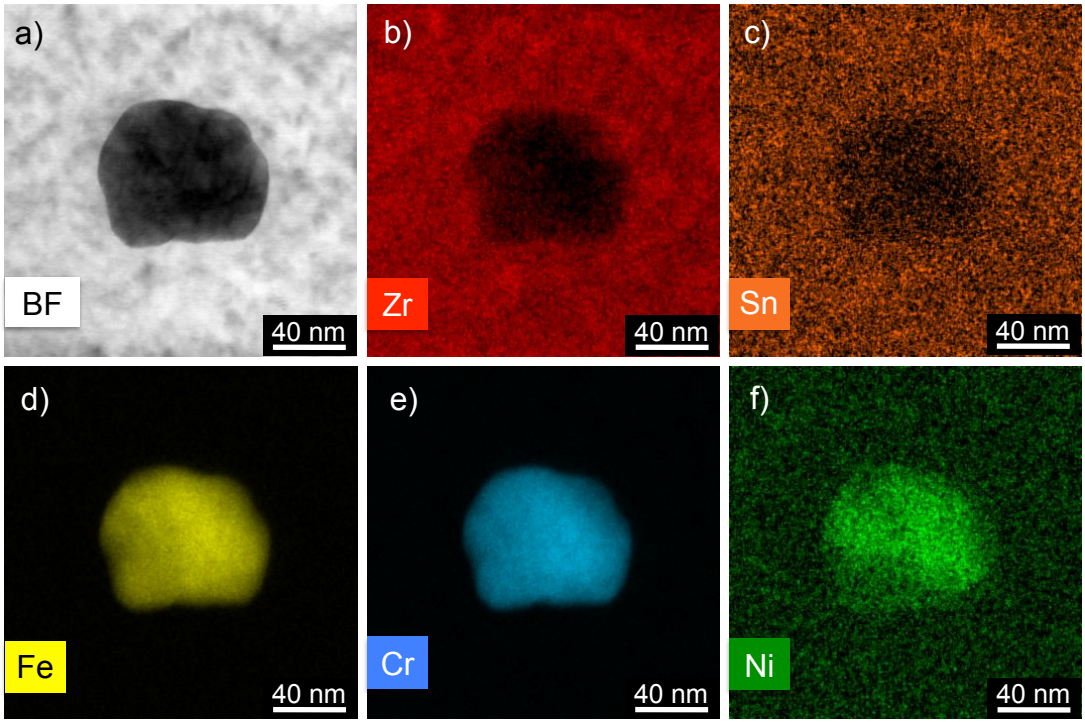

Figure 3-14 SPP chemical maps extracted from the spectral image, displayed in raw counts, individually scaled.

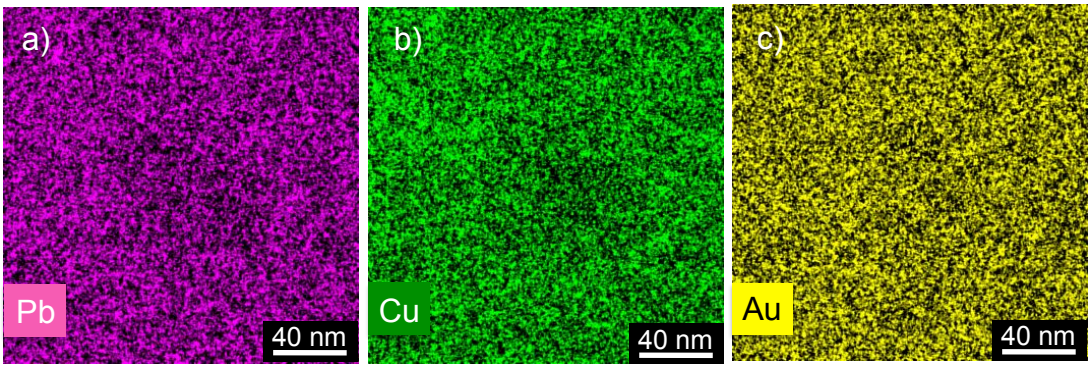

Figure 3-15 Pb, Cu and Au chemical maps, extracted from the spectral image, displayed in raw counts, individually scaled.

The low characteristic X-ray energy range is displayed in **Figure 3-16**, which shows a possible contribution from the O Kα at 0.5(3) keV, although there is overlapping with the Cr L at 0.5(5) keV. Of course such X-rays are prone to absorption effects, but the O is mapped in **Figure 3-17**a and shows differences to the Cr K_α map in **Figure 3-14**e. As such, there may be O present in this region, but the counts are low at ~50 counts per pixel after a 70 minute map in comparison to that of Fe at ~900 counts per pixel. Although no C is observed in the low keV spectrum in **Figure 3-16**, the C map is always considered due to the propensity for contamination after washing samples in methanol. While the C map in **Figure 3-17**b shows some depletion in the SPP, the average C counts per pixel is ~0 in the matrix and also ~0 in the region of the SPP, and, as such, is not significant.

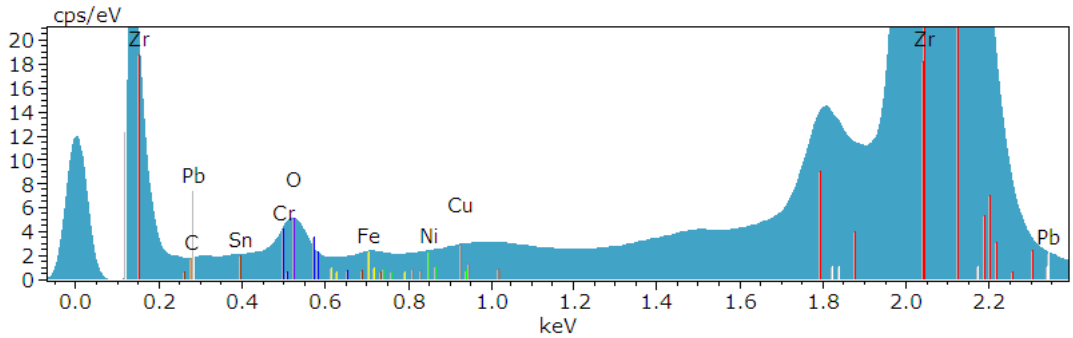

Figure 3-16 The low X-ray energy range for the SPP spectral image.

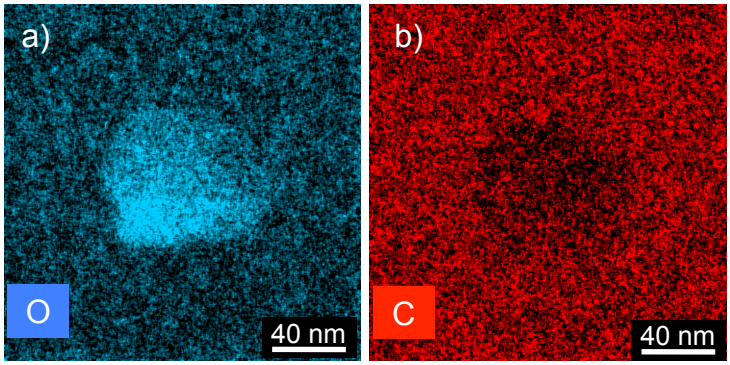

Figure 3-17 O, C chemical maps, extracted from the spectral image, displayed in raw counts, individually scaled.

The background subtraction for the whole 0-20 keV spectrum is summarised in **Figure 3-18**, which calculates the Bremsstrahlung by sampling parts of the spectra which are devoid of characteristic peaks, i.e. areas 1-9 in **Figure 3-18**a. The Bremsstrahlung is then deduced from the whole spectra to give the background-subtracted spectra in **Figure 3-18**b. As the O, C, Cu and Pb signals do not originate from the sample with any real significance, they are deconvoluted in the Cliff-Lorimer quantification. Calculation of composition then assumes the following for a binary system:

$$\frac{C_A}{C_B} = k_{AB}\frac{I_A}{I_B} \quad (3\text{-}4)$$

$$C_A + C_B = 100\% \quad (3\text{-}5)$$

where C_A is the concentration of element A, C_B the concentration of element B, I_A the intensity of the characteristic A X-ray peak in the spectrum, I_B the intensity of the characteristic B X-ray peak in the spectrum, and k_{AB} is a sensitivity factor (Williams & Carter 2009b). This is then applied to a five-element system such as Zircaloy-2. The *k*-factors were calculated theoretically based on microscope parameters and a matrix Zircaloy-2 spectrum, consisting mainly of Zr and ~1.5

wt.% Sn. The elemental concentrations are then calculated assuming no effect of thickness. The suitability of this assumption is assessed in **Figure 3-19**, which is plotted after Cliff-Lorimer quantifications performed for the whole map containing the SPP in **Figure 3-14**, averaging every pixel and applying thickness corrections in 10 nm increments from 0 to 200 nm at the density of pure Zr, 6.49 g cm^{-3}. The at.% for Sn, Fe, Cr and Ni is displayed on the left *y* axis and the Zr on the right, at different ranges but on the same scale. Further, the Fe/Cr atomic ratio is plotted as a dotted black line, as this is the value often sought in the present work. All elements change in calculated concentration as the thickness correction increases. A summary of this plot in terms of the percentage change in concentration from 0 to 200 nm thickness is shown in **Figure 3-19Figure 3-20**a. It can be seen from **Figure 3-20**a that the sensitivity to thickness is in the order Sn > Cr > Fe > Ni > Zr, which demonstrates that lower energy X-rays are better absorbed by the thin foil. The absolute Fe/Cr ratio changes by a value of -0.03 over the 0 to 200 nm thickness range, which is a relative change of -2.8%.

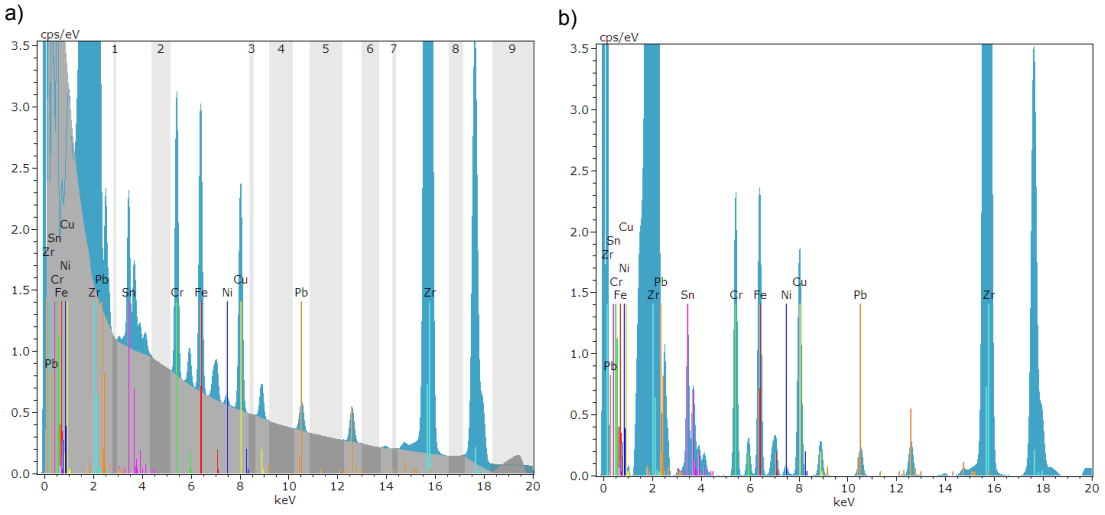

Figure 3-18 The background subtraction is performed by automatically defining regions without characteristic peaks, fitting the Bremsstrahlung in a) and subtracting it to leave the characteristic peaks in b) for Cliff-Lorimer quantification.

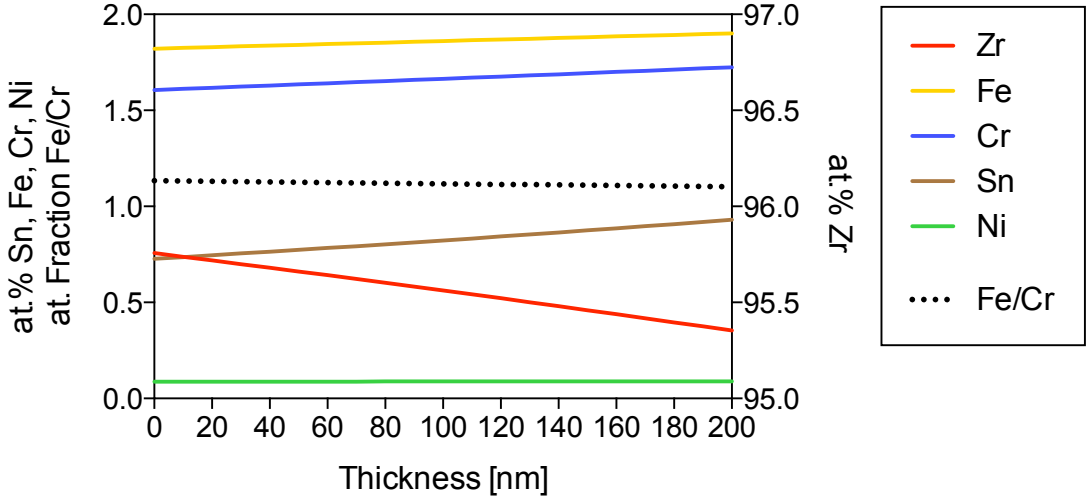

Figure 3-19 The average composition of the whole spectral image in **Figure 3-13** is calculated by the Cliff-Lorimer approach with varying thickness at a density 6.49 g cm^{-3}.

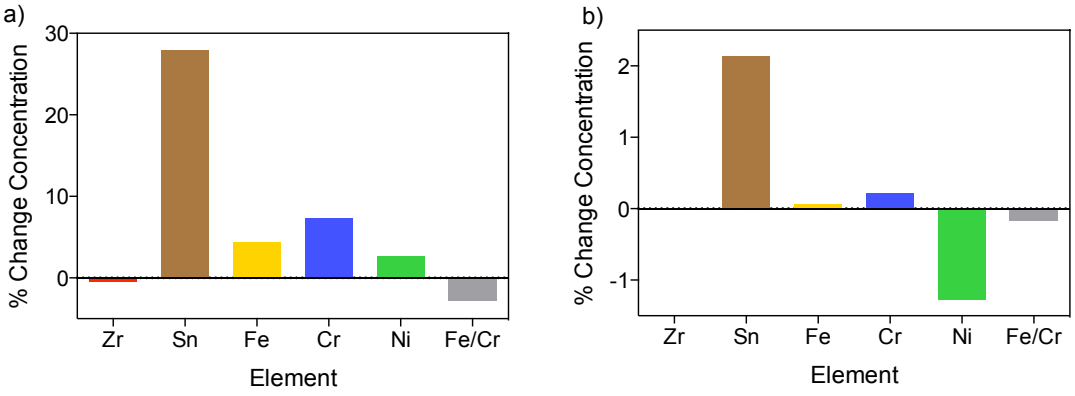

Figure 3-20 The relative change in concentration of the whole spectral image in **Figure 3-13** between 0 and 200 nm thickness is displayed in a) and the relative change in concentration due do the correction of detector effects is shown in b).

Effects due the detector may also be corrected for, such as escape peaks due to the ionisation of Si atoms in the detector, pulse pileup, etc. The effect of adding such corrections to the quantification of the whole map in **Figure 3-14** is shown in **Figure 3-20**b, in which thickness effects are ignored. It can be seen from **Figure 3-**

20b that Sn and Ni are the most severely affected by the addition of detector corrections, and the Fe/Cr ratio remains almost the same after a relative change of -0.13%.

From **Figure 3-19** and **Figure 3-20**, it is clear that Sn is affected the most by X-ray absorption and detector effects. Fe and Cr, the main constituents of the SPP, remain relatively unchanged after correcting for both thickness and detector effects. As the Fe/Cr ratio is the most important aspect of this investigation, making such corrections is not deemed necessary. While Ni is affected by detector effects such that it induces a relative change in the calculated concentration of -1.3%, this is a small change in comparison to the concentration one would expect within SPP in which Fe and Ni are the main constituents, where the concentrations would be similar to that of Fe and Cr in the SPP of **Figure 3-14**. As such, the Fe/Ni ratio is not thought to be affected significantly either. Of course, care should be taken when quoting low concentrations and reporting the concentration of Sn should be approached with doubt. Therefore, results should be referred to as semi-quantitative. Further, if small concentrations are investigated or the concentration of Sn is under question, then only net counts should be reported in a purely qualitative assessment.

Taking such conclusions under advisement, the spectral image obtained from the SPP in **Figure 3-14** has been fully quantified on a pixel-by-pixel basis, averaging 4 x 4 pixels to reduce both noise and the time required for the calculation. The results of this approach are shown in **Figure 3-22**, which displays the fully quantified chemical maps, all on the same scale. The scale is altered such that detail in the Fe and Cr maps are highlighted. Of course, the problem with the quantified maps of **Figure 3-22** is that the Zr content is so high that the depletion within the SPP cannot be observed and, likewise, detail in the Sn and Ni maps is lost due to their low concentration. In order to plot the maps on individual scales, the maps were exported as text files and plotted on individual colour scales with the use of the MATLAB for data manipulation. The result of this approach is shown in **Figure 3-21**, which reveals details due to each of the alloying elements.

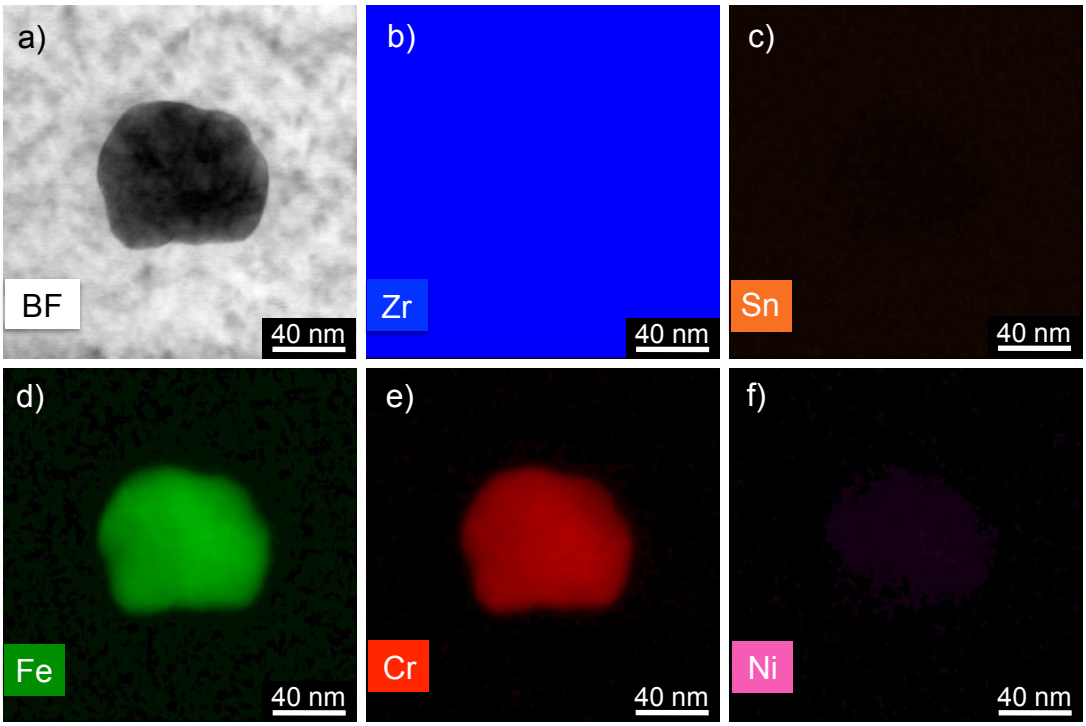

Figure 3-22 Chemical maps, extracted from the whole spectral image in **Figure 3-13** and quantified in at.%. maps are plotted on the same scale to reveal details in Fe and Cr.

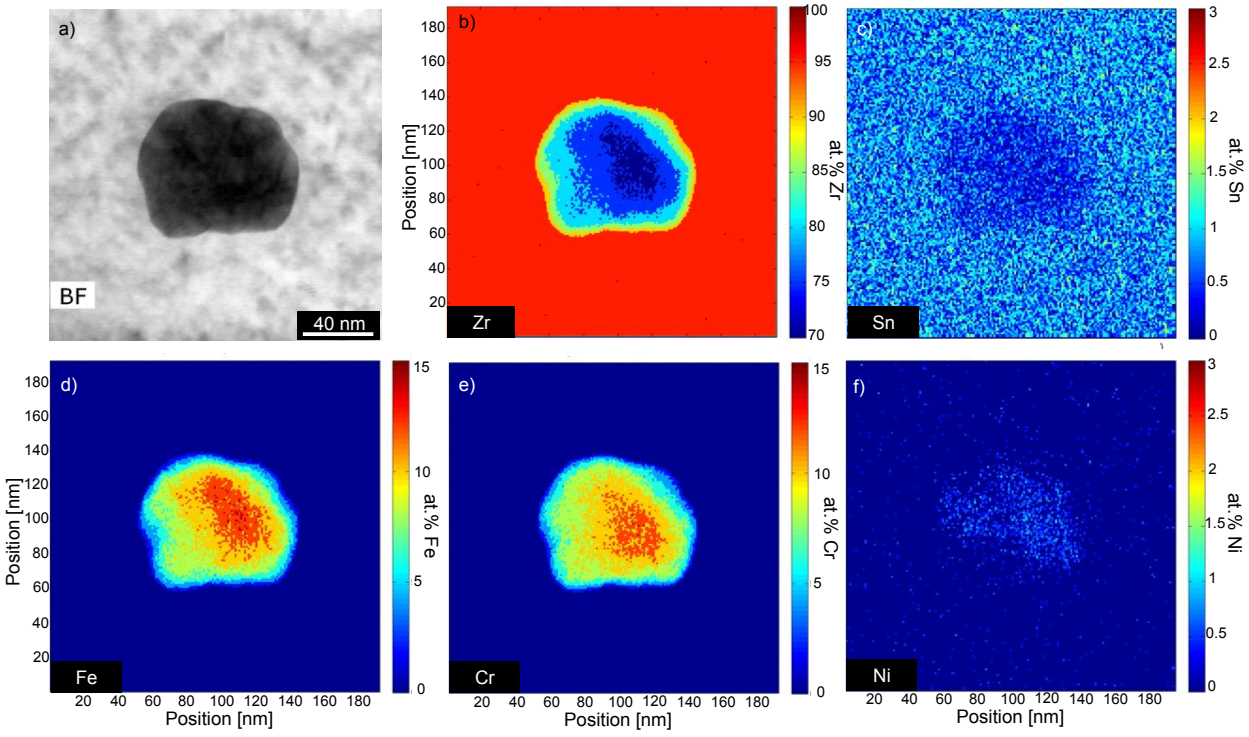

Figure 3-21 Chemical maps, extracted from the whole spectral image in **Figure 3-13** and quantified in at.%. Maps are plotted individual scales to reveal details in all maps.

The Zr map in **Figure 3-21**b demonstrates the depletion in the matrix due to the SPP and reveals details about the projected shape of the SPP in the transmission direction, the Sn map acting in a similar manner but with less detail due to the low concentration, high corresponding noise and the low reliability due to absorption and detector effects. The Fe and Cr maps show high concentration in the centre of the SPP where it is thickest and low concentration at the edges where it is thinnest. Interestingly, the Fe follows the contouring of the Zr but the Cr does not, suggesting that Fe is homogenous within the SPP but that Cr is segregated. The Ni shows the highest concentration associated with the region of highest Fe content. All such details are impossible in the raw maps of **Figure 3-15** and lend themselves to insight regarding the behaviour of elements within SPPs, even prior to irradiation. The difference between the Fe and Cr maps may be easily observed by the calculation of an Fe/Cr atomic ratio map, which is achieved simply by dividing the Fe concentration in each pixel by that of Cr and displaying the results. The Fe/Cr map for the SPP in **Figure 3-21** is shown in **Figure 3-23**. Obtaining such maps are important as they eliminate the selector bias involved in the selection of regions for simple Point & ID and line scan approaches to the characterisation of composition. Further, if the average chemical content is desired, then all pixels relating to a concentration > 1 at.% may be selected and the average concentration immediately obtained.

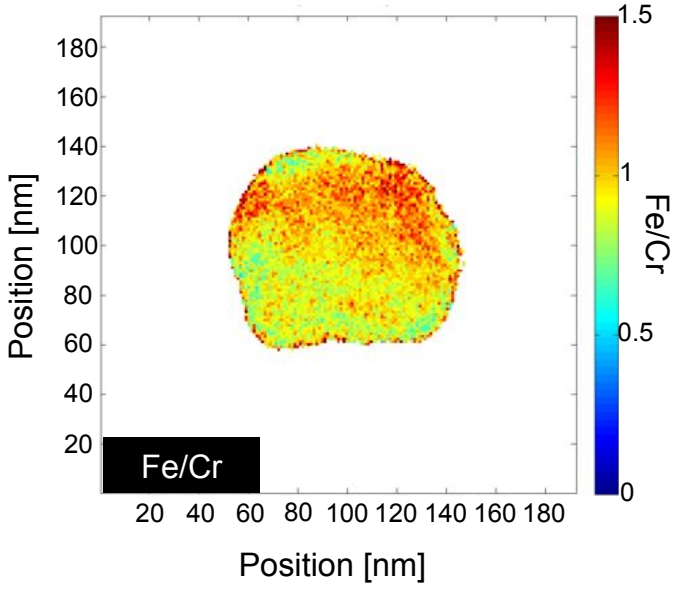

Figure 3-23 The Fe data from **Figure 3-21** is divided by the Cr data to produce an Fe/Cr atomic fraction map.

3.3.5.1 ERRORS IN ELEMENTAL QUANTIFICATION

The major source of error in the calculation of composition, or relative composition C_A/C_B for elements A and B, is that in the calculation of the *k*-factor used in Equation (3-4). The relative error in the calculation of, for instance, Fe/Cr in an SPP can be determined from the following propagation of errors (adapted from pp. 647 (Williams & Carter 2009d))

(3-)
$$\sigma_{rel} = \frac{\sigma\left(\frac{C_{Fe}}{C_{Cr}}\right)}{\frac{C_{Fe}}{C_{Cr}}} = \left[\left(\frac{\sigma \mathrm{k}_{FeCr}}{k_{FeCr}}\right)^2 + \left(\frac{\sigma \mathrm{I}_{Fe}}{I_{Fe}}\right)^2 + \left(\frac{\sigma \mathrm{I}_{Cr}}{I_{Cr}}\right)^2\right]^{\frac{1}{2}}$$

where σ(X) is a single standard deviation in X (assumed Gaussian), C_{Fe}/C_{Cr} is the atomic ratio Fe/Cr, I_{Fe} and I_{Cr} are the intensities of the Fe and Cr spectrum peaks used for quantification and k_{FeCr} is the *k*-factor k_{Fe}/k_{Cr} = 1.02 as calculated in the Quantax software. If the systematic error in the calculation of k_{FeCr} is assumed to be at best ±10% (Williams & Carter 2009d), then the total error varies with Fe+Cr counts as in **Figure 3-24**.

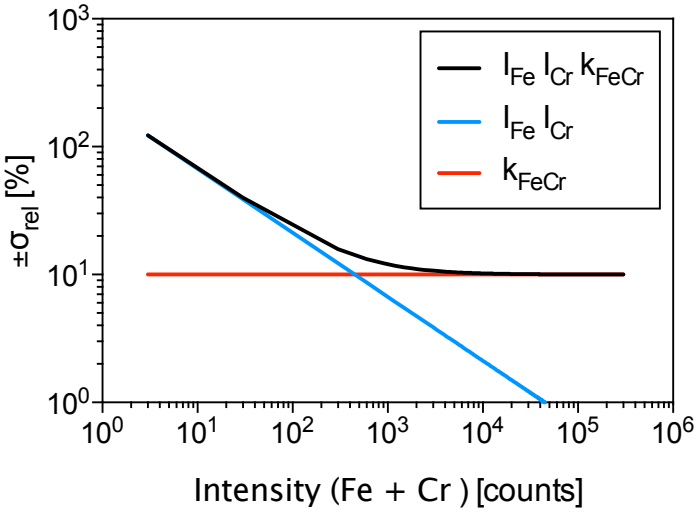

Figure 3-24 The error associated with quantification of C_{Fe}/C_{Cr} as a function of total counts for an SPP in which the atomic ratio Fe/Cr = 0.5. The three sets of data correspond to the total error (black), that due to counts alone (blue) and the systematic error associated with *k*-factor calculation.

With reference to **Figure 3-24**, averaging pixels for Fe+Cr > ~10^4 counts will not give any improved reliability. The Quantax software does not take this into account and simply quotes the error due to counts (blue line). Another source of error arises in the spatial domain due to beam spreading effects. As the thickness of pure Zr increases, a probe-corrected 0.4 nm (90% diameter) beam will result in spatial resolution,

(3-) $$R = q[\sigma^2 + \beta(\kappa t)^3/2]^{\frac{1}{2}}$$

where q = 4.29 and κ = 0.68 are parameters that describe the spatial resolution that contains 90% of the incident intensity, t is the thickness and

(3-) $$\sigma = \frac{d(90\%)}{4.29}, \text{and } \beta = 500\left(\frac{4\bar{Z}}{E_0}\right)^2\left(\frac{\rho}{\bar{A}}\right)$$

where $\bar{Z}$ and $\bar{A}$ are the mean atomic number and atomic weight, respectively, ρ is the material density and E_0 the incident accelerating voltage. The result for pure Zr at $E_0 = 200$ keV is very similar to that of Cu in the example in Pennycook (pp. 310-311 of (Pennycook & Nellist 2011)) and is displayed in **Figure 3-25**. At the thicknesses probed in the present work (100-150 nm) the spatial resolution in the spectral images and chemical maps is therefore no better than 8-15 nm.

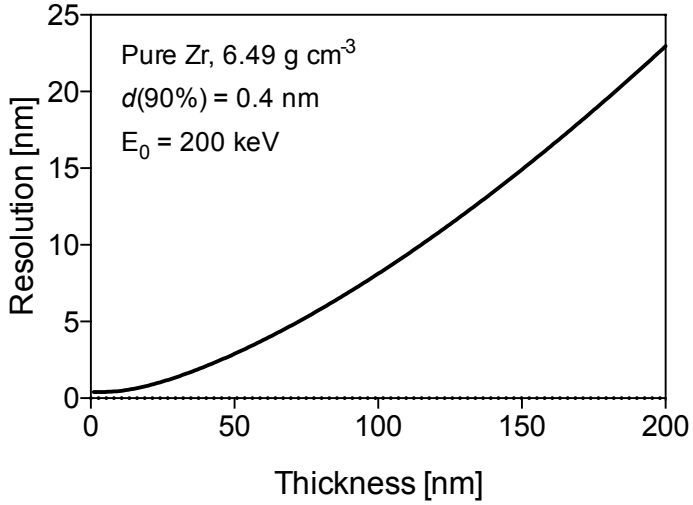

Figure 3-25 Spatial resolution deteriation due to beam spreading effects as a function of thickness in pure Zr.

3.3.6 DETERMINATION OF ORIENTATION

As imaging (§3.3.4) and energy-dispersive X-ray spectroscopy (§3.3.5) was performed in STEM mode and frequently from on-axis matrix orientations, it was vital to be able to determine matrix orientation in STEM mode. This was accomplished by calculating the fast Fourier transform (FFT) of a high-resolution STEM (HR STEM) image, made possible by the sub-angstrom probe of the

spherical aberration-corrected FEI Titan microscope. The FFT was calculated within the FEI TIA software and, although not as clear as selected area diffraction patterns, was a useful experimental aid. A HR STEM image at the <0001> zone axis is given in **Figure 3-26**a with an inset of higher magnification, showing the hexagonal arrangement of the Zr atoms when observed from the <0001> matrix orientation. The FFT of **Figure 3-26**a is shown in **Figure 3-26**b, which demonstrates the 3-fold symmetry of the <0001> zone axis and the visibility of the $\{1\bar{1}00\}$ and $\{11\bar{2}0\}$ planes. The symmetry of such FFTs were compared to simulated patterns within the JEMS crystal software package for identification. At low symmetry orientations, the Kikuchi patterns surrounding the Ronchigram were used to navigate reciprocal space. Such a Kikuchi map is shown in **Figure 3-27**.

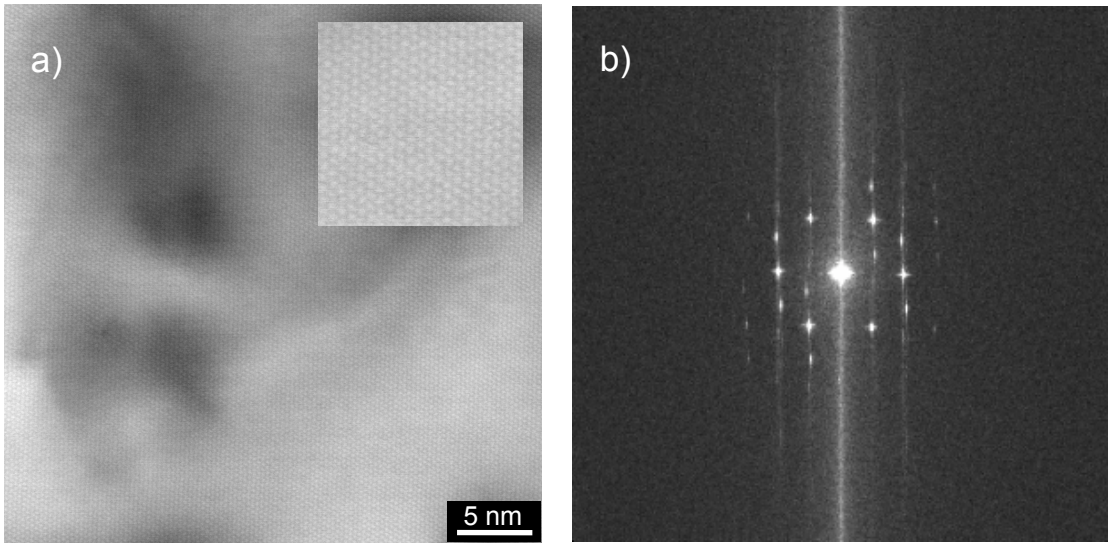

Figure 3-26 HR STEM image, with magnified inset, from the <0001> zone axis orientation in Zircaloy-2 proton-irradiated to 2.3 dpa in a) and the FFT of that image in b), demonstrating the hexagonal symmetry of the <0001> zone axis and the visibility of the $\{1\bar{1}00\}$ and the $\{11\bar{2}0\}$ planes.

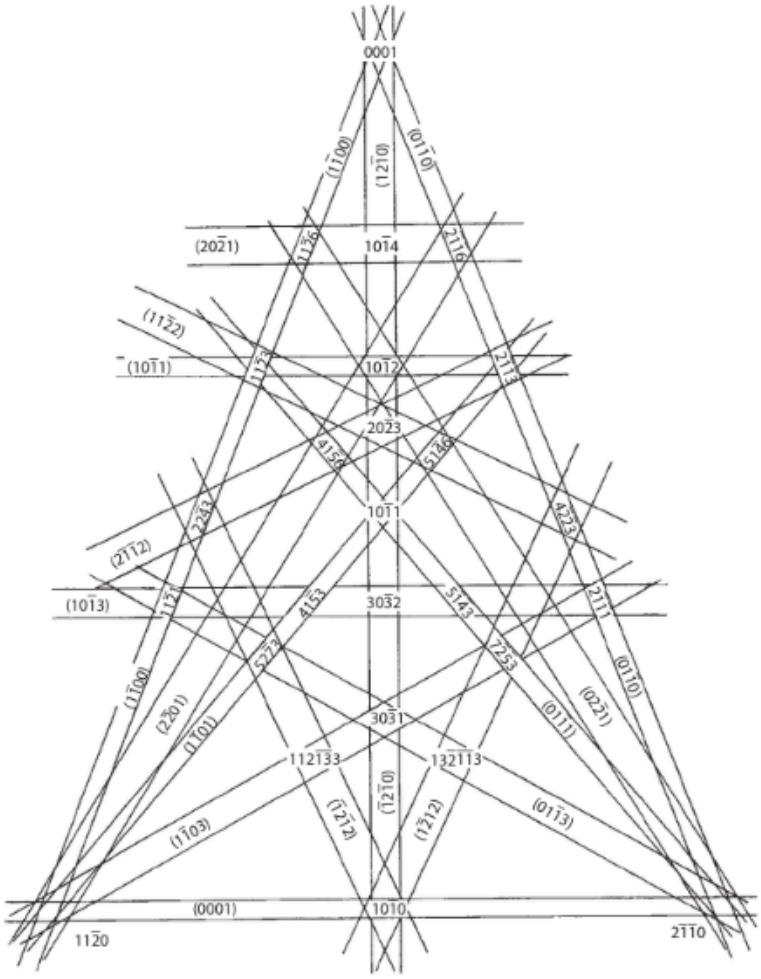

Figure 3-27 The Ti hcp Kikuchi map from (Randle & Engler 2014).

3.3.7 DISLOCATION ANALYSIS

The dislocation analysis in the present work was concerned with defining the dislocation Burgers vector, the habit plane and number density calculations. The dislocation Burgers vector was investigated based on the principle of the invisibility criteria (Dingley 1970) and utilising the expected Burgers vectors for dislocations in hcp systems (Okamoto 1967) and those proposed for dislocation loops in irradiated Zr alloys, i.e. a-loops with Burgers vector $\frac{1}{3}<11\bar{2}0>$ that

inhabit $\{10\bar{1}0\}$ planes (Jostsons et al. 1977; Griffiths 1988) and c-loops with Burgers vector $\frac{1}{6}<20\bar{2}3>$ that inhabit basal planes. As such, one third of a-loops should be invisible when imaging in dark field with g = $1\bar{1}00$, all a-loops visible with g = $11\bar{2}0$ and all a-loops should be invisible with g = 0002. In this third condition, all c-loops should be visible.

The dislocation counting measurements were made in BF STEM. For dislocation counting, a direct comparison of bright-field (BF) images from TEM and STEM of the same region of the same grain at the same magnification is given in **Figure 3-28**. In this Zircaloy-2 sample, proton-irradiated to 2.3 dpa, the BF TEM image was obtained parallel to the g = $11\bar{2}0$ systematic row ~6° from the $<1\bar{1}00>$ zone axis and the BF STEM image was obtained directly parallel to the $<1\bar{1}00>$ zone axis. The STEM image is rotated to match the TEM and the hydride in the upper right corner acts as a fiducial marker. It is immediately obvious that there is less strain contrast in the BF STEM image, which is due to the convergence of the scanning probe as many diffraction conditions contribute to the image and so the contrast is reduced. Counting of the loops within the TEM image gives 43 dislocations with good loop contrast, i.e. 'double-arc' contrast or clear ellipticity with 'inside' contrast. If one considers a loop to be a loop if it becomes invisible under a certain diffraction conditions then one would multiply the number of invisible loops by three. If, as is done here, one uses the bright-field image to count loop-looking structures, then all loops with Burgers vector $<11\bar{2}0>$ -type should be visible using the g = $11\bar{2}0$ reflection. Likewise, all loops in the BF STEM image with Burgers vector $<11\bar{2}0>$ -type should be visible at the $<1\bar{1}00>$ zone axis. In the BF STEM image, the loop double-arc contrast is more easily observed due to less matrix strain, and, as such, more dislocations are counted. A total of 114 dislocation loops were recorded in **Figure 3-28**b, with the majority of them having good double-arc contrast and very few with elliptical inside contrast. The ratio of loop length/width as determined by TEM was 1.56 and by STEM 1.82, the former being smaller due to the angle with which the dislocations are viewed with respect to the habit plane normal. As such, there are differences between imaging

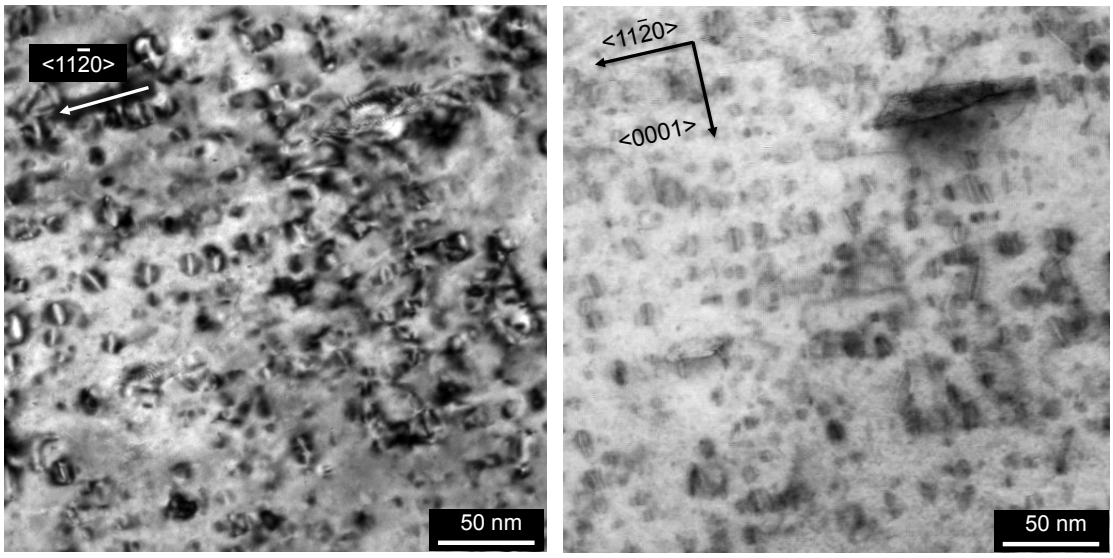

Figure 3-28 Dislocation loops in Zircaloy-2 proton-irradiated to 2.3 dpa. In a) the BF TEM image, taken ~6° from the $<1\bar{1}00>$ zone axis parallel to the g = $11\bar{2}0$ systematic row, and in b) the BF STEM image, taken from parallel to the $<1\bar{1}00>$ zone axis.

techniques and different results may be obtained. However, the BF STEM technique gives good dislocation contrast as matrix strain is reduced. It is therefore considered more accurate and has been used as the technique of choice in the manuscripts presented here.

Weak beam dark field (WBDF) microscopy is another method by which strain contrast can be reduced in the matrix and highlighted only in regions where the crystal is distorted significantly, such as at dislocation line cores. The following example was performed on a FEI Tecnai TF30 300 kV FEG-AEM microscope. **Figure 3-29** contains images taken from a grain in the 2.3 dpa sample, and demonstrates the orientation at which both the g = $11\bar{2}0$ and $1\bar{1}00$ conditions were obtained, ~17° from the <0001> zone axis and almost 15° from the $\{11\bar{2}0\}$ towards the $\{10\bar{1}0\}$ Kikuchi band, i.e. half way between them. A double exposure of the central zero order Laue zone (ZOLZ) and the Kikuchi pattern is given in **Figure 3-29**a, which is a useful way of determining the weak beam condition. An image is truly weak beam if the following equation, adapted from (Jenkins & Kirk 2001), is satisfied:

$$s_g = \frac{(n-1)\lambda}{2d_{hkil}^2} \geq 0.2nm^{-1} \quad (3\text{-}9)$$

where s_g is a parameter describing the deviation of reflection g from the Bragg condition in units of nm^{-1}, n is the deviation from the Bragg condition in multiples of g, λ is the relativistic electron wavelength (1.961 $x10^{-3}$ nm for the 300 kV microscope used here) and d_{hkil} is the interplanar spacing of the g reflection in units of nm, such that $d_{hkil} = 1/g$, where g is the magnitude of g in nm^{-1}, measured directly from the diffraction pattern. The weak beam condition is then denoted g(ng), where n is that given in the equation above and is equal to the the distance of the g reflection from the Bragg condition divided by the magnitude g, both in units of nm^{-1}.

In the g = $11\bar{2}0$ image of **Figure 3-29**c, the WBDF condition is g(7.8g), i.e. n in e Equation (3-) is equal to 7.8. As the interplanar spacing was measured as 0.162 nm from the ZOLZ, $s_{<11\bar{2}0>}$ = 0.25 nm^{-1}, which satisfies the condition required for WBDF. In the g = $1\bar{1}00$ image of **Figure 3-29**d, the WBDF condition is g(12.3g) and the interplanar spacing was measured as 0.274 nm from the ZOLZ pattern. This gives a value of $s_{<1\bar{1}00>}$ = 0.13 nm^{-1}, which does not satisfy the condition required for a WBDF image, and, as such, part d) of the figure should be regarded as a semi-WBDF image only. For reference, using the magnitudes of g presented here as d_{hkil}, in order to obtain s_g = 0.2 for 300 keV electrons, one would require g(6.3g) and g(16.9g) conditions for g = $11\bar{2}0$ and $1\bar{1}00$, respectively, the latter being larger due to a larger d_{hkil} and consequently smaller g.

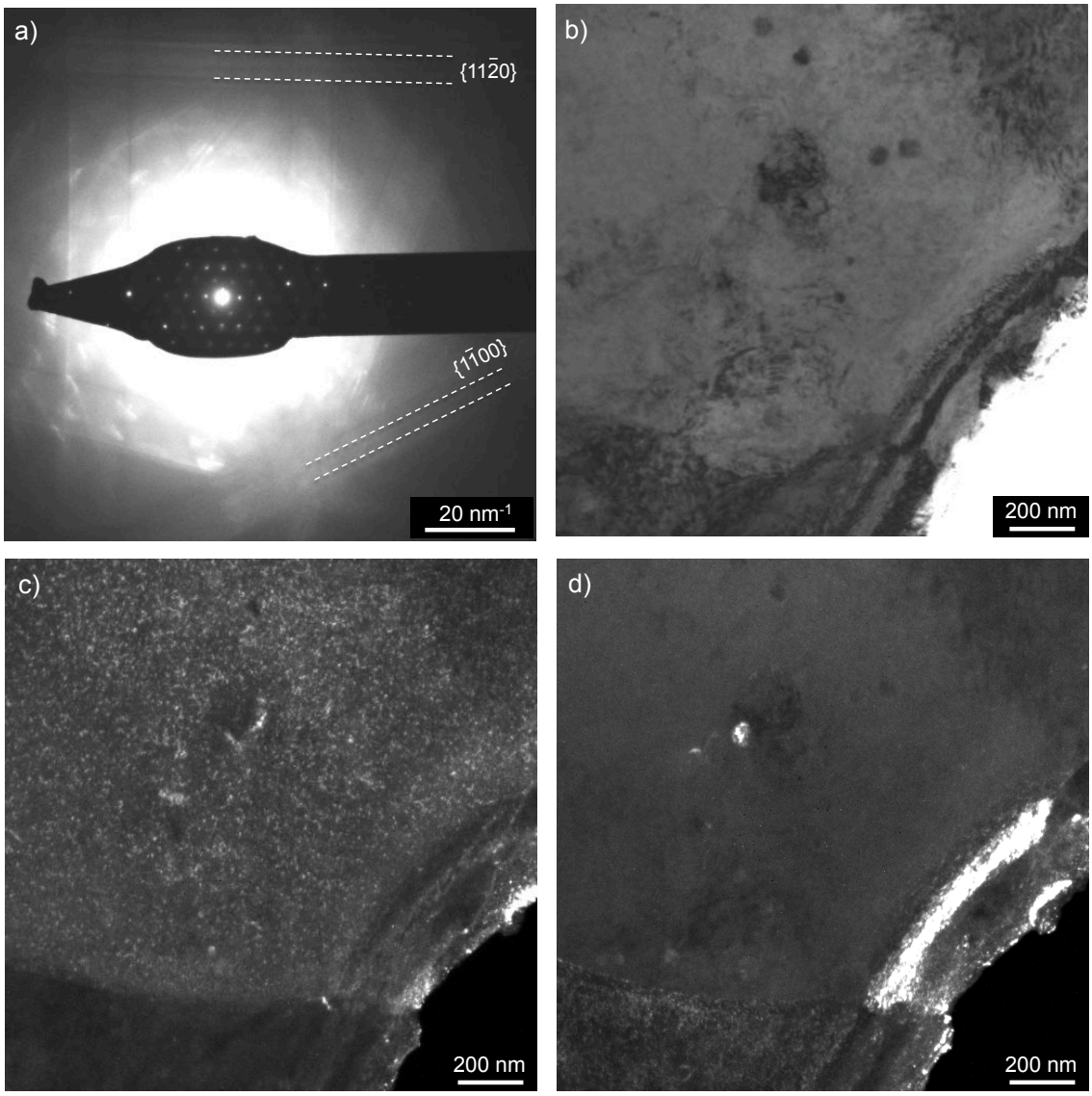

Figure 3-29 Burgers vector analysis by WBDF microscopy in TEM mode. The double exposure of the zero order Laue zone and Kikuchi bands in a) allows simple determination of the WBDF condition. The kinematical bright field image is taken from the orientation in a) and shows little defect contrast in the matrix. The g(7.8g), g = $11\bar{2}0$, s_g = 0.25 nm^{-1} condition is shown in c), displaying defect contrast, invisible in d) in the g(12.3g), g = $1\bar{1}00$, s_g = 0.13 nm^{-1} condition.

Although **Figure 3-29**c and d are WBDF and semi-WBDF images, respectively, they remain a useful comparison because the true WBDF image in **Figure 3-29**c

displays an accurate measure of defect number whereas the image in **Figure 3-29**d gives an overestimate. As there are no defects observed in overestimated **Figure 3-29**d we can say with certainty that the defects in **Figure 3-29**c satisfy the invisibility criterion with g = $1\bar{1}00$ and are visible with g = $11\bar{2}0$, a property consistent with a-loops with Burgers vector $<11\bar{2}0>$-type.

However, as these images were obtained at 17° from <0001>, one cannot confirm that such defects do not have a pyramidal Burgers vector and it is difficult to comment with any certainty on the size and shape of such loops. For a more detailed analysis, one requires images of loops obtained from or closer to the habit plane normal, i.e. an <a>-direction, such that the g = 0002 diffraction vector may be used to assess any pyramidal contribution to strain. This is possible in BF STEM, which has been used for Burgers vector and number density quantification as well as size and shape analysis at orientations such as that demonstrated in **Figure 3-28**b. A WBDF approach at such an axis was attempted, but the necessary tilts for WBDF far from the Bragg condition resulted in changes in dislocation size and shape and as such were not as useful as near- and on-axis BF STEM.

3.3.8 CBED FOR THICKNESS DETERMINATION

The majority of discussion so far has related to STEM. Thickness determination was performed in TEM mode. The determination of the thin foil thickness was required for dislocation loop number density quantification, as well as estimations of the composition of features embedded within a Zr matrix. Thickness measurements were obtained by the analysis of intensity oscillations within convergent beam electron diffraction (CBED) patterns by the graphical method, which is described well in §21.2 of Williams & Carter (Williams & Carter 2009c). The following is a description of the procedure necessary for such a measurement, by way of example in Zircaloy-2 proton-irradiated to an irradiation dose of 4.7 dpa.

In the first instance, a 2-beam condition is obtained such that a systematic row of reflections is highlighted. While the term '2-beam' is not strictly correct, as many reflections are simultaneously observed, it is a common phrase in the literature. As such, the term 'systematic row' will be used here. In TEM mode, a convergent beam of illumination of a sufficient angle of convergence will result in diffraction disks projected onto the back focal plane. Within the cone of illumination, a 2-dimensional plane will be at the perfect Bragg condition and, as such, a deficiency line will appear in the bright field diffraction disk and an excess line will appear in the dark field diffraction disk. This is summarised in **Figure 3-30**, which is one of the many beautiful 3-dimensional ray diagrams of Morniroli (Morniroli 2002). In addition to the excess and deficiency lines due to diffraction, the diffraction disk will contain an increasing number of parallel intensity oscillations with increasing sample thickness. This occurs due to the interaction of the electron with the atomic periodicity of the lattice planes belonging to the diffraction condition chosen. When highlighting a systematic row, the bright-field and dark-field disks act as coupled harmonic oscillators such that the intensity is transferred from one disk to another. One cycle of this sinusoidal oscillation is termed the extinction distance, and it occurs over a physical distance in the transmission direction. Therefore, thicker samples undergo a larger number of oscillations, and this can be used to

determine thickness. This process is summarised in **Figure 3-31**, in which I_g is the intensity in the diffracted state and ξ_g is the extinction distance, which is a physical distance as so can be measured in terms of thickness.

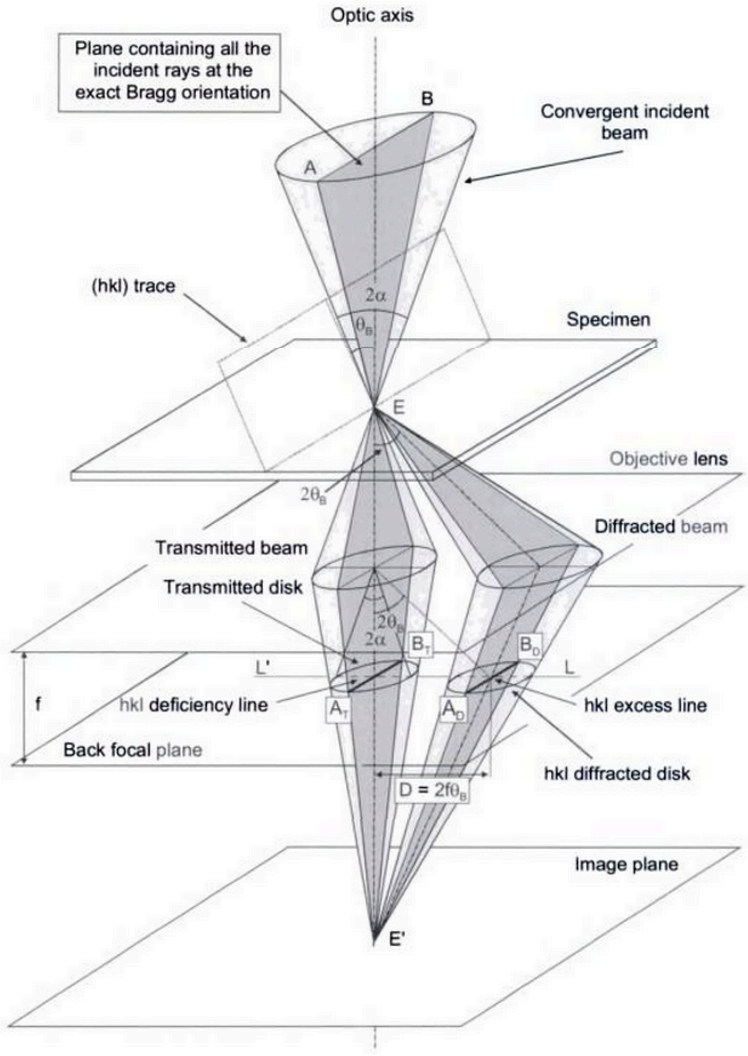

Figure 3-30 CBED pattern formation from (Morniroli 2002) pp.48. The convergent probe is incident on the sample at E. The plane AB is at the Bragg condition and diffracts by the Bragg angle (θ_B) to produce the excess line (L) at A_DB_D and the deficiency line (L') at A_TB_T.

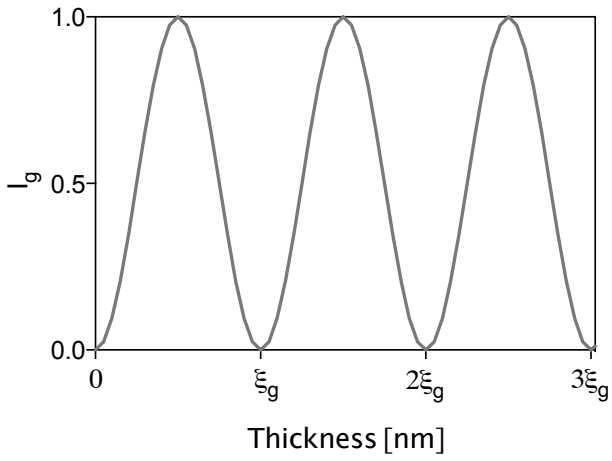

Figure 3-31 The variation in the Bragg-diffracted intensity (I_g) is sinusoidal with thickness. One oscillation in intensity is equal to one extinction distance, ξ_g.

In Zr, it has been shown that higher order reflections produce better agreement when calculating the extinction distance -thickness relationship for a specific diffraction condition (Cann 1978). The extinction distance is a function of the deviation from the Bragg angle (Cann 1977) and it is therefore important to take great care such that the exact Bragg angle is used for collection of the CBED pattern. An example of such a pattern for the g = $10\bar{1}5$ reflection ~10° from the closest $<11\bar{2}0>$ zone axis is given in **Figure 3-32**a, which was obtained on the FEI Titan microscope at 200 keV in TEM mode.

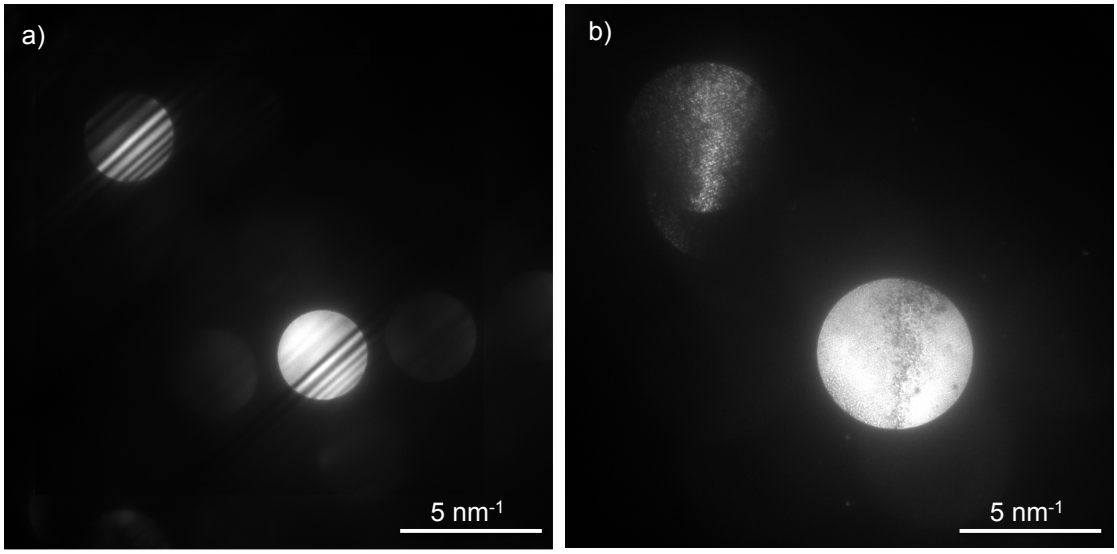

Figure 3-32 A CBED pattern from 4.7 dpa proton-irradiated Zy-2, corresponding to the g = $10\bar{1}5$ condition ~10° away from the $<11\bar{2}0>$ zone axis, a) focused and in b) defocused with condenser intensity to reveal the BF and DF shadow images.

In **Figure 3-32**a, the exact Bragg condition is recognised as the excess and deficiency lines in the very centre of their respective disks. Due to mechanical hysteresis in the stage, it is not always simple to tilt the sample into such an exact Bragg condition. Alternatively, the dark-field deflection coils may be used to tilt the beam when the sample is tilted very close to, but not exactly act, the Bragg condition. If this is done, then it is recommended that the pivot point alignment is good and that shape of the beam is investigated after beam tilting just prior to obtaining the CBED pattern, as beam tilting may induce beam distortions that may

destroy the convergence necessary to produce good CBED patterns. **Figure 3-32**b is the same CBED pattern but defocused using the condenser lens. This produces a bright field and g = $10\bar{1}5$ dark-field image within the respective diffraction disks and demonstrates a visible bend contour in the sample. This ben contour is useful, as it shows the position in the sample at which the exact Bragg condition is satisfied, and, as such, the CBED patterns was obtained from the spatial point at which the bend contour contrast is highest

To obtain thickness information from the CBED pattern in **Figure 3-32**a, a line scan is obtained from across the patterns and is shown in **Figure 3-33**a. The dark-field disk is highlighted in **Figure 3-33**a by red lines, within which the intensity oscillations are used to find s_i, where

(3-10)
$$s_i = \lambda \frac{\Delta\theta_i}{2\theta_B d^2}$$

where λ is the electron wavelength, $\Delta\theta_i$ is the distance in the CBED pattern between the excess line and the other intensity maxima due to thickness variation, θ_B is the Bragg angle and d is the interplanar spacing of the 2-beam g vector selected (Williams & Carter 2009c). To find thickness, the following is determined

(3-11)
$$\frac{s_i^2}{n_k^2} + \frac{1}{\xi_g^2 n_k^2} = \frac{1}{t^2}$$

where n_k is an integer ξ_g is the extinction distance and t is the thickness (Williams & Carter 2009c). As ξ_g is rarely known, the plot in **Figure 3-33**b is drawn with successive but arbitrary values of n_k until a straight line is obtained. The intercept of this line with the y axis is equal to $t^{-0.5}$ and so the thickness as determined from **Figure 3-33**b is equal to 164 nm.

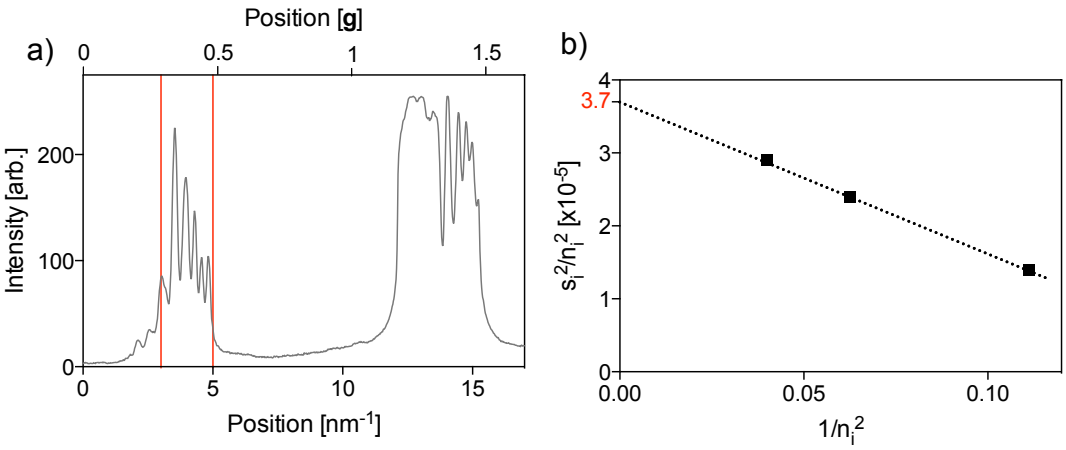

Figure 3-33 A line scan is extracted from the BF and DF diffraction disks in **Figure 3-32**a and is shown in a) together with red lines indicating the DF disk and the three highest intensity maxima used for thickness determination by the graphical method, b).

While this graphical method is considered to result in measurements correct to ±10%, experimental ability and reproducibility in addition to care in obtaining the CBED pattern from the exact Bragg condition increase the uncertainty. To corroborate the measurement, a Bloch wave calculation may be performed to simulate the appearance of the diffraction pattern with the same microscope conditions and sample thickness. This calculation was performed with the JEMS crystal software using the Bethe correction (Stadelmann 2007). The calculation was performed 9.81° from the $<11\bar{2}0>$ zone axis, which is similar to the orientation at which the experimental pattern was obtained. In **Figure 3-34**a and b the kinematical approximation (no intensity oscillations due to dynamic extinction distance effects) is shown at shorter and longer camera lengths, respectively. It is important to note that the Bloch wave calculation must be performed in a region where no low index (red) or high index (green) Kikuchi lines cross the diffracting disk of interest other than the $\{10\bar{1}5\}$ excess line of interest, as any other excess lines will cause interference in the intensity oscillations within the disk. The result of the dynamical calculation is shown in **Figure 3-34**c, in which intensity oscillations are found in both the bright-field and dark-field g = $10\bar{1}5$ diffraction disks. A line scan of intensity with respect to position was then obtained from the dark-field disk, which is displayed in **Figure 3-35** together with the relevant

section of the line scan of the experimental diffraction pattern. As can be seen from **Figure 3-35**, there is good agreement between the intensity maxima for the experimental and theoretical CBED patterns. As such, the calculated thickness of 164 nm in **Figure 3-33**b is deemed reliable. While such an extensive analysis was not performed for every thickness measurement made in the present work, great care was taken to reproduce the conditions outlined here.

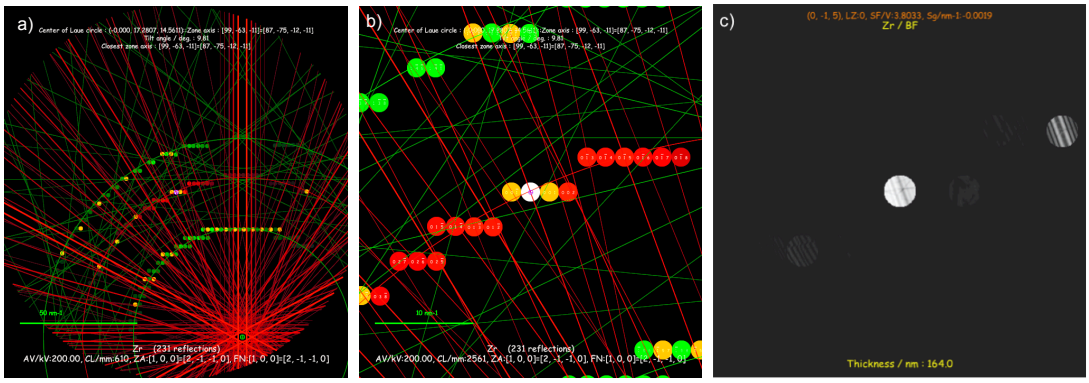

Figure 3-34 JEMS a) and b) kinematical simulation of the g = $10\bar{1}5$ diffraction condition nm 9.81° from $<11\bar{2}0>$ zone axis and at different camera lengths, and c) the Bloch wave calculation at 164 nm, as calculated in **Figure 3-33**b, showing thickness fringes in the disks.

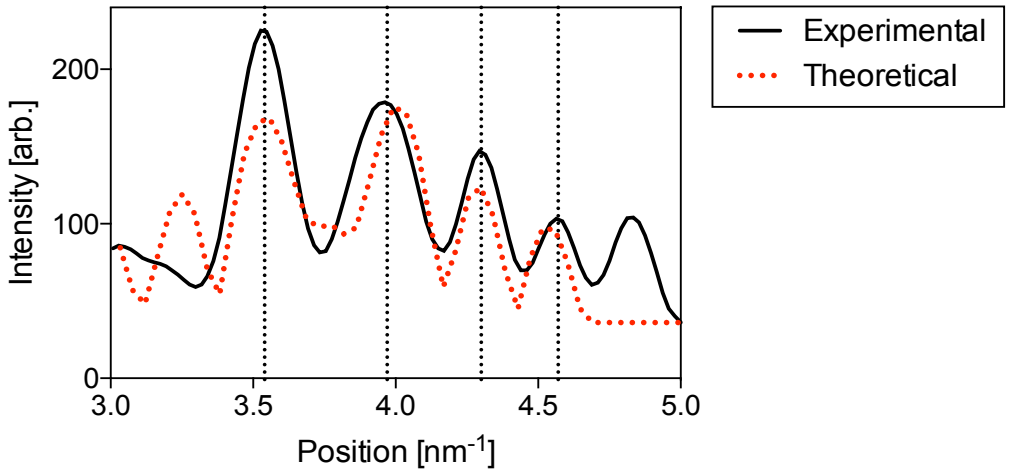

Figure 3-35 Comparison of experimental and theoretical intensity oscillations within the DF disk of the g = $10\bar{1}5$ reflection at 164 nm shows good agreement.

It should be noted that separate thickness measurements were not obtained from regions separated by < 3 um parallel to the hole edge. As an alternative, the total energy-dispersive X-ray counts obtained at the same crystal orientation, beam current and counting time (60 s) was used to extrapolate thickness between different parts of the same gain. As such, the thickness determination was made by CBED at one position within the grain, correlated to a number of counts per minute, and then the number of counts per minute in a neighbouring part of the same grain was used to infer the local thickness. Of course, this approach assumes that the only variation in counts is due to thickness under such conditions, which was deemed appropriate given the local nature of sample movement within such regions.

3.4 ATOM PROBE TOMOGRAPHY

Atom probe tomography (APT) was performed on needle-shaped samples on the Local Electrode Atom Probe (LEAP) Cameca - 3000X at The University of Oxford, UK, predominantly by the team at Oxford, although data analysis was performed by the present author and Prasath Babu Revathy Rajan at The University of Manchester.

The principles of APT are detailed in the schematic of **Figure 3-36**. An intense electric field of the order 1010 V m^{-1} is applied to the tip of radius ~50 nm, which results in the ionisation of surface atoms. Field evaporation occurs, accelerated towards a position-sensitive detector through a local electrode, capturing 2-dimensional information. A laser pulse is used to evaporate surface atoms such that a single ion is detected for a given time interval. The time-of-flight between the ionisation of the surface atom and it hitting the detector is recorded and the mass-to-charge ration calculated. This allows element identification as a function of position. The samples were held at a temperature of 50 K during data acquisition. The field evaporation of ions was carried out in laser pulse mode with a green laser of energy 0.4 nJ and a frequency of 200 kHz.

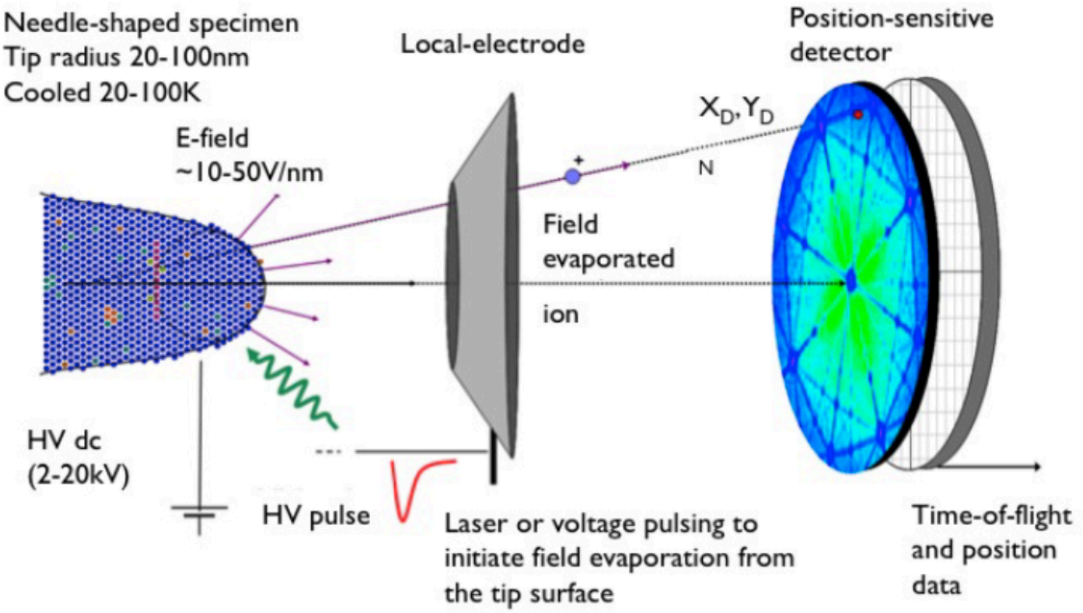

Figure 3-36 Schematic detailing the principles of APT (B Gault et al. 2012).

APT has a spatial resolution of ~1 nm, but is limited by preferential evaporation and surface diffusion (Baptiste Gault et al. 2012). While preferential evaporation was not a significant concern for the present work, surface diffusion of Sn resulted in unreliable spatial information regarding this element especially. The detection of Ni was not carried out due to the overlapping of Ni^{+} peaks with Sn^{2+} peaks at 58 and 60Da and the Ni^{2+} peak with Zr^{3+} peak at 30Da, leaving only 29Da for detection of Ni, proving difficult with the low concentration of Ni (Da = mass to charge ratio). The detection efficiency of the micro-channel plate in the LEAP is 37%, which means one-third of the field evaporated ions are lost, but this is independent of element type (Hellsing et al. 1985). The reconstruction of the analysed volumes was made on the basis of the needle profile from the SEM images of the sharpened needles.

3.5 References

Bell, D.C. & Erdman, N., 2013. Introduction to the theory and advantages of low voltage electron microscopy. In *Low voltage electron microscopy: Principles*

and applications. Chichester, West Sussex, UK: Royal Microscopy Sopciety, Wiley, pp. 1–23.

Cann, C.D., 1978. *Convergent beam thickness determination of thin foil zirconium specimens*,

Cann, C.D., 1977. *Many-beam electron extinction distances in zirconium*,

Charquet, D. et al., 1988. Solubility limits and formation of intermetallic precipitates in ZrSnFeCr alloys. *Zirconium in the Nuclear Industry: Eighth International Symposium*, pp.405–422.

Dingley, D.J., 1970. Dislocation invisibility in dark-field electron microscopy. *Physica Status Solidi B*, 38(1), pp.345–355.

Egerton, R.F. et al., 2010. Basic questions related to electron-induced sputtering in the TEM. *Ultramicroscopy*, 110(8), pp.991–997.

Fultz, B. & Howe, J., 2008. The creation of X-rays. In *Transmission electron microscopy and diffractometry of materials*. Springer Berlin Heidelberg New York, p. 14.

Gammon, L.M. et al., 2004. Metallography and microstructures of titanium and its alloys. *ASM Handbook*, 9: Metallo, pp.899–917.

Gault, B. et al., 2012. Atom probe crystallography : structure & composition. *Materials Today*, 15(3), pp.2–10.

Gault, B. et al., 2012. *Atom Probe Microscopy*, Springer.

Griffiths, M., 1988. A review of microstructure evolution in zirconium alloys during irradiation. *Journal of Nuclear Materials*, 159, pp.190–218.

Hallstadius, L., Johnson, S. & Lahoda, E., 2012. Cladding for high performance fuel. *Progress in Nuclear Energy*, 57, pp.71–76.

Hellsing, M. et al., 1985. Performance of a microchannel plate ion detector in the energy range 3-25 keV. *Journal of Physics E: Scientific Instruments*, 18(11), pp.920–925.

Jenkins, M.L. & Kirk, M.A., 2001. *Characterisation of Radiation Damage by Transmission Electron Microscopy*, Insitute of Physics Publishing.

Jostsons, A., Kelly, P.M. & G, B.R., 1977. The Nature of Dislocation Loops in Neutron Irradiated Zirconium. *Journal of Nuclear Materials*, 66, pp.236–256.

Morniroli, J.P., 2002. *Large-Angle Convergent-Beam Electron Diffraction (LACBED): Application to Crystal Defects*, Paris: Monograph of the French Society of Microscopies.

Nellist, P.D., 2011. The principles of STEM imaging. In *Scanning Transmission Electron Microscopy. Imaging and Analysis*. Springer New York Dordrecht Heidelberg London, p. 92.

Nishikawa, S. & Kikuchi, S., 1928. Diffraction of cathode rays by calcite. *Nature*, 122(3080), p.726.

Oen, O.S., 1965. *Cross sections for atomic displacements in solids by fast electrons*,

Okamoto, P.R., 1967. Kikuchi Maps for hcp and bcc crystals. *Journal of Applied Physics*, 38(1), pp.289–296.

Pasianot, R.C. & Pérez, R. a., 2013. First-principles appraisal of solute ultra-fast diffusion in hcp Zr and Ti. *Journal of Nuclear Materials*, 434, pp.158–161.

Pennycook, S.J. & Nellist, P.D., 2011. *Scanning Transmission Electron Microscopy. Imaging and Analysis* S. J. Pennycook & P. D. Nellist, eds., Springer New York Dordrecht Heidelberg London.

Perez, R.A., Nakajima, H. & Dyment, F., 2003. Diffusion in alpha-Ti and Zr. *Materials Transactions*, 44(1), pp.2–13.

Randle, V. & Engler, O., 2014. Appendix A. In *Introduction to Texture Analysis: Macrotexture, Microtexture and Orientation Mapping*. CRC Press, Taylor & Francis Group, p. 365.

Stadelmann, P., 2007. *Simulation of diffraction patterns and high resolution images using jems*,

Stoller, R.E. et al., 2013. On the use of SRIM for computing radiation damage exposure. *Nuclear Instruments and Methods in Physics Research B*, 310, pp.75–80.

Stupel, M.M., Bamberger, M. & WEiss, B.Z., 1985. Determination of Fe solubility in αZr by Mössbauer spectroscopy. *Scripta Metallurgica*, 19, pp.739–740.

Thompson, K. et al., 2007. In situ site-specific specimen preparation for atom probe tomography. *Ultramicroscopy*, 107(2-3), pp.131–9.

Tournadre, L. et al., 2012. Experimental study of the nucleation and growth of c-component loops under charged particle irradiations of recrystallized Zircaloy-4. *Journal of Nuclear Materials*, 425(1-3), pp.76–82.

Williams, D.B. & Carter, C.B., 2009a. Bremsstrahlung X-rays. In *Transmission Electron Microscopy: A Textbook for Materials Science*. Springer Science+Business Media, LLC, 223 Spring Street, New York, NY, 10013, USA, p. 60.

Williams, D.B. & Carter, C.B., 2009b. The cliff-lorimer ratio technique. In

Transmission Electron Microscopy: A Textbook for Materials Science. Springer Science+Business Media, LLC, 223 Spring Street, New York, NY, 10013, USA, p. 640.

Williams, D.B. & Carter, C.B., 2009c. Thickness determination. In *Transmission Electron Microscopy: A Textbook for Materials Science*. Springer Science+Business Media, LLC, 223 Spring Street, New York, NY, 10013, USA, pp. 352–354.

Williams, D.B. & Carter, C.B., 2009d. *Transmission Electron Microscopy: A Textbook for Materials Science* 2nd ed., Springer Science+Business Media, LLC, 223 Spring Street, New York, NY, 10013, USA.

Woo, O.T. et al., 2000. Corrosion of Electron-Irradiated Zr-2.5Nb and Zircaloy-2. *Zirconium in the Nuclear Industry: Twelfth International Symposium, ASTM STP 1354*.

Zou, H. et al., 1995. The solid solubility of Ni and Co in α-Zr: a secondary ion mass spectrometry study. *Journal of Nuclear Materials*, 223, pp.186–188.

4 MANUSCRIPTS

INTRODUCTION

The present work takes advantage of scanning transmission electron microscopy (STEM) and energy dispersive X-ray spectroscopy (EDS) analysis. The use of an aberration-corrected microscope has allowed a relatively high electron current of 600 pA in a sub-angstrom sized probe, such that we are able to create a high X-ray count rate in a total detection solid angle of 0.7 srad. This methodology has been employed in conjunction with knowledge of hcp α-Zr crystallography, such that on-axis spectral imaging may reveal details about orientation-dependent irradiation-induced defect structures and their evolution with dose.

The first manuscript is an analysis of second phase particle (SPP) and grain boundary evolution during proton and neutron irradiation. The Cliff-Lorimer method was employed, assuming no absorption or fluorescence, and as such the results are considered to be semi-quantitative. The SPPs undergo irradiation-induced dissolution and the grain boundaries deplete in solute. This results in an increase in solute content within the matrix. The effect of this matrix supersaturation on irradiation-induced dislocation loop evolution is then assessed in the second manuscript. Here, dislocation density is quantified and dislocation arrangement in the matrix is correlated with microchemical observations of crystallographic solute segregation. In the final manuscript, the nature of the segregation is analysed in more detail to reveal trends in stoichiometry that suggest the irradiation-induced precipitation of new phases. This was accomplished by comparing the result of STEM-EDS and atom probe tomography (APT), which provide both parallel and complimentary information.

The present author conducted the proton irradiation experiments at the Michigan Ion Beam Laboratory (MIBL) with the aid of Matthew Topping and Thomas

Seymour. The present author performed the sample preparation (UoM), the electron microscopy and the subsequent data analysis (UoM) that comprises the majority of this work. Daniel Jädernäs at Studsvik Nuclear AB, in conjunction with Westinghouse electric company, performed the conventional TEM dislocation analysis of the neutron-irradiated samples, although the present author performed all STEM-EDS analysis of the active material at UoM. The present author and Prasath Babu Revathy Rajan performed all APT sample preparation at UoM but Charles Hirst, Tomas Martin and Michael Moody at The University of Oxford performed all APT experiments on their Local Electrode Atom Probe (LEAP) Cameca - 3000X. The Oxford team also performed all of the tomographic reconstruction of the APT needles in addition to some crystallographic analysis of the APT data, but the present author and Prasath Babu Revathy Rajan conducted all APT data analysis in terms of assessing the composition and morphology of the irradiation-induced precipitates. The present author wrote all three manuscripts presented here with the aid of essential comments and suggestions from Prasath Babu Revathy Rajan, Christopher Race, Philipp Frankel and Michael Preuss. Helpful discussions were had with Sarah Haigh, Mhairi Gass, Matthew Topping, Thomas Seymour and Maria Yankova.

4.1 MANUSCRIPT 1: A COMPARISON OF PROTON AND NEUTRON IRRADIATION-INDUCED MICROCHEMICAL EVOLUTION IN ZIRCALOY-2

Submission: The following anuscript will be submitted to *Acta Materialia* or *The Journal of Nuclear Materials*

Contribution: The present author wrote this manuscript and performed all of the chemical analysis in the proton- and the neutron-irradiated material, as well as the interpretation and discussion of all results. Daniel Jädernas prepared the neutron-irradiated material for microscopy as part of collaboration with Studsvik Nuclear AB. Philipp Frankel and Michael Preuss provided supervisory support and contributed helpful corrections to the main body of the text. Javier Romero, Lars Hallstadius and Edward C. Darby are industrial collaborators and contributed to the present work by provision of material and insightful discussion.

A COMPARISON OF PROTON AND NEUTRON IRRADIATION-INDUCED MICROCHEMICAL EVOLUTION IN ZIRCALOY-2

A. Harte[1], D. Jädernäs[2], P. Frankel[1], J. Romero[3], L. Hallstadius[4], E. C. Darby[5],M.Preuss[1].

[1]The University of Manchester, Manchester Materials Science Centre, Grosvenor Street, Manchester, M13 9PL, United Kingdom

[2]Studsvik Nuclear AB, SE 611 82 Nyköping, Sweden

[3]Westinghouse Electric Company, Columbia, SC, United States

[4]Westinghouse Electric Sweden AB, SE---72163 Västerås, Sweden

[5]Rolls Royce Plc., Nuclear Materials, Derby, UK

Contact: Allan Harte, allan.harte@manchester.ac.uk

1 ABSTRACT

Zircaloy-2 plate irradiated with 2 MeV protons at ~6.7 x10^{-6} dpa s^{-1} and 350 °C to doses of 2.3, 4.7 and 7.0 dpa and Zircaloy-2 clad and channel material, irradiated in a BWR to neutron fluences between 14.5 and 24.5 dpa (8.7 and 14.7 x10^{25} n m^{-2}) are compared in terms of the microchemical evolution within second phase particles (SPPs) $Zr(Fe,Cr)_2$ and $Zr_2(Fe,Ni)$ and at α-Zr grain boundaries. This is accomplished through high spatial resolution scanning transmission electron microscopy and the use of energy-dispersive X-ray spectroscopic methods of excellent detection capability. Fe-depletion is observed from both SPP types after irradiation with both irradiative species, but is predominantly from the edge region in the case of $Zr(Fe,Cr)_2$ and from almost homogeneously within the whole $Zr_2(Fe,Ni)$ SPP. Further, there is evidence of a delay in the dissolution of the $Zr_2(Fe,Ni)$ SPP with respect to the $Zr(Fe,Cr)_2$. Segregation of Fe and Ni to grain boundaries is observed prior to irradiation. After both, proton and neutron irradiation, Fe and Ni deplete from the grain boundaries, while Sn segregates there. As such, both SPP and grain boundary evolution result in matrix supersaturation with solute and proton irradiation is considered well suited to emulate the effects of neutron irradiation in this context. The mechanisms of solute

redistribution processes from SPPs and grain boundaries and the consequences for irradiation-induced growth phenomena are discussed.

2 INTRODUCTION

The use of Zr alloys as the cladding and structural components of nuclear reactor cores is widespread due to their low average neutron absorption cross section and their retention of mechanical properties and corrosion resistance at operating temperatures (Hallstadius et al. 2012). Due to their limited solubility in hcp α-Zr (Stupel et al. 1985; Charquet et al. 1988; Zou et al. 1995), the common alloying elements Fe, Cr and Ni precipitate as thermodynamically stable second phase particles (SPPs) in both the matrix and at grain boundaries (Kuwae et al. 1983; Yang et al. 1986; Griffiths, R.W. Gilbert, et al. 1987; Zou et al. 1994). In Zircaloy-2, the major intermetallic secondary phases are $Zr(Fe,Cr)_2$ and $Zr_2(Fe,Ni)$ with size ranges 20-170 nm for Fe-Cr SPPs and 30-650 nm for Fe-Ni SPPs (Goll & Ray 2002). While Zr-Fe binary SPP intermetallics are sometimes observed in Zircaloy-4 when the alloy composition is Fe/Cr > 4 (Charquet et al. 1988) and zirconium silicides, phosphides and zirconium copper sulphides have been observed in Zircaloy-2 (Yang et al. 1986; Meng & Northwood 1989), their number densities are low by comparison to the $Zr(Fe,Cr)_2$ and $Zr_2(Fe,Ni)$ SPPs and so will not be considered explicitly here. As the stoichiometry of the SPPs is variable after irradiation, the $Zr(Fe,Cr)_2$ and $Zr_2(Fe,Ni)$ SPPs will hereafter be referred to as Fe-Cr type and Fe-Ni type, respectively. The nature and morphology of SPPs have been shown to be the principal factor affecting in-reactor corrosion of the Zircaloys (Garzarolli et al. 1994). Better corrosion resistance, and hence reduced hydrogen ingress, has recently been shown to correlate with decreased growth strain (Valizadeh et al. 2014), a macroscopic deformation process that is characterised by axial expansion and radial contraction of cladding tube and is understood as an excess of interstitials in prismatic planes and vacancies in basal planes as a result of the diffusional anisotropy of irradiation-induced point defects in hcp systems (Buckley 1961; Woo & Göslel 1983; Woo 1987; Woo 1988; Holt 1988). The evolution of intermetallic phases under irradiation is of importance to the system as a whole, as mechanical behaviour and corrosion properties are intrinsically dependent on

microstructural features. A comparison of irradiation-induced growth strain at a given fluence in the binary system Zr-1.5Sn (wt.%) at 280 °C (Zee et al. 1984) as compared with that of Zircaloy-2 at ~290 °C (Holt & Gilbert 1986) shows that the latter, in which the dominant microstructural difference is the presence of SPPs, demonstrates a reduced growth strain in comparison to the Zr-1.5Sn (wt.%) alloy. As such, the behaviour of secondary phases under irradiation in different alloy systems is of interest, as are systematic studies that make use of electron, proton and heavy ion irradiation to better understand the mechanisms of SPP evolution and their effect on microstructural features such as the density of c-component dislocations (c-loops) that is correlated to accelerated irradiation-induced growth strain (Holt & Gilbert 1986; Griffiths et al. 1989). For instance, a higher c-loop density (Burgers vector 1/6<20-23>, aligned parallel to the trace of the basal plane (Jostsons et al. 1977; Griffiths 1988)) has been observed in the vicinity of partially dissolved Fe-Cr SPPs in neutron-irradiated Zircaloy-4 in the temperature range ~290-310 °C and proton-irradiated Zircaloy-4 at 350 °C (Griffiths & Gilbert 1987; Tournadre et al. 2012; de Carlan et al. 1996). As such, Fe is generally thought to have the effect of stabilising the nucleation of the invariably vacancy c-loops, likely through an elastic interstitial (Fe)-vacancy interaction or through stable, crystallographic Fe-vacancy pairing (de Carlan et al. 1996).

While chemical segregation to grain boundaries in Zr alloys has been suggested for some time due to the observation of SPP morphology as elongated along the boundary (Griffiths, R.W. Gilbert, et al. 1987) and the precipitation at grain boundaries either during irradiation or post-irradiation annealing (Griffiths, R.W. Gilbert, et al. 1987; Yang 1988; Gilbon & Simonot 1994), direct observations of continuous grain boundary segregation have not been made until more recently. Such observations have predominantly been achieved by way of atom probe tomography (Hudson & Smith 2009; Gault et al. 2013; Dong et al. 2013; Sundell et al. n.d.) but some segregation has also been observed via energy-dispersive X-ray spectroscopy (EDS) in the (scanning) transmission electron microscope (STEM) after neutron irradiation in Zircaloy-2 (Cockeram et al. 2013). As may be expected, the effect of grain size on irradiation-induced growth strain is inversely proportional (Fidleris 1988), with small-grained Zr (~5 μm) experiencing higher

growth strains than large-grained Zr (~40 and up to 225 μm), this effect increasing with temperature (Griffiths et al. 1989). The effect of grain boundary area as a sink for point defects and their clusters is scarcely reported in the literature, although the orientation of a grain boundary with respect to a defect's preferred diffusion path is included in current theories of irradiation-induced growth mechanisms (Woo 2000). As such, the evolution of grain boundaries during irradiation and any associated microchemical changes are essential to gaining an understanding of the effects of alloying elements on macroscopic deformation phenomena.

The aim of the present work is to assess the microchemical evolution in Zircaloy-2 after both proton and neutron irradiation by taking advantage of new developments in STEM-EDS. Further, correlations and differences will be highlighted between the effects of the different irradiative species in regards to the irradiation-induced changes within SPPs and grain boundaries. As the two main observations in the present work are of irradiation-induced SPP dissolution and the depletion of alloying elements from the grain boundary, it was deemed appropriate to group such observations together in a single publication as to describe the gradual supersaturation of the matrix with solute.

3 EXPERIMENTAL

3.1 MATERIAL

The material under investigation is Zircaloy-2, nominally Zr-1.5Sn-1.4Fe-0.1Cr-0.06Ni (wt.%) (Hallstadius et al. 2012), supplied by Westinghouse Electric Company. The non-irradiated material was fully recrystallised plate with equiaxed grains of ~5-15 μm diameter and a strong basal texture in the normal direction, split ± 30° in the transverse direction. The plate was cut into bars of dimensions 2 x 2 x 20 mm and mechanically polished from the normal direction to a quality typical for electron backscatter diffraction such that the flat surface provides a uniform proton penetration depth. The bars were then proton-irradiated from the normal direction at the Michigan Ion Beam Laboratory's 1.7 MeV Tandertron accelerator facility at 2 MeV and 350 ±9 °C to doses of 2.3, 4.7 and 7.0 displacements per atom (dpa) at a current of ~0.2 μA mm^{-2}, resulting in a damage

rate ~6.7 x10^{-6} dpa s^{-1}. The proton irradiation dose (dpa) level was calculated at 60% of the maximum proton penetration depth (max 30 μm), calculated by the quick Kinchin-Pease calculation in SRIM as recommended by Stoller et al. (Stoller et al. 2013). As such, TEM foils were prepared for examination at this depth by carefully grinding from the non-irradiated face to a thickness of ~160 μm and then electropolishing using a twin-jet Tenupol-5 electropolisher together with a Julabo FP50 cooling unit. An electrolyte of 10% perchloric acid and 20% 2-butoxyethanol in ethanol (Tournadre et al. 2012) was used to electropolish ~12-15 μm from both the irradiated and non-irradiated faces. Then, Elektron Technology's acid-resistant Lacomit varnish was used to protect the irradiated face while electropolishing to perforation from the non-irradiated face. The non-irradiated bulk material was prepared by the same method.

The neutron-irradiated material was supplied by Westinghouse and Studsvik in the form of electropolished TEM foils which were previously studied to investigate SPP chemical evolution (Valizadeh et al. 2014). These are studied in the present work for a direct comparison to the proton-irradiated material. These samples were prepared from cladding and channel material of a BWR (280-330 °C (Azevedo 2011)), irradiated to neutron fluences between 8.7 and 14.7 x10^{25} n m^{-2}. Assuming a conversion between neutron fluence and dpa of 0.6 x10^{25} n m^{-2} dpa^{-1} (Shishov et al. 2005), such fluence values correspond to the range 14.5 to 24.5 dpa. Assuming the damage rate in light water reactors to be ~6-1 x10^{17} n m^{-2} s^{-1} (Griffiths et al. 1996; Shishov et al. 2005; Adamson 2014), the BWR damage rate is ~1 x10^{-7} dpa s^{-1}. As such, the proton irradiations in the present work incurred a damage rate higher than that of the neutron-irradiated material by a factor of ~70. To allow more diffusion to occur under such a high damage rate, a temperature shift (Was 2007) of 40 °C was applied to the proton irradiation experiment, which was performed at 350 °C as opposed to the range 280-330 °C in a BWR.

3.2 MICROSCOPIC ANALYSIS

All microscopy in the present work was performed on a G2 80-200 kV spherical aberration-corrected (single, probe) FEI Titan microscope operating at 200 kV in

scanning mode with a current of 0.6 nA. The microscope is equipped with a high brightness X-FEG electron gun and the FEI ChemiSTEM™ system, comprising four energy-dispersive X-ray (EDS) detectors in close proximity to the sample, resulting in a maximum collection angle of 0.7 srad. While the sample was loaded in a low-background double-tilt holder, the determination of chemistry may be considered to be semi-quantitative as the Cliff-Lorimer approach was used with calculated K-factors, assuming no absorption and not accounting for Fe-scattering from the pole piece. All chemical data was obtained by spectral imaging (a full spectrum up to 20 keV at every pixel), after which chemical maps were extracted for the relevant alloying elements.

Second phase particles (SPPs) were analysed for their chemical content at magnifications high enough to produce a bright-field STEM image in which the SPP constituted ~75% of the image (between 320k x and 640k x). The semi-quantification of SPP chemistry was consistently obtained from low symmetry orientations to avoid electron-channelling phenomena. The semi-quantification was performed within the FEI ESPRIT software. While it has been shown that it is necessary to subtract a blank background emitting radiation from the neutron-irradiated ZIRLO™ (Francis et al. 2014), the Zircaloy-2 studied here was of low enough activity for this to be unnecessary. It was important to obtain spectral images from high symmetry orientations in order to observe crystallographic nano-clustering in the matrix. Fe/X (X = Cr, Ni, depending on SPP type) atomic ratio maps were obtained by quantifying the spectral image in terms of atomic per cent and dividing the Fe concentration within a pixel by the concentration of alloying element X, assuming that the concentration of Zr + Sn + Fe + Cr + Ni = 100% and, as such, ignoring the detection of impurity elements or thin foil surface oxide. The Fe/X ratio maps were calculated after averaging 4 x 4 pixels, such that the spatial resolution is a quarter that of the original spectral image. All data for semi-quantification were obtained for at least 30 minutes at an X-ray detection rate of ~20 kcps to allow significant pixel intensity to reduce error in measurement to that within the calculated *k*-factor (~ ±10%). The average composition of an SPP was obtained by selecting all pixels containing concentration above background (> ~1 at.%).

Grain boundaries were analysed for their chemical content by carefully tilting the sample such that the boundary plane is parallel to the electron beam direction. Such a condition was recognised by a thin (~2 nm) dark line in the bright field and corresponding bright line in the high-angle annular dark field STEM image. Semi-quantification of chemistry was performed in a similar manner to that of the SPPs. A straight section of the boundary was necessary to observe continuous segregation and to extract meaningful line scans from the spectral image. As such, a magnification of 450k x was used for all grain boundary data acquisition.

4 RESULTS

4.1 SPP DISSOLUTION

Low magnification spectral imaging provides a useful diagnostic tool for identifying areas of interest, as small regions of chemical segregation are commonly overlooked by traditional bright field imaging methods where irradiation-induced dislocation strain in the matrix can cause second phase particle (SPP) contrast to be masked. An overview of SPPs in a typical sample of non-irradiated Zircaloy-2 is provided in Figure 4.1.1, in which the dark central grain has its surface normal parallel to the $<11\bar{2}0>$ direction. The chemical maps for Zr, Sn, Fe, Cr and Ni are also displayed. The different size and number densities observed for Fe-Cr and Fe-Ni type SPPs are immediately obvious, the latter being larger and in fewer number. There is no obvious relationship between SPP shape and matrix orientation when spectral imaging is performed from the $<11\bar{2}0>$ and <0001> matrix orientations, only the former of which is shown here. The benefit of using Bright-Field Scanning TEM (BF-STEM) can be seen from Figure 4.1.1a, in which detail of the microstructure can be observed from a high-symmetry low-index zone axis. This is inconceivable in conventional TEM, in which the large degree of diffraction contrast prevents meaningful images of SPPs and crystallographic segregation being obtained. As STEM uses a convergent beam, any contrast arising from bending or local strain due to SPPs, hydrides or oxides is avoided as the high convergence angle samples many diffraction conditions, reducing contrast in regions of relatively low strain. Electropolishing-induced

hydrides can be seen nucleating parallel to the basal plane (vertically) in Figure 4.1.1a, highlighted by depletions in contrast within the Zr map. Interestingly, by comparison of the BF image and the Cr and Ni maps it may be that electropolishing-induced hydrides nucleate preferentially at the alpha-Zr grain boundaries and at the Fe-Ni SPP-matrix interfacial region, but rarely at the Fe-Cr SPP-matrix interfacial region.

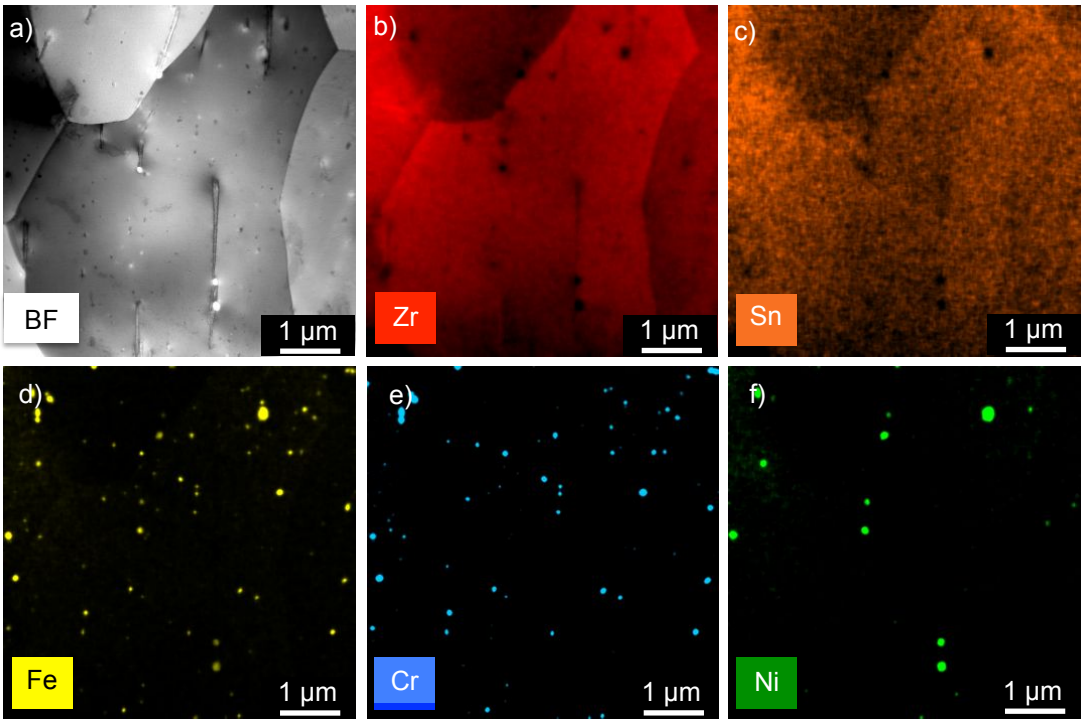

Figure 4.1.1 The central grain shown in the BF STEM image of a) is at the $<11\bar{2}0>$ orientation, the $<1\bar{1}00>$ direction vertical and the <0001> horizontal. The corresponding chemical maps are shown for Zr, Sn, Fe, Cr and Ni in b)-f), respectively. Each chemical map is displayed in raw counts and is individually scaled with no background subtraction.

A higher magnification (320kx) BF-STEM image of a typical Fe-Cr SPP in non-irradiated Zircaloy-2 is shown in Figure 4.1.2 together with the relevant chemical maps. The maps are quantified in terms of atomic per cent (at.%) and are plotted on individual colour scales to reveal various details. For instance, the Zr map indicates the projected shape of the SPP in the third spatial dimension, a detail usually lost in transmission techniques without tomographic reconstruction. The Sn map also reflects the SPP shape but levels of Sn should only be considered

qualitative due to the absorption of the low energy Sn L_α X-ray. Interestingly, the Fe and Cr maps demonstrate spatial differences in their distribution, even before irradiation. A small amount of Ni was detected in all non-irradiated Fe-Cr SPPs studied. In Figure 4.1.2f, the location of the Ni is coincident with the region of higher Fe concentration relative to Cr.

In a similar manner to that in Figure 4.1.2, Figure 4.1.3 provides a BF-STEM image and the relevant chemical maps for a typical Fe-Ni SPP in non-irradiated Zircaloy-2. No Cr was detected within any of the Fe-Ni SPPs studied. Furthermore, the regions of highest concentration in Fe and Ni seem to be coincident.

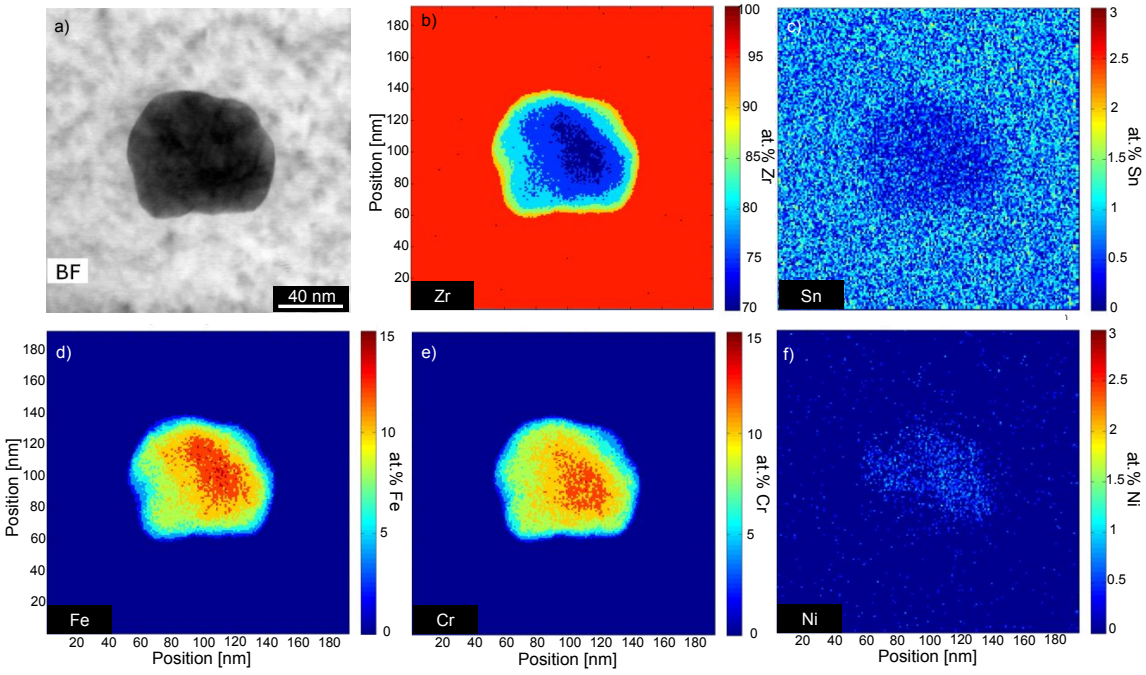

Figure 4.1.2 A single Fe-Cr Laves phase SPP in non-irradiated Zircaloy-2 is displayed in terms of its chemistry, each chemical map having its own colour scale indicating atomic per cent (at.%) concentration. The BF STEM image is shown in a). The Zr, Sn, Fe, Cr and Ni maps are shown in b)-f), respectively.

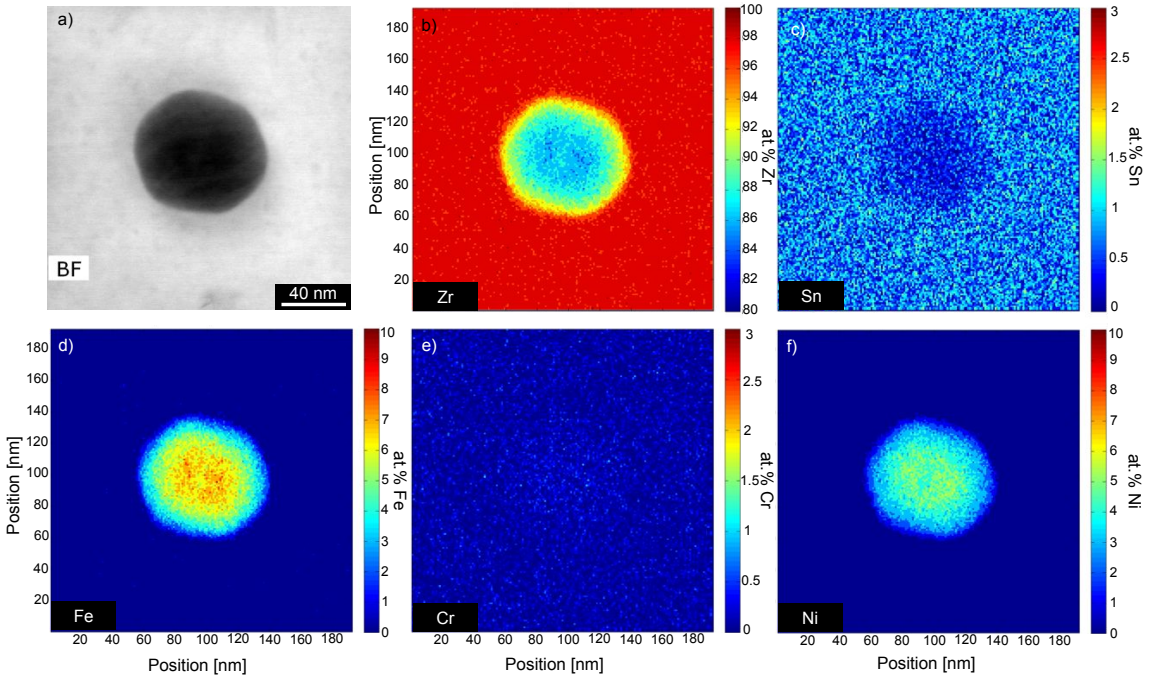

Figure 4.1.3 A single Fe-Ni SPP in non-irradiated Zircaloy-2 is displayed in terms of its chemistry, each chemical map having its own colour scale indicating atomic per cent (at.%) concentration. The BF STEM image is shown in a). The Zr, Sn, Fe, Cr and Ni maps are shown in b)-f), respectively.

To more easily compare Fe and Cr distributions within Fe-Cr SPPs, Fe/Cr maps were calculated such that the Fe or Cr content in a pixel must be ≥ 1 at.% for the Fe/Cr ratio to be displayed. The Fe/Cr ratio maps in Figure 4.1.4a-d, show a change in the distribution of Fe relative to Cr in the non-irradiated state and after proton-irradiation to 2.3, 4.7 and 7.0 dpa, respectively. The reader should note that the colour scale has been adjusted for the different SPPs to highlight details, such that in Figure 4.1.4a it is Fe/Cr range 0-1.5 and in Figure 4.1.4b-d 0-1. A core-edge structure is formed in the Fe-Cr SPPs during proton irradiation. The initial development of this can be seen in Figure 4.1.4b, which increases in clarity at the higher dose levels. Line scans quantified in terms of at.% are shown in Figure 4.1.4f-h which indicate that this edge region occurs due to a decrease in the Fe content relative to the Cr. All Fe-Cr SPPs at all proton dose levels were fully crystalline and no amorphisation was observed in the Fe-depleted edge regions. Further, no observation was made to suggest any crystallographic preference for dissolution within the Fe-Cr SPP.

In a similar manner to that in Figure 4.1.4, Figure 4.1.5 demonstrates typical Fe/Ni ratio maps for the Fe-Ni type SPP after proton-irradiation to 0, 2.3, 4.7 and 7.0 dpa. Unlike the Fe-Cr type SPPs, the Fe-Ni type does not show a clear edge-core structure, although the very periphery does seem to have a higher Fe/Ni ratio than the rest of the SPP. Note that at 2.3 dpa, the Fe/Ni ratio within the core of the SPP is close to 1 and the peak in Fe/Ni at the SPP periphery approaches 2. The shape of the Fe-Ni SPPs becomes irregular after proton irradiation to 4.7 dpa. Interestingly, after proton irradiation to 7.0 dpa a channel of Fe/Ni ~1 is observed close to the edge of the SPP, while most of the inner part of this SPP has a much lower ratio (Figure 4.1.5d). All Fe-Ni SPPs at all doses in the proton-irradiated material were fully crystalline and no observation was made to suggest any crystallographic preference for dissolution within the Fe-Ni SPP. It is interesting to note that the Fe-Ni SPP is observed as irregular in shape after proton irradiation to 4.7 dpa, continued at 7.0 dpa, but the Fe-Cr SPP is not. This was found to be typical for the respective SPP types.

The data in Figure 4.1.6 presents a summary of the maps in Figure 4.1.4a-d and Figure 4.1.5a-d on the same spatial and Fe/X (X = Cr, Ni) scales. The figure contains the eight histograms of the Fe/X ratios in the previous two figures, which have each been plotted as a line graphic for a greater ease of comparison, binned in Fe/X increments of 0.05. The evolution towards a bimodality of the Fe/Cr ratio is clear from this data, as is the lack of such a feature in the Fe/Ni ratio. The Fe/Cr bimodality values remain almost the same between 4.7 and 7.0 dpa.

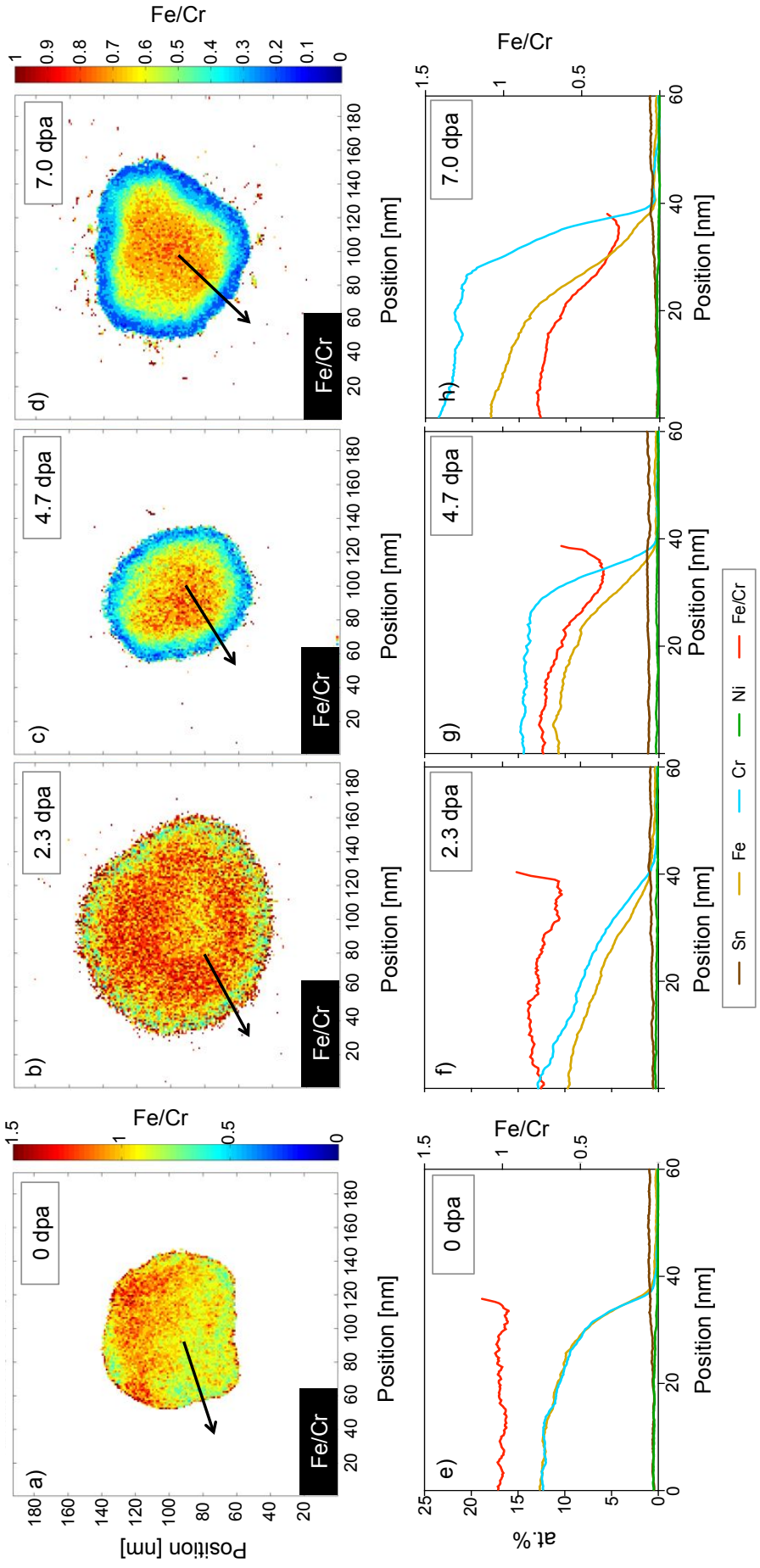

Figure 4.1.4 The Fe/Cr ratio maps for four typical Fe-Cr SPPs, each taken from samples with increasing proton dose levels, are displayed from a) at 0 dpa (from **Figure 4.1.2**) to b) 2.3, c) 4.7 and d) 7.0 dpa. Each map is of the same spatial scale but the atomic ratio scale is different to reveal details; a) is at 0-1.5 (shown right of a)) and b)-d) are at 0-1 (shown right of d)). Line scans are displayed in e)-h) that correspond to the arrows in a)-d), respectively, averaged over 20 nm perpendicular to the arrow (i.e. ±10 nm either side of the arrow).

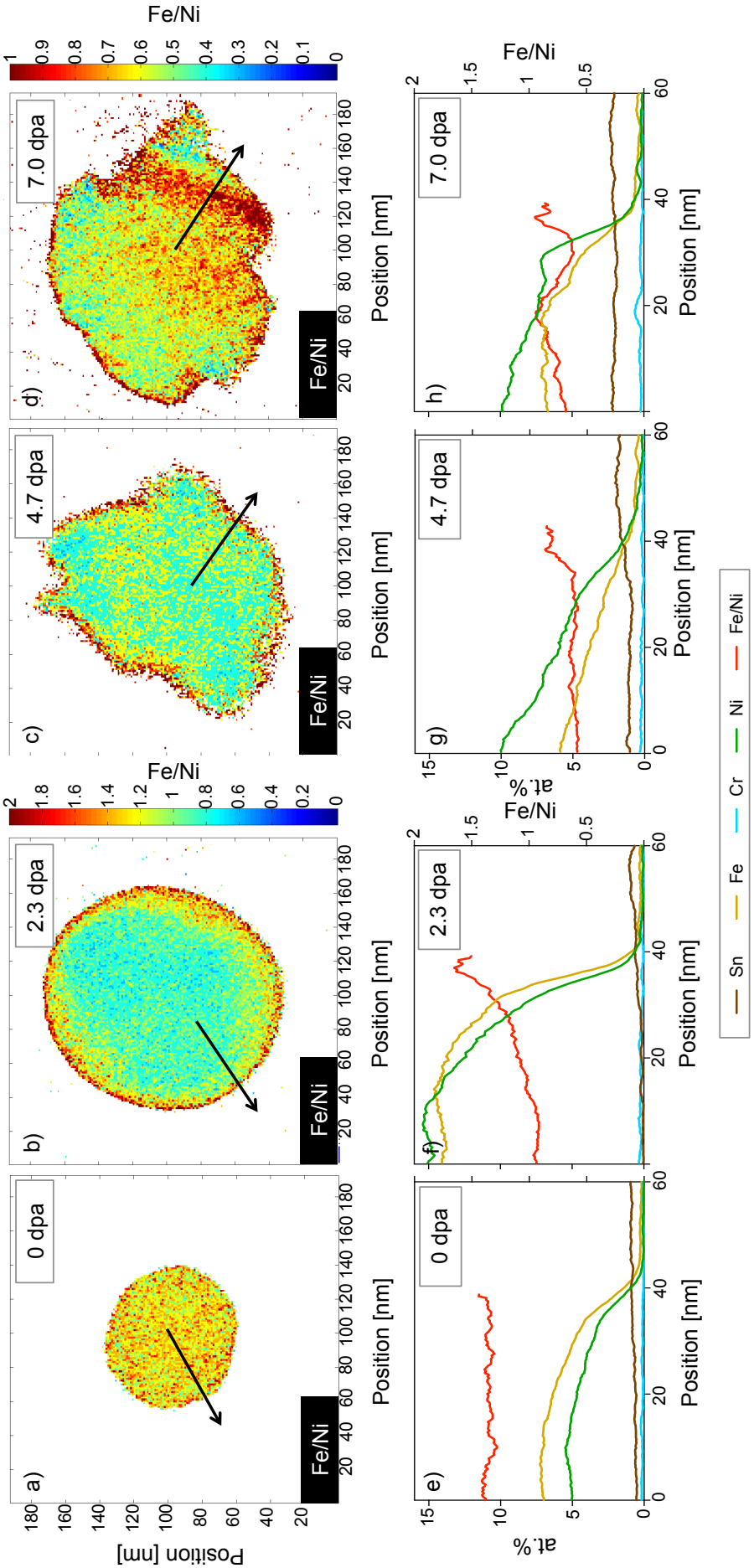

Figure 4.1.5 The Fe/Ni ratio maps for four typical Fe-Ni SPPs are displayed at increasing proton dose levels from a) 0 (from **Figure 4.1.3**) to b) 2.3, c) 4.7 and d) 7.0 dpa. Each map is of the same spatial scale but the atomic ratio scale is different to reveal details; a) and b) are 0-2 (shown right of b)) and c) and d) are 0-1 (shown right of d)). Line scans are displayed at the bottom of the figure that correspond to the arrows in a)-d), averaged over 20 nm perpendicular to the arrow (i.e. ±10 nm either side of the arrow).

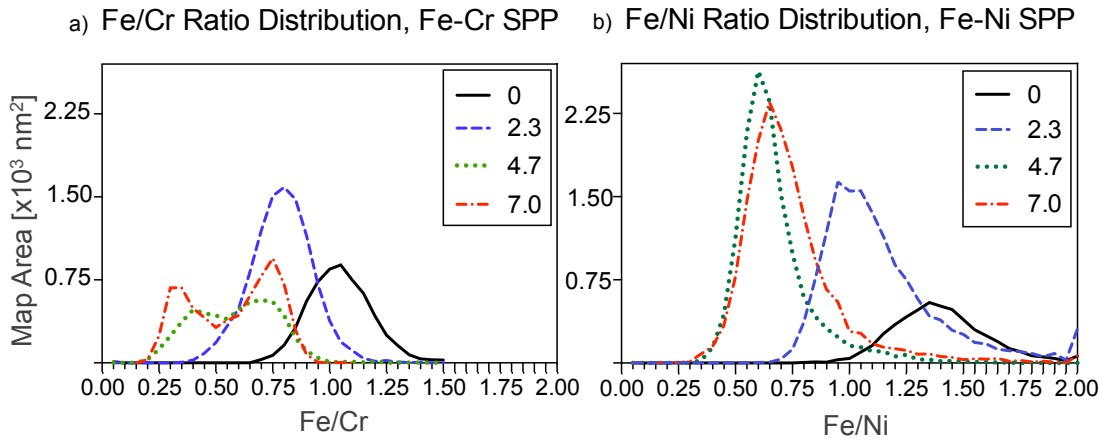

Figure 4.1.6 A histogram of the area in **Figure 4.1.4** a)-d) and **Figure 4.1.5** a)-d), displayed in a) and b), respectively to act as a summary of those previous figures. The histograms are displayed as a line graphic for ease of comparison, binned in Fe/X (X = Cr, Ni) increments of 0.05, corresponding to 0, 2.3, 4.7 and 7.0 dpa. The differences in the area under each curve are due to differences in SPP size. A bimodal distribution is evident in the Fe-Cr system and not in the Fe-Ni.

A similar analysis has been performed for the neutron-irradiated material, but the semi-quantification performed for the proton-irradiated material proved unsuitable in this case due to the higher dose of the material (> 8.7 x10^{25} n m^{-2} ~ 14.5 dpa) and the correspondingly lower concentration of alloying elements within SPPs. Alternatively, Figure 4.1.7 displays a partially dissolved SPP with both Fe-Cr and Fe-Ni regions in Zircaloy-2, neutron-irradiated to the highest fluence in this study, 14.7 x10^{25} n m^{-2} ~24.5 dpa. The figure shows the BF STEM image from the $<11\bar{2}0>$ direction in Figure 4.1.7a and the Zr, Sn, Fe, Cr and Ni maps in parts b-f, respectively, as images displaying X-ray counts, individually scaled without background subtraction. The BF STEM image in Figure 4.1.7a shows c-component dislocation loops (c-loops) lying parallel to the trace of the basal plane (horizontal). While the SPP shape is difficult to discern from the BF STEM image due to the c-loop strain contrast, the chemical maps reveal the SPP shape clearly. The Fe-Ni SPP is of an irregular shape, whilst the Fe-Cr SPP retains spheroidal character but with uneven peripheries. Some alignment of Sn, Fe, Cr and Ni can be seen parallel to the trace of the basal plane in the matrix, but this is more evident for Cr in close proximity to the SPP (Figure 4.1.7e), where segregation to c-loop positions is observed. While the Sn map demonstrates depletion in a region larger

than the size of the dissolving SPP, the Zr map is almost perfectly anti-correlated with the sum of the Fe, Cr and Ni maps.

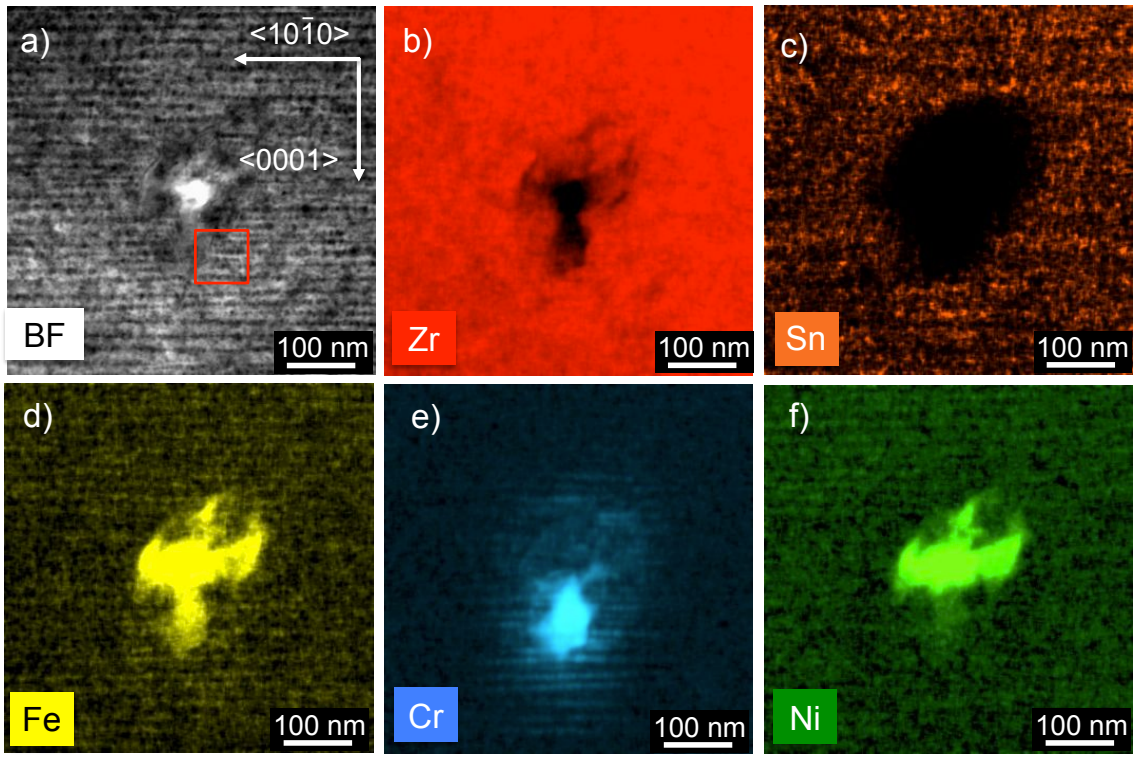

Figure 4.1.7 The BF STEM image and Zr, Sn, Fe, Cr and Ni chemical maps are displayed in a)-f), receptively for an dissolving SPP with both Fe-Cr and Fe-Ni SPP regions, irradiated in a BWR clad to a fluence of 14.7 x1025 n m-2 ~24.5 dpa. The grain is orientated in the $<11\bar{2}0>$ matrix orientation with the basal plane horizontal. Segregation parallel to basal planes is evident for Fe, Cr, and, less so, Ni and Sn. The red box indicates the region for higher magnification chemical mapping in **Figure 4.1.8**.

A quantification was attempted of the small region highlighted by the red square in Figure 4.1.7a so that an Fe/Cr map could be calculated. The raw images displaying X-ray counts, individually scaled without background subtraction, are presented in Figure 4.1.8a and b, in which the Fe and Cr maps are shown, respectively, and the quantified Fe/Cr atomic ratio map is given in Figure 4.1.8c. The segregation of Fe and Cr to the c-loops surrounding the SPP is discontinuous when observed from the $<11\bar{2}0>$ zone axis, forming what seems to be nano-clusters or nano-precipitates. As a crystallographic analysis was not performed on this segregation, it shall be referred to as nano-clustering. The Fe/Cr map demonstrates that both

the SPP and the nano-clustering close to the SPP are severely depleted in Fe relative to Cr. However, Cr does not extend far into the matrix and so the nano-clusters become depleted in Cr at a distance of 30-50 nm.

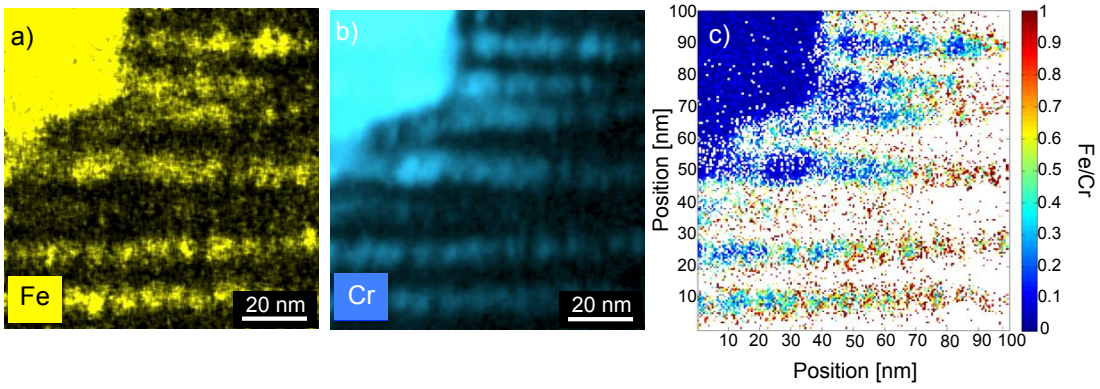

Figure 4.1.8 The Fe and Cr maps are shown in a) and b), respectively, for the region highlighted by a red square in **Figure 4.1.7**a at the same matrix orientation $<11\bar{2}0>$. Each chemical map is displayed in raw counts and is individually scaled. The chemical segregation to c-loops in the immediate vicinity of the dissolving Fe-Cr SPP is discontinuous. These maps were quantified in at.% and the atomic fraction Fe/Cr map in c) was calculated. Crystal vectors are parallel to those displayed in **Figure 4.1.7**.

Although quantification maps in the neutron-irradiated material demonstrated a lot of noise due to low concentrations in the transmission direction, obtaining the average concentration of all pixels with an alloying element concentration above background (> ~1 at.%) at high magnification after long counting times (> 30 minutes at 20 kcps) gave reliable Fe/X (X = Cr, Ni) ratios. This was accomplished for both proton- and neutron-irradiated material by selecting all pixels corresponding to Fe, Cr or Ni concentrations above background (> ~1 at.%). The variation in the Fe/X atomic ratio with increasing proton and neutron dose can be seen in Figure 4.1.9a and b, in which the individual SPPs are shown to display the scatter in the data. In total, 97 Fe-Cr SPPs and 64 Fe-Ni SPPs were analysed in this way. There is a general decrease in the Fe/Cr ratio with increasing proton dose, the mean values for which are given in Table 1. This decreasing trend is continued in the higher dose neutron-irradiated SPPs. In a similar manner to the Fe/Cr data, Figure 4.1.9b displays a general decrease in Fe/Ni ratio with increasing proton and

neutron dose. However, the trend is not continuous between the proton- and neutron-irradiated material as in the Fe/Cr. The mean Fe/Ni ratios for the various proton and neutron dose levels are also given in Table 1.

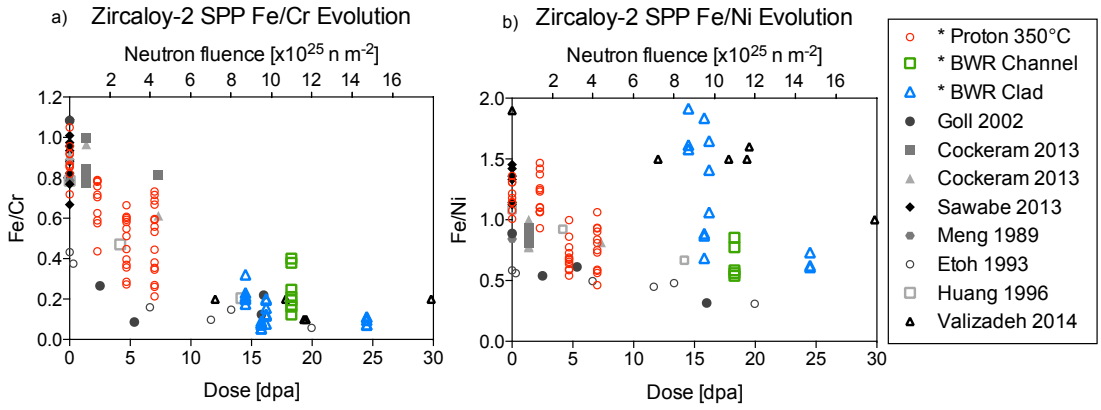

Figure 4.1.9 The variation with irradiation dose in the Fe/Cr and the Fe/Ni ratio for Fe-Cr and Fe-Ni SPPs is shown in a) and b), respectively, with '*' indicating the present study. All literature values are taken from BWR-irradiated Zircaloy-2 with the exception of Cockeram 2013 from a test HFIR reactor. Literature values were obtained by STEM EDS by (Goll & Ray 2002), (Cockeram et al. 2013) for a-annealed and b-treated material as squares and triangles, respectively, (Meng & Northwood 1989), (Etoh & Shimada 1993), (Huang et al. 1996) and (Valizadeh et al. 2014) , and analysis by atom probe tomography by (Sawabe et al. 2013).

Table 1 The mean Fe/Cr and Fe/Ni atomic ratios for Fe-Cr and Fe-Ni SPPs after proton irradiation between 2.3 and 7.0 dpa at 350 °C and for neutron irradiation between ~14.5 and ~24.5 dpa (8.7 to 14.7 x10^{25} n m^{-2}) in a BWR. The error given is a single standard deviation from the mean. The number in parentheses is the number of SPPs studied.

Dose [dpa]	Mean Fe/Cr		Mean Fe/Ni	
0	0.86 ± 0.07	(8)	1.19 ± 0.12	(9)
2.3	0.68 ± 0.01	(10)	1.19 ± 0.17	(12)
4.7	0.48 ± 0.13	(13)	0.70 ± 0.13	(12)
7.0	0.49 ± 0.18	(15)	0.76 ± 0.18	(12)
14.5	0.22 ± 0.05	(6)	1.70 ± 0.18	(3)
15.8	0.07 ± 0.01	(6)	1.07 ± 0.52	(4)
16.2	0.14 ± 0.04	(13)	1.55 ± 0.42	(4)
18.3	0.24 ± 0.10	(16)	0.66 ± 0.14	(5)
24.5	0.09 ± 0.02	(10)	0.65 ± 0.07	(3)

There is considerable scatter in the measurements presented here for Fe/Cr and Fe/Ni in the proton-irradiated Zircaloy-2 plate, although most measurements agree with the neutron-irradiated measurements from the literature included in Figure 4.1.9 for the low fluence levels. All literature data points are from Zircaloy-2 irradiated in a BWR at nominally ~300 °C with the exception of those from Cockeram et al., which were irradiated in neutron test reactor HFIR at ~358 °C (Cockeram et al. 2013). First we will consider the Fe-Cr system. The scatter in the Fe/Cr measurements may be explained by consideration of the size and chemistry of the Fe-depleted edge region of the Fe-Cr SPP and with reference to Figure 4.1.11. It can be seen from Figure 4.1.11a that the Fe/Cr in the edge region is positively correlated with the Fe/Cr in the core region of the SPP, and it can be seen from Figure 4.1.11b that the size of the edge region is positively correlated with the size of the whole SPP. With reference to Figure 4.1.11a, the ratio of (Fe/Cr edge) : (Fe/Cr core) is at 2.3 dpa ~ 1.01, at 4.7 dpa this ratio is equal to ~0.74 and at 7.0 dpa ~0.75. With reference to Figure 4.1.11b, the fraction of the edge width with respect to the whole SPP radius increases from ~0.42 at 2.3 dpa to ~0.49 at 4.7 dpa and ~0.73 at 7.0 dpa. In comparing Figure 4.1.11a and b, the most significant amount of Fe depletion occurs between 2.3 and 4.7 dpa but an acceleration in edge size occurs between 4.7 and 7.0 dpa. As there is variable SPP size in the non-irradiated material, the final Fe/Cr measured is scattered such that the largest SPPs at 7.0 dpa retain a large enough core region to give an average Fe/Cr similar to that observed in the non-irradiated state. The average effect is shown in Figure 4.1.11a and b, which display the Fe/Cr averaged over the whole SPP and its variation with the effective SPP radius, $r = (A/\pi)^{0.5}$, where A is the SPP area as determined by EDS spectral imaging. The mean Fe/Cr ratios in the core and edge regions are given in Table 2 in addition to the mean core and edge sizes at each proton dose level. While no variation in the Fe/Cr ratio was observed with SPP size in the non-irradiated material, the Fe/Cr in the core region alone is shown to increase with SPP size at all dose levels indicating that although Fe-depletion is occurring from the edge preferentially, there is some dissolution from the core region. In support of this, the decrease in the Fe/Cr ratio with respect to proton dose is larger in the edge region than in the core. This effect is smaller as the SPP size increases. Unfortunately, in the neutron-irradiated material, due to the higher

dose levels and consistently low Fe/Cr throughout the whole SPP, such an analysis with respect to SPP size was not possible.

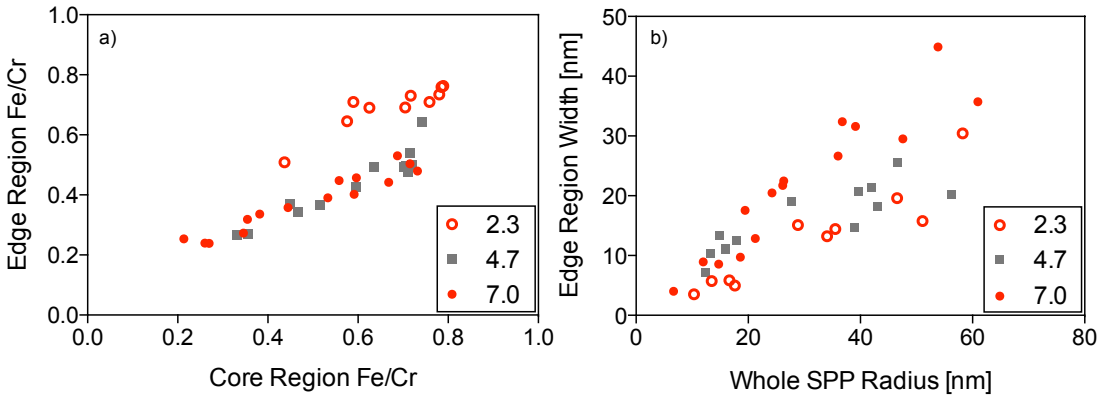

Figure 4.1.11 The relationship between the Fe/Cr atomic ratio in the core and edge regions of Fe-Cr SPPs at various proton dose levels in displayed in a) and the relationship between the width of the edge region and the radius of the whole Fe-Cr SPP at various proton dose levels is displayed in b).

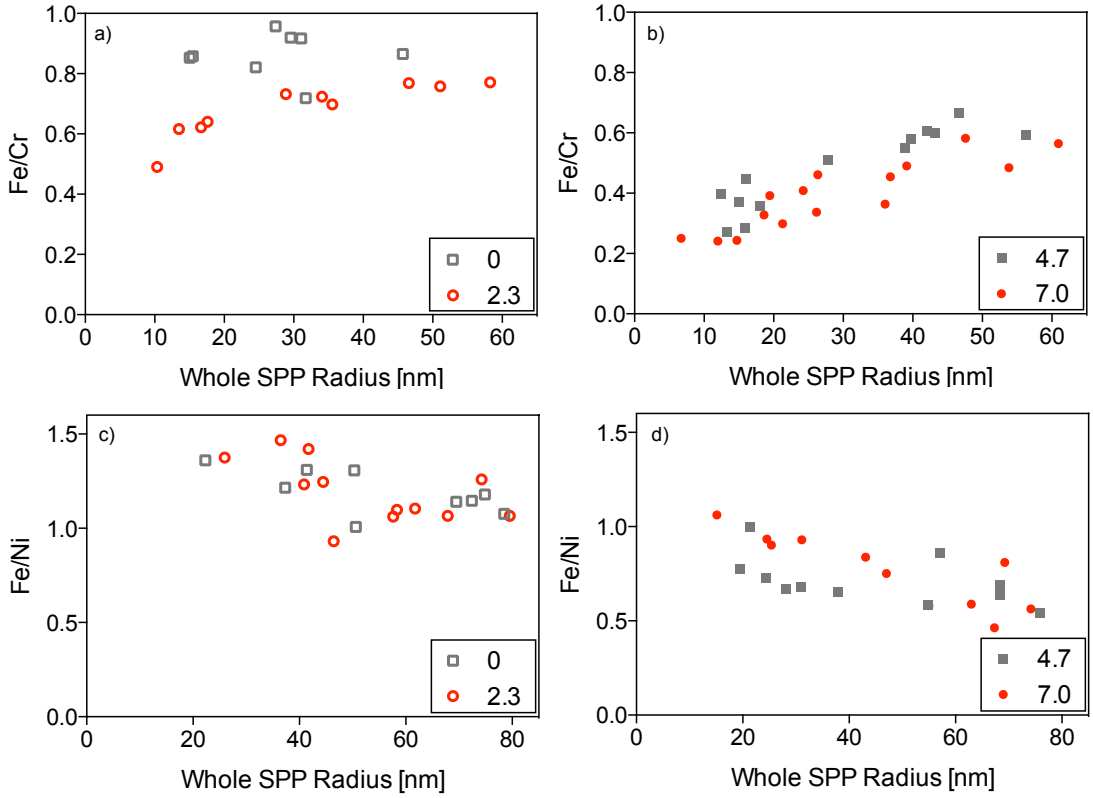

Figure 4.1.11 The scatter in Fe/X (X = Cr,Ni) determination is displayed for the proton data in relation to the effective radius of the whole SPP, $r = (A/\pi)^{0.5}$, where A is the area of the (rarely circular) SPP. The figure shows the Fe/Cr at a) 0 and 2.3 dpa, b) 4.7 and 7.0 dpa, and for Fe/Ni at c) 0 and 2.3 dpa and d) 4.7 and 7.0 dpa.

Table 2 The edge and core properties of Fe-Cr SPPs after proton irradiation to 2.3, 4.7 and 7.0 dpa are detailed with variation given as ± the standard deviation. The non-irradiated SPP has a mean Fe/Cr ratio of 0.86 ±0.07 with no edge structure. The edge radius varies linearly with the radius of the whole SPP and the relationship is given by the ratio Edge/Whole. The Decrease in Fe/Cr with respect to proton dose in larger in the edge region than in the core.

	Mean Radius		Fe/Cr Ratio		
Proton Dose [dpa]	Edge/Whole	Edge [nm]	Core/Edge	Core	Edge
2.3	0.42	13 ±8	~1	0.68 ±0.12	0.69 ±0.07
4.7	0.49	16 ±5	1.35	0.59 ±0.15	0.43 ±0.11
7.0	0.73	22 ±12	1.30	0.49 ±0.18	0.38 ±0.10

As no clear edge-core structure was observed for the Fe-Ni SPPs, such an analysis cannot be used to explain the scatter in the Fe/Ni measurements displayed in Figure 4.1.9. However, the Fe/Ni has been plotted as a function of the effective SPP radius in Figure 4.1.11c and d, where the radius $r = (A/\pi)^{0.5}$, where A is the SPP area as determined by EDS spectral imaging. Interestingly, all Fe-Ni SPPs at all proton dose levels show a similar decrease in the Fe/Ni atomic ratio with increasing SPP size.

4.2 GRAIN BOUNDARY EVOLUTION

In addition to studying the chemical evolution of SPPs with proton and neutron dose level, a similar analysis was also carried out at grain boundaries for the non-irradiated, 7.0 dpa proton and ~15.8 dpa (9.5×10^{25} n m^{-1}) neutron irradiated sample. In the non-irradiated material, all 10 grain boundaries studied were rich in Fe and Ni, as exemplified in Figure 4.1.13. The HAADF image shows both diffraction and atomic number contrast and, as such, may be an indication of segregation to the grain boundary causing an increase in the average atomic number. It is important to note that no compositional variation at the boundary is observed with respect to Sn in the non-irradiated state. Additionally, the absolute misorientation between grains was determined by electron diffraction techniques (not shown), and no correlation was found between absolute grain misorientation and segregation in at.% Fe, Ni.

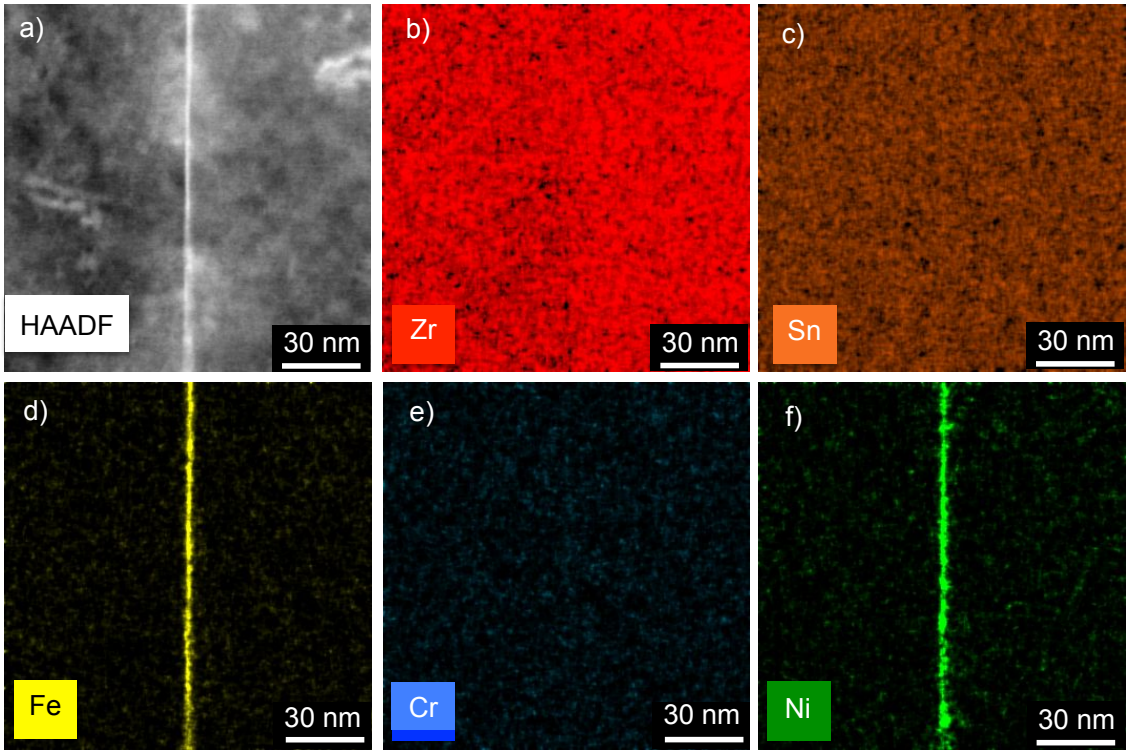

Figure 4.1.13 The HAADF image is given in a) for a typical grain boundary in non-irradiated Zircaloy-2, tilted such that the boundary plane is parallel to the beam direction. Chemical maps are displayed in raw counts, each individually scaled, for b) Zr c) Sn, d) Fe, e) Cr and f) Ni. All 10 boundaries studied in this manner exhibited both Fe and Ni segregation to the boundary.

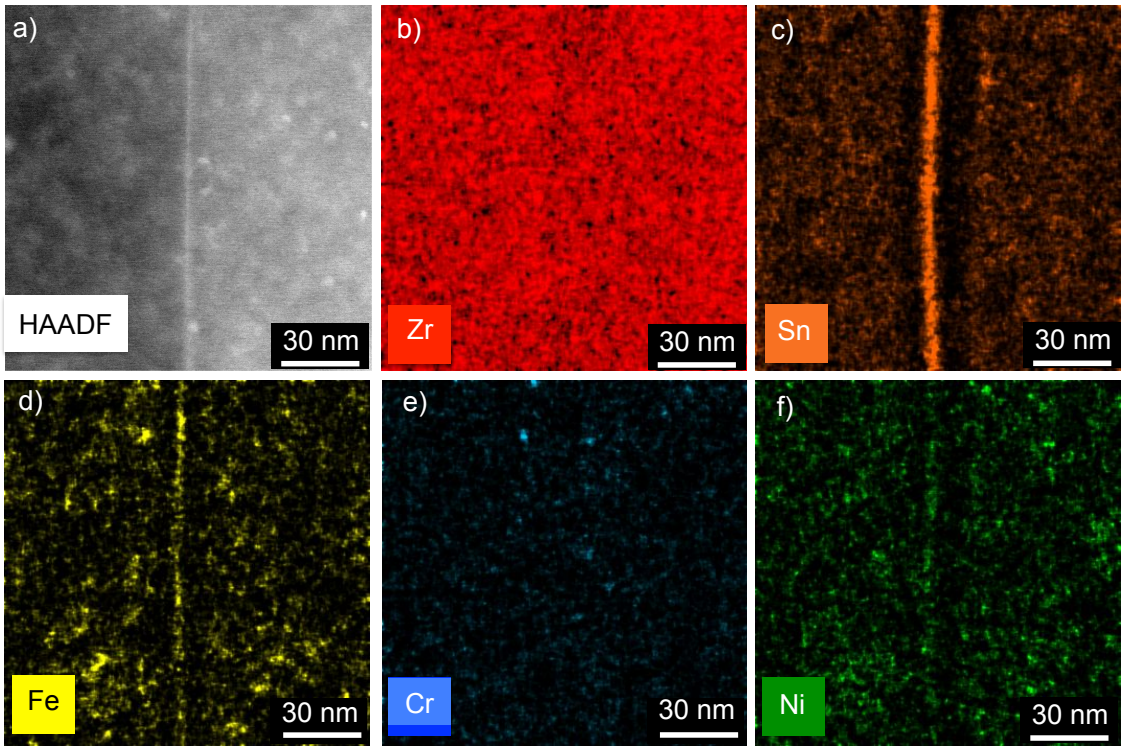

Figure 4.1.12 The HAADF image is given in a) for a grain boundary in Zircaloy-2 proton-irradiated to 7.0 dpa, tilted such that the boundary plane is parallel to the beam direction. Chemical maps are displayed in raw counts, each individually scaled, for b) Zr c) Sn, d) Fe, e) Cr and f) Ni. All boundaries exhibit Sn segregation and Fe, Ni depletion.

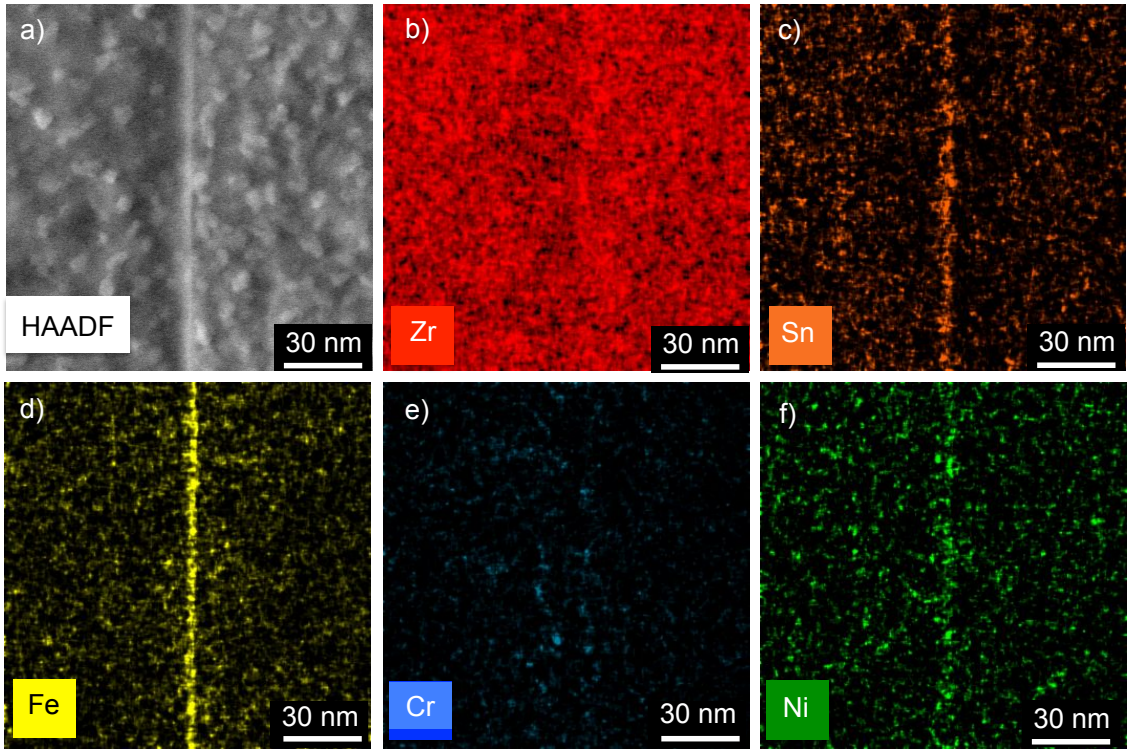

Figure 4.1.14 The HAADF image is given in a) for a grain boundary in Zircaloy-2 clad neutron-irradiated in a BWR to 9.5 x10^{25} n m^{-2} ~15.8 dpa, tilted such that the boundary plane is parallel to the beam direction. Chemical maps are displayed in raw counts, each individually scaled, for b) Zr c) Sn, d) Fe, e) Cr and f) Ni. All boundaries exhibit Sn segregation and Fe, Ni depletion.

A typical grain boundary after proton irradiation to 7.0 dpa is shown in Figure 4.1.12, in which Sn segregation to the boundary is observed, as is a depletion in Fe and Ni relative to the non-irradiated case. Additionally, the maps indicate some nano-clustering of Fe and Ni within the boundary-adjacent matrix, and provide evidence of Sn depletion very close to the grain boundary. These phenomena were consistent across all 8 grain boundaries studied for the 7.0 dpa proton dose level. A total of 9 grain boundaries were studied in the neutron-irradiated channel material at the fluence level 9.5 x10^{25} n m^{-1} ~15.8 dpa. Figure 4.1.14 shows that the observations were similar to the proton-irradiated material although Sn segregation and loss of Fe and Ni segregation from grain boundaries was less severe despite the much higher dpa level. However, it should be noted that the neutron-irradiated electropolished foils were older, thicker and of a lower surface quality than the proton-irradiated electropolished foils, which makes direct comparisons difficult.

Line scans were taken across the horizontal centre of the maps in Figure 4.1.13, Figure 4.1.12 and Figure 4.1.14, averaging in the vertical direction and quantified in at.%, plotted along the horizontal direction. The results of this approach are shown in Figure 4.1.15. This data should not be considered a true representation of composition because small concentrations are being considered (< 3 at.%) which are significantly affected by Fe-scattering from the microscope pole piece and the absorption of the Sn L_α X-ray, both of which are ignored in the quantification. However, the calculation gives an idea of the spatial distribution of the relative elements in the system. Interestingly, the depletion in Sn adjacent to the boundary is clear after proton-irradiation to 7.0 dpa and is reflected in an increase in the Zr content. In the neutron-irradiated data, there is no such short-range displacement.

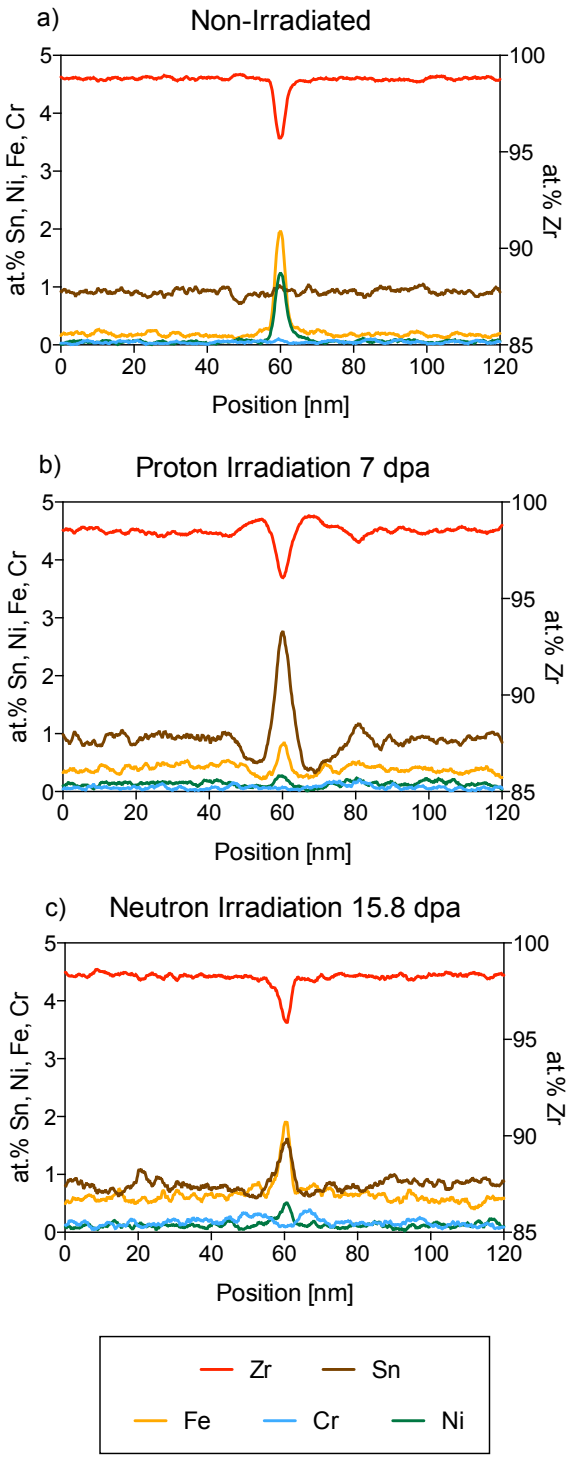

Figure 4.1.15 The line scans shown in a), b) and c) correspond to a horizontal profile across **Figure 4.1.13**, **Figure 4.1.12** and **Figure 4.1.14**, respectively. The line scans are quantified in terms of atomic per cent (at.%) to provide a graphical representation of the spatial distribution of elements.

5 DISCUSSION

5.1 SPP DISSOLUTION

5.1.1 INTERNAL SPP DIFFUSIONAL CAPACITY AND HOMOGENEITY

In comparing the chemical maps of the non-irradiated Fe-Cr and Fe-Ni SPPs in Figure 4.1.2 and Figure 4.1.3, respectfully, one may draw certain conclusions about the self-diffusivity of components within the different SPP types. For instance, the Zr map in Figure 4.1.2b provides information about the shape of the Fe-Cr SPP in the transmission direction and so any other map with similar contouring might be considered to be homogeneous within the SPP. As the Fe map in Figure 4.1.2d displays similar contouring to the Zr, one might suggest that Fe is evenly distributed throughout the SPP. Likewise, as the Cr map in Figure 4.1.2e does not follow the Zr contouring, it is unevenly distributed within the SPP. The cause of this may be found in the Ni map of Figure 4.1.2e, which is coincident with Fe and may cause some partitioning of the Cr. In support of this, Fe-Cr type and Fe-Ni type SPPs are commonly observed in Zircaloy-2, as displayed in Figure 4.1.1, but never SPPs with Cr and Ni as dominating constituents. Instead, Fe-Cr and Fe-Ni SPP clusters are known to form with orientation relationship $(1\bar{1}0)_{Fe-Ni} \| (10\bar{1}1)_{Fe-Cr}$ and $(002)_{Fe-Ni} \| (\bar{2}110)_{Fe-Cr}$ (Chemelle et al. 1983), and have indeed been found in the present work, e.g. in Figure 4.1.7, although such orientation relationships have not been determined here. The Fe-Ni regions are frequently the larger within a cluster, suggesting that Fe-Ni SPPs act as nucleation sites for Fe-Cr SPPs. This is supported by the respective diffusivities of the elements in α-Zr Fe > Ni >> Cr (Perez et al. 2003) such that Fe-Ni SPPs nucleate first. All of the Fe-Ni SPPs studied in the present work contained no Cr, suggesting more chemical homogeneity in Fe-Ni in contrast to Fe-Cr SPPs. Such a property may be important with respect to behaviour under irradiation, as chemical mixing is thought to be the primary form of disorder in intermetallic systems (Motta 1997) and Brimhall et al. have argued that a tendency for increased self-solubility or greater stoichiometric range is a deciding factor in regards to resistance to irradiation-induced amorphisation (Brimhall et al. 1983). It is well-known that Fe-Ni SPPs resist amorphisation under neutron irradiations at intermediate temperatures, whereas Fe-Cr SPPs do not

(Griffiths, R W Gilbert, et al. 1987). Chemical homogeneity as a property correlated to irradiation damage resistance is shown in the lack of amorphisation in relatively pure or solid solution phases, such as in the α-Zr matrix or the β-Nb phase in Zr-Nb-type alloy systems (Shishov et al. 2005). The Fe-Ni SPPs in the present work are shown to be chemically homogeneous in comparison to the Fe-Cr SPP, both before and after irradiation. This may suggest increased diffusional capacity within the Fe-Ni SPP, and its resulting homogeneity may be related to its resistance to irradiation-induced amorphisation at irradiation temperatures 280-330 °C (Griffiths, R W Gilbert, et al. 1987).

The Fe-Cr SPP is known to become partially amorphous at such irradiation temperatures (Gilbert et al. 1985; Yang et al. 1986; Griffiths, R W Gilbert, et al. 1987; Etoh & Shimada 1993). This amorphous region starts at the matrix-SPP interfacial region and progresses inwards radially at a rate ~10-13 nm per neutron fluence 1 $x10^{25}$ n m^{-2} under normal power reactor operating conditions (Griffiths, R W Gilbert, et al. 1987; Griffiths 1990; Gilbon & Simonot 1994), but at higher rates under higher fluxes and at lower temperatures (Bajaj et al. 2002). This amorphous zone is known to be depleted in Fe relative to the crystalline SPP core (Gilbert et al. 1985; Yang et al. 1986; Griffiths, R W Gilbert, et al. 1987; Yang 1988; Etoh & Shimada 1993), and so Fe depletion from the edge region into the surrounding matrix is thought to be responsible for the amorphous transformation.

5.1.2 SPP DISSOLUTION AND AMORPHISATION

While no amorphisation was observed in any SPP studied in the present work, Fe depletion from the edge region of Fe-Cr SPPs is evident from the Fe/Cr ratio maps and line scans of Figure 4.1.4. Thermal recovery mechanisms at the proton irradiation temperature of 350 °C are therefore thought to be sufficient such that the rate of annealing is equal to or greater than the rate of damage accumulation (Motta 1997). Zu et al. have studied proton irradiation damage in Zircaloy-4 under a similar damage rate and have demonstrated an amorphous rim in Fe-Cr SPPs at an irradiation temperature of 310 °C but not at 350 °C (Zu et al. 2005). This suggests that the critical temperature for amorphisation for the Fe-Cr SPP (T_{crit}),

above which no amorphisation occurs, is between 310°C and 350 °C, in agreement with the observations presented here and similar to that under neutron irradiation at power reactor fluxes T_{crit} ~330-360 °C (Griffiths, R W Gilbert, et al. 1987; Motta et al. 1991). While Griffiths et al. have suggested that the amorphisation rate in Zircaloy-2 Fe-Cr SPPs may be greater than that in Zircaloy-4 SPPs due to the higher Fe/Cr in the SPPs of the latter (Griffiths, R W Gilbert, et al. 1987), this conclusion was drawn from materials experiencing very different neutron fluxes, and other studies have shown the rate of amorphous rate ingress to be similar for Zircaloy-2 Fe-Cr SPPs at ~10 per 1 $x10^{25}$ n m^{-2} under BWR conditions (Huang et al. 1996). In this regard, proton irradiation has greater similarity to neutron irradiation in comparison to electron or heavy ion irradiation, for which T_{crit} is equal to ~30 °C (Pêcheur et al. 1993) and ~380-580 °C (Motta et al. 1994; Pêcheur et al. 1993), respectfully, depending of course on particle flux and type of heavy ion. The reason for such discrepancies may be deduced from a consideration of the various damage rates and the nature of the damage rate created. Under neutron irradiation, the damage rate is equal to ~0.7-1 $x10^{-7}$ dpa s^{-1} (Shishov et al. 2005; Adamson 2014). Electron irradiation may be performed at damage rates higher than neutron irradiations by a factor of ~10^5 (de Carlan et al. 1996), but the damage is in the form of isolated Frenkel pairs (Woo & Singh 1992) which will not require significant thermal agitation to annihilate. Irradiation by heavy ions produces damage cascades smaller than that of neutron-induced cascades, and those of proton irradiations are smaller still (Was 2000). However, the damage rate of heavy ion irradiation is higher than neutron irradiation by a factor of ~10^4 (Idrees, Yao, Kirk, et al. 2013; Zu et al. 2005) and proton irradiation damage rates are higher by a factor of ~10^2 (Zu et al. 2005), accounting for the relative values of T_{crit} for the Fe-Cr SPP.

While Zu et al. reported no chemical variation within the Fe-Cr SPPs of Zircaloy-4 after proton irradiation at 350 °C up to a dose of 7 dpa (Zu et al. 2005), Fe depletion from such particles is evident in the present work under almost identical irradiation conditions and is shown as a function of dose in Figure 4.1.6. The histogram presented in Figure 4.1.6a demonstrates the bimodal distribution of Fe/Cr ratios at 4.7 and 7.0 dpa. Interestingly, the two Fe/Cr modal values do not

change significantly between 4.7 and 7.0 dpa, suggesting an equilibrium Fe/Cr ratio in the edge region that is suitable for the temperature and which may prevent the amorphous transformation from occurring. In Figure 4.1.6b, the Fe/Ni histograms again show little difference in the ratio between 4.7 and 7.0 dpa. At 2.3 dpa, the very edge of the Fe/Ni SPPs seems to have greater Ni depletion relative to Fe, resulting in a slight skew to the right for the histograms of Figure 4.1.6b. This is unexpected as the diffusivity of Fe is slightly greater than that of Ni in α-Zr (Perez et al. 2003). However, at higher irradiation doses 4.7 and 7.0 dpa, the Fe/Ni at the periphery approaches unity, supporting the similar matrix diffusivities of Fe and Ni and suggesting that their diffusivity within the Fe-Ni SPP is not the same as that in α-Zr. While Zu et al. did not demonstrate chemical evolution within SPPs in Zircaloy-4, this could be due to either a better stability because of the higher Fe/Cr ratio in Zircaloy-2 Fe-Cr SPPs (Gilbert et al. 1985; Van der Sande & Bement 1974; Kuwae et al. 1983; Pêcheur et al. 1993; Yang et al. 1986) or due to the limitations associated with single-point EDS sampling or line scans. However, the authors presented energy-filtered TEM, which suggested the possibility of post-irradiation Fe segregation to the matrix-SPP interfacial region for an Fe-Cr SPP and to that of a small SPP the authors referred to as $ZrFe_2$ (Zu et al. 2005). One must be careful with respect to the interpretation of both observations, as the data presented here would suggest that Fe dissolve into the matrix from interfacial boundaries. Further, the Fe-Cr SPP in question was located at a grain boundary (Zu et al. 2005), which may act as a solute pathway, and the determination of '$ZrFe_2$' stoichiometry is difficult given the matrix contribution to the signal from such a small SPP and given that zirconium silicides are known to be coated in Fe and Ni, segregated to their interface with the matrix after neutron irradiation (Griffiths et al. 1992; Griffiths 1993). Impurity elements such as Si may be easily overlooked if unexpected.

The lack in bimodality for the Fe-Ni SPP in Figure 4.1.6 suggests that it has better internal diffusion in comparison to the Fe-Cr SPP. While this is supported in the literature by the resistance to amorphisation of Fe-Ni SPPs, commonly explained by the relative diffusivities of Fe, Ni and Cr in α-Zr, there is little work published regarding self-diffusion in the defective Fe-Cr or Fe-Ni structure. Recent

calculations have given the point defect formation energies in the hcp C14 $ZrCr_2$ and the bct C16 Zr_2Ni systems (Chen et al. 2005; Moura et al. 2001). In the $ZrCr_2$ system, the vacancy-type defects are the least energetically favourable and antisite defects, where Zr substitutes onto a Cr site (Zr^{Cr}) or Cr onto a Zr site (Cr^{Zr}), are more likely (Chen et al. 2005). Therefore, a defective state may be made up of more chemical disorder than of vacancies and interstitials. In the Zr_2Ni system, the vacancy and antisite defects are on average lower in formation energy than in the $ZrCr_2$ system (Moura et al. 2001). This may suggest that if both systems had an equal number of such defects then the Zr_2Ni would be in a lower free energy state. Although this could account for why the Fe-Ni SPPs recover irradiation damage more effectively than the Fe-Cr, arguments towards free energy are not strictly valid when one considers the dynamic and localised nature of ballistic collision cascades (Motta 1997). Interestingly, vacancy migration in the Zr_2Ni system was determined to be anisotropic with a preference in the [001] direction (Moura et al. 2001), which will of course have a profound effect on point defect interactions and larger, extended defects and their evolution, especially in regard to SPP clusters containing both Fe-Cr and Fe-Ni regions. The Fe-Ni system does indeed become defective under neutron irradiation, as Kuri et al. have demonstrated by comparing the EXAFS and XANES with and without neutron irradiation in a BWR (Kuri et al. 2010). The degree of disorder is, however, difficult to discern and although Kuri et al. described a lack in post-irradiation long-range order, the spectra show signs of local order that may exceed that of an amorphous system. Of course, verification by TEM would be beneficial, but such fine detail is not always possible in the microscope when stoichiometry is variable and antisite defects probable, even in the non-irradiated state.

While such a detailed analysis of segregation within SPPs is not provided here for the neutron-irradiated material, due to the higher irradiation doses and correspondingly lower concentration of Fe, Cr and Ni in the transmission direction causing significant noise in quantifications, spectral imaging to extracts maps such as those in Figure 4.1.7 may still provide useful information. For instance, the SPP shape is difficult to discern from the BF STEM image but is clear from the Fe, Cr and Ni maps. Interestingly, the Fe-Ni part of the SPP cluster has an unusual shape

in comparison to the Fe-Cr part; the former has a more irregular morphology and the latter is predominantly spheroid with irregular peripheries. Etoh and Shimada et al. have noted the more irregular morphology of dissolving Fe-Ni SPPs in comparison to the Fe-Cr, as have other authors (Etoh & Shimada 1993; Mahmood et al. 2000; Goll & Ray 2002; Valizadeh et al. 2014). However, the neutron fluence onset of this morphological irregularity has not been reported. In the present work, the irregular shape of the Fe-Ni type SPP is also observed after proton irradiation at 4.7 and 7.0 dpa dose levels, accentuated at the highest proton dose levels by channelling phenomena. As there is no irregularity in the Fe-Ni type SPPs at 2.3 dpa (see Figure 4.1.5), it may be the case that there is a delay in the dissolution of the Fe-Ni intermetallic phases to between 2.3 and 4.7 dpa. Huang et al. have noted that the Fe/Ni ratio remains constant for longer than the Fe/Cr in the early stages of neutron irradiation at ~290 °C, which means that either the Fe-Ni SPP resists dissolution for longer or that Fe and Ni are dissolving at the same rate (Huang et al. 1996). An assessment of SPP morphology may allude as to which. Evidence toward the mechanism for dissolution may be deduced from Figure 4.1.7 and Figure 4.1.8, in the directional segregation of Fe, Cr, and to some extent of Ni, to the basal plane (horizontal). The segregation is coincident with dislocation positions, which has been shown for Fe and Cr segregation in the vicinity of Fe-Cr type SPPs at similar distances from the SPPs to those presented here (Griffiths et al. 1995; Valizadeh et al. 2014). Recent calculations have shown that Fe, Cr and Ni diffusion is anisotropic with a preference in the <0001> direction (Christensen et al. 2014) and has confirmed that Zr self interstitials (SIAs) are anisotropic with preferable diffusion in the basal plane and that vacancies are only weakly anisotropic (Woo & Göslel 1983; Christensen et al. 2015). As such, the segregation of Fe, Cr and Ni to basal planes in Figure 4.1.7 and Figure 4.1.8 cannot be a result of their individual diffusion anisotropy but is likely due to the diffusion of SIAs in the basal plane toward SPPs and the resulting diffusion of alloying elements in the reverse direction. The role of SPPs as sinks for SIAs has been discussed previously (Griffiths 1990) and is supported by a lack in SPP dissolution in the neutron irradiation of 20% cold worked Zircaloy-2 (Griffiths, R W Gilbert, et al. 1987). This behaviour was attributed to network dislocations hindering outward diffusion, but it may be more likely that the network dislocations become the dominant sink for

SIAs and SIA clusters, which would serve as indirect evidence for SPPs as SIA sinks in fully recrystallised systems. Further, the close anti-correlation of Zr with that of Fe, Cr and Ni in Figure 4.1.7 may be evidence of Zr SIAs preferentially dissolving the SPP; the fact that Sn does not follow this same anti-correlation indicates that the SPP dissolution is not simply a result of ballistic mixing.

5.1.3 CHEMICAL QUANTIFICATION

The average Fe/X (X = Cr, Ni) ratio over the whole SPP displayed in Figure 4.1.9 gives an idea of the scatter in measurement; the mean and standard deviations (σ) are given in Table 1, where σ is a single standard deviation from the mean of the number of SPPs analysed (assuming a Gaussian distribution), which is given in parentheses. Both the proton- and neutron-irradiated Fe/Cr data presented in Figure 4.1.9a fit well with data in the literature and describe a decrease in the average Fe/Cr with respect to dose. This is expected from the depletion of Fe from SPP edge regions, exemplified in Figure 4.1.4. In Figure 4.1.9b, the Fe/Ni ratio is displayed in a similar manner. The proton-irradiated data fits reasonably well with that in the literature and displays a retention of the mean Fe/Ni ratio between 0 and 2.3 dpa, agreeing with the observation of Etoh and Shimada that Fe/Ni remains constant for longer than Fe/Cr at low dose neutron irradiation (Etoh & Shimada 1993) and supporting the SPP morphology evolution in Figure 4.1.5 that suggests a resistance to irradiation-induced dissolution within the Fe-Ni SPP until between 2.3 and 4.7 dpa. The trend between the Fe/Ni for the proton and neutron-irradiated material presented here is not, however, as continuous as for the Fe/Cr. The reader is reminded that the non- and proton-irradiated material was Zircaloy-2 plate and the neutron-irradiated cladding or channel material. As such, the Fe/X ratios of SPPs in the starting material may be different. This is thought to be more significant for Fe-Ni than for Fe-Cr SPPs, as Yang has reported that aging of non-irradiated Zircaloy-2 in the high α-phase temperature range caused an increase in the Fe/Ni of Fe-Ni SPPs from 0.9 to ~1.1, but did not cause any change in the Fe/Cr ratio of the Fe-Cr phase (Yang et al. 1986), suggesting more flexibility in the Fe/X stoichiometry of the former. It should be noted that the same neutron-irradiated samples investigated here were recently studied for SPP

chemistry by Valizadeh et al. and the results from the present work are in good agreement (Valizadeh et al. 2014). As such, a wider stoichiometric range of Fe-Ni SPPs may be of significance both before and after neutron irradiation. Indeed, the range given by Valizadeh for the non-irradiated state is larger for the Fe-Ni system (Fe/Ni = 1.6-2.1) than for the Fe-Cr (Fe/Cr = 0.7-1.1) and larger than the F/Ni range for the non-irradiated plate presented here. The mean Fe/Ni at the highest proton dose is similar to the Fe/Ni at the highest neutron dose, which may suggest that a stable Fe/Ni is eventually reached under both irradiative species at Fe/Ni ~0.7.

In an analysis of the chemical composition of the Fe-Cr SPP Fe-depleted edge region with respect to its core, Figure 4.1.11a suggests that the greatest change in Fe-depletion occurs between 2.3 and 4.7 dpa, after which there is little change in the relative chemistry between the two regions. Further, in an analysis of the size of the Fe-Cr SPP Fe-depleted edge region with respect to its core, Figure 4.1.11b suggests that the greatest increase in edge size occurs between 4.7 and 7.0 dpa, before which there is relatively little increase in edge size. Figure 4.1.11 suggests that the degree of Fe-depletion is directly proportional to the surface area of the SPP and hence preferential dissolution from the edge. As the SPP volume : surface area ratio decreases with increasing SPP size, Fe-depletion from the core must be limited. This is reflected in the mean Fe/Cr values for the core and edge regions with respect to dose in Table 2. An analogy from the literature is that of the Fe-depleted amorphous rim in neutron-irradiated Fe-Cr SPPs irradiated at ~300 °C, which is known to ingress towards the crystalline core (Griffiths, R W Gilbert, et al. 1987; Griffiths 1990; Gilbon & Simonot 1994). However, the rate of amorphous rim ingress in neutron-irradiated material is reported to be linear and independent of SPP size. As a linear rate of ingress of the edge region was not observed in the present work, it may be the case that a stable and equilibrium chemistry is first formed by Fe-depletion in the edge region between 2.3 and 4.7 dpa, after which this equilibrium defective region may ingress towards the central SPP core at a faster rate. The reason for an acceleration in edge ingress rate may be due to either reaching the an equilibrium Fe/Cr ratio or due to the nucleation of c-loops in the matrix after ~4.5 dpa proton irradiation at 350 °C (*Manuscript 2, present work*),

which may act as a strong Fe sink. The large decrease in Fe/Cr between 2.3 and 4.7 dpa could result in matrix segregation that create c-loop nucleation sites, as could be large decrease in Fe/Ni.

The proton irradiations were conducted at 350 C, a temperature higher than that of a BWR. This might allow for an equilibrium concentration of Fe to be attained in the defective Fe-Cr SPP without transformation to the amorphous phase. Such a suggestion might be investigated by the extraction of SPPs from the matrix in order to quantify their chemistry accurately and by the simulation of the stability of the defective region at temperature. These investigations are currently underway. SPP edge and core size effects, coupled with a variable SPP size prior to irradiation, contributes to an explanation of scatter in Figure 4.1.9. The average over the whole SPP is displayed in Figure 4.1.11 for both the Fe-Cr and Fe-Ni SPPs. As has been already mentioned, Fe/Ni stoichiometry is known to be variable prior to irradiation (Valizadeh et al. 2014) and variable with respect to heat treatment parameters (Yang et al. 1986). Further, with reference to Figure 4.1.11c and d, there seems to be a decrease in the Fe/Ni stoichiometry with Fe-Ni SPP size that is retained throughout irradiation to 7.0 dpa, again suggesting good diffusional capacity within Fe-Ni type SPPs. In Figure 4.1.11c and d, the slope of the line of best fit is similar at all dose levels and this slope is also present in the non-irradiated case. Therefore, it may be the case that relationship between Fe-Ni SPP chemistry and size is not an irradiation-induced phenomenon but one pertaining to the thermomechanical history and alloy heat treatment prior to irradiation.

5.2 GRAIN BOUNDARY EVOLUTION

The chemical content of grain boundaries was investigated, as boundaries are a likely sink for the solute dispersed from SPPs. However, it was found that grain boundaries initially contain Fe and Ni segregation that depletes into the matrix during irradiation at while Sn segregated to the boundary during irradiation by both protons to 7.0 dpa at 350 °C, Figure 4.1.12, and by neutrons to ~15.8 dpa in a BWR, Figure 4.1.14. This suggests an inverse Kirkendall-type mechanism, proposed as a possible mechanism to explain grain boundary segregation in

irradiated steels (Bruemmer et al. 1999), by which vacancies diffuse to the boundary and cause the depletion of fast-diffusing solutes, i.e. Fe > Ni >> Cr (Perez et al. 2003; Pasianot & Pérez 2013), and the enrichment of relatively slow-diffusing solutes, i.e. Sn (Perez et al. 2003). This is supported by the line scan in Figure 4.1.15b, which shows Sn depletion in the grain boundary-adjacent region and a corresponding Zr increase. However, observations related to grain boundary-adjacent zones denuded in certain types of defects may suggest otherwise. It has been reported that grain boundaries in pure Zr have a larger interstitial a-loop denuded zone than vacancy a-loop denuded zone, regardless or grain boundary orientation (Griffiths et al. 1988). As such, grain boundaries may be preferably Zr self-interstitial sinks. Alternatively, Idrees et al. have demonstrated grain boundary-adjacent zones denuded in c-loops after Kr heavy ion irradiation of Zr alloy Excel, coupled with possible Fe depletion in this zone (Idrees, Yao, Sattari, et al. 2013). This suggests that the grain boundary is both a vacancy sink (if we assume the c-loops to be vacancy in nature; no determination of nature was possible due to the c-loops' small size) and a sink for Fe, which is not reconcilable with the inverse Kirkendall mechanism. However, segregation of Fe to the boundary was not suggested by Idrees et al. as boundaries were not tilted parallel to the beam direction in order to properly assess the chemistry. Further, a systematic series of irradiation does levels would be desirable to determine the order in which such observations arise.

Grain boundary segregation in steels has predominantly been studied by STEM-EDS (Vatter & Titchmarsh 1989; Simonen et al. 1995; Allen et al. 1997; Jiao & Was 2011a; Jiao & Was 2011b; Wharry et al. 2011; Wharry et al. 2012), Auger electron spectroscopy (AES) (Damcott et al. 1995; Allen et al. 1997) and more recently by electron energy loss spectroscopy (EELS) (Marquis, Lozano-Perez, et al. 2011) and especially by atom probe tomography (APT) (Etienne et al. 2010; Marquis, Hu, et al. 2011; Jiao & Was 2011a; Marquis, Lozano-Perez, et al. 2011; Jiao & Was 2011b; Kuksenko et al. 2012; Hu et al. 2012). In STEM-EDS this is a tedious task due to the limiting geometry of the sample stage and the EDS detector; the one-detector system requires the sample to be tilted towards it and grain boundaries require tilting such that the boundary plane is parallel to the beam direction. These two

conditions can be difficult to satisfy simultaneously. The benefit of the current work is in the four EDS detectors that surround the sample in the ChemiSTEM™ system, and so grain boundary chemistry may be studied with less constraint on allowable tilting. Although not a comprehensive study, recent work has reported no segregation to grain boundaries in neutron-irradiated Zircaloy-2 BWR cladding (Valizadeh et al. 2014). In a recent study of neutron irradiation in a HFIR test reactor at ~358 °C, EDS line scans over grain boundaries have demonstrated some segregation in both Zircaloy-2 and -4 (Cockeram et al. 2013). In the Zircaloy-4 observations by Cockeram et al., no segregation to boundaries was observed at 0.11 and 0.55 $x10^{25}$ n m^{-2} but both Fe and Sn segregation after irradiation to 2.93 $x10^{25}$ n m^{-2}. Likewise, in Zircaloy-2, segregation of Fe, Sn, Ni and/or Cr was detected at some grain boundaries after irradiation to 2.93 $x10^{25}$ n m^{-2} but not for all boundaries. In conclusion, the authors suggested that segregation to grain boundaries occurs after a threshold neutron dose that may be related to the onset of irradiation-induced second phase particle dissolution (Cockeram et al. 2013). However, the difference in segregation between different grain boundaries was large, few grain boundaries were studied and no boundaries were studied in the non-irradiated material. Further, a clear boundary line is not evident from some of the images shown in the work (see, for instance, Figure 9d image 1 and 3 of Ref. (Cockeram et al. 2013)), and, as such, some of the boundaries studied may not have been tilted such that the boundary plane was exactly parallel to the beam direction, thereby diluting any segregation signal with that of the matrix.

Better detection of grain boundary segregation is possible with atom probe tomography (APT) although the volume sampled is significantly smaller than that possible by TEM. The first success in this regard concerned continuous Fe and Nb segregation to grain boundaries in non-irradiated ZIRLO™ (Hudson & Smith 2009). Likewise, APT has been used to detect Fe segregation to grain boundaries in the non-irradiated state of β-quenched binary alloy Zr-0.8Fe (wt.%) (Gault et al. 2013), in crystal bar Zr and model alloy Zr-0.4Fe-0.2Cr (wt.%) (Dong et al. 2013), and both Fe and Sn segregation to grain boundaries in Zircaloy-4 (Dong et al. 2013), all at similar local concentrations to that shown in the present work in Figure 4.1.15. While there is little in the literature regarding chemical segregation

to grain boundaries in Zircaloy-2, 'significant' Fe segregation to some (but not all) grain boundaries has recently been observed by APT in Zircaloy-2 cladding after neutron irradiation in a BWR and no segregation of Sn, Cr or Ni (Sundell et al. n.d.). However, grain boundaries were not the main focus of that particular work and as such the number of grain boundaries studied was, although not stated explicitly, likely few.

In summary, there is conflicting evidence in the literature in regards to segregation at grain boundaries before and after irradiation, and there is especially a lack in a systematic approach to the characterisation. Modelling of grain boundaries and their likely segregation behaviour both before and after irradiation is required to explain trends, as absolute grain misorientation was found in the present work to have little influence on such phenomena. Indeed, the anisotropic diffusion of point defects, their clusters and the orientation of a grain boundary with respect to this bias will have an effect on differing sink strengths between boundaries (Woo & Göslel 1983). As Zr self interstitials diffuse preferentially in the basal plane and vacancies only slightly anisotropically (Christensen et al. 2015), there will be a net flux of SIAs in the basal plane and vacancies in the <0001> direction. It has been shown that, after neutron irradiation in test reactor EBR-II at ~430 °C, cavities (vacancy agglomerations) preferentially form close to grain boundaries in crystal bar and sponge Zr that have a line perpendicular to the basal plane (Griffiths et al. 1988), i.e. grain boundaries receive a net flux of interstitials result in cavity nucleation close to the boundary. While the authors of that study noted that this may not be the case in alloyed Zr (Griffiths et al. 1988), diffusional anisotropy must be considered when assessing grain boundary chemistry after irradiation. As such, an inverse Kirkendall mechanism may be expected at boundaries that receive a net flux of vacancies parallel to the basal plane, and an interstitial association mechanism may be expected to occur at grain boundaries that receive a net flux of interstitials perpendicular to the basal plane. The anisotropic diffusion of Fe, Ni and Cr in hcp Zr (Christensen et al. 2014) and the tendency of such elements to cluster in the presence of Zr vacancies (Burr et al. 2015) may affect segregation or depletion at boundaries orientated differently. Such a concept, theoretical or experimental, has not to date been investigated.

6 CONCLUSIONS

The irradiation-induced dissolution of SPPs, Fe-Cr and Fe-Ni type, and the ejection of Fe and Ni from grain boundaries have been exemplified in the present work for both proton- and neutron-irradiated Zircaloy-2. The development of transmission electron microscopy in its high spatial resolution through aberration-corrected probes and the development of EDS detectors of large total solid angles, surrounding the sample to allow flexibility in tilting, have been essential in obtaining such measurements. The following is a summary of the main conclusions:

- Fe-Cr SPPs are heterogeneous before irradiation and contain Ni, whereas Fe-Ni SPPs are homogeneous and contain no Cr.
- Neutron irradiation results in Fe-depletion from both Fe-Cr and Fe-Ni SPPs, the former incurs an amorphous transformation and the latter remains crystalline.
- Proton irradiation at 350 C resulted in no amorphisation for either the Fe-Cr or Fe-Ni SPPs .
- Proton irradiation results in a core-edge structure for Fe-Cr SPPs. The edge region is Fe-depleted with a composition and size directly proportional to that of the non-irradiated SPP.
- Proton irradiation results in Fe-depletion from the whole of the Fe-Ni SPP, suggesting better self-diffusion in the defective phase in comparison to the Fe-Cr SPP. Larger SPPs have lower Fe contents, likely due to pre-irradiation thermomechanical heat treatment parameters.
- Under both proton and neutron irradiation, Fe-Ni SPPs incur irregular morphologies whereas Fe-Cr SPPs retain their original shape. The delay in the Fe-Ni morphological change and the delay in the decrease in the average Fe/Ni ratio is evidence of better irradiation resistance in comparison to the Fe-Cr SPP.
- Under both proton and neutron irradiation, Fe and Ni deplete from grain boundaries and Sn segregates to grain boundaries.

As such, a supersaturation of the matrix with solute is indirectly evident and irradiation-induced precipitation or clustering, either during irradiation or upon cooling, is expected. This has been observed in the present work close to partially dissolved SPPs in neutron-irradiated Zircaloy-2 and an assessment of solute segregation and its interaction with other defect structures is underway. The diffusivity and self-solubility of Fe, Cr and Ni within the defective SPP structures are scarcely-studied but likely mechanisms by which different SPPs respond differently to both proton and neutron irradiation, as is the initial heterogeneity in the Fe-Cr type SPP and its increase in heterogeneity during irradiation.

7 ACKNOWLEDGEMENTS

This work is funded by an EPSRC Leadership Fellowship for the study of irradiation damage in zirconium alloys [EP/I005420/1], with additional industrial contributions especially from Westinghouse and Studsvik Nuclear in terms of both material acquisition and useful discussions. The authors would like to thank Malcolm Griffiths for insightful discussions, Maria Yankova for advice in data analysis, Thomas Seymour and Matthew Topping for aid in experimental accomplishments and Gary Was and Ovidiu Toader at the Michigan Ion Beam Laboratory for the use of their facility in the proton irradiation experiments.

8 REFERENCES

Adamson, R., 2014. *Charged particle bombardment of zirconium alloys: A review*, Sweden.

Allen, T.R., Was, G.S. & Kenik, E. a., 1997. The effect of alloy composition on radiation-induced segregation in Fe-Cr-Ni alloys. *Journal of Nuclear Materials*, 244(3), pp.278–294.

Azevedo, C.R.F., 2011. Selection of fuel cladding material for nuclear fission reactors. *Engineering Failure Analysis*, 18(8), pp.1943–1962.

Bajaj, R., Kammenzind, B.F. & Farkas, D, M., 2002. Effects of Neutron Irradiation on the Microstructure of Alpha-Annealed Zircaloy-4. *Zirconium in the Nuclear*

Industry: Thirteenth International Symposium, ASTM STP 1423, pp.400–406.

Brimhall, J.L., Kissinger, H.E. & Charlot, L. a., 1983. Amorphous phase formation in irradiated intermetallic compounds. *Radiation Effects*, 77, pp.273–293.

Bruemmer, S.M. et al., 1999. Radiation-induced material changes and susceptibility to intergranular failure of light-water-reactor core internals. *Journal of Nuclear Materials*, 274(3), pp.299–314.

Buckley, S.N., 1961. Properties of Reactor Materials and the Effects of Irradiation Damage. In London: Butterworths, p. 443.

Burr, P. a et al., 2015. From solid solution to cluster formation of Fe and Cr in α-Zr. *Submitted to Acta Materiallia*.

de Carlan, Y. et al., 1996. Influence of Iron in the Nucleation of <c> Component Dislocation Loops in Irradiated Zircaloy-4. *Zirconium in the Nuclear Industry: Eleventh International Symposium, ASTM STP 1295*, pp.638–653.

Charquet, D. et al., 1988. Solubility limits and formation of intermetallic precipitates in ZrSnFeCr alloys. *Zirconium in the Nuclear Industry: Eighth International Symposium*, pp.405–422.

Chemelle, P. et al., 1983. Morphology and composition of second phase particles in Zircaloy-2. *Journal of Nuclear Materials*, 113, pp.58–64.

Chen, X.-Q. et al., 2005. Ab initio study of ground-state properties of the Laves phase compounds TiCr2, ZrCr2, and HfCr2. *Physical Review B*, 71(174101), pp.1–11.

Christensen, M. et al., 2015. Diffusion of point defects , nucleation of dislocation loops , and effect of hydrogen in hcp-Zr : Ab initio and classical simulations. *Journal of Nuclear Materials*, 460, pp.82–96.

Christensen, M. et al., 2014. Effect of alloying elements on the properties of Zr and the Zr–H system. *Journal of Nuclear Materials*, 445(1-3), pp.241–250.

Cockeram, B.V. et al., 2013. The use of a laser-assisted Local Electrode Atom Probe and TEM to examine the microstructure of Zircaloy and precipitate structure following low dose neutron irradiation at nominally 358°C. *Journal of Nuclear Materials*, 433(1-3), pp.460–478.

Damcott, D.L., Allen, T.R. & Was, G.S., 1995. Dependence of radiation-induced segregation on dose, temperature and alloy composition in austenitic alloys. *Journal of Nuclear Materials*, 225, pp.97–107.

Dong, Y., Motta, A.T. & Marquis, E. a., 2013. Atom probe tomography study of alloying element distributions in Zr alloys and their oxides. *Journal of Nuclear Materials*, 442(1-3), pp.270–281.

Etienne, A. et al., 2010. Atomic scale investigation of radiation-induced segregation in austenitic stainless steels. *Journal of Nuclear Materials*, 406(2), pp.244–250.

Etoh, Y. & Shimada, S., 1993. Neutron irradiation effects on intermetallic precipitates in Zircaloy as a function of fluence. *Journal of Nuclear Materials*, 200, pp.59–69.

Fidleris, V., 1988. The irradiation creep and growth phenomena. *Journal of Nuclear Materials*, 159, pp.22–42.

Francis, E.M. et al., 2014. Iron redistribution in a zirconium alloy after neutron and proton irradiation studied by energy-dispersive X-ray spectroscopy (EDX) using an aberration-corrected (scanning) transmission electron microscope. *Journal of Nuclear Materials*.

Garzarolli, F., Schumann, R. & Steinberg, E., 1994. Corrosion optimized Zircaloy for boiling water reactor (BWR) fuel elements. *Zirconium in the Nuclear Industry: Tenth International Symposium, ASTM STP 1245*, pp.709–723.

Gault, B. et al., 2013. Atom probe microscopy characterization of as quenched Zr–0.8wt% Fe and Zr–0.15wt% Cr binary alloys. *Materials Letters*, 91, pp.63–66.

Gilbert, R.W., Griffiths, M. & Carpenter, G.J.C., 1985. Amorphous intermetallics in neutron irradiated Zircaloys after hIgh fluences. *Journal of Nuclear Materials*, 135, pp.265–268.

Gilbon, D. & Simonot, C., 1994. Effect of Irradiation on the Microstructure of Zircaloy-4. *Zirconium in the Nuclear Industry: Tenth International Symposium, ASTM STP 1245*, pp.521–548.

Goll, W. & Ray, I., 2002. The Behavior of Intermetallic Precipitates in Highly Irradiated BWR LTP Cladding. *Zirconium in the Nuclear Industry: Thirteenth International Symposium, ASTM STP 1423*, pp.80–95.

Griffiths, M., 1988. A review of microstructure evolution in zirconium alloys during irradiation. *Journal of Nuclear Materials*, 159, pp.190–218.

Griffiths, M., 1993. Comment on Fe-distribution in zr-2.5Nb pressure tubing. *Journal of Nuclear Materials*, 207, pp.353–356.

Griffiths, M., 1990. Comments on precipitate stability in neutron-irradiated Zircaloy-4. *Journal of Nuclear Materials*, 170, pp.294–300.

Griffiths, M. et al., 1992. *Evolution of microstructure in zirconium allo core components of nuclear reactors during service*, Ontario K0J 1J0.

Griffiths, M., Gilbert, R.W., et al., 1987. Neutron damage in zirconium alloys irradiated at 644 to 710 K. *Journal of Nuclear Materials*, 150(2), pp.159–168.

Griffiths, M. & Gilbert, R.W., 1987. The Formation of c-component defects in zirconium alloys during neutron irradiation. *Journal of Nuclear Materials*, 150, pp.169–181.

Griffiths, M., Gilbert, R.W. & Carpenter, G.J.C., 1987. Phase instability, decomposition and resdistribution of intermetallic precipitates in Zircaloy-2 and -4 during neutron irradiation. *Journal of Nuclear Materials*, 150, pp.53–66.

Griffiths, M., Gilbert, R.W. & Coleman, C.E., 1988. Grain boundary sinks in neutron-irradiated Zr and Zr-alloys. *Journal of Nuclear Materials*, 159, pp.405–416.

Griffiths, M., Gilbert, R.W. & Fidleris, V., 1989. Accelerated irradiation growth of zirconium alloys. *Zirconium in the Nuclear Industry: Eighth International Symposium*, pp.658–677.

Griffiths, M., Holt, R.A. & Rogerson, A., 1995. Microstructural aspects of accelerated deformation of Zircaloy nuclear reactor components during service. *Journal of Nuclear Materials*, 225, pp.245–258.

Griffiths, M., Mecke, J.F. & Winegar, J.E., 1996. Evolution of Microstructure in Zirconium Alloys During Irradiation. *Zirconium in the Nuclear Industry: Eleventh International Symposium, ASTM STP 1295*, pp.580–602.

Hallstadius, L., Johnson, S. & Lahoda, E., 2012. Cladding for high performance fuel. *Progress in Nuclear Energy*, 57, pp.71–76.

Holt, R. a. & Gilbert, R.W., 1986. c-component dislocations in annealed Zircaloy irradiated at about 570 K. *Journal of Nuclear Materials*, 137(3), pp.185–189.

Holt, R.A., 1988. Mechanisms of irradiation growth of alpha-zirconium alloys. *Journal of Nuclear Materials*, 159, pp.310–338.

Hu, R., Smith, G.D.W. & Marquis, E.A., 2012. Atom probe study of radiation induced grain boundary segregation/depletion in a Fe-12%Cr alloy. *Progress in Nuclear Energy*, 57, pp.14–19.

Huang, P.Y., Mahmood, S.T. & Adamson, R.B., 1996. Effects of thermomechanical processing on in-reactor corrosion and post-irradiation mechanical properties of Zircaloy-2. *Zirconium in the Nuclear Industry: Eleventh International Symposium, ASTM STP 1295*, pp.726–757.

Hudson, D. & Smith, G.D.W., 2009. Initial observation of grain boundary solute segregation in a zirconium alloy (ZIRLO) by three-dimensional atom probe. *Scripta Materialia*, 61(4), pp.411–414.

Idrees, Y., Yao, Z., Kirk, M. a., et al., 2013. In situ study of defect accumulation in zirconium under heavy ion irradiation. *Journal of Nuclear Materials*, 433(1-3), pp.95–107.

Idrees, Y., Yao, Z., Sattari, M., et al., 2013. Irradiation -nduced microstructural changes in Zr-Excel alloy. *Journal of Nuclear Materials*, 441, pp.138–151.

Jiao, Z. & Was, G.S., 2011a. Novel features of radiation-induced segregation and radiation-induced precipitation in austenitic stainless steels. *Acta Materialia*, 59(3), pp.1220–1238.

Jiao, Z. & Was, G.S., 2011b. Segregation behavior in proton- and heavy-ion-irradiated ferritic-martensitic alloys. *Acta Materialia*, 59(11), pp.4467–4481.

Jostsons, A. et al., 1977. Faulted loops in neutron-irradiated zirconium. *Journal of Nuclear Materials*, 68, pp.267–276.

Kuksenko, V., Pareige, C. & Pareige, P., 2012. Intra granular precipitation and grain boundary segregation under neutron irradiation in a low purity Fe-Cr based alloy. *Journal of Nuclear Materials*, 425(1-3), pp.125–129.

Kuri, G. et al., 2010. Micro-focussed XAFS spectroscopy to study Ni-bearing precipitates in the metal of corroded Zircaloy-2. *Applied Physics A: Materials Science and Processing*, 98, pp.625–633.

Kuwae, R. et al., 1983. Mechanism of Zircaloy nodular corrosion. *Journal of Nuclear Materials*, 119, pp.229–239.

Mahmood, S.T. et al., 2000. Post-Irradiation Characterization of ultra-high fluence zircaloy-2. *Zirconium in the Nuclear Industry: Twelfth International Symposium, ASTM STP 1354*, pp.139–169.

Marquis, E.A., Hu, R. & Rousseau, T., 2011. A systematic approach for the study of radiation-induced segregation/depletion at grain boundaries in steels. *Journal of Nuclear Materials*, 413(1), pp.1–4.

Marquis, E.A., Lozano-Perez, S. & Castro, V. De, 2011. Effects of heavy-ion irradiation on the grain boundary chemistry of an oxide-dispersion strengthened Fe-12 wt.% Cr alloy. *Journal of Nuclear Materials*, 417(1-3), pp.257–261.

Meng, X. & Northwood, D., 1989. Second phases in Zircaloy-2. *Journal of Nuclear Materials*, 168, pp.125–136.

Motta, A.T., 1997. Amorphization of intermetallic compounds under irradiation — A review. *Journal of Nuclear Materials*, 244, pp.227–250.

Motta, A.T., Howe, L.M. & Okamoto, P.R., 1994. *Amorphization Kinetics of Zr(Fe,Cr)2 under ion irradiation*,

Motta, A.T., Lefebvre, F. & Lemaignan, C., 1991. Amorphization of Precipitates in Zircaloy under Neutron and Charged-Particle Irradiation. *Zirconium in the Nuclear Industry: Ninth International Symposium, ASTM STP 1132*, pp.718–

739.

Moura, C.S. et al., 2001. Point defect energetics in the ZrNi and Zr2Ni intermetallics. *Nuclear Instruments and Methods in Physics Research B*, 175(177), pp.526–531.

Pasianot, R.C. & Pérez, R. a., 2013. First-principles appraisal of solute ultra-fast diffusion in hcp Zr and Ti. *Journal of Nuclear Materials*, 434, pp.158–161.

Pêcheur, D. et al., 1993. Effect of irradiation on the precipitate stability in Zr alloys. *Journal of Nuclear Materials*, 205, pp.445–451.

Perez, R.A., Nakajima, H. & Dyment, F., 2003. Diffusion in alpha-Ti and Zr. *Materials Transactions*, 44(1), pp.2–13.

Van der Sande, J.B. & Bement, A.L., 1974. An investigation of second phase particles in Zircaloy-4 alloys. *Journal of Nuclear Materials*, 52, pp.115–118.

Sawabe, T. et al., 2013. Analysis of atomic distribution in as-fabricated Zircaloy-2 claddings by atom probe tomography under high-energy pulsed laser. *Journal of Nuclear Materials*, 442, pp.168–174.

Shishov, V.N. et al., 2005. Influence of structure-phase state of Nb containing Zr alloys on irradiation-induced growth. *Zirconium in the Nuclear Industry: 14th Symposium*, 2(8), pp.666–685.

Simonen, E.P., Chariot, L.A. & Bruemmer, S.M., 1995. Quantification of defect-solute coupling from inverse-Kirkendall segregation. *Journal of Nuclear Materials*, 225, pp.117–122.

Stoller, R.E. et al., 2013. On the use of SRIM for computing radiation damage exposure. *Nuclear Instruments and Methods in Physics Research B*, 310, pp.75–80.

Stupel, M.M., Bamberger, M. & WEiss, B.Z., 1985. Determination of Fe solubility in αZr by Mössbauer spectroscopy. *Scripta Metallurgica*, 19, pp.739–740.

Sundell, G. et al., Redistribution of alloying elements in Zircaloy-2 after in-reactor exposure. *Journal of Nuclear Materials*.

Tournadre, L. et al., 2012. Experimental study of the nucleation and growth of c-component loops under charged particle irradiations of recrystallized Zircaloy-4. *Journal of Nuclear Materials*, 425(1-3), pp.76–82.

Valizadeh, S. et al., 2014. Effects of Secondary Phase Particle Dissolution on the In-Reactor Performance of BWR Cladding. *Journal of ASTM International*, 8(2), pp.729–753.

Vatter, I.A. & Titchmarsh, J.M., 1989. measurement of grain boundary segregation

by STEM-EDX analysis. *Ultramicroscopy*, 28, pp.236–239.

Was, G.S., 2007. Fundamentals of Radiation Materials Science. In *Fundamentals of Radiation Materials Science*. Springer Berlin Heidelberg New York, p. 83.

Was, G.S., 2000. The damage cascade. In *Fundamentals of Radiation Materials Science*. Springer Berlin Heidelberg New York, pp. 125–154.

Wharry, J.P. et al., 2011. Radiation-induced segregation and phase stability in ferritic-martensitic alloy T 91. *Journal of Nuclear Materials*, 417(1-3), pp.140–144.

Wharry, J.P., Jiao, Z. & Was, G.S., 2012. Application of the inverse Kirkendall model of radiation-induced segregation to ferritic-martensitic alloys. *Journal of Nuclear Materials*, 425(1-3), pp.117–124.

Woo, C.., 2000. Defect accumulation behaviour in hcp metals and alloys. *Journal of Nuclear Materials*, 276(1-3), pp.90–103.

Woo, C.H., 1987. Effects of Anisotropic Diffusion on Irradiation Deformation. In *Radiation-Induced Changes in Microstructre: 13th International Symposium (PART I), ASTM STP 955*. pp. 70–89.

Woo, C.H., 1988. Theory of irradiation deformation in non-cubic metals: effects of anisotropic diffusion. *Journal of Nuclear Materials*, 159, pp.237–256.

Woo, C.H. & Göslel, U., 1983. Dislocation bias in an anisotropic diffusive medium and irradiation growth. *Journal of Nuclear Materials*, 119, pp.219–228.

Woo, C.H. & Singh, B.N., 1992. Production bias due to clustering of point defects in irradiation-induced cascades. *Philosophical Magazine A*, 65(4), pp.889–912.

Yang, W.J.S., 1988. Precipitate stability in neutron-irradiated Zircaloy-4. *Journal of Nuclear Materials*, 158, pp.71–80.

Yang, W.J.S., Tucker, R.P. & Adamson, R.B., 1986. Precipitates in Zircaloy: Identification and the Effects of Irradiation and Thermal Treatment. *Journal of Nuclear Materials*, 138, pp.185–195.

Zee, R.H. et al., 1984. Effect of tin on the irradiation growth of polycrystalline zirconium. *Journal of Nuclear Materials*, 120, pp.223–229.

Zou, H. et al., 1994. Solute distribution in annealed Zircaloy-2 and Zr-2.5Nb. *Journal of Nuclear Materials*, 208, pp.159–165.

Zou, H. et al., 1995. The solid solubility of Ni and Co in α-Zr: a secondary ion mass spectrometry study. *Journal of Nuclear Materials*, 223, pp.186–188.

Zu, X.T. et al., 2005. Effect of proton and Ne irradiation on the microstructure of Zircaloy 4. *Philosophical Magazine*, 85(4-7), pp.649–659.

4.2 MANUSCRIPT 2: A COMPARISON OF PROTON AND NEUTRON IRRADIATION-INDUCED DISLOCATION LOOP EVOLUTION AND ASSOCIATED MICROCHEMICAL CHANGES IN ZIRCALOY-2

Submission: The following anuscript will be submitted to *Acta Materialia* or *The Journal of Nuclear Materials*

Contribution: The present author wrote this manuscript and performed all dislocation and chemical analysis in the proton-irradiated material and all of the chemical analysis in the proton- and the neutron-irradiated material, as well as the interpretation and discussion of all results. Daniel Jãdernas prepared the neutron-irradiated material for microscopy and performed the dislocation analysis in the neutron-irradiated material as part of collaboration with Studsvik Nuclear AB. Philipp Frankel, Christopher Race and Michael Preuss provided supervisory support and contributed helpful corrections to the main body of the text. Javier Romero, Lars Hallstadius and Edward C. Darby are industrial collaborators and contributed to the present work by provision of material and insightful discussion.

A COMPARISON OF PROTON AND NEUTRON IRRADIATION-INDUCED DISLOCATION LOOP EVOLUTION AND ASSOCIATED MICROCHEMICAL CHANGES IN ZIRCALOY-2

A. Harte[1], D. Jädernäs[2], P. Frankel[1], C. Race[1], J. Romero[3], L. Hallstadius[4], E. C. Darby[5], M.Preuss[1]

[1]The University of Manchester, Manchester Materials Science Centre, Grosvenor Street, Manchester, M13 9PL, United Kingdom

[2]Studsvik Nuclear AB, SE 611 82 Nyköping, Sweden

[3]Westinghouse Electric Company, Columbia, SC, United States

[4]Westinghouse Electric Sweden AB, SE---72163 Västerås, Sweden

[5]Rolls Royce Plc., Nuclear Materials, Derby, UK

Contact: Allan Harte, allan.harte@manchester.ac.uk

1 Abstract

We compare the dislocation type, morphology and density of a-loops and c-loops in Zircaloy-2 between test samples irradiated with 2 MeV proton at ~6.7 x10^{-6} dpa s^{-1} and 350 °C to doses of 2.3, 4.7 and 7.0 dpa and samples of BWR cladding irradiated in reactor to neutron fluences between 14.5 and 24.5 dpa (8.7 and 14.7 x10^{25} n m^{-2}). The a- and c-loop density increase with irradiation dose. We provide evidence that may explain the delayed onset of c-loop nucleation and its dependence on the alignment of a-loops parallel to the trace of the basal plane. In both the proton- and neutron-irradiated material, chemical segregation of Fe, Ni and Cr to dislocation positions in basal traces is observed, as is the segregation of Sn in rows, anticorrelated to the positions of the light transition elements. We discuss the implications for irradiation-induced growth phenomena.

2 Introduction

Zr alloys are commonly used in nuclear reactor cores due to their low average neutron absorption cross section and their retention of acceptable mechanical

properties and corrosion resistance at operating temperatures (Hallstadius et al. 2012). Zr alloys exhibit irradiation-induced growth, which is independent of an applied stress and is characterised by a volume-conservative shape change. Pilgered, recrystallised, single phase α-Zr alloy tube has a texture corresponding to grain <0001> axes orientated at ±20-40° to the radial direction (Mahmood et al. 2000; Tenckhoff 2005). As such, the majority of <c> axes are radially aligned and the majority of <a> axes are aligned close to parallel to the axial direction of the tube. As such, irradiation-induced changes in individual grains along <c> and <a> directions is thought to contribute to macroscopic deformation along the corresponding textured tube axes. In pile, Zr alloy cladding tube grows in the axial direction and contracts in the radial, which Buckley first attributed to dislocation loops of interstitial and vacancy nature on prism and basal planes, respectively (Buckley 1961). The current framework for describing irradiation-induced growth includes Buckley's postulations, adding to it the implications of the anisotropic diffusion of point defects in the hcp lattice (Woo & Göslel 1983; Woo 1987; Woo 1988). The role of small defect clusters has gained importance in theories such as Woo's diffusional anisotropy difference model, as has the concept of a bias in the production of defects themselves (Woo & Singh 1992; Holt et al. 1993).

In Zr and its alloys there are two dominating types of dislocation loops that form during neutron irradiation and are thought to contribute to irradiation-induced growth, known as a-loops and c-loops. a-loops are the primary observable form of damage and are so-called due to their Burgers vector $\frac{1}{3}<11\bar{2}0>$ and their $\{10\bar{1}0\}$ prism habit planes (A Jostsons et al. 1977; Griffiths 1988). c-loops form after a delay to higher fluence levels and are of interest due to the correlation of the onset of their formation with increased growth strain (Holt & Gilbert 1986). c-loops have Burgers vector $\frac{1}{6}<20\bar{2}3>$ and are observed to form in rows parallel to (0001) basal planes (A. Jostsons et al. 1977; Griffiths 1988; Holt & Gilbert 1986). This type of loop is known as <c/2+p> due to its c-component and prismatic fault. Other types of c-component loops are <c/2> type with Burgers vector ½<0001> and <c+a>-type with Burgers vector $\frac{1}{3}<11\bar{2}3>$, which have been observed after electron irradiation (Griffiths 1988). Basal c-loops of $<20\bar{2}3>$-type are of special

interest due to their correlation with increased growth strain (Holt & Gilbert 1986).

An increased density of c-loops has been observed in the vicinity of partially dissolved $Zr(Fe,Cr)_2$ second phase particles (SPPs) in neutron-irradiated Zircaloy-4 in the temperature range ~290-310 °C and in proton-irradiated Zircaloy-4 at 350 °C (Griffiths & Gilbert 1987; Tournadre et al. 2012; de Carlan et al. 1996). As such, the influence of secondary phases and irradiation-induced solute redistribution on dislocation structure is of importance. This is reflected in the reduced growth strain of Zircaloy-2 in comparison with binary alloy Zr-1.5Sn (wt.%), in which the dominant microstructural difference is the lack of SPPs in the latter. The inconsistency in increased dislocation density associated with SPPs, higher growth strains associated with higher dislocation density and better irradiation-induced growth resistance in alloys containing SPPs is one that is not addressed in the literature. There is also a lack of investigations that address the irradiation-induced change matrix chemistry and its effect on the evolution of dislocation structures. The objective of the present work is to explore such relationships.

Proton irradiation has been used successfully to nucleate both a- and c-loops in Zr alloys (Zu et al. 2005; Tournadre et al. 2012; Tournadre et al. 2013), as have heavy ion irradiation experiments (Zu et al. 2005; Idrees et al. 2012; Idrees et al. 2013; Tournadre et al. 2012), although not in Zircaloy-2. The purpose of the present investigation is to quantitatively assess the dislocation structure, its evolution and its correlation with chemical evolution in the matrix of Zircaloy-2. We will examine both proton- and neutron-irradiated material in order to compare the effects of the different irradiating species and to assess the extent to which proton irradiation may be used to emulate neutron irradiation with regards to dislocation evolution with increasing irradiation dose.

3 EXPERIMENTAL

3.1 MATERIAL

Fully recrystallised Zircaloy-2 plate, nominally Zr-1.5Sn-1.4Fe-0.1Cr-0.06Ni (wt.%) (Hallstadius et al. 2012), was provided by Westinghouse Electric Company and served as the non-irradiated baseline and the material for proton irradiation experiments. The plate consisted of equiaxed grains of mean diameter ~5-15 μm. The texture of the plate was assessed by orientation analysis of low spatial resolution electron backscatter diffraction scans in a FEI Quanta 650 scanning electron microscope with a field emission gun source, operating at a step size equal to 4 μm, 80% of the lower end of the grain size range. This approach samples tens of thousands of grains to obtain the macrotexture, displayed in Figure 4.2.1 as pole figures with colour contouring in multiples of random as calculated in Mambo of the the HKL CHANNEL5 software package. The plate exhibits a split basal texture ±30° in the transverse direction, in agreement with X-ray diffraction measurements of texture in rolled and recrystallised Zircaloy-2 plate (Mahmood et al. 2000).

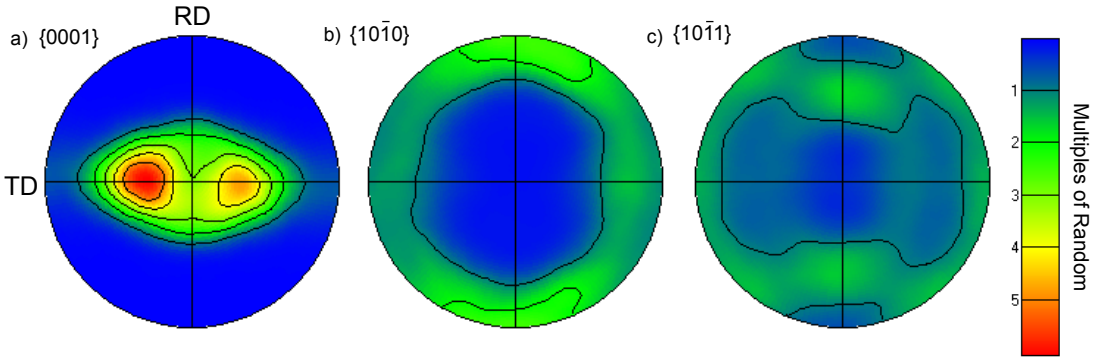

Figure 4.2.1 a)-c) give the pole figures for the {0001}, {10$\bar{1}$0} and {10$\bar{1}$1} planes from the normal direction (ND) of the non-irradiated Zircaloy-2 plate. The transverse direction (TD) and rolling direction (RD) are in the horizontal and vertical direction, respectively. The split basal shown in {0001} is typical of recrystallised Zr alloys and is an important feature as the grains are both proton-irradiated and examined by S/TEM from the ND.

In preparation for the proton irradiation experiments, the plate was cut into bars of dimensions 2 x 2 x 20 mm with the long axis in the TD-RD plane (transverse and rolling direction, respectfully) and mechanically polished from the normal direction to a quality such that the grains were visible by polarised light microscopy and the sample suitable was for electron backscatter diffraction analysis. The bars were then proton-irradiated from the normal direction at the Michigan Ion Beam Laboratory's 1.7 MeV Tandertron accelerator facility at 2 MeV and 350 ±9 °C to doses of 2.3, 4.7 and 7.0 displacements per atom (dpa) at a current of ~0.2 μA mm^{-2}, resulting in a damage rate of ~6.7 $x10^{-6}$ dpa s^{-1}. The proton irradiation dose (dpa) level was determined at 60% of the maximum proton penetration depth (max 30 μm), calculated by the quick Kinchin-Pease calculation in SRIM as recommended by Stoller *et al.* (Stoller et al. 2013). TEM foils were prepared for examination at this depth by grinding from the non-irradiated face to a thickness of ~160 μm and then electropolishing using a twin-jet Tenupol-5 electropolisher together with a Julabo FP50 cooling unit. An electrolyte of 10% perchloric acid and 20% 2-butoxyethanol in ethanol (Tournadre et al. 2012) was used at 0 °C to electropolish ~12-15 μm from both the irradiated and non-irradiated faces. Then, Elektron Technology's acid-resistant Lacomit varnish was used to protect the irradiated face while electropolishing to perforation for the non-irradiated face. The non-irradiated bulk material was prepared by the same method.

The neutron-irradiated material was supplied by Westinghouse and Studsvik in the form of electropolished TEM foils from the cladding material of a BWR (280-330 °C (Azevedo 2011)), irradiated to neutron fluences between 8.7 and 14.7 $x10^{25}$ n m^{-2}. For the purposes of the present work, the conversion between neutron fluence and dpa is taken to be be 0.6 $x10^{25}$ n m^{-2} dpa^{-1} (Shishov et al. 2005) and the damage rate in light water reactors is considered to be ~6-1 $x10^{17}$ n m^{-2} s^{-1} (Griffiths et al. 1996; Shishov et al. 2005; Adamson 2014). As such, the neutron irradiated material was irradiated at a damage rate of ~1 $x10^{-7}$ dpa s^{-1} to doses of between 14.5 and 24.5 dpa. The damage rate in the proton irradiation experiments is therefore higher than that experienced by the neutron-irradiated material by a

factor of ~70. To allow more diffusion to occur under such a high damage rate, a temperature shift of 40 °C was applied to the proton irradiation experiment (as recommended by Was et al. (Was 2007)), which was performed at 350 °C as opposed to the average 280-330 °C in a BWR (Azevedo 2011).

3.2 MICROSCOPIC ANALYSIS

With the exception of Figure 4.2.2, all microscopy was performed on a G2 80-200 kV spherical aberration-corrected (single, probe) FEI Titan microscope operating at 200 kV in scanning mode with a current of 0.6 nA. The microscope is equipped with a high brightness X-FEG electron gun and the FEI ChemiSTEM™ system, comprising four energy-dispersive X-ray sprectroscopy (EDS) detectors in close proximity to the sample, resulting in a total collection solid angle of 0.7 srad. Due to the close proximity of the EDS detectors to the sample, conventional transmission electron microscopic bright-field (TEM BF) imaging was deemed inappropriate as the large number of secondary electrons that arise from collision with the objective aperture would saturate the detectors and limit their lifetime. As such, the BF TEM/STEM comparison in Figure 4.2.2 was performed on a FEI Tecnai TF30 300 kV FEG-AEM operated at 300 kV.

Before quantification of a-loop dislocation density two sensitivity studies were performed. First, a focal series was obtained by recording images at varying focus. This was done to ensure that no dislocations were missed by the sub-angstrom aberration-corrected probe. Additionally, a series of images with different convergence angles was obtained by varying the size of the second condenser aperture. This was done in order to account for larger convergence angles allowing more diffraction to take place and thus highlighting more dislocations. Neither investigation proved to change the number of dislocations counted in a single image. Quantification of a-loop density in the proton-irradiated material was achieved by obtaining BF STEM images at the $<10\bar{1}0>$ zone axis and counting defects with an elliptical nature. All loops are considered visible at this orientation. Quantification of c-loop density was performed in BF STEM from an orientation parallel to the **g** = 0002 systematic row, such that they are observed edge-on as

projected line segments. Indexing of matrix orientation was performed on fast Fourier transforms (FFTs) of atomic or lattice plane high-resolution BF STEM images. At least five images were obtained for each of the a- and c-loop quantifications at all proton dose levels. For quantification, all images of a-loops were obtained at magnification 225k x and all images of c-loops were obtained at magnification 115k x. Foil thickness measurements were made by an assessment of intensity oscillations in convergent beam electron diffraction (CBED) patterns by way of the graphical method (Williams & Carter 2009). Error in thickness measurements are therefore assumed to be ±10%, given that great care was taken to obtain CBED patterns from the exact Bragg condition.

Quantification of dislocation loop density in the neutron-irradiated material was performed by Studsvik Nuclear AB using a JEOL 2100F microscope, operating at 200 kV in BF mode. a-loop determination was made parallel to the $\mathbf{g} = 10\bar{1}1$ systematic row, where ⅓ of a-loops are invisible. As such, a-loop measurements made at this orientation were multiplied by a factor of 1.5 to obtain the true density. c-loop determination was made parallel to the $\mathbf{g} = 0002$ systematic row. At least 5 images from different grains were obtained. a-loop images were obtained at a magnification 40-60k x and c-loops at 80-120k x. All thickness measurements were made by t/λ determinations in the EELS spectra, and as such are considered to be correct to within ±10%.

For chemical analysis in both the proton- and neutron-irradiated material, the sample was loaded in a low-background double-tilt holder. Due to the small concentration of alloying elements within the matrix, no quantification was attempted. All chemical data was obtained by spectral imaging (a full spectrum up to 20 keV at every pixel), after which chemical maps were extracted for the relevant alloying elements and are displayed in raw counts, each individually scaled. All chemical segregation data were obtained from high symmetry zone axes, and as such electron channelling phenomena may be occurring in the pristine matrix but les so at defect positions.

It is important to note that the results presented here are shown together with manipulated values from literature. For instance, c-loop sizes from the literature are commonly provided as a length when projected from the **g** = 0002 systematic row and in the present work these lengths have been taken as diameters of a circular loop and have therefore been multiplied by π to obtain the loop line length. This is the approach used for the proton and neutron-irradiated data obtained in the present work and is justified by the circular shape of c-loops shown here for the first time. For the proton-irradiated material, the thickness of the foil was taken into account, such that if the loop diameter was larger than the thickness then a loop of diameter equal to the thickness was ascribed to that loop.

4 RESULTS

4.1 DISLOCATION LOOP BURGERS VECTOR AND HABIT PLANE IN PROTON-IRRADIATED ZIRCALOY-2

A BF TEM and STEM image of the same grain at the same magnification is given in Figure 4.2.2. The grain was found in a sample proton-irradiated to 2.3 dpa and shows pronounced bend contours corresponding to the $<11\bar{2}0>$ zone axis (indexed by the selected area diffraction pattern given in inset of Figure 4.2.2a. A bent grain such as this would be unsuitable for dislocation analysis, but it is useful as an extreme example of the difference between imaging techniques. The bend contours are much reduced in the BF STEM image due to the convergence of the electron beam, as many diffraction conditions contribute to the image and so the contrast is reduced. As such, dislocations may be observed close to high symmetry orientations, which is difficult in conventional TEM analysis of irradiated Zr alloys. Dislocation loops in the red square of Figure 4.2.2b are readily observed near this $<11\bar{2}0>$ zone axis by way of BF STEM, shown in Figure 4.2.2c.

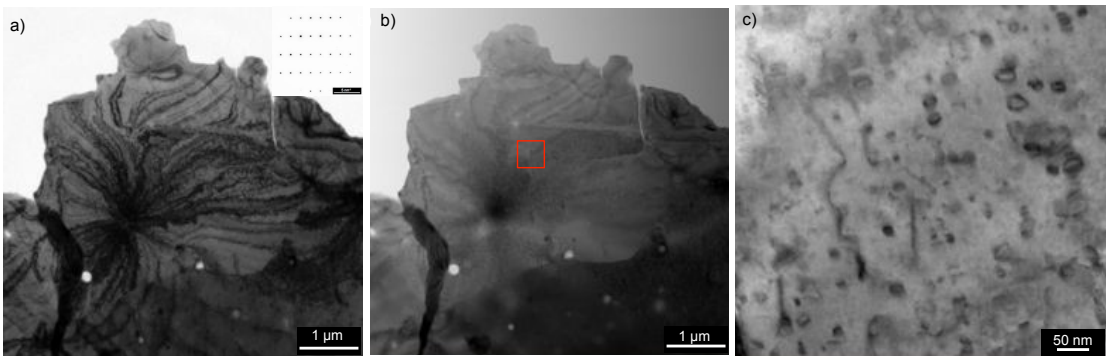

Figure 4.2.2 a) and b) show BF TEM and STEM images for the same grain at the same orientation and magnification after proton irradiation to 2.3 dpa. The inset in a) is a selected area diffraction pattern, indexing the zone axis at the centre of the bend contours as the $<11\bar{2}0>$. The bend contours are greatly reduced in b) due to the convergence of the scanning probe. The BF STEM image of irradiation-induced dislocations in c) is from the region highlighted by the red square in b) at an orientation close to the zone axis.

The images in Figure 4.2.3 demonstrate a Burgers vector analysis of dislocations in Zircaloy-2, proton-irradiated to 2.3 dpa. The fiducial marker at the top of the image is a large surface oxide. The inserts at the top right of each image are fast Fourier transforms (FFTs) of the high resolution BF STEM image at the orientation that the image was acquired. The image in Figure 4.2.3a was obtained ~9° from the $<1\bar{1}00>$ zone axis along the $\{11\bar{2}0\}$ Kikuchi band, highlighting the $\mathbf{g} = 11\bar{2}0$ systematic row and showing defect contrast. The image in Figure 4.2.3b shows the same region but ~9° from the $<11\bar{2}0>$ zone axis, highlighting the $\mathbf{g} = 1\bar{1}00$ systematic row. The defect contrast is greatly reduced in Figure 4.2.3b. In Figure 4.2.3c, the sample is tilted such that the beam is parallel to the **g** = 0002 systematic row. In this final image, the defect contrast is reduced in comparison to Figure 4.2.3a. This confirms that the defect contrast arises from dislocation loops with Burgers vector $<11\bar{2}0>$-type, i.e. a-loops. It should be noted that for the Burgers vector analysis in Figure 4.2.3, images were taken on the $<1\bar{1}00>$ and $<11\bar{2}0>$ zone axes and then every 3° away from these zone axes, along the $\{11\bar{2}0\}$ and $\{1\bar{1}00\}$ Kikuchi bands, respectively. The dislocations showed contrast at both zone axes, but they retained their contrast along $\{11\bar{2}0\}$ and lost their contrast along

$\{1\bar{1}00\}$. After 9° tilting the images did not further change in contrast, but the size and shape of defects along $\{11\bar{2}0\}$ differed as the deviation from the habit plane increased. Therefore, care must be taken when determining the Burgers vector of dislocations with BF STEM, as the convergence of the probe highlights more diffraction conditions than the parallel beam in conventional TEM. The $<11\bar{2}0>$-type a-loops were observed at all proton dose levels studied, 2.3, 4.7 and 7.0 dpa.

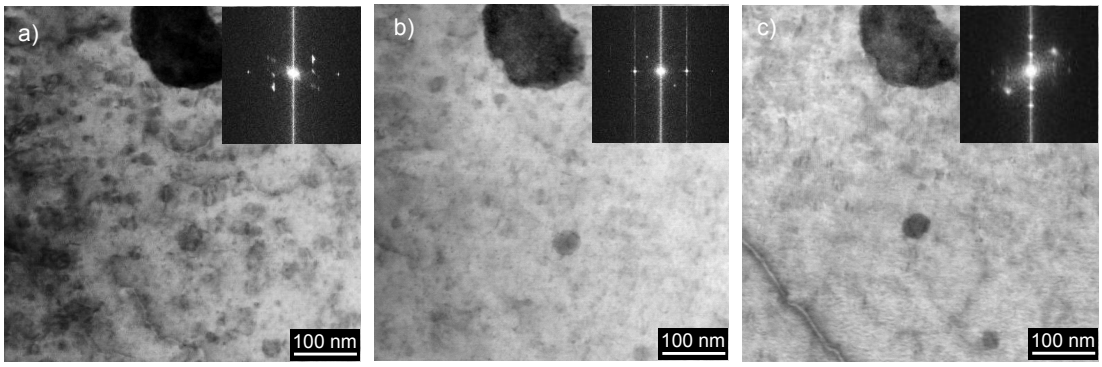

Figure 4.2.3 BF STEM images obtained after proton irradiation to 2.3 dpa. a) and b) were obtained from parallel to the **g** = $11\bar{2}0$ and $1\bar{1}00$ systematic rows, respectively, ~9° from the $<1\bar{1}00>$ and $<11\bar{2}0>$ zone axes, respectively. Part c) shows a BF STEM image of the same region with the crystal parallel to the **g** = 0002 systematic row. The insets in each image are the fast Fourier transforms of the high resolution BF STEM image at that orientation. The large particle at the top of the image is a surface oxide and acts as a fiducial marker. The visibility of defects in a) and not b) and c) confirms the defects to be a-loops with Burgers vector $<11\bar{2}0>$-type. The long defect to the bottom left of c) is invisible in a) and b), and, as such, is a dislocation of Burgers vector <0001>-type.

A longer line defect is shown in Figure 4.2.3c which is invisible under the diffraction conditions of Figure 4.2.3a and b, suggesting the presence of larger loops with Burgers vector <0001>-type, i.e. likely <c/2> loops. However, such loops were only present in very low number density. When imaging from the $<11\bar{2}0>$ zone axis or close to it parallel to the **g** = 0002 systematic row, other defects were observed as rod- or plate-like and tilted by 15° from the <0001> direction, i.e. with their long axis in the $<10\bar{1}4>$ direction and having a possible habit plane of {20-21} if it is assumed that the defects are viewed edge-on from the $<11\bar{2}0>$ orientation. These defects may be dislocation loops with Burgers vector

$<11\bar{2}3>$-type, i.e. <c+a> loops, and were observed to some degree at all of the proton dose levels studied (2.3, 4.7 and 7dpa) although a full Burgers vector analysis was not performed as such dislocations were in low number density. Alternatively, these defects could be platelets or rods as a result of irradiation-induced nano-precipitation. As the <c/2>-loops were in low density and the nature of the possible <c+a>-loops uncertain, they have not been included in any density quantification; they are simply noted for completeness. <c/2+p> loops, i.e. those with a Burgers vector <2-203>-type, referred to as c-loops hereafter, were observed at 4.7 and 7.0 dpa lying parallel to the trace of the (0001) plane and were quantified in terms of number and line density, as were the a-loops with Burgers vector $<11\bar{2}0>$-type.

It was found that the best way to observe the a-loops was to view them from parallel to an <a>-direction zone axis. The determination of the habit plane by BF STEM is shown in Figure 4.2.4, in which Figure 4.2.4a and b show the same area at two different zone axes; the $<1\bar{1}00>$ and $<11\bar{2}0>$ axes, respectively. Higher magnification images for the two zone axes are given in Figure 4.2.4c and d for the $<1\bar{1}00>$ and $<11\bar{2}0>$ zone axes, respectively. Images from $<1\bar{1}00>$ show dislocations with double arc contrast, whereas images from $<11\bar{2}0>$ show the same dislocations with closed inside contrast. This is evidence in support of the majority of a-loops lying on $\{1\bar{1}00\}$ habit planes. At the $<11\bar{2}0>$ zone axis, one may expect one third of the dislocations with Burgers vector $<11\bar{2}0>$ to be invisible with respect to an image acquired at the $<1\bar{1}00>$ zone axis. However, all dislocations seem visible at the $<11\bar{2}0>$ orientation. This is likely to be due to a high amount of diffraction occurring at the zone axes from multiple pyramidal reflections, coupled with the high convergence of the electron probe, which samples a wide range of reflections simultaneously.

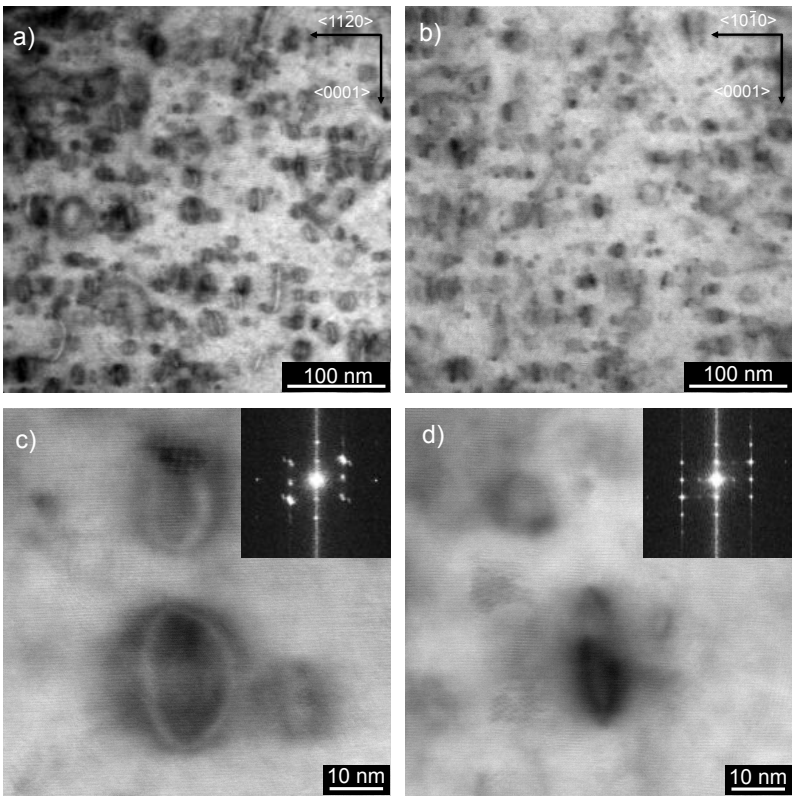

Figure 4.2.4 BF STEM images are obtained in material proton-irradiated to 2.3 dpa in the same region from a) and c) the $<1\bar{1}00>$ zone axis and b) and d) the $<11\bar{2}0>$ zone axis. Images c) and d) are taken from the very central region of images a) and b), respectively. As such, the axes in the upper right of a) and b) are the same for c) and d), respectfully, and the fast Fourier transform insets in c) and d) are applicable to a) and b), respectfully.

4.2 DISLOCATION LOOP EVOLUTION IN PROTON- AND NEUTRON-IRRADIATED ZIRCALOY-2

A qualitative summary of a-loop evolution under proton irradiation is given in Figure 4.2.5, which includes BF STEM images from samples after proton irradiation to 2.3, 4.7 and 7.0 dpa, each at the $<1\bar{1}00>$ zone axis in order to observe the loops on their habit plane. It can be seen that a-loops appear to increase in number density and become smaller and more organised with increasing proton dose from 2.3 to 4.7 dpa. While some alignment of loops along the trace of the basal plane is observed at 2.3 dpa, this behaviour is more evident at 4.7 dpa and 7.0 dpa. At the 7.0 dpa dose level, there seems to be a decrease in the number density of the a-loops, although this is difficult to discern from images alone of grains with varying thickness. No local decrease in the a-loop number

density was observed close to grain boundaries in the proton-irradiated Zircaloy-2.

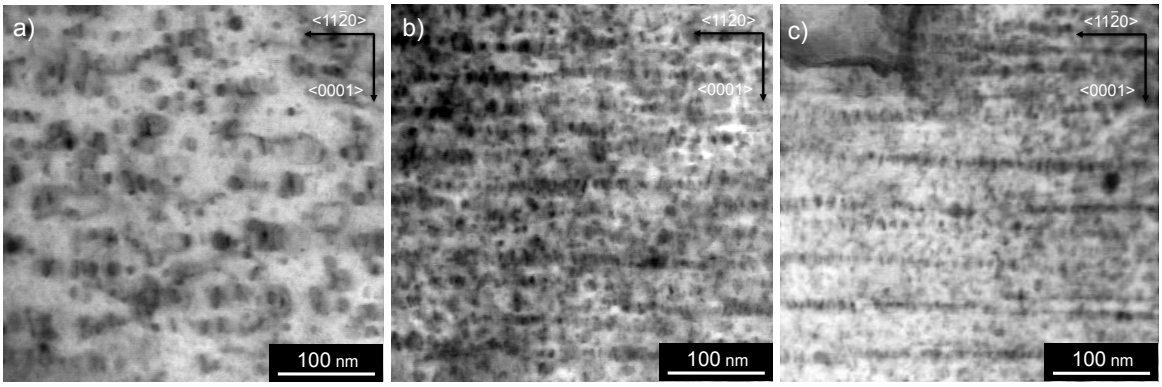

Figure 4.2.5 BF STEM images of a-loops are displayed from the $< 1\bar{1}00 >$ zone axis after proton irradiation to 2.3, 4.7 and 7.0 dpa in a)-c), respectfully. a-loops become smaller and more organised between 2.3 and 4.7 dpa, aligning parallel to the trace of the basal plane.

While no loops with the Burgers vector <2-203>-type, i.e. c-loops on basal planes, were observed at 2.3 dpa (See Figure 4.2.3c), they were observed at 4.7 and 7.0 dpa. Representative images of c-loops at these dose levels are shown in Figure 4.2.6a and b, imaged by BF STEM parallel to the **g** = 0002 systematic row such that the loops are viewed edge-on. The number density of c-loops increases between 4.7 and 7.0 dpa. Although some c-loops appeared to nucleate in the vicinity of SPPs at 4.7 dpa, as shown in Figure 4.2.6b (transmission projection issues aside), this was not statistically significant as a preferential nucleation site as there were many more c-loops observed within the matrix. At 7.0 dpa, the c-loops are of a higher number density, and some c-loops at this dose level seem larger in diameter, while others remain small. This suggests that both nucleation and growth processes are occurring at this dose level. At 7.0 dpa, the spacing between layers of aligned c-loops in the <0001> direction is ~50 nm. Figure 4.2.6c shows c-loops in Zircaloy-2 proton-irradiated to 7.0 dpa as circular from the <0001> direction. Tilting experiments proved these defects to be dislocation loops and not electropolishing-induced artefacts. To the authors' knowledge, this is the first time that c-loops have been imaged from this orientation. Finding a grain with its surface normal almost parallel to <0001> was necessary to observe these features; grains with their

surface normal close to <0001> show large similar features when imaged along <0001> but as arcs due to the loop cutting the free surface. The mean diameter of the 8 loops in Figure 4.2.6c is 161 nm with a standard deviation of 53 nm. The c-loop lines appear quite thick at ~15-20 nm.

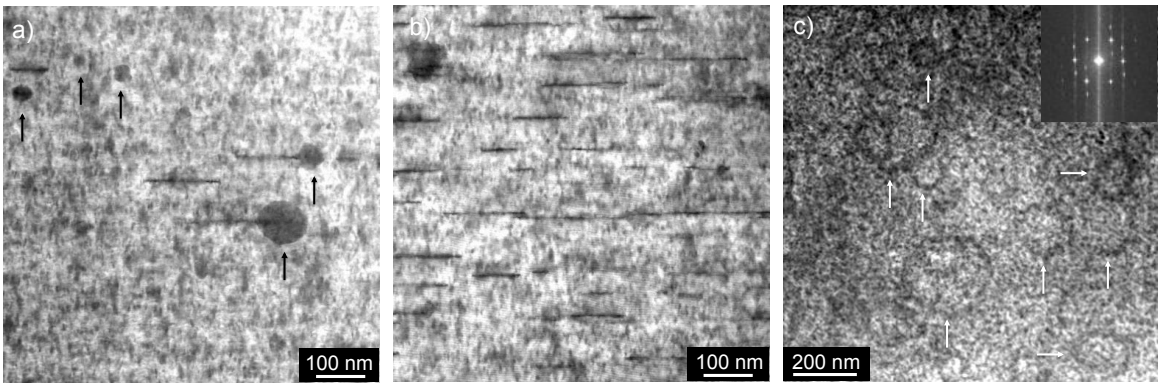

Figure 4.2.6 BF STEM images are displayed obtained from parallel to the **g** = 0002 systematic row in a) and b) after proton irradiation to 4.7 and 7.0 dpa, respectfully, with SPPs highlighted by black arrows in a). An image at this orientation for the 2.3 dpa material is shown in **Figure 4.2.3**c). No c-loops (Burgers vector <2-203>-type) are observed at 2.3 dpa, some are observed at 4.7 dpa and a higher number density is observed at 7.0 dpa. After 7.0 dpa, c-loops may be observed in c) from the <0001> zone axis (inset FFT of high resolution BF STEM image); white arrows indicate the presence of circular c-loops.

The alignment of a-loops along the trace of the basal plane at 4.7 and 7.0 dpa in Figure 4.2.5 is so similar to the alignment of c-loops that one may suggest a relationship between such damage structures. Figure 4.2.7 shows two BF STEM images in 7.0 dpa Zircaloy-2 at the same position but in slightly different orientations to highlight different diffraction conditions, the SPP in the top right corner acting as a fiducial marker. The images in Figure 4.2.7a and b are, respectively, at the $<11\bar{2}0>$ zone axis and 4° from $<11\bar{2}0>$ along the {0002} Kikuchi band. As such, the image in Figure 4.2.7a shows both a- and c-loops whereas that in Figure 4.2.7b shows only c-loops. The figures suggest that while a- and c-loops coexist along the same basal plane trace, their positions along the trace are anticorrelated. Determination of a-loop nature by way of the inside-outside contrast method (Foll & Wilkens 1975; A Jostsons et al. 1977) was attempted, but

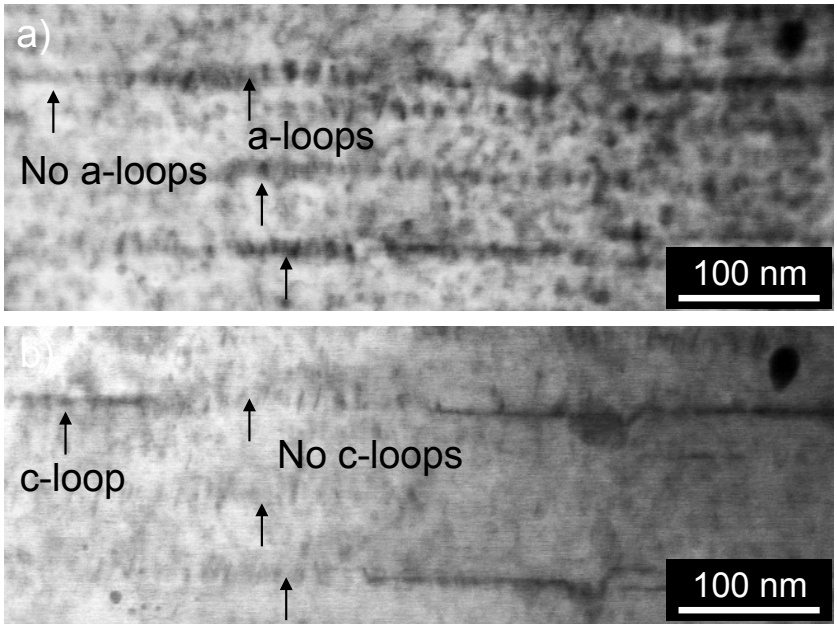

Figure 4.2.7 In Zircaloy-2 proton-irradiated to 7.0 dpa, BF STEM images are taken on-axis parallel to $<11\bar{2}0>$ in a) and 4° from $<11\bar{2}0>$ along the **g** = 0002 systematic row in b). As such, a) shows both a- and c-loops whereas b) shows only c-loops. The SPP in the upper right corner acts as a fiducial marker. The annotation shows that where there are a-loops in a) there are no c-loops in b). Likewise, where there are no a-loops n a) there is a c-loop in b). Additionally, if one looks closely, defects tilted ~15° from <0001> (vertical) can be seen above the 'No c-loops' annotation in part b).

the loops proved too small for such analysis when projected from the safe $<11\bar{2}3>$ orientation.

Representative images of a- and c-loops in neutron-irradiated Zircaloy-2 BWR cladding are given in Figure 4.2.8, acquired by conventional BF TEM imaging. Some of the a-loops in Figure 4.2.8a at neutron fluence 9.5 $x10^{25}$ n m^{-2} (~ 15.8 dpa) are indicated by white arrows. The c-loops are imaged in orientations such that all a-loops are invisible and the example in Figure 4.2.8b is also at the neutron fluence 9.5 $x10^{25}$ n m^{-2}, with evidence of preferential c-loop nucleation surrounding second phase particles. The image in Figure 4.2.8c demonstrates that c-loops dominate the microstructure at high neutron fluences of 14.7 $x10^{25}$ n m^{-2} (~24.5 dpa).

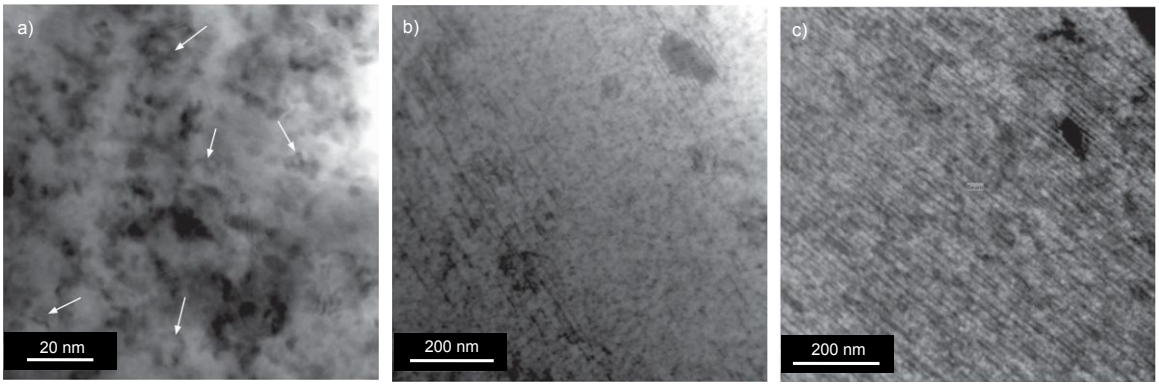

Figure 4.2.8 Representative images of a- and c-loops in the neutron-irradiated material are given in a) and b), respectively, for Zircaloy-2 irradiated in a BWR to a fluence of 9/5 x1025 n m-2 ~15.8 dpa. a-loops are imaged in BF and parallel to **g** = $10\bar{1}1$, c-loops in BF and parallel to **g** = 0002. In c), c-loops are imaged in Zircaloy-2 cladding at a neutron fluence 14.7 x10^{25} n m^{-2} ~24.5 dpa.

Quantification of a-loop number density, size and shape is given in Figure 4.2.9. For the proton-irradiated material at 2.3, 4.7 and 7.0 dpa, the number of dislocations(images) studied were 463(6), 740(5) and 437(6), respectively. In this case the BF STEM analysis was carried out from the $<1\bar{1}00>$ zone axis. In contrast, the neutron-irradiated dislocation analysis was performed by Studsvik Nuclear AB, Sweden, in conjunction with Westinghouse, using conventional TEM techniques and the invisibility criteria for a-loop determination. In Figure 4.2.9a, there is a general increase in a-loop number density in comparing the proton- and neutron-irradiated samples; a linear trend line between all of the data through the origin gives a rate of increase in number density with dose of 9 x10^{20} m^{-3} dpa^{-1}. Individually, the proton and neutron linear trend lines give rates of 8 and 9 x10^{20} m^{-3} dpa^{-1}, respectively. However, the proton data in Figure 4.2.9a show an increase in a-loop number density between 2.3 and 4.7 dpa, and a significant decrease between 4.7 and 7.0 dpa. No local decrease in the a-loop number density was observed close to grain boundaries in either the proton- or neutron-irradiated Zircaloy-2 at any dose level.

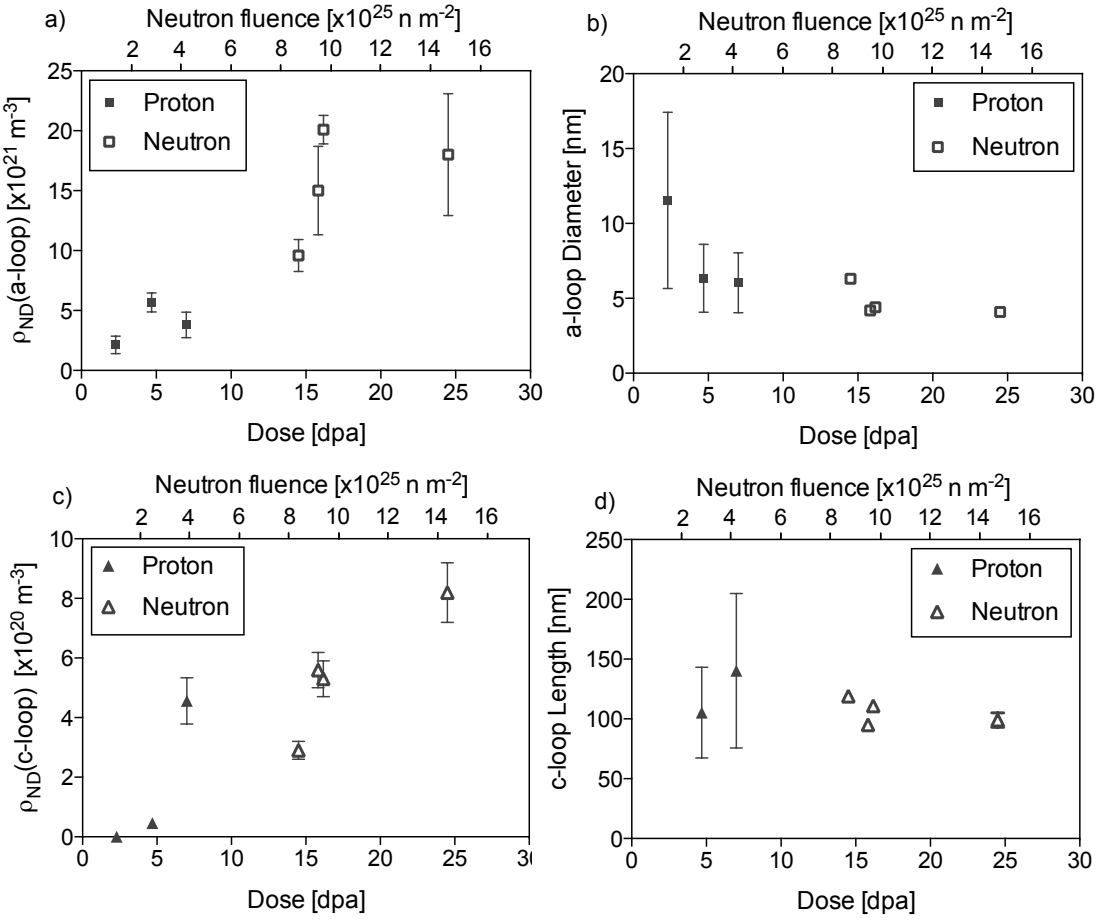

Figure 4.2.9 Quantification of dislocation number density and size. The *x*-axes in each part of the figure are on both the irradiation dose scales of displacements per atom (dpa) for the proton- and neutron-irradiated material and in neutron fluence at the top for the neutron-irradiated material. In a) and b) the a-loop number density and shape parameters are plotted, where length and width indicate the long and short axes, respectively, of the elliptical loops. The c-loop number density and diameter variation with irradiation dose is plotted in c) and d), with the latter measured as projected from parallel to the **g** = 0002 systematic row.

The a-loop size analysis is presented in Figure 4.2.9b, in which the proton data were obtained from the $<1\bar{1}00>$ zone axis by BF STEM and the neutron data by conventional TEM from close to the $<11\bar{2}0>$ zone axis. Figure 4.2.9b displays a general decreasing trend in a-loop diameter (average of ellipse length and width) with proton dose, as also evident from Figure 4.2.5. This trend is continued in the neutron-irradiated data, in which the size is relatively unchanged with increasing dose and is similar to those in the proton-irradiated material at 4.7 and 7.0 dpa.

Note that the standard deviation is small for the neutron-irradiated material (±0.2 nm) and so the error bars are smaller than the size of the data points. It should be noted that the a-loop diameters in neutron-irradiated material may be underestimated as they were not obtained from the habit plane normal and no geometrical correction was applied.

A quantification of the c-loop number density is shown in Figure 4.2.9c, which compares both proton- and neutron-irradiated material, the former determined by BF STEM at **g** = 0002 and the latter by BF TEM under similar imaging conditions. There is a general increase in c-loop number density with dose. If a linear trend line is plotted for the proton data alone (not shown in figure), c-loop nucleation is predicted to start at 4.5 dpa. Likewise, a trend line in the neutron data alone predicts c-loop nucleation at 4.9 dpa. For all of the proton and neutron data combined, the c-loop number density increases by 0.31 $x10^{20}$ dpa^{-1} after ~4.7 dpa. For the separate proton and neutron data, the number density increases by 1.78 and 0.43 $x10^{20}$ dpa^{-1}, respectively. An analysis of c-loop size is given in Figure 4.2.9d, from an orientation parallel to the **g** = 0002 systematic row. Note that the standard deviations for the neutron-irradiated c-loop lengths are smaller than the data points in the figure and so cannot be seen. Although the scatter in the proton data is large in comparison to the neutron, due to the smaller number of loops present, the mean loop diameter is approximately the same at 100-150 nm.

The dislocation number density and size data can be combined to provide the line density in units of m m^{-3} = m^{-2}, which is shown in Figure 4.2.10 as a function of irradiation dose. It can be seen that there is an almost linear increase in total (a-plus c-loop) line density with irradiation dose for both the individual proton and neutron data and for the data combined. For the proton data alone the rate of linear density increase is 0.32 $x10^{14}$ m^{-2} dpa^{-1}, although the difference in total line density between 2.3 and 4.7 dpa is smaller than between 4.7 and 7.0 dpa, which may be significant considering that at 7.0 dpa there is a decrease in a-loop line density to a level almost equal to that at 2.3 dpa and a sharp increase in c-loop line density. As such, the total proton line density data follows the trend of an irradiation-induced growth curve. For the neutron-irradiated data the linear

increase in total line density is 0.23 x10^{14} m^{-2} dpa^{-1} and for all of the proton and neutron data combined it is also 0.23 x10^{14} m^{-2} dpa^{-1}.

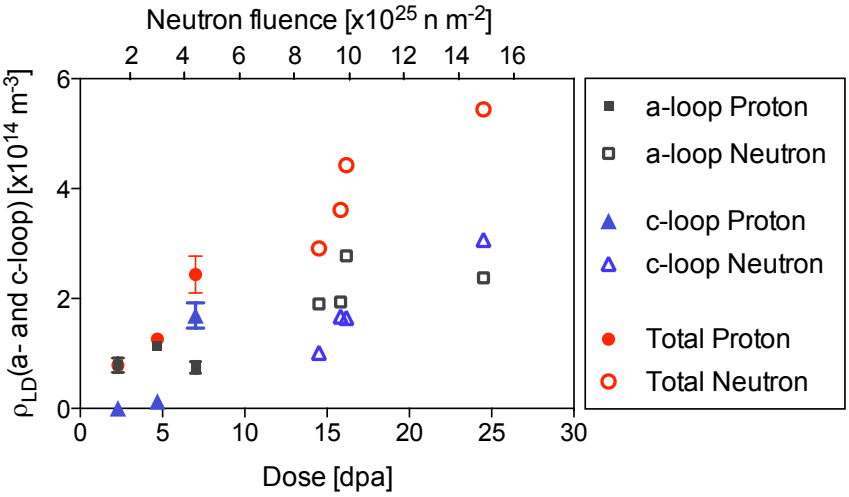

Figure 4.2.10 The variation in a- and c-loop line density is plotted as a function of irradiation dose for both proton- and neutron-irradiated Zircaloy-2, together with the total line density, a-loops + c-loops. Such data is a combination of the dislocation number density and size given in **Figure 4.2.9**.

4.3 MICROCHEMICAL CORRELATIONS TO DISLOCATION STRUCTURES

Spectral imaging at the $<11\bar{2}0>$ crystal orientation has been performed for all proton dose levels and in several of the neutron-irradiated samples, of which the BF STEM image and Zr, Sn, Fe, Cr and Ni chemical maps are displayed for proton dose levels 2.3 and 4.7 dpa in Figure 4.2.11 and Figure 4.2.13, respectively, and for a neutron fluence of 9.5 x10^{25} n m^{-2} (~15.8 dpa) in Figure 4.2.12. Each figure is representative of their respective dose levels. Figure 4.2.11c indicates that, after proton irradiation to 2.3 dpa, some segregation of Sn is observed in rows parallel to the trace of the basal plane and Figure 4.2.11d demonstrates that some nano-clustering of Fe is observed. The segregation of alloying elements within the matrix becomes more apparent after proton irradiation to 4.7 dpa, which is displayed in Figure 4.2.13. Fe and Ni are commonly coincident at this dose level and segregate in parallel rows along the trace of the basal plane. Further, the Sn segregation to the basal trace remains from the previous dose level and is spatially anti-correlated with the rows of Fe and Ni. The spatial ordering of defects in the BF image is coincident with the Fe and Ni segregation. The Cr map shows some nano-

clustering of Cr in the matrix in close proximity to the dissolving Fe-Cr SPP. Cr was found in small quantities elsewhere in the matrix, but the presence of Fe and Ni dominates. Segregation of alloying elements to the trace of the basal plane after proton irradiation to 7.0 dpa has also been observed but is not presented here due to its similarity to observations at 4.7 dpa.

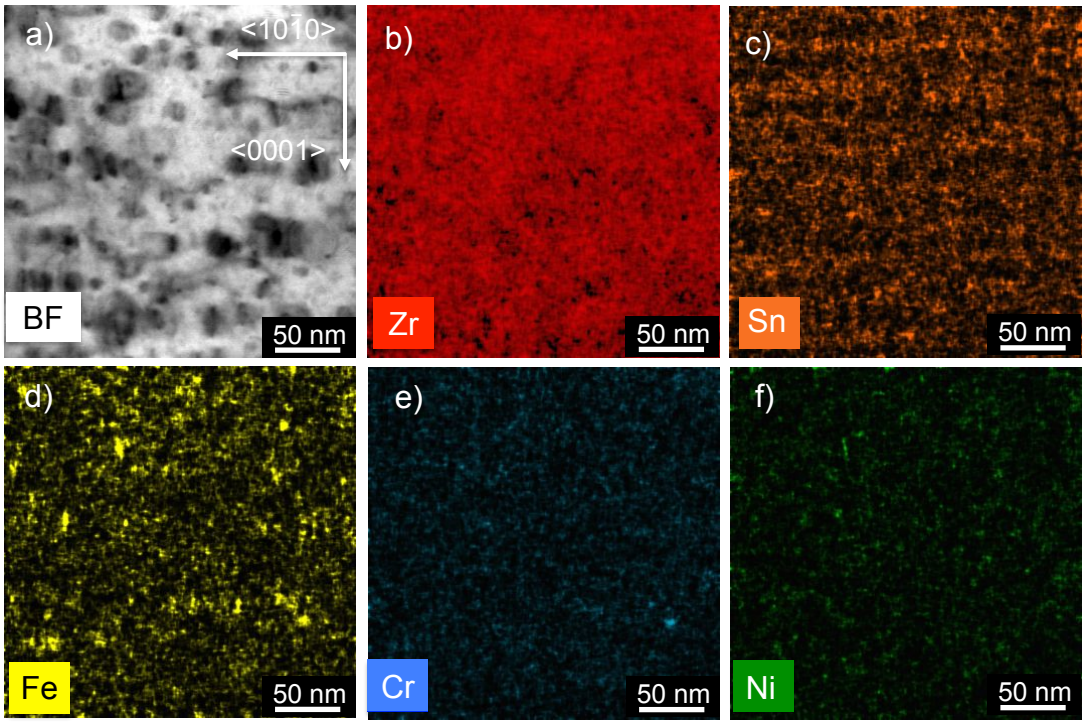

Figure 4.2.11 The BF STEM image in a) was obtained in Zircaloy-2 from the $<11\bar{2}0>$ orientation after proton irradiation to 2.3 dpa. The Zr, Sn, Fe, Cr and Ni maps are displayed in b)-f), respectively.

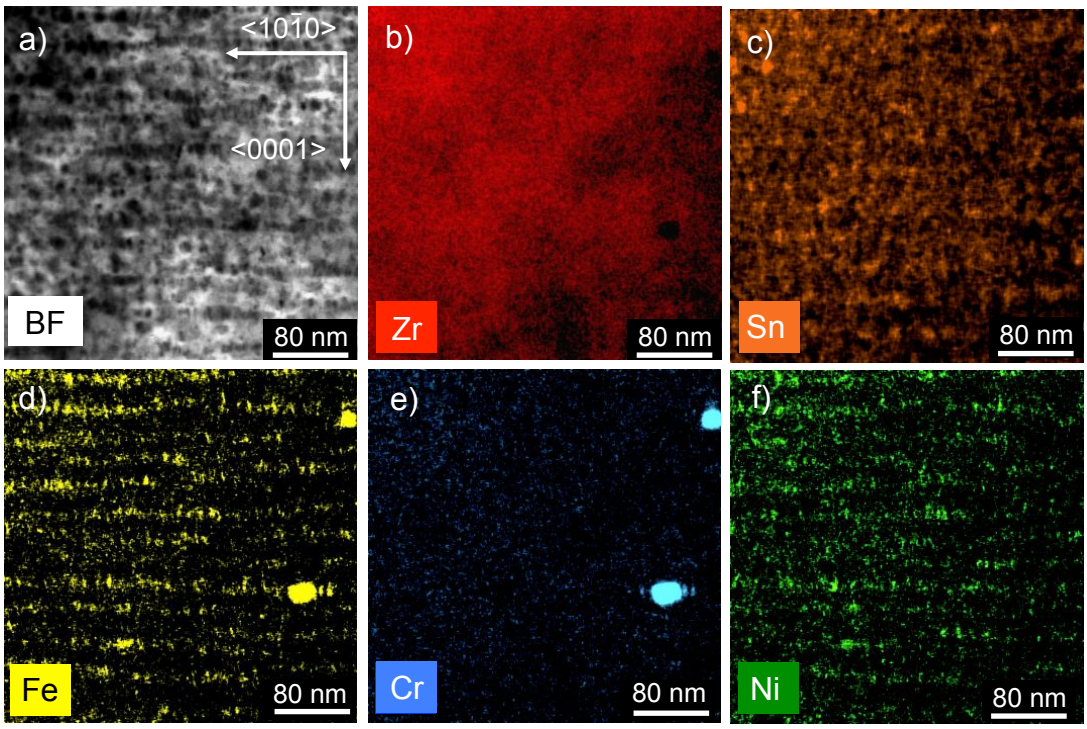

Figure 4.2.13 The BF STEM image in a) was obtained in Zircaloy-2 from the $<11\bar{2}0>$ orientation after proton irradiation to 4.7 dpa. The Zr, Sn, Fe, Cr and Ni maps are displayed in b)-f), respectively.

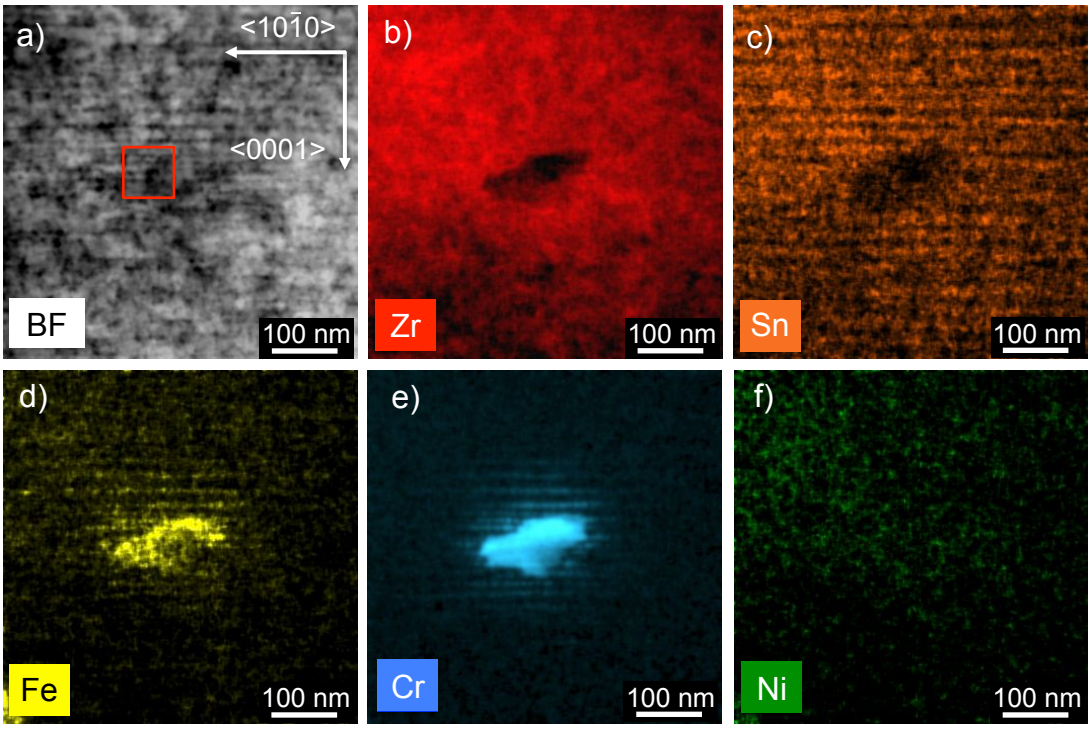

Figure 4.2.12 The BF STEM image in a) was obtained in Zircaloy-2 cladding from the $<11\bar{2}0>$ orientation after neutron irradiation in a BWR to a fluence of 9.5 x10^{25} n m^{-2} ~15.8 dpa. The Zr, Sn, Fe, Cr and Ni maps are displayed in b)-f), respectively. The region highlighted by a red square in a) is the position of the =higher magnification map displayed in **Figure 4.2.14**.

Chemical segregation in the neutron irradiated material is demonstrated in Figure 4.2.12 and is similar to the proton-irradiated case. The segregation of Sn in rows parallel to the trace of the basal plane is clear from Figure 4.2.12c. In Figure 4.2.12d and e, segregation of Fe and Cr is also observed in rows parallel to basal trace, surrounding a pre-existing Fe-Cr SPP. Any segregation in Ni is difficult to discern from the map. The red box in the BF STEM image of Figure 4.2.12a indicates the region used for a higher magnification spectral map, the results of which are displayed in Figure 4.2.14. This figure demonstrates that the segregation in Fe and Cr is discontinuous in the basal plane and takes the form of nano-clusters, not dissimilar to the nano-clusters observed after 2.3 and 4.7 dpa proton irradiation. Further, the Sn segregation may also be discontinuous. The steps in the SPP of Figure 4.2.14 are parallel to the trace of the basal plane and are equal in size to the diameter of the adjacent nano-clusters.

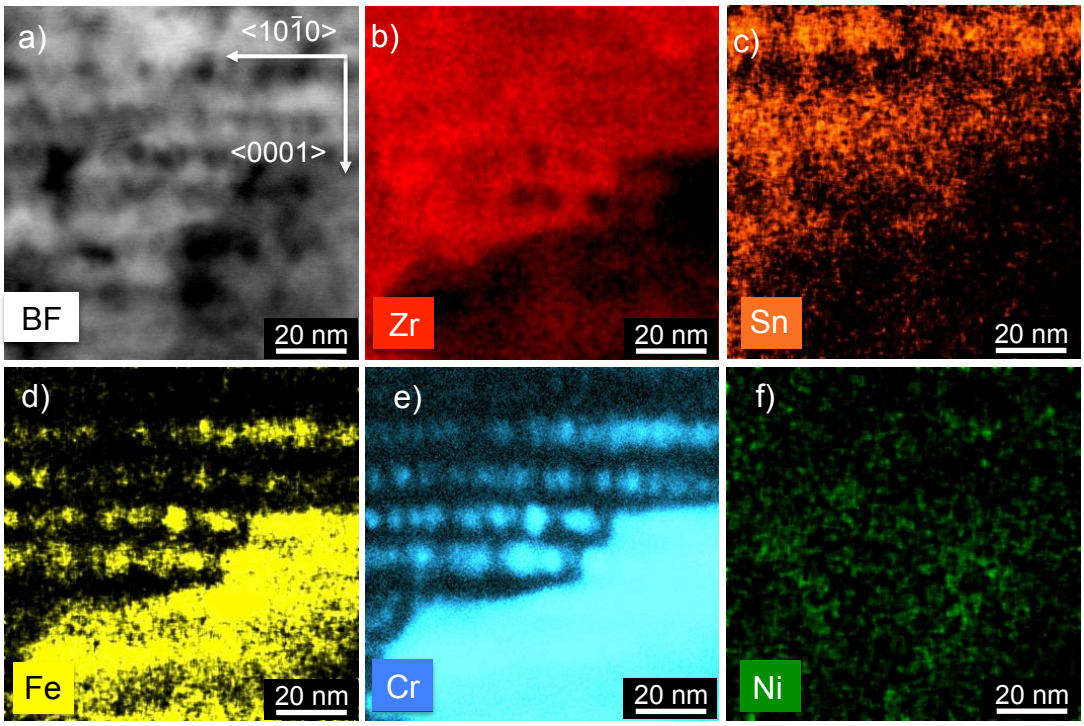

Figure 4.2.14 The BF STEM image in a) and Zr, Sn, Fe, Cr and Ni chemical maps in b)-f), respectively, were obtained from the region highlighted by a red square in **Figure 4.2.12** a) from the $<11\bar{2}0>$ orientation after neutron irradiation in a BWR to a fluence of 9.5 x10^{25} n m^{-2} ~15.8 dpa. Discontinuous segregation of Fe and Cr to c-loop positions is evident. Possible discontinuity in Sn segregation between c-loop positions is shown in c).

Each of the BF STEM images in Figure 4.2.11, Figure 4.2.13 and Figure 4.2.12 is repeated in Figure 4.2.15a, c and e, respectively, indicating the positions of line scans extracted from the chemical maps in the previous figures. The line scans are presented in Figure 4.2.15 for 2.3 dpa protons in Figure 4.2.15a and b, for 4.7 dpa protons in Figure 4.2.15c and d and for a neutron fluence of 9.5 x10^{25} n m^{-2} (~15.8 dpa) in Figure 4.2.15e and f. In each line scan, the position along the direction of the arrow in the corresponding BF STEM image is given in the *x*-axis and each data set is averaged over the area highlighted in the BF STEM image perpendicular to the arrow. The BF STEM intensity was also recorded as a function of position but was not included in the line scans for the sake of clarity. Instead, significant minima in the BF intensity were plotted on the line scans as vertical dotted lines, and as such indicate the positions of dislocation loop alignment parallel to the basal plane. Note that the scaling of the elemental counts and their grouping on the ordinate axes has been varied between the figures in order to highlight trends. The mean number of counts are given here for clarity but are not intended to be representative of relative concentrations. For 2.3 dpa protons, $\overline{Sn}$ = 1.24 x10^3 counts, $\overline{Fe}$ = 1.06 x10^3 counts and $\overline{Ni}$ = 0.04 x10^3 counts. For 4.7 dpa protons, $\overline{Sn}$ = 0.65 x10^3 counts, $\overline{Fe}$ = 0.12 x10^3 counts and $\overline{Ni}$ = 0.02 x10^3 counts. For 15.8 dpa neutrons, $\overline{Sn}$ = 0.69 x10^3 counts, $\overline{Fe}$ = 0.45 x10^3 counts and $\overline{Ni}$ = 0.06 x10^3 counts.

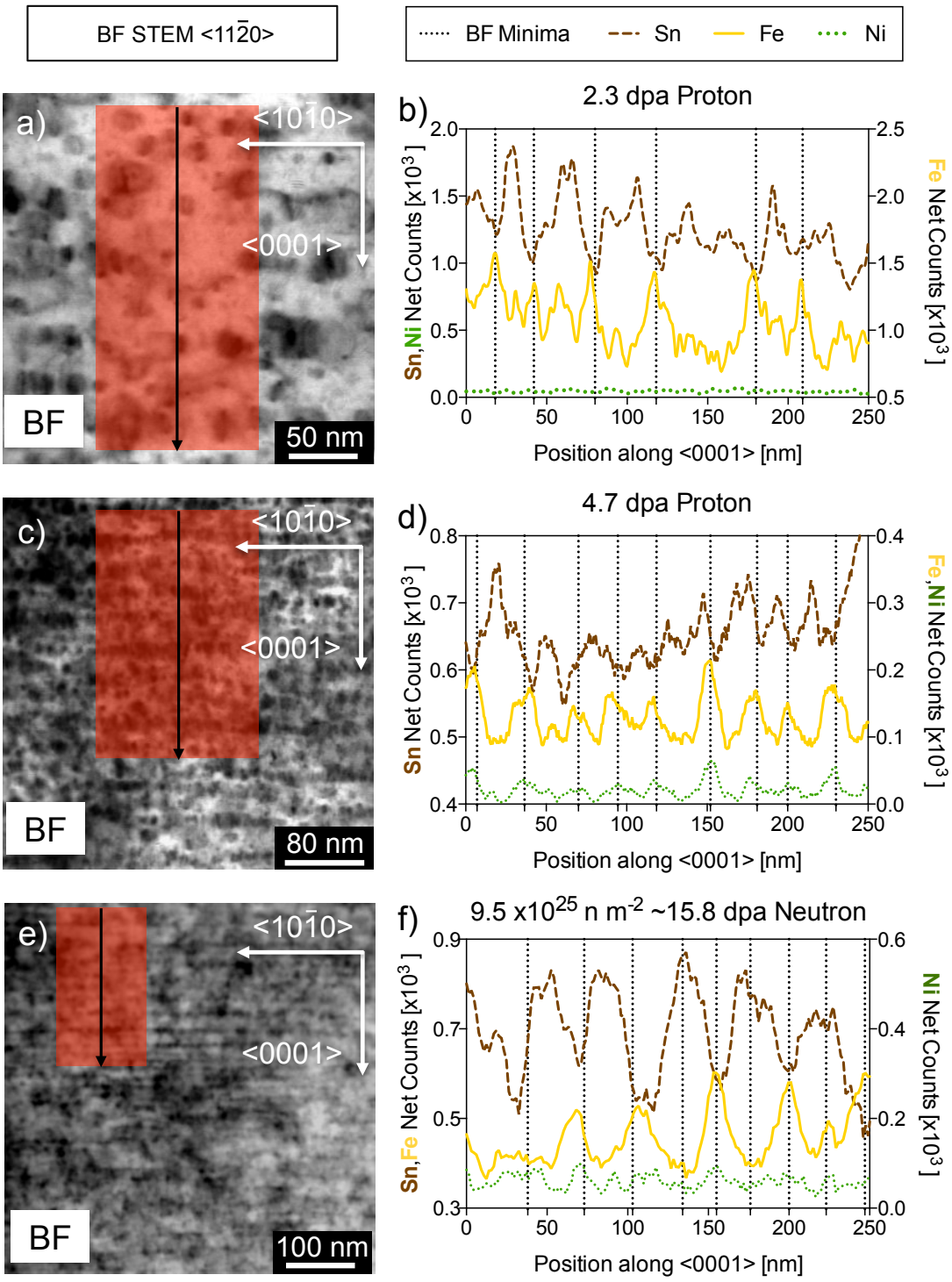

Figure 4.2.15 BF STEM images at the $<11\bar{2}0>$ orientation and the corresponding EDS line scans are given in a) and b) after 2.3 dpa proton irradiation, in c) and d) after 4.7 dpa proton irradiation and in e) and f) after neutron irradiation in a BWR to a fluence of 9.5 x10^{25} n m^{-2} ~15.8 dpa. The line scans are taken from the black arrows in the BF STEM images and averaged over the area in red perpendicular to the arrow. Minima in the BF STEM intensity are denoted in the line scan by vertical black dotted lines.

As can be seen from each of the line scans, the X-ray counts due to Sn are anti-correlated with those due to Fe. Further, the peaks in Fe and troughs in Sn correlate with the minima in BF STEM intensity. Some Ni segregation is observed to follow that of Fe, especially after proton irradiation to 4.7 dpa in Figure 4.2.15d but also after neutron irradiation in Figure 4.2.15f. After 2.3 dpa proton irradiation the average distance between BF minima is 38 nm, after 4.7 dpa it is 28 nm and after 9.5 x10^{25} n m^{-2} ~15.8 dpa neutron irradiation it is ~23 nm. However, the small sample areas analysed make such a comparison questionable. In the non-irradiated material (not shown), line scans from the same orientation produce only noise signals with no such correlative trends.

5 DISCUSSION

5.1 DISLOCATION PROPERTIES AND EVOLUTION UNDER IRRADIATION

The Burgers vector of small dislocation loops in proton-irradiated Zircaloy-2 has been determined in Figure 4.2.3 as $<11\bar{2}0>$-type in agreement with the Burgers vector determined for both the small dislocation loops in neutron-irradiated Zircaloy-2 of the present work and in pure Zr and its alloys in the literature (A Jostsons et al. 1977; Griffiths 1988). However, it should be noted that the magnitude of the a-loop Burgers vector has not been determined here as it has for neutron-irradiated material in the literature as $\frac{1}{3}<11\bar{2}0>$ (A Jostsons et al. 1977; Griffiths 1988). Further, the habit plane of the a-loops in proton-irradiated Zircaloy-2 is likely to be the $\{10\bar{1}0\}$ as shown in Figure 4.2.4, and loops tend to align parallel to the trace of the basal plane. Both observations are also in agreement with the preference of a-loops to inhabit first-order prismatic planes in neutron-irradiated Zr and their tendency to align parallel to the basal trace (A Jostsons et al. 1977). The a-loop number density has been shown to rise with increasing dose when one combines the data from proton and neutron-irradiated material in Figure 4.2.9a, although this is unexpected with reference to the literature. Early observations by Carpenter and Northwood demonstrated that a-loop number density gradually decreases at higher irradiation doses (Carpenter & Northwood 1975) and X-ray diffraction line broadening analysis by Griffith *et al.*

has demonstrated a saturation in strain relating to prism planes (Griffiths et al. 1996).

To put the data presented here into context, the a-loop line density has been plotted together with those from several other sources and is shown in Figure 4.2.16. On the scale given in Figure 4.2.16, the increase in a-loop line density between the proton (black circles) and neutron (black squares) does not seem as significant. While the data presented here provides low a-loop line densities in comparison to those observed from previous Zircaloy-2 from PWRs and BWRs (Carpenter & Northwood 1975; Northwood et al. 1979; Griffiths et al. 1996), (Carpenter & Northwood 1975), it is in reasonable agreement with line densities from test reactor HFIR and proton irradiations of Zircaloy-2 and -4 (Cockeram et al. 2011; Cockeram et al. 2014). One key difference between the conditions in Figure 4.2.16 is that of temperature. Most of the material with a-loop line densities 4-8 $x10^{14}$ m^{-2} was irradiated at ≤ 300 °C with the exception of one irradiation at 342 °C. All of the neutron test reactor line densities and those from proton-irradiated material, including those presented here, were from material irradiated in the temperature range 350-400 °C. Additionally, the 400 °C neutron irradiations were performed in a test reactor, and at neutron flux ~3 times that of a power reactor (Cockeram et al. 2014) whereas the 358 °C HFIR irradiations were performed at fluxes almost equal to that in power reactors (Cockeram et al. 2011). Likewise, the proton-irradiated material in the present work and that studied by Zu *et al.* was irradiated at a dose (dpa) rate higher than that of a power reactor by a factor of ~70-100 (Zu et al. 2005).

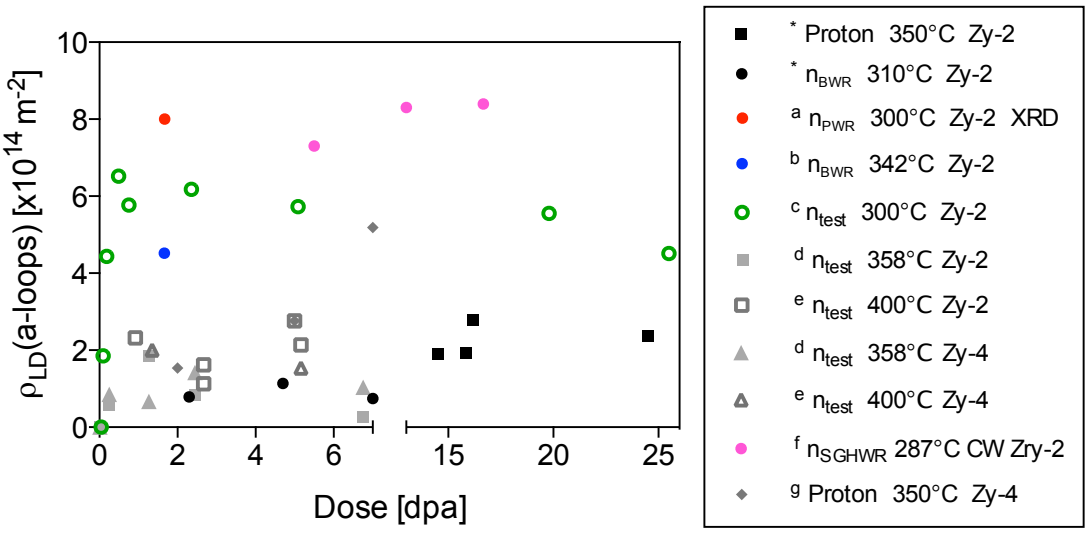

Figure 4.2.16 a-loop line density as a function of irradiation dose (dpa) for p, proton irradiation and n, neutron irradiation after ' * ' the present work, a (Griffiths et al. 1996), b (Northwood et al. 1979), c (Carpenter & Northwood 1975), d (Cockeram et al. 2011), e (Cockeram et al. 2014), and f (Holt et al. 1996)..

The effects of flux and temperature are thought to be competing processes when one considers damage accumulation in phases that result in irradiation-induced phase transformations toward the amorphous state (Motta 1997). On a more local scale, the effect of increasing flux in austenitic stainless steels is to increase the density and decrease the size of irradiation-induced voids (Allen et al. 2006). However, such an effect of flux may not be applicable to a-loop morphology and density at power reactor operating temperatures ~300 °C. In an analysis of Zircaloy-2 a-loop number density and size, Carpenter and Northwood studied material irradiated at a flux ~3 times that of power reactors but at similar temperatures ~300 °C (Carpenter & Northwood 1975). The line densities obtained from this study are in good agreement with those obtained from material in power reactors (Griffiths et al. 1996; Northwood et al. 1979), and, as such, flux does not seem to have a large effect on a-loop line density in this temperature range. Temperature, on the other hand, has been shown to increase the a-loop size and decrease the number density (A Jostsons et al. 1977; Gilbert et al. 1979; Northwood et al. 1979; Griffiths 1988), resulting in the overall effect of decreasing line density. However, a comparison of two recent studies by Cockeram *et al.*

demonstrates that, for both Zircaloy-2 and -4, an increase in temperature and a decrease in flux from ~358 °C and ~3 x10^{18} n m^{-2} s^{-1} (Cockeram et al. 2011) to ~400 °C and 0.1-0.8 x10^{18} n m^{-2} s^{-1} (Cockeram et al. 2014) results in a decrease in a-loop size, an increase in number density and an overall increase in a-loop line density. This is unexpected, as higher temperatures are known to reduce a-loop line density and flux is thought to have little effect. As such, it may be the case that a higher flux increases a-loop line densities at higher temperatures ~400 °C but not at temperatures closer to the normal operating temperatures of a power reactor. Importantly, in the later study by Cockeram *et al.*, the flux is similar to that observed in a power reactor and, with reference to Figure 4.2.16, the line densities obtained are approximately one third of those expected from power reactors, which can be attributed to the higher temperature.

While proton irradiations at higher temperatures (~350 °C) than power reactors (~300 °C) allow more diffusion to take place and therefore allow defect structures to form, it may be the case that point defects and their clusters are so mobile that annihilation and/or diffusion to grain boundary and other interfacial sinks is preferred over a-loop formation, reducing the observed line density. Further, the higher dose (dpa) rate of proton irradiation and smaller cascade volumes (Was 2000) may encourage a higher density of point defects that are not directly observable by TEM and which do not form stable dislocation loops. Under proton irradiation, small cascade volumes that are more widely separated from each other than for the neutron irradiation case will result in further distances for point defects to diffuse in order to agglomerate and collapse into observable defects. While the higher temperature of proton irradiation is designed to reduce this effect, alternative sinks at varying temperatures, the anisotropy of the hcp system and the geometrical arrangement of sinks with respect to the anisotropic diffusion of defects needs to be considered (Woo & Göslel 1983). Neutron-induced collision cascades and the resulting point defects and clusters (Wooding et al. 1998; Gao et al. 2001), their stability (de Diego et al. 2011; Vérité et al. 2013; Peng et al. 2014; Domain & Legris 2005) and mobility (de Diego et al. 2002; de Diego et al. 2008; Christensen et al. 2014; Christensen et al. 2015) are well studied for zirconium, but

studies of the effects of proton and ion irradiation in this regard are lacking in the literature.

Zu et al. have performed 2 MeV proton irradiation in Zircaloy-4, and a-loop line densities were shown to increase almost linearly with dose up to 7 dpa (Zu et al. 2005), in contrast to the decrease in line density observed in the present work between 4.7 and 7.0 dpa. While the 7.0 dpa Zircaloy-4 a-loop line density by Zu is more representative of the neutron-irradiated Zircaloy-2 a-loop line densities reported by Carpenter and Northwood in Zircaloy-2 (Carpenter & Northwood 1975), Zu et al. considered black-spot damage in BF TEM images and, as such, what constitutes a dislocation becomes difficult to define. This can lead to overestimations in observed density. In the present work, BF STEM is subject to the same issue but the observation of loops normal to their habit plane allows their identification by their ellipticity. No such orientation information was provided by Zu et al. Onimus et al. have reported an a-loop line density of ~4.7 x10^{14} m^{-2} after 0.6-1 MeV 350 °C Zr ion irradiation to a dose of 1.3 dpa (Onimus et al. 2012). While this is in the correct range of neutron irradiations at 300 °C provided by Carpenter and Northwood (Carpenter & Northwood 1975), and is therefore more representative of power reactor line densities than any other test reactor neutron or proton irradiation experiment described thus far (Northwood et al. 1979; Griffiths et al. 1996), the a-loop structure is different in that the line density is comprised of a very high number density of small loops (~50 x10^{21} m^{-3}, mean diameter 3 nm). Additionally, Onimus *et al.* simply assumed the thickness of their TEM foil for their a-loop quantifications as 150 nm without any actual thickness measurement, and as such there may be significant errors associated with the density reported.

In the present work we estimate the onset dose for c-loop nucleation as similar for the proton- and neutron-irradiated Zircaloy-2 at ~4.5 and ~4.9 dpa, respectively. These values were calculated by fitting a line of best fit to the data and determining the intersection of this line with the abscissa, and are in agreement with literature values for the onset of c-loop nucleation at 3 x10^{25} n m^{-2} ~5 dpa for both Zircaloy-2 PWR control blades at ~290 °C (Mahmood et al. 2000) and for Zircaloy-4 at ~297

°C (Holt & Gilbert 1986). The agreement between c-loop nucleation fluences in Zircaloy-2 and -4 under neutron irradiation is consistent with their similarity in breakaway growth fluences; 3-4 $x10^{25}$ n m^{-2} at 280-297 °C (Griffiths et al. 1995). The c-loop line densities in the present work are plotted together with those from the literature in Figure 4.2.17 and show good agreement. In addition to providing c-loop densities in the correct number density and size range, the spacing between c-loops in the <0001> direction at 20-50 nm and the linear increase in c-loop density is also in agreement with literature (Mahmood et al. 2000; Griffiths et al. 1996; Bossis et al. 2011). Interestingly, the thickness of c-loops when imaged from the <0001> orientation in Figure 4.2.6c may demonstrate that their alignment in the basal trace is staggered in the <0001> direction. While proton irradiation seems suitable for emulating the nucleation and morphology of c-loops by neutron irradiation, the gradient of the linear trend line is higher for the proton-irradiated material than for the neutron-irradiated material. As such, it may be the case that, with respect to increasing dose in dpa, the proton irradiation experiments presented here result in a faster increase in c-loop line density than would be expected in neutron-irradiated material. In Figure 4.2.17, the c-loop line density is shown after proton irradiation of Zircaloy-4 at 350 °C to 19 dpa as determined in Ref. (Tournadre et al. 2013) (blue cross). This data point continues the high rate of c-loop nucleation with respect to proton dose, and gives an almost perfect linear trend when combined with the present proton irradiation of Zircaloy-2. Proton irradiation to higher doses for Zircaloy-2 is required for further investigation, but could be c-loop nucleation rates could be slowed by a reduction in the temperature (Holt & Gilbert 1986). Whether this is desirable is debatable, as it is partly the rapid nature of proton irradiation that makes it an attractive method of study. The c-loop line density presented here is in better agreement with the literature than the a-loop line density. This may be due to the higher temperature used having a greater effect on self-interstitial defects, which are known to have a higher diffusivity than vacancies (Christensen et al. 2015). As such, grain boundaries may become the dominant sinks for interstitials and the vacancy c-loops that form may be indicative of a greater concentration of vacancy a-loops with respect to interstitial a-loops. The a-loops in the present work proved too small for a determination of vacancy or interstitial character by way of the inside-outside

method close to the $<11\bar{2}3>$ zone axis (Foll & Wilkens 1975; A Jostsons et al. 1977). While this would have been desirable, Jostsons *et al.* have noted that in pure Zr the ratio of vacancy to interstitial a-loops varies from grain to grain (A Jostsons et al. 1977), and so a reliable study of this character may not be possible by TEM methods alone.

The 600 keV Zr heavy-ion irradiation of Tournadre *et al*. gave appropriate c-loop line densities, but in a similar manner to the production of a-loops by heavy ions, the c-loops were small and in high density (Tournadre et al. 2012) as they are in Kr ion-irradiated Zr alloy EXCEL (Idrees et al. 2013). Further, as c-loops are larger than a-loops, exemplified from the <0001> orientation in Figure 4.2.6c, and the Zr or Kr heavy ions only penetrate ~300 nm into the Zr matrix, c-loops are more likely to be hindered by the physical constraint of the non-irradiated remainder of the grain and the sink strength of this region in addition to the free surface 300 nm above it. In regards to electron irradiation, Griffiths *et al.* have shown that both basal vacancy c-loops of Burgers vector $\frac{1}{6}<20\bar{2}3>$ that inhabit (0001) planes and non-basal interstitial <c+a>-loops of Burgers vector $\frac{1}{3}<11\bar{2}3>$ that inhabit $\{10\bar{1}1\}$ planes can be induced in pure Zr (Griffiths et al. 1983), are also observed after electron irradiation of Zircaloy-2 and -4 (Griffiths et al. 1993). Basal c-loops have been observed by de Carlan *et al.* after electron irradiation at various temperatures (de Carlan et al. 1996), but have shown a much lower line density than those produced by neutron irradiation and so have not been included in Figure 4.2.17. This may be explained by the presence of cavities in Zircaloy-4 after electron irradiation at 300 °C (de Carlan et al. 1996), which act as an alternative vacancy sink. No cavities and higher c-loop densities were observed at higher electron irradiation temperatures ~350 °C, but the density data were not provided by the authors and so could not be included in the present analysis. de Carlan *et al.* showed clearly that an increase in Fe implantation in Zircaloy-2 was related to an increase in c-loop density and a decrease in cavity formation (de Carlan et al. 1996), and Griffiths *et al.* have shown that both c-loops and cavities are associated with regions of high Fe content (Griffiths, R.W. Gilbert, et al. 1987).

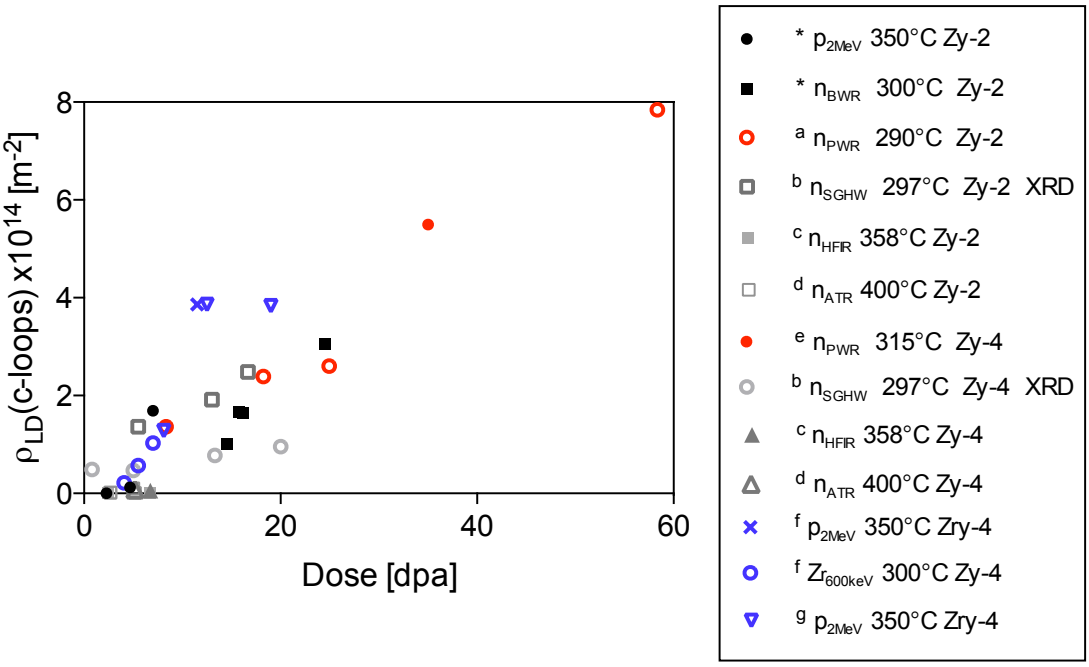

Figure 4.2.17 c-loop line density as a function of irradiation dose (dpa) for p, proton irradiation and n, neutron irradiation after * the present work, a (Mahmood et al. 2000), b (Griffiths et al. 1995), c (Cockeram et al. 2011), d (Cockeram et al. 2014), e (Bossis et al. 2011), f (Tournadre et al. 2012), and g (Tournadre et al. 2013).

5.2 CORRELATIONS BETWEEN MATRIX CHEMISTRY AND DISLOCATION EVOLUTION

The effect of matrix chemistry on c-loop formation has been shown to be important by increasing alloying and impurity additions to increase c-loop density (Griffiths, R.W. Gilbert, et al. 1987). Likewise, Zircaloy-2 has been shown to experience a lower growth strain in comparison to Zr-1.5Sn (wt.%) (Zee et al. 1984; Rogerson & Zee 1988), the primary difference between the two alloys being the presence of Fe-, Cr- and Ni-containing second phase particles (SPPs) in the former. A higher density of c-loops has been observed in the vicinity of partially-dissolved second phase particles (SPPs) in Zircaloy-4 after both neutron irradiation at ~290-310 °C and proton irradiation at 350 °C (Griffiths & Gilbert 1987; Tournadre et al. 2012; de Carlan et al. 1996) and de Carlan *et al.* demonstrated Fe segregation to the position of a c-loop by EDS line scans (de Carlan et al. 1996). Cr has also been shown to segregate along c-loop positions parallel to the basal plane in close proximity to SPPs in neutron-irradiated material

(Griffiths et al. 1995; Valizadeh et al. 2014). As higher c-loop densities are correlated to higher growth strain in the Zircaloys (Holt & Gilbert 1986) and as increased Fe content in the Zircaloys is known to increase c-loop density (de Carlan et al. 1996), one could assume that increased Fe content would increase irradiation-induced growth. However, this is inconsistent with the lower growth strain of Zircaloy-2 (Holt & Gilbert 1986) in comparison to that of Zr-1.5Sn (wt.%) at similar temperatures (Zee et al. 1984). It may of course be the case that c-loops do not induce anisotropic growth but relax the strain caused by growth, which may also extend to c-loops acting to relax the strain induced in the matrix upon supersaturation with solute from a dissolving SPP. While no preference for c-loop nucleation at SPPs was found in the present work in the proton-irradiated material at 4.7 and 7.0 dpa, it was observed in the neutron-irradiated samples. This suggests that higher doses would be required to observe such a phenomenon in the proton-irradiated material, after which a higher degree of SPP dissolution will have taken place. Alternatively, higher doses may not produce such a phenomenon if it is a time-at-temperature effect and as such, the dose rate may be too high for it to occur.

In the present work, irradiation-induced segregation of all Zircaloy-2 alloying elements, Sn, Fe, Cr and Ni has been demonstrated. All such segregation is aligned along the trace of the basal plane. Cr segregation in nano-clusters or, alternatively, to the core of a-loops, has been observed close to partially-dissolved Fe-Cr SPPs in both proton- and neutron-irradiated material at all doses, but is exemplified here in Figure 4.2.13 for proton irradiation to 4.7 dpa and in Figure 4.2.12 and Figure 4.2.14 for neutron irradiation to ~15.8 dpa. This is similar to the Cr segregation observed close to such SPPs by other authors (Griffiths et al. 1995; Valizadeh et al. 2014), but the images herein provide the evidence that the segregation is discontinuous. Such discontinuity can in fact be observed (although not remarked upon) in BF TEM images by others, although those authors did not have the EDS capability necessary to detect the nano clusters (See the dot contrast aligned parallel to the trace of the basal plane along the $<01\bar{1}0>>$ direction in *Figure2b* and *c* of *Ref*. (Yang 1988) and parallel to the basal plane in *Figure 7c* of *Ref*. (Valizadeh et al. 2014)). Novelty is found in the present work in the high spatial

resolution and EDS detection efficiency, which provide a clear picture of the crystallographic nature of Cr segregation and indeed that of Fe and Ni. Steps parallel to the trace of the (0001) basal plane are observed at the periphery of the Fe-Cr SPP in Figure 4.2.14 in agreement with the directional dissolution shown by others (Yang 1988), suggesting SPP dissolution by a basal self interstitial flux mechanism (Griffiths 1990). Fe and Cr depletion from SPPs as a response to SIA inward flux is probable as recent calculations have shown that Fe and Cr diffuse anisotropically with a preference for diffusion in the <0001> direction (Christensen et al. 2014), perpendicular to the observed segregation in the basal plane. As SIAs are known to diffuse in the basal plane (Woo & Göslel 1983; Christensen et al. 2015), basal solute segregation as a result of this SIA mobility seems likely.

Fe and Ni are also observed to segregate to dislocation positions but are more widespread in the matrix than Cr, probably because of the relative diffusivities in α-Zr Fe > Ni >> Cr (Perez et al. 2003). In analogy to the Fe-Cr and Fe-Ni type SPPs $Zr(Fe,Cr)_2$ and $Zr_2(Fe,Ni)$, the nano clustering within the matrix is coincident in either Fe and Cr or Fe and Ni. The Fe and Ni clustering occurs at aligning a-loop positions, which are likely to align due to their anisotropic strain field being greater in the <0001> direction and less in the (0001) plane (Griffiths 1988). Interestingly, at 2.3 dpa, Figure 4.2.11, Fe segregation to dislocations is observed but not Ni segregation, suggesting that Fe-Cr SPPs have begun to dissolve but that Fe-Ni SPPs have not. This is in agreement with the relative stability of the Fe-Ni SPP compared with the Fe-Cr in respect of amorphisation at normal reactor operating temperatures (Gilbert et al. 1985; Griffiths, R W Gilbert, et al. 1987) and the observation by Etoh and Shimada that the Fe/Ni ratio in $Zr_2(Fe,Ni)$ SPPs remains constant for longer than the Fe/Cr ratio in $Zr(Fe,Cr)_2$ SPPs (Etoh & Shimada 1993).

Segregation of Sn has also been demonstrated here in both proton- and neutron-irradiated material as banding in rows parallel to the trace of the basal plane and with reference to Figure 4.2.14 the segregation may also be discontinuous. In the EDS

line scans of Figure 4.2.15, the Sn and (Fe+Ni) are shown to be anticorrelated. Interestingly, the Sn if often segregated between rows of dislocations (BF minima) and the (Fe+Ni) at the position of dislocation rows. Planar arrays of nano-clustering Fe, Cr and Ni have recently been observed in atom probe tomography of neutron-irradiated Zircaloy-2 (Sundell et al. n.d.). While it was proposed that the segregating planes may be parallel to the trace of basal planes, crystallographic information was not available from the APT data. The present work confirms the proposed crystallographic relationship and adds the observation for Sn. Sundell *et al.* did not observe clustering in Sn but this could be due to difficulties in confidently identifying Sn spatial segregation determined with APT due to evaporation field effects (Wadman et al. 1988), which causes enhanced diffusion during analysis to regions of high electric field and therefore evaporation from high symmetry zone axes (Sundell et al. 2015).

It should be noted that there is some uncertainty in regard to the mobility of species during cooling and, as such, it is unclear whether the segregation observed in the present work occurs during irradiation or upon cooling. Analytical and experimental work is on-going in order to determine which. However, in the seminal works on irradiation-induced precipitation in Zircaloys it is assumed that the precipitation is irradiation-induced (Griffiths, R W Gilbert, et al. 1987; Woo & Carpenter 1988), and, some types of precipitate have been shown to be affected by post-irradiation heat treatments while others have not (Griffiths, R W Gilbert, et al. 1987). A more detailed analysis of precipitates is underway by the present authors in regards to the nano-clustering or nano-precipitation observed here.

It has been suggested that vacancy a-loops align parallel to the trace of the basal plane and that interstitial a-loops lie in between these vacancy a-loop rows (A Jostsons et al. 1977; Griffiths 1988). Considering that the order of diffusivity is likely to be Fe > Ni >> Cr > SIA ~ Sn > vacancy, the following situation is probable in the present work: dislocation loops form and arrange themselves according to

their strain fields in rows parallel to the trace of the basal plane, after which Fe, Cr and Ni from dissolving SPPs segregates to the dislocation positions and finally Sn, in solid solution and a slower diffuser, responds by segregating into alternate rows to the Fe, Ni and Cr. Alternatively, the depletion of the light transition elements from SPPs may take some time to occur, and so it may be the opposing strain fields of substitutional Sn (compressive) and the vacancy a-loops (tensile) that cause the loops to align. This could be a self-sustaining mechanism, as the Sn may trap vacancy defects (Hood 1977; Hood 1988) and repels interstitials (Christensen et al. 2014). While small solute segregation to dislocation positions has been suggested previously (Griffiths, R.W. Gilbert, et al. 1987) and is predicted theoretically (Christensen et al. 2014), it has not been demonstrated until recently (Sundell et al. n.d.) and in the present work. There is evidence from positron annihilation spectroscopy that Sn traps vacancies (Hood 1977; Hood 1988) such that they would be unable to form dislocation loops. Evidence for such a proposition is found in the lower growth strain of binary alloy Zr-1.5Sn with respect to Zr-0.1Sn (wt.%) at 80 °C (Zee et al. 1984). Although this was not found to hold true for a higher irradiation temperature of 300 °C (Zee et al. 1984), Sn has been shown to precipitate in neutron-irradiated Zircaloy-2 at very high irradiation temperatures 600-710 °C (Griffiths, R W Gilbert, et al. 1987; Woo & Carpenter 1988), probably as the Zr_5Sn_3 phase. While no Sn-rich precipitates were observed in the present work, the crystallographic segregation of Sn into bands provides evidence for its possibility.

Evidence for the presence of Sn acting as a barrier to the diffusion of point defects and their clusters may be found in an experiment in which low dose neutron irradiations were performed for both Zircaloy-2 and pure Zr at both 300 and 400 °C (Gilbert et al. 1979). At 300 °C, the a-loop density in Zircaloy-2 was larger than in pure Zr by a factor of ~2 and at 400 °C the a-loop line density decreased for both materials, but this decrease was ~3 times as severe for Zircaloy-2 than for pure Zr. As such, at ~300 °C Sn may act as a barrier to diffusion, causing higher degrees of defect agglomeration and dislocation nucleation. At higher temperatures this barrier to diffusion may be overcome. Of course, the effects of texture and grain

size have not been taken into account here which have been shown to affect growth strain (Fidleris 1988) and are therefore likely to affect the resulting dislocation structure (Holt & Gilbert 1986).

If the relatively slow-moving vacancies were to trap Sn at irradiation temperatures 300-350 °C, vacancy a-loops would be more likely to form in between the rows of Sn. Of course such a mechanism would depend on the binding energy of the vacancy-Sn complex and successive binding energies of further vacancies, in addition to the propensity of a substitutional Sn atom to swap with a neighbouring Zr self interstitial (Christensen et al. 2014) and hence the reversibility of the vacancy trap would be in question. However, a concentration of vacancy-type a-loops in between Sn rows would support the observation that it is the vacancy a-loops that align (A Jostsons et al. 1977; Griffiths 1988), and support the idea that Sn acts as a barrier to defect diffusion (Gilbert et al. 1979). Figure 4.2.7 demonstrates that after proton irradiation to 7.0 dpa the position of c-loops, although aligned in the same basal plane trace as a-loops, may be anticorrelated with the positions of a-loops along the planar trace. As such, the absence of a-loops at a c-loop position may be evidence for the nucleation of the latter by the former, especially in considering the complete alignment of a-loops observed without interruption at 4.7 dpa in Figure 4.2.13a. Therefore, if Sn acts as a barrier to vacancy diffusion, it may concentrate the vacancy a-loops into bands, which results in conditions favourable for transformation of vacancy a-loops into vacancy c-loops. Supporting evidence for this can be seen in the decrease in number density and line density of a-loops between proton irradiation doses of 4.7 and 7.0 dpa in Figure 4.2.9 and Figure 4.2.10. In impure Zr, Griffiths and Gilbert noted that the number density of a-loops decreases as that of c-loops increases at higher fluences (Griffiths & Gilbert 1987). Griffiths *et al.* have explained c-loop growth at the expense of a-loops due to the difficulty in climb of the latter once c-loops provide a physical barrier in rows parallel to the basal plane (Griffiths, R.W. Gilbert, et al. 1987). However, recent molecular dynamics calculations by Di *et al.* demonstrate that vacancy a-loops may nucleate vacancy c-loops directly by interaction with a cascade event (Di et al. n.d.). This is interesting because such an event may require a concentration in a-loop alignment parallel to the basal plane, which is a common

feature of irradiated zirconium alloys (A Jostsons et al. 1977; Griffiths 1988) and is demonstrated in the present work, but which may take time to develop, accounting for the delay in observable c-loop nucleation. The work by Di et al. is, however, rather preliminary as the a-loop modelled is a pure edge loop and inhabits the $\{11\bar{2}0\}$ plane as opposed to the $\{10\bar{1}0\}$ and so further work is required to solidify the results as representative. The formation of c-loops is predominantly dependent on temperature and fluence and hence barriers to diffusion, as it has been shown that for different neutron fluxes there is little difference in c-loop density or growth strain for a given fluence and temperature (Griffiths, R.W. Gilbert, et al. 1987).

5.3 REGARDING IRRADIATION-INDUCED GROWTH

The increase in total dislocation density (a- and c-loops) and the associated strain has been shown to follow the same trend as irradiation growth strain (Griffiths et al. 1989), and, the total line density in the proton-irradiated material demonstrated in the present work provides a similar trend. As such, it may be expected that proton irradiation experiments may emulate macroscopic growth strain in Zirconium alloys. Higher proton penetration depths (higher energies) and the development of beamline growth rigs are necessary to fully assess this proposition. Holt *et al.* has suggested that irradiation-induced growth may saturate and even decrease after the density of c-loops becomes greater than that of a-loops (Holt et al. 1996). However, Mahmood *et al.* have reported c-loop densities that are greater than that expected for a-loop densities without any saturation in irradiation-induced growth strain (Mahmood et al. 2000), assuming, as does conventional wisdom, that a-loops saturate in density at low fluences (Carpenter & Northwood 1975; Griffiths et al. 1996). The present work, however, suggests that a-loop density continues to increase after c-loop nucleation, which would account for the increase in <a>-direction strain observed due to growth and would reconcile the work of Mahmood *et al.* and the predictions of Holt *et al.* The difficulty in direct observation of a-loops at high doses due to the strain fields of c-loops may to some degree be made easier by advances in TEM-based imaging techniques, CCD cameras and especially by BF STEM to reduce strain contrast and

image very localised strain fields in the line of dislocation loops as an alternative to weak-beam dark-field imaging, which requires large sample tilts from the loop habit plane.

6 CONCLUSIONS

The use of BF STEM and on-axis imaging has proven useful in the determination of dislocation loop habit plane, relationships between different types of loops and the correlation of chemical segregation to dislocation structures. The following highlights the main findings of the present work:

- Proton irradiation at 350 °C results in the nucleation of a-loops at a low dose and a delay in the nucleation of c-loops to ~4.5 dpa. We estimate this threshold dose in the neutron-irradiated material at ~4.9 dpa, which agrees with the literature at ~5 dpa (Holt & Gilbert 1986; Mahmood et al. 2000).
- The a-loop line density is similar to that in the literature for neutron test reactor experiments and the c-loop density for both test reactor and power reactor studies. a-loop dose decreases at low dose 2-3 to 4.7 dpa, after which it is comparable to higher neutron dose sizes.
- In comparing the proton- and neutron-irradiated material, there is a general increasing trend in the a-loop density which is unexpected from convectional arguments towards a-loop density saturation but which may reconcile observations relating to irradiation-induced growth.
- The c-loop line density is in excellent agreement with power reactor studies. As such, the high temperature and dose rate of proton irradiation in comparison to that in power reactors may affect interstitial a-loops more than vacancy c-loops. This is likely due to the increased diffusional capacity of SIAs in comparison to vacancies (Christensen et al. 2015).
- The proton-irradiated material demonstrates that the alignment of a-loops may be responsible for the nucleation of c-loops. Further, a decrease in a-loop density is coincident with c-loop nucleation.
- The alignment of a-loops and c-loops is coincident with Fe, Ni, and to a lesser extent Cr, segregation. Sn segregation is observed between loop

positions, parallel to the basal plane trace. Sn may act as a barrier to defect formation, encouraging a-loop alignment and c-loop nucleation

7 ACKNOWLEDGEMENTS

This work is funded by an EPSRC Leadership Fellowship [EP/I005420/1] for the study of irradiation damage in zirconium alloys, and is supported heavily by industrial contributors and especially Westinghouse, Studsvik and Rolls-Royce plc. in terms of material acquisition, top up funding and useful discussions. The authors would like to thank Sarah Haigh and Mhairi Gass for insightful discussions, Thomas Seymour and Matthew topping for aid in experimental accomplishments and Gary Was and Ovidiu Toader at the Michigan Ion Beam Laboratory for the use of their facility in the proton irradiation experiments.

8 REFERENCES

Adamson, R., 2014. *Charged particle bombardment of zirconium alloys: A review*, Sweden.

Allen, T.R. et al., 2006. The effect of dose rate on the response of austenitic stainless steels to neutron radiation. *Journal of Nuclear Materials*, 348(1-2), pp.148–164.

Azevedo, C.R.F., 2011. Selection of fuel cladding material for nuclear fission reactors. *Engineering Failure Analysis*, 18(8), pp.1943–1962.

Bossis, P. et al., 2011. In PWR comprehensive study of high burn-up corrosion and growth behaviour of M5 and Recrystallized low-tin Zircaloy-4. *Journal of ASTM International*, 6(2), pp.430–4565.

Buckley, S.N., 1961. Properties of Reactor Materials and the Effects of Irradiation Damage. In London: Butterworths, p. 443.

De Carlan, Y. et al., 1996. Influence of Iron in the Nucleation of <c> Component Dislocation Loops in Irradiated Zircaloy-4. *Zirconium in the Nuclear Industry: Eleventh International Symposium, ASTM STP 1295*, pp.638–653.

Carpenter, G.J.C. & Northwood, D.O., 1975. The contribution of dislocation loops to radiation growth and creep of Zircaloy-2. *Journal of Nuclear Materials*, 56, pp.260–266.

Christensen, M. et al., 2015. Diffusion of point defects , nucleation of dislocation loops , and effect of hydrogen in hcp-Zr : Ab initio and classical simulations. *Journal of Nuclear Materials*, 460, pp.82–96.

Christensen, M. et al., 2014. Effect of alloying elements on the properties of Zr and the Zr–H system. *Journal of Nuclear Materials*, 445(1-3), pp.241–250.

Cockeram, B. V. et al., 2011. Development of microstructure and irradiation hardening of Zircaloy during low dose neutron irradiation at nominally 358 C. *Journal of Nuclear Materials*, 418, pp.46–61.

Cockeram, B. V. et al., 2014. Development of microstructure and irradiation hardening of Zircaloy during low dose neutron irradiation at nominally 377-440 C. *Journal of Nuclear Materials*, 449, pp.69–87.

Di, S. et al., <c> Component Dislocation Loop Nucleation in Zirconium under Irradiation: Atomic-level Simulations. *Unpublished*.

De Diego, N. et al., 2011. On the structure and mobility of point defect clusters in alpha-zirconium: a comparison for two interatomic potential models. *Modelling and Simulation in Materials Science and Engineering*, 19, p.35003.

De Diego, N., Osetsky, Y.N. & Bacon, D.J., 2002. Mobility of interstitial clusters in alpha-zirconium. *Metallurgical and Materials Transactions A*, 33(13), pp.783–789.

De Diego, N., Osetsky, Y.N. & Bacon, D.J., 2008. Structure and properties of vacancy and interstitial clusters in α-zirconium. *Journal of Nuclear Materials*, 374, pp.87–94.

Domain, C. & Legris, A., 2005. Ab initio atomic-scale determination of point-defect structure in hcp zirconium. *Philosophical Magazine*, 85(4-7), pp.569–575.

Etoh, Y. & Shimada, S., 1993. Neutron irradiation effects on intermetallic precipitates in Zircaloy as a function of fluence. *Journal of Nuclear Materials*, 200, pp.59–69.

Fidleris, V., 1988. The irradiation creep and growth phenomena. *Journal of Nuclear Materials*, 159, pp.22–42.

Foll, H. & Wilkens, M., 1975. A Simple Method for the Analysis of Dislocation Loops by Means of the Inside-Outside Contrast on Transmission Electron Micrographs. *Physica Status Solidi A*, 519(31), pp.519–524.

Gao, F. et al., 2001. Temperature-dependence of defect creation and clustering by displacement cascades in a-zirconium. *Journal of Nuclear Materials*, 294, pp.288–298.

Gilbert, R.W., Farrell, K. & Coleman, C.E., 1979. Damage structure in zirconium alloys neutron irradiated at 573 to 923 K. *Journal of Nuclear Materials*, 84, pp.137–148.

Gilbert, R.W., Griffiths, M. & Carpenter, G.J.C., 1985. Amorphous intermetallics in neutron irradiated Zircaloys after hIgh fluences. *Journal of Nuclear Materials*, 135, pp.265–268.

Griffiths, M., 1988. A review of microstructure evolution in zirconium alloys during irradiation. *Journal of Nuclear Materials*, 159, pp.190–218.

Griffiths, M., 1990. Comments on precipitate stability in neutron-irradiated Zircaloy-4. *Journal of Nuclear Materials*, 170, pp.294–300.

Griffiths, M. et al., 1993. HVEM study of the effects of alloying elements and impurities on radiation damage in Zr-alloys. *Journal of Nuclear Materials*, 205, pp.273–283.

Griffiths, M., Gilbert, R.W., et al., 1987. Neutron damage in zirconium alloys irradiated at 644 to 710 K. *Journal of Nuclear Materials*, 150(2), pp.159–168.

Griffiths, M. & Gilbert, R.W., 1987. The Formation of c-component defects in zirconium alloys during neutron irradiation. *Journal of Nuclear Materials*, 150, pp.169–181.

Griffiths, M., Gilbert, R.W. & Carpenter, G.J.C., 1987. Phase instability, decomposition and resdistribution of intermetallic precipitates in Zircaloy-2 and -4 during neutron irradiation. *Journal of Nuclear Materials*, 150, pp.53–66.

Griffiths, M., Gilbert, R.W. & Fidleris, V., 1989. Accelerated irradiation growth of zirconium alloys. *Zirconium in the Nuclear Industry: Eighth International Symposium*, pp.658–677.

Griffiths, M., Holt, R.A. & Rogerson, A., 1995. Microstructural aspects of accelerated deformation of Zircaloy nuclear reactor components during service. *Journal of Nuclear Materials*, 225, pp.245–258.

Griffiths, M., Loretto, M.H. & Smallman, R.E., 1983. Electron Damage in Zirconium II . Nucleation and growth of c-component loops. *Journal of Nuclear Materials*, 115, pp.323–330.

Griffiths, M., Mecke, J.F. & Winegar, J.E., 1996. Evolution of Microstructure in Zirconium Alloys During Irradiation. *Zirconium in the Nuclear Industry: Eleventh International Symposium, ASTM STP 1295*, pp.580–602.

Hallstadius, L., Johnson, S. & Lahoda, E., 2012. Cladding for high performance fuel. *Progress in Nuclear Energy*, 57, pp.71–76.

Holt, R. a. & Gilbert, R.W., 1986. c-component dislocations in annealed Zircaloy irradiated at about 570 K. *Journal of Nuclear Materials*, 137(3), pp.185–189.

Holt, R. a., Woo, C.H. & Chow, C.K., 1993. Production bias — A potential driving force for irradiation growth. *Journal of Nuclear Materials*, 205, pp.293–300.

Holt, R.A. et al., 1996. Non-Linear Irradiation Growth of Cold-Worked Zircaloy-2. *Zirconium in the Nuclear Industry: Eleventh International Symposium, ASTM STP 1295*, pp.623–637.

Hood, G.M., 1988. Point defect diffusion in a-Zr. *Journal of Nuclear Materials*, 159, pp.149–175.

Hood, G.M., 1977. *Point defect properties of α-Zr and their influence on irradiation behaviour of Zr alloys*, Chalk River National Laboratories, Chalk River, Ontario, Canada.

Idrees, Y. et al., 2012. In-situ study of defect accumulation in zirconium under heavy ion irradiation. *Journal of Nuclear Materials*.

Idrees, Y. et al., 2013. Irradiation -nduced microstructural changes in Zr-Excel alloy. *Journal of Nuclear Materials*, 441, pp.138–151.

Jostsons, A. et al., 1977. Faulted loops in neutron-irradiated zirconium. *Journal of Nuclear Materials*, 68, pp.267–276.

Jostsons, A., Kelly, P.M. & G, B.R., 1977. The Nature of Dislocation Loops in Neutron Irradiated Zirconium. *Journal of Nuclear Materials*, 66, pp.236–256.

Mahmood, S.T. et al., 2000. Post-Irradiation Characterization of ultra-high fluence zircaloy-2. *Zirconium in the Nuclear Industry: Twelfth International Symposium, ASTM STP 1354*, pp.139–169.

Motta, A.T., 1997. Amorphization of intermetallic compounds under irradiation — A review. *Journal of Nuclear Materials*, 244, pp.227–250.

Northwood, D.O. et al., 1979. Characterization of neutron irradiation damage in zirconium alloys - an international “round-robin” experiment. *Journal of Nuclear Materials*, 79, pp.379–394.

Onimus, F., Dupuy, L. & Mompiou, F., 2012. In situ TEM observation of interactions between gliding dislocations and prismatic loops in Zr-ion irradiated zirconium alloys. *Progress in Nuclear Energy*, 57, pp.77–85.

Peng, Q. et al., 2014. Pressure effect on stabilities of self-Interstitials in HCP-Zirconium. *Scientific Reports*, 4, pp.1–7.

Perez, R.A., Nakajima, H. & Dyment, F., 2003. Diffusion in alpha-Ti and Zr. *Materials Transactions*, 44(1), pp.2–13.

Rogerson, A. & Zee, R.H., 1988. Irradiation growth in zirconium-tin alloys at 353 and 553 K. *Journal of Nuclear Materials*, 152, pp.220–224.

Shishov, V.N. et al., 2005. Influence of structure-phase state of Nb containing Zr alloys on irradiation-induced growth. *Zirconium in the Nuclear Industry: 14th Symposium*, 2(8), pp.666–685.

Stoller, R.E. et al., 2013. On the use of SRIM for computing radiation damage exposure. *Nuclear Instruments and Methods in Physics Research B*, 310, pp.75–80.

Sundell, G. et al., Redistribution of alloying elements in Zircaloy-2 after in-reactor exposure. *Journal of Nuclear Materials*.

Sundell, G., Thuvander, M. & Andrén, H., 2015. Tin clustering and precipitation in the oxide during autoclave corrosion of Zircaloy-2. *Journal of Nuclear Materials*, 456, pp.409–414.

Tenckhoff, E., 2005. Review of deformation mechanisms, texture, and mechanical anisotropy in zirconium and zirconium base alloys. *Zirconium in the Nuclear Industry: 14th Symposium*, 2(4), pp.25–50.

Tournadre, L. et al., 2012. Experimental study of the nucleation and growth of c-component loops under charged particle irradiations of recrystallized Zircaloy-4. *Journal of Nuclear Materials*, 425(1-3), pp.76–82.

Tournadre, L. et al., 2013. Toward a better understanding of the hydrogen impact on the radiation induced growth of zirconium alloys. *Journal of Nuclear Materials*, 441, pp.222–231.

Valizadeh, S. et al., 2014. Effects of Secondary Phase Particle Dissolution on the In-Reactor Performance of BWR Cladding. *Journal of ASTM International*, 8(2), pp.729–753.

Vérité, G. et al., 2013. Self-interstitial defects in hexagonal close packed metals revisited: Evidence for low-symmetry configurations in Ti, Zr, and Hf. *Physical Review B*, 87, p.134108.

Wadman, A., Andren, H.O. & Rolander, U., 1988. Preferential field evaportation during atom probe analysis of Zircaloy-4. *Journal de Physique*, 49, pp.C6–323–327.

Was, G.S., 2007. Fundamentals of Radiation Materials Science. In *Fundamentals of Radiation Materials Science*. Springer Berlin Heidelberg New York, p. 83.

Was, G.S., 2000. The damage cascade. In *Fundamentals of Radiation Materials Science*. Springer Berlin Heidelberg New York, pp. 125–154.

Williams, D.B. & Carter, C.B., 2009. Thickness determination. In *Transmission Electron Microscopy: A Textbook for Materials Science*. Springer Science+Business Media, LLC, 223 Spring Street, New York, NY, 10013, USA, pp. 352–354.

Woo, C.H., 1987. Effects of Anisotropic Diffusion on Irradiation Deformation. In *Radiation-Induced Changes in Microstructre: 13th International Symposium (PART I), ASTM STP 955*. pp. 70–89.

Woo, C.H., 1988. Theory of irradiation deformation in non-cubic metals: effects of anisotropic diffusion. *Journal of Nuclear Materials*, 159, pp.237–256.

Woo, C.H. & Göslel, U., 1983. Dislocation bias in an anisotropic diffusive medium and irradiation growth. *Journal of Nuclear Materials*, 119, pp.219–228.

Woo, C.H. & Singh, B.N., 1992. Production bias due to clustering of point defects in irradiation-induced cascades. *Philosophical Magazine A*, 65(4), pp.889–912.

Woo, O.T. & Carpenter, G.J.C., 1988. Radiation-induced precipitation in Zircaloy-2. *Journal of Nuclear Materials*, 159, pp.397–404.

Wooding, S.J. et al., 1998. A molecular dynamics study of high-energy displacement cascades in α-zirconium. *Journal of Nuclear Materials*, 254, pp.191–204. Available at: http://www.sciencedirect.com/science/article/pii/S0022311597003656.

Yang, W.J.S., 1988. Precipitate stability in neutron-irradiated Zircaloy-4. *Journal of Nuclear Materials*, 158, pp.71–80.

Zee, R.H. et al., 1984. Effect of tin on the irradiation growth of polycrystalline zirconium. *Journal of Nuclear Materials*, 120, pp.223–229.

Zu, X.T. et al., 2005. Effect of proton and Ne irradiation on the microstructure of Zircaloy 4. *Philosophical Magazine*, 85(4-7), pp.649–659.

4.3 MANUSCRIPT 3: NANOPRECIPITATION IN PROTON-IRRADIATED ZIRCALOY-2

Submission: The following anuscript will be submitted to *Acta Materialia* or *The Journal of Nuclear Materials*

Contribution: The present author wrote this manuscript and performed all of the structural chemical analysis in the STEM, as well as the interpretation and discussion of all results. Prasath Babu took the lead in APT sample preparation and APT data analysis, but was aided by the present author in both. Charles Hirst, Tomas Martin and Michael Moody performed all APT experiments and tomographic reconstructions at their LEAP facility as part of collaboration with The University of Oxford. Philipp Frankel and Michael Preuss provided supervisory support and contributed helpful corrections to the main body of the text. Javier Romero, Lars Hallstadius and Edward C. Darby are industrial collaborators and contributed to the present work by provision of material and insightful discussion.

NANOPRECIPITATION IN PROTON-IRRADIATED ZIRCALOY-2

A. Harte[1], R. Prasath Babu[1], C. Hirst[2], T. Martin[2], M. Moody[2], P. Frankel[1], J. Romero[3], L. Hallstadius[4],E. C. Darby[5], M.Preuss[1]

[1]The University of Manchester, Manchester Materials Science Centre, Grosvenor Street, Manchester, M13 9PL, United Kingdom

[1]The University of Oxford, United Kingdom

[3]Westinghouse Electric Company, Columbia, SC, United States

[4]Westinghouse Electric Sweden AB, SE---72163 Västerås, Sweden

[5]Rolls Royce Plc., Nuclear Materials, Derby, UK

Contact: Allan Harte, allan.harte@manchester.ac.uk

1 ABSTRACT

The irradiation-induced precipitation of Fe- and Cr-rich nano-rods has been observed in Zircaloy-2 following 2 MeV proton irradiation at ~0.2 μA mm^{-2} and 350 °C to low doses ~2 dpa. Atom probe tomography (APT) and scanning transmission electron microscopy (STEM) with energy dispersive X-ray spectroscopy (EDS) have been used in parallel for compositional and morphological characterisation of the nano-rods, showing good agreement between the techniques. The nano-rods are long in the <0001> matrix orientation or inclined to it by 12-15°, and align in the basal plane. The nano-rods are of length 5-30 nm and width 1.5-5 nm with smaller rods of average APT-determined composition $Zr_4(Fe_{0.67}Cr_{0.33})$, tending towards $Zr_3(Fe_{0.69}Cr_{0.31})$ as the rod volume increases to > ~400 nm^3, in agreement with STEM-EDS determination of composition resembling that of Zr_3Fe with Cr replacing some of the Fe. The Fe/Cr ratio has been shown to vary with respect to distance from the nearest partially-dissolved $Zr(Fe,Cr)_2$ SPP. The implications for macroscopic irradiation-induced

growth, irradiation-induced hardening and the interaction of clusters with dislocation loops are discussed.

2 INTRODUCTION

Zr alloys are used as the cladding and structural components of nuclear reactor cores due to their low average neutron absorption cross section and their retention of mechanical properties and corrosion resistance at operating temperatures (Hallstadius et al. 2012). Of the common alloying elements of Zr in the Zircaloy family of alloys, Fe, Cr and Ni, the light transition elements, are of low solubility in the α-Zr matrix (Stupel et al. 1985; Charquet et al. 1988; Zou et al. 1995) and precipitate as thermodynamically stable second phase particles (SPPs) in both the matrix and at grain boundaries (Kuwae et al. 1983; Yang et al. 1986; Griffiths, R.W. Gilbert, et al. 1987; Zou et al. 1994). The Sn remains homogenous in solid solution at low concentrations and acts as an α-stabiliser such that supersaturated solid solutions of Zr-6.5Sn (at.%) are stable up to 953 °C (Okamoto 2010) as α-phase.

SPPs in the Zircaloys are known to undergo irradiation-induced dissolution processes at intermediate to high neutron irradiation temperatures (280-450 °C), depleting preferentially in Fe but also in Cr and Ni in the $Zr(Fe,Cr)_2$ and $Zr_2(Fe,Ni)$ SPPs, respectively (Gilbert et al. 1985; Yang et al. 1986; Griffiths, R W Gilbert, et al. 1987; Yang 1988; Griffiths 1990; Meng & Northwood 1989; Etoh & Shimada 1993; Cockeram et al. 2013; Sawabe et al. 2013; Valizadeh et al. 2014). As such, the matrix becomes increasingly saturated in solute elements and has been shown to precipitate new rod-shaped Fe-, Cr- and Ni- rich phases, extending throughout the matrix with a rod-like morphology (Griffiths, R W Gilbert, et al. 1987; Woo & Carpenter 1988) and in higher concentration close to partially dissolved SPPs (Griffiths 1988) compared to other parts of matrix. Binary Zr-Fe phases, most notably Zr_3Fe, have been reported to nucleate during irradiation under PWR conditions in Zircaloy-4 (Garzarolli et al. 1996) and under BWR conditions in Zircaloy-2 (Goll & Ray 2002). Such phases are though to be relatively resistant to neutron irradiation at ~315-350 °C (Shishov et al. 1996; Garzarolli et al. 1996).

More recently, smaller clusters have been observed in high number density in Zircaloy-2, neutron-irradiated in a BWR to high fluences of 16.5 x10^{25} n m^{-2} ~27.5 dpa (Sundell et al. n.d.), and the growth of small Fe, Cr clusters has been suggested as dependent on the presence of Zr vacancies (Burr et al. 2015).

It is the objective of the present work to assess the irradiation-induced precipitation in Zircaloy-2 after exposure to low dose proton irradiation, and to discuss the findings in the context of similar reports in the literature with regards to neutron-irradiated material. Further, we aim to utilise both atom probe tomography and scanning transmission electron microscopy with significant energy-dispersive X-ray spectroscopy capability to investigate both the compositional and crystallographic properties of the defects observed.

3 EXPERIMENTAL

3.1 MATERIAL

Fully recrystallised Zircaloy-2 plate was provided by Westinghouse Electric Company with nominal composition Zr-1.5Sn-1.4Fe-0.1Cr-0.06Ni (wt.%) (Hallstadius et al. 2012), an equiaxed grain size in the range ~5-15 μm diameter and a strong basal texture in the normal direction, split ± 30° in the transverse direction. The plate was cut into bars of dimensions 2 x 2 x 20 mm and mechanically polished from the normal direction to a quality suitable for electron backscatter diffraction, such that the grains were visible by polarised light microscopy. The bars were then proton-irradiated in the normal direction at the Michigan Ion Beam Laboratory's 1.7 MeV Tandertron accelerator facility at 2 MeV and 350 ±9 °C and a current of ~0.2 μA mm^{-2} for a total of 96 hr. The proton irradiation dose in displacements per atom (dpa) was calculated by the quick Kinchin-Pease calculation in SRIM as recommended by Stoller *et al.* (Stoller et al. 2013) in pure, amorphous Zr with a displacement energy (E_d) of 40 eV (Was 2007). The calculated dose level as a function of proton penetration depth is shown in Figure 4.3.1, in which three depths are highlighted; 0.5 μm at which depth the atom probe tomography (APT) needles were extracted, 12 μm at which depth the electropolished foils were prepared for transmission electron

microscopy (TEM) analysis, and 29 μm, the Bragg peak. As such, the APT data is obtained from material after ~1.5 dpa at a damage rate ~4.3 x10^{-6} dpa s^{-1} and the TEM analysis after ~2.3 dpa and ~6.7 x10^{-6} dpa s^{-1}.

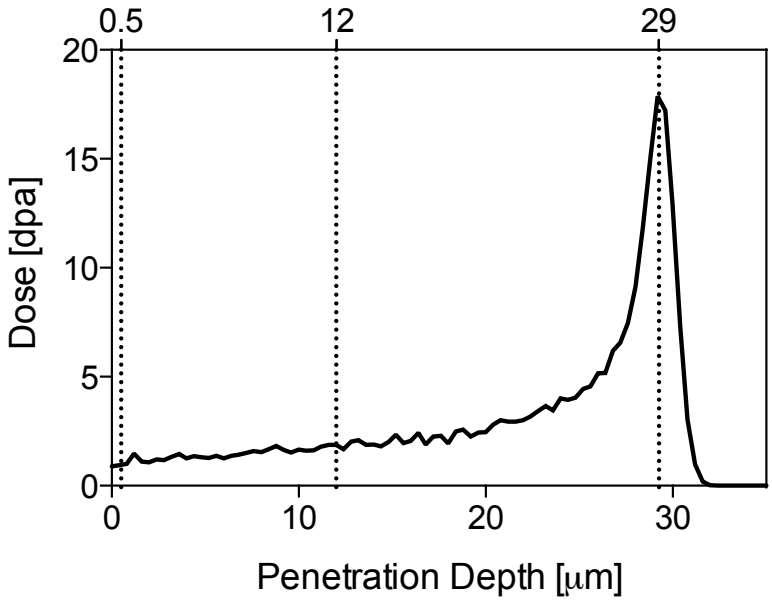

Figure 4.3.1 Damage profile in displacements per atom (dpa) for a pure, amorphous Zr matrix with the atomic density of pure, hcp α-Zr, calculated by SRIM with the quick Kinchin-Pease option (Ed(Zr) = 40 eV) and adjusted for 96 hr 2MeV proton irradiation at ~0.2 μA m-2. The electropolished TEM foils were prepared at a depth of ~12 um (2.3 dpa), and the APT needles were prepared from the surface by FIB, resulting in a depth of ~0.5 um (1.5 dpa).

3.2 ANALYSIS

For APT analysis, both irradiated and non-irradiated samples were mounted on arrays of silicon micro tips and annular milled with a gallium focused ion beam to obtain sharp needles with an end radius of ~50nm. This was accomplished by milling with successively smaller annular masks and successively lower gallium ion currents on a duel beam FEI Novalab 660 at The University of Manchester. The samples were then loaded into the Local Electrode Atom Probe (LEAP) Cameca - 3000X at The University of Oxford, and were held at a temperature of 50 K during data acquisition. The field evaporation of ions was carried out in laser pulse mode with a green laser of energy 0.4 nJ and a frequency of 200 kHz. The reconstruction of the analysed volumes was made on the basis of the needle profile from the SEM images of the sharpened needles.

For analysis of samples in the TEM, electropolished foils were prepared for examination by carefully grinding from the non-irradiated face to a thickness of ~160 μm and then electropolishing using a twin-jet Tenupol-5 electropolisher together with a Julabo FP50 cooling unit. An electrolyte of 10% perchloric acid and 20% 2-butoxyethanol in ethanol (Tournadre et al. 2012) was used to electropolish ~12-15 μm from both the irradiated and non-irradiated faces. Subsequently, Elektron Technology's acid-resistant Lacomit varnish was used to protect the irradiated face while electropolishing to perforation from the non-irradiated face. The non-irradiated bulk material was prepared by the same method. All microscopy presented here was performed on a G2 80-200 kV spherical aberration-corrected (single, probe) FEI Titan microscope operating at 200 kV in scanning mode with a current of 0.6 nA. The microscope is equipped with a high brightness X-FEG source and the FEI ChemiSTEM™ system, comprising four energy-dispersive X-ray spectroscopy (EDS) detectors in close proximity to the sample, resulting in a total collection angle of 0.7 srad. While the sample was loaded in a low-background double-tilt holder, the determination of chemistry may be considered to be semi-quantitative as the Cliff-Lorimer approach was used with calculated K-factors, assuming no absorption and not accounting for Fe-scattering from the pole piece. All chemical data was obtained by spectral imaging (a full spectrum up to 20 keV at every pixel), after which chemical maps were extracted for the relevant alloying elements. Foil thickness measurements were made by an assessment of intensity oscillations in convergent beam electron diffraction (CBED) patterns by way of the graphical method (Williams & Carter 2009). Error in thickness measurements are therefore assumed to be ±10%, given that great care was taken to obtain CBED patterns from the exact Bragg condition.

For the calculation of rod dimensions in the APT reconstruction, the rod-matrix interface was assumed to be the position at which the Fe concentration is equal to that of the average between rod-maximum and the matrix. For this calculation, 1D concentration profiles were generated across length and width dimensions of the rods with cylindrical regions of interest (ROIs) of dimensions defined by a length exceeding that of the rod and a constant diameter of 3nm. The 1D concentration profiles were consistently binned with 500 ions per sample and 200 ions per step.

The composition of the rods was calculated with the volume ROI defined as a cylinder with a constant diameter of 2 nm and a reduced length to avoid the edge of the rod where the concentration is skewed and the Zr content becomes high due to the matrix contribution. The detection of Ni was not carried out due to the overlapping of Ni^{+} peaks with Sn^{2+} peaks at 58 and 60Da and the Ni^{2+} peak with Zr^{3+} peak at 30Da, leaving only 29Da for detection of Ni, proving difficult with the low concentration of Ni (Da = mass to charge ratio). The detection of Sn in the reconstruction was also erroneous due to the Sn ions diffusing readily on the sample surface and evaporating towards the crystallographic poles of the Zr matrix [Sundell et al 2014].

For the rod dimensions analysis by STEM, spectral imaging and the resulting Fe maps from the <0001> direction provided good contrast against the defective α-Zr matrix and was used to obtain detailed rod width information. BF STEM imaging from the $<11\bar{2}0>$ matrix orientation gave the best contrast for rod length as opposed to the Fe or Cr EDS signal, which is weak from this orientation, in which the rods are side-on and at their thinnest in the transmission direction. For quantification of number density, four images were obtained in BF STEM from the <0001> matrix orientation of a single grain. Much of the chemical analysis was performed at specific zone axes, such as the <0001> or the $<11\bar{2}0>$. The determination of matrix orientation was performed by the indexing of the fast Fourier transforms (FFTs) of high resolution STEM images.

4 RESULTS

The defect structures after proton irradiation to 2.3 dpa involve two distinct defect types which can be observed from or close to the $<11\bar{2}0>$ matrix orientation, both of which are demonstrated in Figure 4.3.2a and have some degree of alignment parallel to the (0001) basal plane. Neither type of defect was observed in non-irradiated material. Type I defects are elliptical loops with their long axis (10-20 nm) parallel to the <0001> direction and their short axis (5-10 nm) parallel to the $<1\bar{1}00>$ direction or the (0001) plane. Type II defects are linear defects with a

short width 2-3 nm (Figure 4.3.2a and b), are of relatively sharp contrast and have their long axis either parallel to the <0001> direction or inclined to it by an angle between 12° and 15° (Figure 4.3.2b). Type II defects are distinct from the Type I in that they are visible when imaged parallel to the g = 0002 systematic row (Figure 4.3.2b), which the dislocation loops are not (not shown). This implies that the Type I defects are dislocation loops with a purely <a>-component Burger's vector and that the Type II defects are either dislocation loops with a <c>-component in their Burger's vector or are platelets or rod-shaped precipitates. From BF STEM images, it is estimated that ~30% of the Type II defects have their long axis parallel to <0001> and ~70% are inclined to the <0001> axis. Type II defects may also be observed from the perpendicular orientation, demonstrated in Figure 4.3.2c and d, imaged from the <0001> direction. The defects are projected as circles, suggesting that they are rods and not platelets. From the <0001> orientation, the number density of rods was calculated as 7.01 ±0.77 $x10^{21}$ m^{-3}, with the error given being a single standard deviation from the mean number of defects counted between four different images within the same grain, resulting in a count of 422 defects. If we assume that Type II defects are observed edge-on from the $<1\bar{1}20>$ orientation, a defect tilted 12° from <0001> will have its long axis in the $<1\bar{1}05>$ direction and a defect tilted 15° in the $<1\bar{1}04>$.

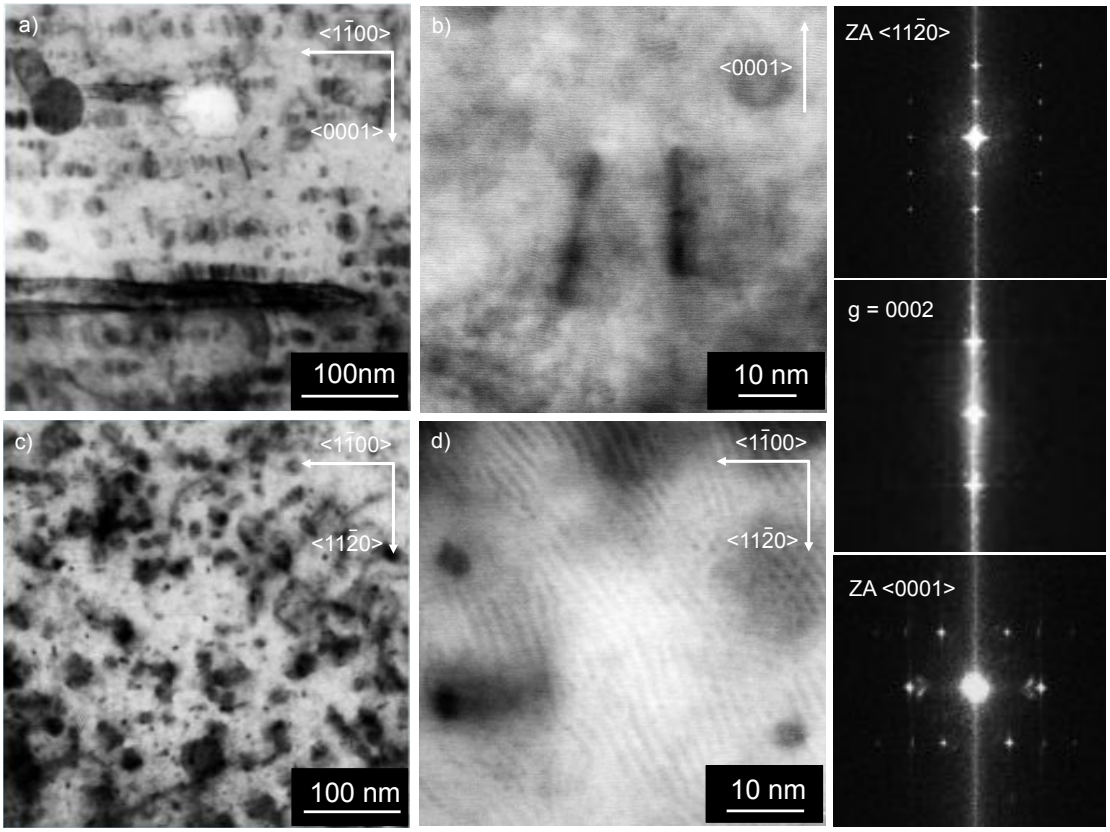

Figure 4.3.2 BF STEM micrographs from a) the $<11\bar{2}0>$ zone axis, b) between the $<11\bar{2}0>$ and $<10\bar{1}0>$ zone axes parallel to the g = 0002 systematic row, and c) and d) from the <0001> zone axis. FFTs of HRSTEM images to the right give the relevant orientations. Dislocation loops and rods are observed in a). The long axes of the rods are either parallel to <0001> or inclined to it, observed in a) and highlighted in b). All rods show c-component contrast, shown in b), whereas a-loops do not. In b) and c), rods are observed as circular ~3 nm in diameter.

A qualitative chemical analysis by STEM energy-dispersive X-ray spectroscopy (EDS) is given in Figure 4.3.3, demonstrating chemical segregation to the defects displayed in Figure 4.3.2b and Figure 4.3.2d. Comparing Figure 4.3.3a-c from the $<11\bar{2}0>$ orientation with Figure 4.3.3d-f from the <0001> orientation immediately demonstrates the rod morphology. However, some rods are circular in cross section (Figure 4.3.3d bottom right) and some seem elliptical in cross section (Figure 4.3.3d top left and bottom left), suggesting either that those rods do not have their long axis exactly parallel to <0001> or they have an ellipsoidal cross section. Of the 33 rods studied by EDS from the <0001> orientation, 19 were circular and 14 elliptical. Of the 14 elliptical, 12 were elongated along the $<1\bar{1}00>$ direction, 2 along $<11\bar{2}0>$ and zero along any direction in between. It should be

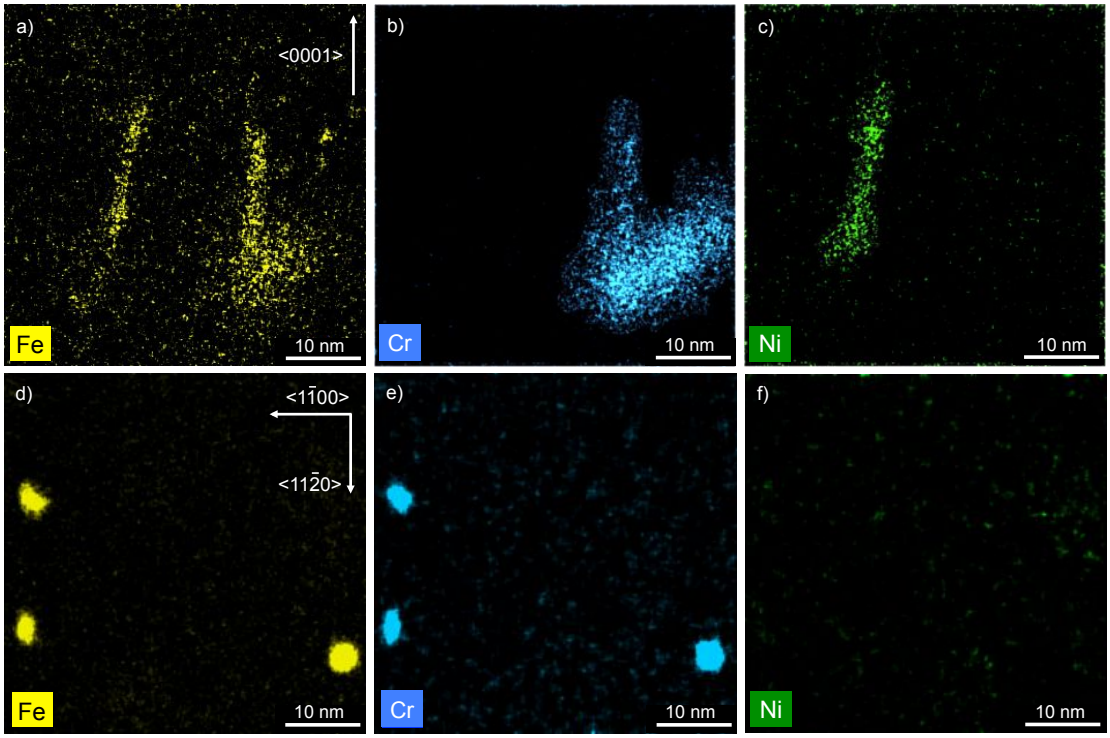

Figure 4.3.3 Qualitative chemical maps by STEM-EDS from the a)-c) $<11\bar{2}0>$ orientation relating to the BF STEM image in **Figure 4.3.2**b, and d)-f) from the <0001> orientation relating to **Figure 4.3.2**d. The defects are rod-shaped and are enriched with Fe, Cr and, less frequently, with Ni.

noted that EDS analysis from the <0001> orientation is biased towards rods with their long axis exactly parallel to <0001>, as these rods will contain the least amount of matrix contribution in the sampling volume in the transmission direction and, as such, are the most suitable for chemical analysis. Therefore, most rods highlighted by EDS mapping are circular from <0001>. All rods observed from the <0001> orientation were rich in Fe and Cr but not Ni. From the $<11\bar{2}0>$ orientation, some Ni segregation was observed (Figure 4.3.3c), but this was uncommon. No obvious difference in chemistry was observed between rods parallel or inclined to [0001]. However, a more thorough analysis from the $<11\bar{2}0>$ orientation is required to corroborate this observation.

The rod-like morphology of the precipitates has also been observed by atom probe tomography (APT), an example of which is shown in Figure 4.3.4, where Fe and Cr enriched regions are shown by iso-concentration surfaces for the volumes with Fe+Cr > 1.2 at%. A total of 5 APT needles were analysed from non-irradiated

Zircaloy-2 and a total of 7 needles for the proton-irradiated Zircaloy-2. Of the 5 non-irradiated needles analysed, no rods were observed. All 7 irradiated APT needles analysed contained rods with their long axis in a common direction, such as those in Figure 4.3.4. All rods were enriched with both Fe and Cr. A crystallographic analysis was performed within a single APT data set, which utilised the preferential evaporation of Sn from high symmetry crystallographic poles and performing a vector analysis (Wahba 1965; Markley 1988). The results of this analysis suggest that the rods in the APT data have their long axis in the [0001] direction, in agreement with the uniqueness of their direction and the observations made by STEM-EDS.

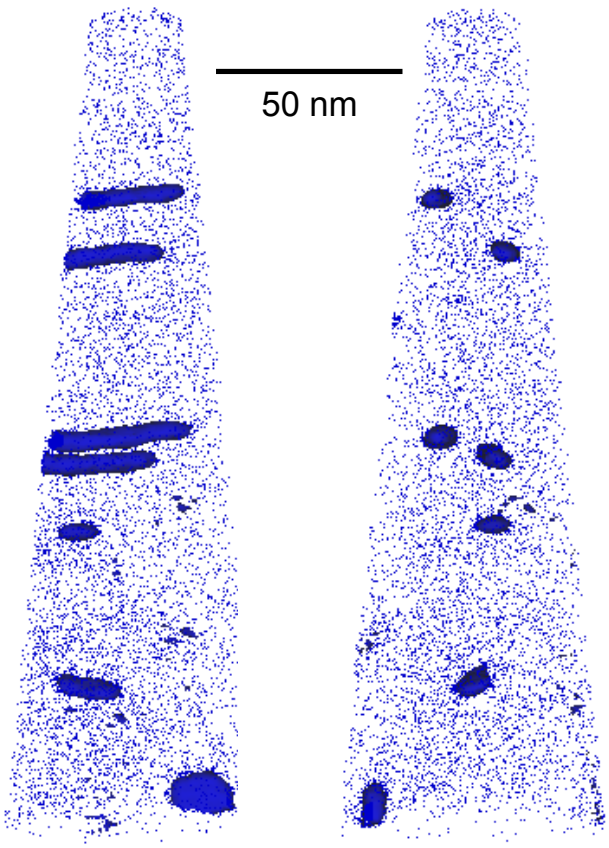

Figure 4.3.4 APT reconstruction showing the Fe+Cr iso-concentration surface (> 1.2 at%) rotated 90° to observe the irradiation-induced precipitates a) edge-on and b) end-on, demonstrating the rod-like morphology of the precipitates

The distribution in rod diameter and length has been determined by both APT and STEM techniques. The data are displayed as number frequency histograms in Figure 4.3.5, which show good agreement between the two techniques considering the small sample size. The reader is reminded that the two techniques correspond to slightly different dose levels of 1.5 and 2.3 dpa for APT (red) and BF STEM (grey), respectively. APT dimension measurements have shown no correlation between rod diameter and length. The rod diameter (Figure 4.3.5a) ranges 2-5 nm with the modal diameter at 3 nm. Both the APT and BF STEM data give rod lengths in the range ~5-30 nm, with APT more suitable for detecting rods in the lower end of this range. The APT lengths are slightly skewed towards a modal value of 12 nm, whereas the BF STEM data gives a modal length range of 15-20 nm. This could be due to the comparably small volume analysed with APT and the rods intersecting the reconstructed volume were not considered for analysis. In BF STEM it was observed that rods of shorter lengths (< ~20 nm) has their length parallel to <0001> whereas rods with longer lengths tended to be inclined to <0001>.

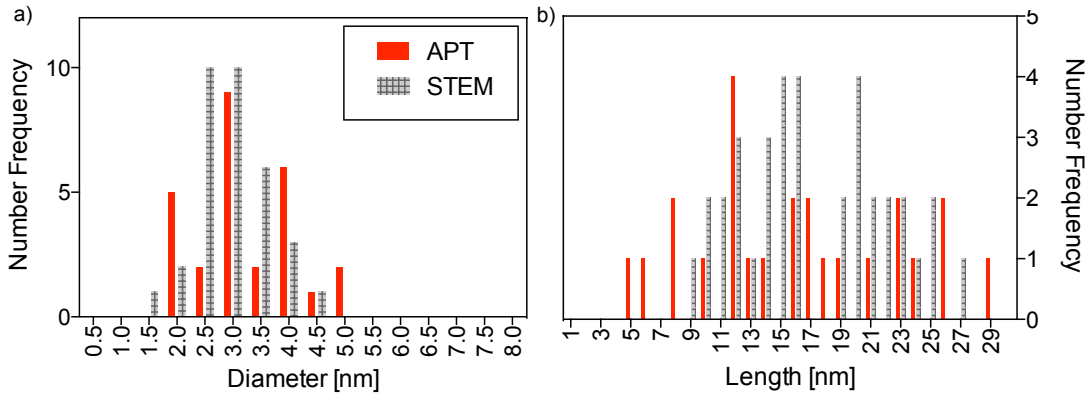

Figure 4.3.5 The distribution in rod a) diameter and b) length have been determined by APT (red) and BF STEM from the $<11\bar{2}0>$ matrix orientation (grey patterned), with good agreement between the two techniques given the small sample size.

Chemical analysis of the rods has been performed by both STEM-EDS and APT. For STEM-EDS, the α-Zr matrix was orientated in the <0001> direction to observe the

rods in their most concentrated form in the transmission direction and hence minimising Zr signal from the matrix. However, the matrix contribution remains large and so the atomic per cent (at.%) of Fe and Cr within the rods remain low at < 4 at.%. The Fe/Cr ratio is thought of as reliable due to the low solubility of the light transition elements in the α-Zr matrix (Stupel et al. 1985; Charquet et al. 1988; Zou et al. 1995). The variation between 33 different rod compositions is displayed in Figure 4.3.6, where data points are separated according to average rod diameter. The compositions are quantified in at.% Fe and Cr even though there is a large contribution from the Zr matrix and pole piece scattering effects are not taken into account. The data shows that rods of ~3nm in diameter have higher Fe and Cr concentrations, suggesting that these are longest in the <0001> transmission direction and hence may be most stable when 3 nm in diameter. While this is supported by the modal diameter of rods as 3 nm (Figure 4.3.5a), APT measurements have shown no correlation between diameter and length. As the thickness of the TEM foil in the <0001> direction is known and the mean rod length determined from the $<1\bar{1}20>$ orientation is also known (~17 nm), we may estimate the stoichiometry of the rods at $Zr_3(Fe_{0.69},Cr_{0.31})$, although the Zr contribution is difficult to be certain of.

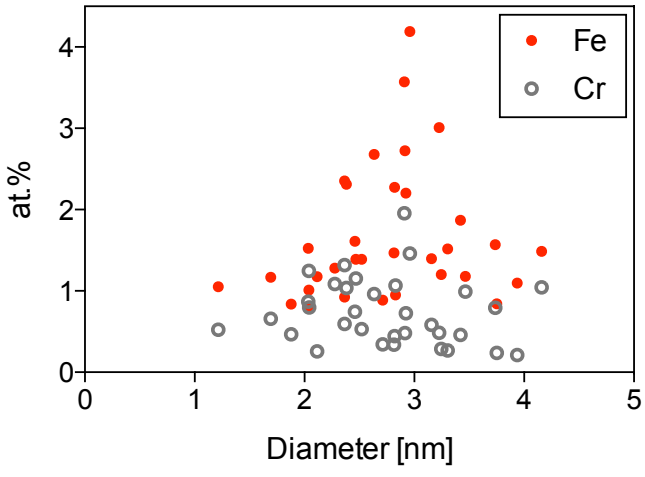

Figure 4.3.6 STEM-EDS determination of Rod composition from the <0001> α-Zr orientation

An example of Fe, Cr and Fe/Cr distribution within a rod, as determined by STEM-EDS from the <0001> orientation, is given in the chemical maps of Figure 4.3.7, quantified in at.% and atomic fraction Fe/Cr. The rod in Figure 4.3.7 is a higher magnification map of the bottom right rod in Figure 4.3.3d. It should be noted that as the pixel size in Figure 4.3.7 is equal to 0.07 nm and the diameter of the spherical aberration-corrected probe is ~0.4 nm, there is significant overlap between pixels. However, one can immediately observe that the concentration of Fe is greater than that of Cr (Figure 4.3.7a and b) and that the Fe/Cr distribution is homogeneous within the rod (Figure 4.3.7c).

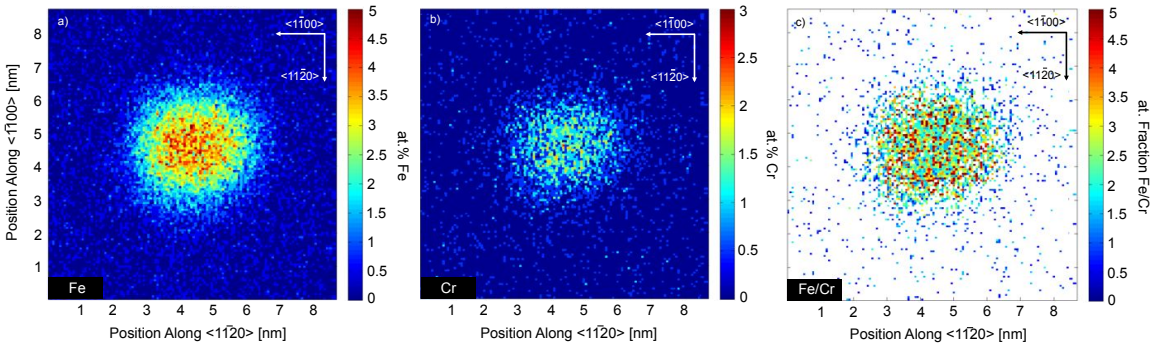

Figure 4.3.7 Chemical maps for a) Fe and b) Cr, quantified in terms of atomic per cent (at.%) are displayed on the same spatial but different concentration scales. The atomic fraction Fe/Cr is displayed in c) to show a homogeneous distribution of Fe with respect to Cr and an average Fe/Cr ~3-4.

The distribution in the Fe/Cr atomic ratio was determined by both APT (red) and by STEM-EDS from the <0001> matrix orientation (grey patterned), and are directly comparable under the assumption that the concentration of Fe and Cr in the matrix is 0 at.% and so do not affect the STEM-EDS results. The results are displayed as a number frequency histogram in Figure 4.3.8a. There is some agreement in the modal value between the two techniques, but APT gives a smaller range at Fe/Cr ~1-2.5 with a modal value of 2 compared to Fe/Cr ~1-6.5 and a modal range of 2-3 for STEM-EDS analysis. The distribution of the APT-determined

atomic ratios Zr/(Fe+Cr) (grey open circles) and Fe/Cr (red closed circles) are shown in Figure 4.3.8b which show little variation with respect to rod volume but a possible tendency towards lower Zr concentrations for larger rods (> ~400 nm^3). Considering both Figure 4.3.8a and b, it may be concluded that the average Fe/Cr = 2 and Zr/(Fe+Cr) = 4. As such, the mean composition of the rods as determined by APT at ~1.5 dpa is $Zr_4(Fe_{0.67}Cr_{0.33})$, possibly tending towards $Zr_{3.1}(Fe_{0.67}Cr_{0.33})$ for rods of volume > ~400 nm^3. Also included in Figure 4.3.8b are the compositions of two Zr-Fe-Cr second phase particles (SPPs) observed by APT in non-irradiated Zircaloy-2 with compositions $Zr_{1.2}(Fe_{0.47}Cr_{0.53})_2$ and $Zr_{1.1}(Fe_{0.49}Cr_{0.51})_2$. As such, the non-irradiated SPPs are of a significantly different composition compared to the irradiation-induced rod precipitates.

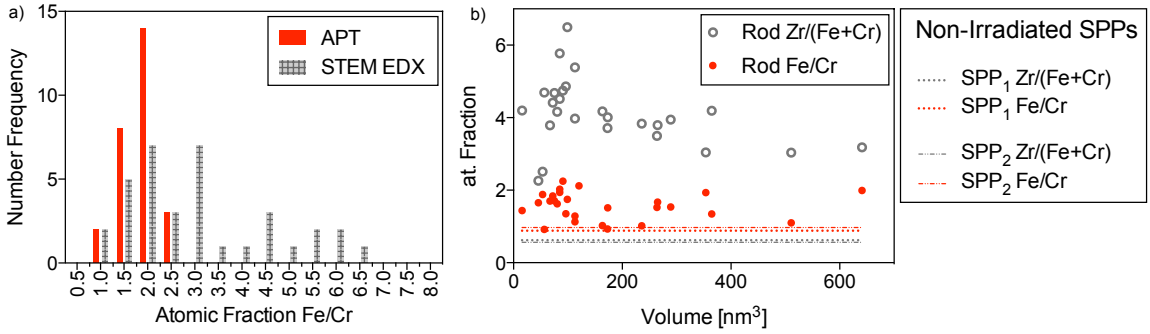

Figure 4.3.8 The distribution of rod composition is displayed in a) a number frequency histogram as determined by APT (red) and STEM-EDS from the <0001> matrix orientation (grey patterned). The Fe/Cr and the Zr/(Fe+Cr) atomic fractions as determined by APT are shown in b), in addition to the fractions in SPPs of non-irradiated Zircaloy-2, also determined by APT.

In using STEM-EDS, it is possible to consider the rod composition in relation to the closest second phase particle (SPP). A qualitative example is given in Figure 4.3.9, which gives chemical maps from the $<1\bar{1}00>$ matrix orientation. It should be noted that this orientation is different to the figures presented previously. At the $<1\bar{1}00>$ orientation the rods with their long axis inclined to the <0001> are inclined a plane parallel to the electron beam, and, as such, all rods appear to have their long axis

parallel to <0001>. This highlights the importance of analysis from multiple orientations in the TEM, a problem avoided in APT. It is clear from Figure 4.3.9 that the rods align parallel to the basal plane. While this was a common observation in the TEM samples, the APT samples revealed no such alignment. In Figure 4.3.9, the rods with the highest BF contrast and the greatest EDS signal arising from Fe+Cr are the rods that are closest to the dissolving SPP; those at the top of figure are relatively weak in contrast.

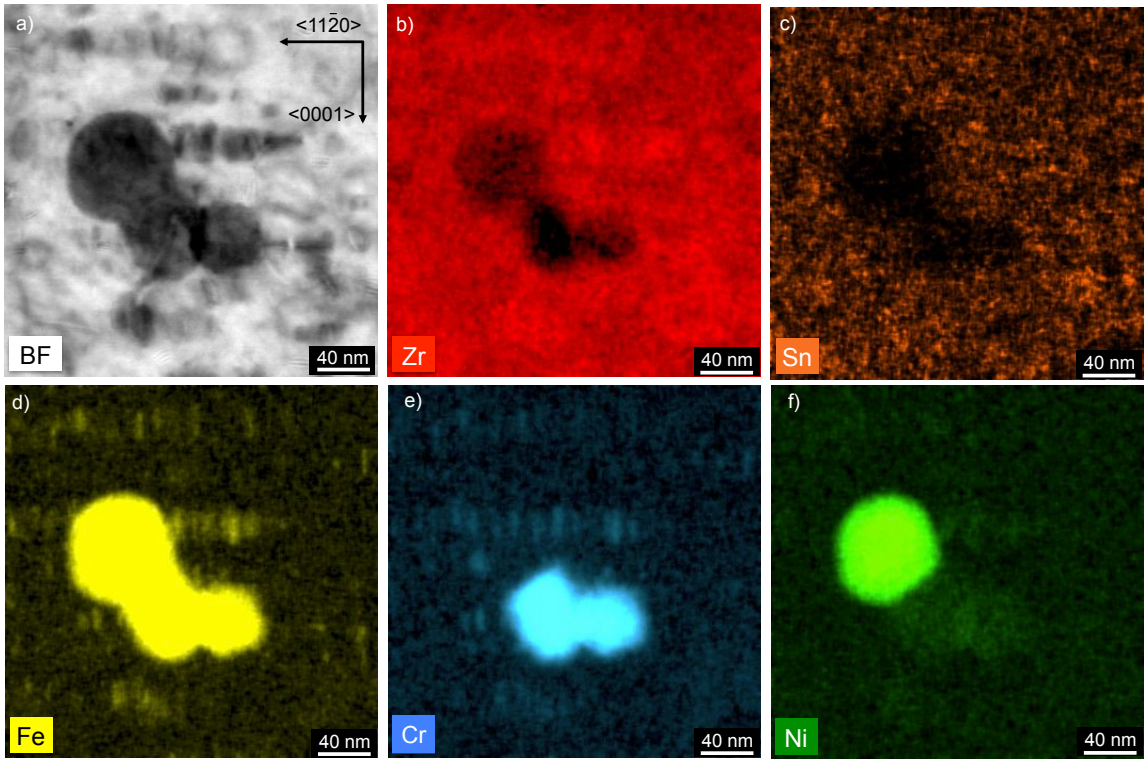

Figure 4.3.9 Irradiation-induced rod composition in close proximity to pre-existing SPPs is qualitatively exemplified from the $<1\bar{1}00>$ matrix orientation. The BF STEM image is given in a) and the chemical maps for Zr, Sn, Fe, Cr and Ni are shown in b)-f), respectively. All rods appear be segregated in Fe and Cr, with Ni segregation observed only very close to the SPP.

For analysis, the chemical composition of the 33 rods quantified by STEM-EDS from the matrix <0001> orientation in Figure 4.3.5a and Figure 4.3.6 were binned into 50 nm wide annular segments from the nearest Fe-Cr type pre-existing SPP. The results are displayed in Figure 4.3.10 as single data points at the maximum radial distance, i.e. in increments of 50 nm up to a maximum distance of 300 nm.

Please note that foil thickness is assumed to vary little within this region. While the errors in single standard deviations are significant, it can be seen that both the Fe and Cr content of rods decrease with increasing distance from the closest Fe-Cr SPP. It can also be seen that the Cr concentration decreases more rapidly than Fe with respect to radial distance after a radius 200 nm, causing the Fe/Cr atomic ratio to increase sharply at this distance.

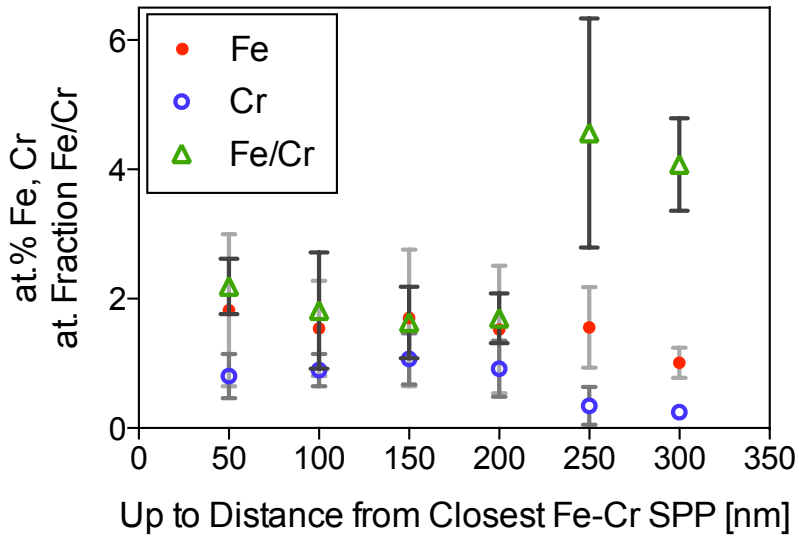

Figure 4.3.10 The composition of rods as a function of radial distance from the closest Fe-Cr SPP are shown. The whole data set comprises the 33 rods quantified by STEM-EDS from the <0001> matrix orientation in **Figure 4.3.5**a and **Figure 4.3.6**, and are binned into 50 nm increments in distance from an SPP. The average composition is then plotted at the maximum radial distance up to a distance of 300 nm from the nearest Fe-Cr SPP.

Matrix compositions were calculated from APT data in both irradiated and non-irradiated samples with Region of Interest (ROI) volumes containing no segregations or clusters of atoms. For this calculation, ~20 million ions were used in the non-irradiated ~30 million ions in the proton-irradiated case. The matrix has 0.023 at% Fe and 0.020 at% Cr in the non-irradiated condition, while after irradiation the concentration increases to 0.053 at% Fe and 0.034 at% Cr, with a relative standard deviation of ~50%. The uncertainty of concentration of these elements was calculated as > $1x10^{-9}$ at%, which is low due to the large number of ions ranged. Measurement of compositions of less than 0.1 at% need to be

approached with caution due to relative standard deviation exceeding 100% for such compositions. The detection efficiency of the micro-channel plate is 37%, which means one-third of the field evaporated ions are lost, but this is independent of element type (Hellsing et al. 1985).

5 DISCUSSION

Rod-shaped structures have been observed in Zircaloy-2 plate after proton irradiation by both atom probe tomography (APT) and scanning transmission electron microscopy (STEM) coupled with energy-dispersive X-ray (EDS) spectroscopy. In the APT data, which corresponds to a dose level of ~1.5 dpa, all rods within a single α-Zr grain were orientated in the same manner, as exemplified in the 90° rotation around the needle axis between Figure 4.3.4a and b. The uniqueness of the rod orientation suggests that the rod long axis is in the [0001] direction, and this is supported by crystallographic analysis of Sn profiles within the needle. However, two types of rod length orientation are observed by STEM-EDS from the $<11\bar{2}0>$ matrix zone axis, which are exemplified in Figure 4.3.2 as either parallel to the [0001] or as inclined to [0001] by ~±12-15°. The former of these is in agreement with observations made in the APT data but the latter requires further investigation. The STEM-EDS observations are made at a proton penetration depth further from the surface of the irradiated bar and, as such, is of an irradiation dose higher than that of the APT samples by a factor of ~1.5. Further, the irradiation dose rate is also higher by a factor of ~1.5 (6.7×10^{-6} dpa s^{-1} as opposed to 4.2×10^{-6} dpa s^{-1}), which may be of importance. It has been suggested that rods inclined to [0001] be rich in Ni (Griffiths 1988), and this is shown in Figure 4.3.3c. However, a more complete investigation into the differences, if any, in chemistry between rods inclined and parallel to [0001] is needed.

Previously reported rod-shaped irradiation-induced precipitates have been observed after neutron irradiations at high fluxes, high temperatures and/or to high fluences (Griffiths, R W Gilbert, et al. 1987; Woo & Carpenter 1988), although post-irradiation annealing of material irradiated under normal power reactor conditions has resulted in the growth of such features (Griffiths, R W Gilbert, et al.

1987). Such rods have been shown to have their long axis in [0001] and to align in basal planes, as has been shown here. Power reactor fluxes result in a dose rate of ~1 x10^{-7} dpa s^{-1} (Shishov et al. 2005; Adamson 2014) at ~310 °C (Azevedo 2011), and, as such, the proton irradiations here provide both a high damage rate and irradiation temperature, which seem to be necessary requirements for the nucleation of these features. It should be noted that no Sn-rich precipitates have been observed in the present work. The precipitation of Zr_5Sn_3 has been observed after neutron irradiation at high flux and temperature and has been attributed to irradiation-enhanced diffusion (Griffiths, R W Gilbert, et al. 1987; Woo & Carpenter 1988).

While rods of average length ~150 nm have been reported in the literature (Woo & Carpenter 1988), such irradiations were performed at high flux in neutron test reactors and at very high irradiation temperatures ~600 °C. The rod dimensions demonstrated in the present work show good agreement in measurements made between APT and BF STEM or STEM-EDS mapping, Figure 4.3.5, although the APT measurements may be skewed towards rods of shorter length due to the small analysed volume. In regards to rod composition, it should be noted that larger scatter in measurements is expected from smaller rods as less ions are used in the calculation and the efficiency of the micro-channel plate detector in the LEAP is 37% such that ⅔ of atoms are not detected, independent of atomic species. While there does not seem to be much variation in rod composition with respect to rod volume, as determined by APT, Figure 4.3.8b, there may be a tendency away from Zr_4(Fe,Cr) and towards Zr_3(Fe,Cr) after rod volumes exceed 400 nm^3 (Fe/Cr ~2 in both cases). As rods in the TEM samples may be longer than that of the APT samples, the stoichiometry estimated from STEM-EDS as Zr_3(Fe,Cr) (Fe/Cr ~2) may suggest that rods do indeed start with an atomic ratio Zr/(Fe+Cr) ~4 that tends to ~3 as the rods increase in size as second phase particles continue to dissolve and disperse solute into the matrix (Gilbert et al. 1985; Yang et al. 1986; Griffiths, R W Gilbert, et al. 1987). The Fe/Cr ratio has been shown to increase at distances > ~ 200 nm from the closest partially-dissolved $Zr(Fe,Cr)_2$ SPP, Figure 4.3.10, which is an indication that the rods nucleate as a result of irradiation-induced dissolute and solute redistribution, in addition to having a dependence on

the relative diffusivities of Fe and Cr in the α-Zr matrix, Fe > Cr (Perez et al. 2003). Of course, due to the issue of projection in the transmission direction, there is uncertainty in that we cannot determine the distance of a rod from the SPP in the direction parallel to the electron beam. However, it is the case that rods rich in Fe and Cr are more frequently found close to partially-dissolved $Zr(Fe,Cr)_2$ SPPs in neutron-irradiated material (Griffiths 1988).

While the existence of the $Zr_4(Fe,Cr)$ phase has been deemed 'questionable' by some (Barberis et al. 2005), as it is not present in the Zr-Fe binary phase diagram (Stein et al. 2002; Okamoto 2006), it has been reported in material after quenching from the α+β- or β-phase region, and is known to dissolve quickly at low fluences (Yang et al. 1986; Cheng et al. 1994). As such, it is thought to be a metastable phase and may be instrumental in the nucleation of the rods presented here. The Zr_3Fe phase, alternatively, has been reported in the literature as nucleating in Zircaloy-4-type alloys under PWR conditions (Garzarolli et al. 1996) and in Zircaloy-2 under BWR conditions (Goll & Ray 2002). Zr-Fe phases are found in the non-irradiated state if the Fe/Cr > 4 (wt.%) in the total alloy composition (Charquet et al. 1988), resulting in the nucleation of either Zr_3Fe or Zr_2Fe, the preference for which possibly depending on cooling rates (Charquet et al. 1988). The Zr_3Fe phase has been shown as stable under neutron irradiation at ~315-350 °C in regards to both changes in chemistry and structure (Shishov et al. 1996; Garzarolli et al. 1996), although its amorphisation behaviour under electron irradiation is well known (Motta et al. 1993; Motta 1997). Such stability may be predicted if one considers the low melting point of the Zr_3Fe phase (885 °C) in comparison to other phases, e.g. $Zr(Fe,Cr)_2$ T_{melt} = 1630 °C (Motta & Lemaignan 1992). As such, for a given irradiation temperature, the Zr_3Fe SPP might be better able to recover the damage incurred by thermal annealing effects in comparison to high T_{melt} SPPs. Further, the growth rate of Zr_3Fe SPPs has been shown as greater than that of $Zr(Fe,Cr)_2$ in non-irradiated material during heat treatments (Garzarolli et al. 1996) and multiple epitaxial relationships between Zr_3Fe and the α-Zr matrix have been reported (Barberis et al. 2005). Barberis *et al.* argued that the almost isotropic nature of the interfacial energy must mean that is not a dominating factor influencing SPP nucleation and stabilisation (Barberis et al. 2005). The rod-shaped

morphology of the precipitates observed in the present work and elsewhere must therefore be due to the preferential <0001> diffusional anisotropy of Fe, Cr and Ni in α-Zr (Christensen et al. 2014), supported by their observation under high neutron irradiation temperatures and flux (Griffiths, R W Gilbert, et al. 1987; Woo & Carpenter 1988).

The rods observed in the present work are thought to be crystalline for the following two reasons, namely the coherency of the rods with the α-Zr matrix and the general consistency in chemical composition. However, the rods proved too small for structural analysis by electron diffraction. In the literature, Zr_3Fe is observed with orthorhombic crystal structure with lattice parameters a = 0.33 nm, b = 1.1 nm and c = 0.88 nm (Charquet et al. 1988). At the beginnings of rod nucleation, the geometric arrangement of clusters has been investigated recently by *ab initio* DFT calculations, which show that clusters of Fe, Cr or Fe+Cr around a Zr vacancy induce less lattice strain than that of an isolated interstitial defect (Burr et al. 2015). The necessity for a Zr vacancy defect for Fe and Cr clustering in the work by Burr *et al.* is interesting, as it lends itself to an understanding of the correlation between matrix solute content and vacancy c-loop nucleation (Griffiths & Gilbert 1987) and the existence of a high density of vacancy c-loops in the vicinity of partially-dissolved SPPs (Griffiths & Gilbert 1987; Tournadre et al. 2012; de Carlan et al. 1996). Recent calculation by Varvenne *et al.* have shown that the binding energy, and therefore the stability, of clusters increases with n up to $n = 7$ (Varvenne et al. 2014) where n refers to the number of atoms/vacancies in the cluster, with the most stable configurations as 3D clusters, in agreement with earlier calculations for clusters of ≤ 10 vacancies (de Diego et al. 2011; Kulikov & Hou 2005). Larger vacancy clusters may induce the nucleation of larger Fe, Cr clusters (Burr et al. 2015). APT is well-suited toward the observation of such clusters, and has been used recently to demonstrate clusters containing predominantly Fe and Cr (Ni to a much lesser extent) in Zircaloy-2 cladding material after irradiation in a BWR to a high fluence of 16.5 $x10^{25}$ n m^{-2} ~27.5 dpa (Sundell et al. n.d.). While the cluster composition was highly variable in the 1-5 nm diameter clusters, and, as such, the structure likely non-crystallographic, Sundell *et al.* clearly demonstrated that the clusters segregate in planar arrays

separated by a distance of ~10 nm (Sundell et al. n.d.). These planes were assumed to be basal (0001) planes due to their uniqueness, but orientation information was not available from the APT data sets. The calculations by Burr *et al.* demonstrate clustering predominantly in basal planes (Burr et al. 2015), which agrees with that observed in the present work and corroborates the assumed plane in the work of Sundell *et al.* (Sundell et al. n.d.) and the alignment of irradiation-induced precipitates in the basal plane reported in the literature (Griffiths, R W Gilbert, et al. 1987; Woo & Carpenter 1988). The number density of clusters reported by APT in neutron-irradiated material was high at 8 ±2 $x10^{23}$ m^{-3}, which is higher than the expected a-loop density; the number density of a-loops is given by Carpenter and Northwood at 25 dpa as ~2 $x10^{22}$ m^{-3} (Carpenter & Northwood 1975), and one may project to 27.5 dpa such that the a-loop density is expected to be approximately the same. This would indicate that the cluster number density is higher than that of a-loops by a factor of 40, although Sundell *et al.* suggest a factor of 10. In the present work, the density of rods is calculated to be 7.01 ±0.77 $x10^{21}$ m^{-3}. According to Carpenter and Northwood, the a-loop number density at ~2.3 dpa should be close to 3 $x10^{22}$ m^{-3} for neutron irradiated Zircaloy-2 (Carpenter & Northwood 1975), which is higher than the rod density by a factor of ~4. However, the a-loop number density is calculated by the present authors for the proton-irradiated Zircaloy-2 at much lower at 2.14 ±0.73 $x10^{21}$ m^{-3} [*Manuscript 2, present work*], and, as such, the rod number density is higher than that of the a-loop number density by a factor of ~3. If one considers the volume of material exhibiting clustering behaviour by Sundell *et al.* (assuming an average cluster sphere of diameter 3 nm) and that of the present work, combining the APT and STEM measurements, the total volume fraction of clusters in the former (~0.0011) is higher than that presented here (~0.00012) by a factor of ~9. Such a difference may be related to the higher degree of SPP irradiation-induced dissolution at the higher dose studied by Sundell *et al*.

The high density of clusters and rods observed after irradiation is likely to have an effect on macroscopic properties. The alignment of rods in the (0001) plane presented here is similar to the alignment of a-loops in neutron-irradiated material (Jostsons et al. 1977) and may suggest significant interactions between the two

structures and even the nucleation of the former by the latter. Chemical segregation to dislocation loops has been discussed as likely to change the loop bias for point defects and clusters, and, as such, is thought to be important in the stability, shape and evolution of dislocation structures (Griffiths 1988). The influence of solute on c-loop density is well known (Griffiths & Gilbert 1987) and a high density of c-loops is correlated to the accelerated regime of irradiation-induced growth (Holt & Gilbert 1986). Further, the effect of variable solute segregation to dislocations in different alloys and at different irradiation doses has been suggested as a source of variation in both a-loop size and in irradiation-induced hardening measurements in Zircaloy-2 and -4 (Cockeram et al. 2011; Cockeram et al. 2013; Cockeram et al. 2014). As dislocation loops are thought to be intrinsically related to macroscopic irradiation-induced growth strain, their interaction with dispersed solute and its clustering is worthy of further investigation.

6 CONCLUSIONS

The proton irradiation-induced precipitation of nano-rods has been observed by both APT and STEM-EDS, with good agreement between the two techniques in terms of rod morphology, dimensions and composition. The following conclusions may be drawn from the present work:

- Small rods are observed to have composition $Zr_4(Fe_{0.67}Cr_{0.33})$, tending towards $Zr_3(Fe_{0.69}Cr_{0.31})$ as the rod volume increases to > ~400 nm^3.
- The Fe/Cr atomic fraction is shown to increase at distances > ~200 nm from the closest partially-dissolved $Zr(Fe,Cr)_2$ SPP. The extent to which Cr replaces Fe in the Zr_3Fe structure is therefore dependent on the relative diffusivities of Fe and Cr in α-Zr.
- The number density of rods is calculated to be higher than that of a-loops by a factor of ~3. As such, the implications for macroscopic strain-related phenomena, such as irradiation-induced growth and hardening, may be significant.

A more thorough investigation is underway by both APT and STEM-EDS to characterise the evolution of nano-rods and -clusters at higher proton irradiation doses and in neutron irradiated material.

7 ACKNOWLEDGEMENTS

This work is funded by an EPSRC Leadership Fellowship [EP/I005420/1] for the study of irradiation damage in zirconium alloys, and is supported heavily by industrial contributors and especially Westinghouse and Studsvik in terms of both material acquisition and useful discussions. The authors would like to thank Thomas Seymour and Matthew topping for aid in experimental accomplishments and Gary Was and Ovidiu Toader at the Michigan Ion Beam Laboratory for the use of their facility in the proton irradiation experiments.

8 REFERENCES

Adamson, R., 2014. *Charged particle bombardment of zirconium alloys: A review*, Sweden.

Azevedo, C.R.F., 2011. Selection of fuel cladding material for nuclear fission reactors. *Engineering Failure Analysis*, 18(8), pp.1943–1962.

Barberis, P. et al., 2005. Microstructure and Phase Control in Zr-Fe-Cr-Ni Alloys: Thermodynamic and Kinetic Aspects. *Journal of ASTM International*, 2(5), pp.129–156.

Burr, P. a et al., 2015. From solid solution to cluster formation of Fe and Cr in α-Zr. *Submitted to Acta Materiallia*.

De Carlan, Y. et al., 1996. Influence of Iron in the Nucleation of <c> Component Dislocation Loops in Irradiated Zircaloy-4. *Zirconium in the Nuclear Industry: Eleventh International Symposium, ASTM STP 1295*, pp.638–653.

Carpenter, G.J.C. & Northwood, D.O., 1975. The contribution of dislocation loops to radiation growth and creep of Zircaloy-2. *Journal of Nuclear Materials*, 56, pp.260–266.

Charquet, D. et al., 1988. Solubility limits and formation of intermetallic precipitates in ZrSnFeCr alloys. *Zirconium in the Nuclear Industry: Eighth International Symposium*, pp.405–422.

Cheng, B.-C., Kruger, R.M. & Adamson, R.B., 1994. Corrosion Behavior of Irradiated Zircaloy. *Zirconium in the Nuclear Industry: Tenth International Symposium, ASTM STP 1245*.

Christensen, M. et al., 2014. Effect of alloying elements on the properties of Zr and the Zr–H system. *Journal of Nuclear Materials*, 445(1-3), pp.241–250.

Cockeram, B. V. et al., 2011. Development of microstructure and irradiation hardening of Zircaloy during low dose neutron irradiation at nominally 358 C. *Journal of Nuclear Materials*, 418, pp.46–61.

Cockeram, B. V. et al., 2014. Development of microstructure and irradiation hardening of Zircaloy during low dose neutron irradiation at nominally 377-440 C. *Journal of Nuclear Materials*, 449, pp.69–87.

Cockeram, B.V. et al., 2013. The use of a laser-assisted Local Electrode Atom Probe and TEM to examine the microstructure of Zircaloy and precipitate structure following low dose neutron irradiation at nominally 358°C. *Journal of Nuclear Materials*, 433(1-3), pp.460–478.

De Diego, N. et al., 2011. On the structure and mobility of point defect clusters in alpha-zirconium: a comparison for two interatomic potential models. *Modelling and Simulation in Materials Science and Engineering*, 19, p.35003.

Etoh, Y. & Shimada, S., 1993. Neutron irradiation effects on intermetallic precipitates in Zircaloy as a function of fluence. *Journal of Nuclear Materials*, 200, pp.59–69.

Garzarolli, F. et al., 1996. Effect of In-PWR Irradiation on Size , Structure , and Composition of Intermetallic Precipitates of Zr Alloys. *Zirconium in the Nuclear Industry: Eleventh International Symposium, ASTM STP 1295*, pp.541–556.

Gilbert, R.W., Griffiths, M. & Carpenter, G.J.C., 1985. Amorphous intermetallics in neutron irradiated Zircaloys after hIgh fluences. *Journal of Nuclear Materials*, 135, pp.265–268.

Goll, W. & Ray, I., 2002. The Behavior of Intermetallic Precipitates in Highly Irradiated BWR LTP Cladding. *Zirconium in the Nuclear Industry: Thirteenth International Symposium, ASTM STP 1423*, pp.80–95.

Griffiths, M., 1988. A review of microstructure evolution in zirconium alloys during irradiation. *Journal of Nuclear Materials*, 159, pp.190–218.

Griffiths, M., 1990. Comments on precipitate stability in neutron-irradiated Zircaloy-4. *Journal of Nuclear Materials*, 170, pp.294–300.

Griffiths, M., Gilbert, R.W., et al., 1987. Neutron damage in zirconium alloys irradiated at 644 to 710 K. *Journal of Nuclear Materials*, 150(2), pp.159–168.

Griffiths, M. & Gilbert, R.W., 1987. The Formation of c-component defects in zirconium alloys during neutron irradiation. *Journal of Nuclear Materials*, 150, pp.169–181.

Griffiths, M., Gilbert, R.W. & Carpenter, G.J.C., 1987. Phase instability, decomposition and resdistribution of intermetallic precipitates in Zircaloy-2 and -4 during neutron irradiation. *Journal of Nuclear Materials*, 150, pp.53–66.

Hallstadius, L., Johnson, S. & Lahoda, E., 2012. Cladding for high performance fuel. *Progress in Nuclear Energy*, 57, pp.71–76.

Hellsing, M. et al., 1985. Performance of a microchannel plate ion detector in the energy range 3-25 keV. *Journal of Physics E: Scientific Instruments*, 18(11), pp.920–925.

Holt, R. a. & Gilbert, R.W., 1986. c-component dislocations in annealed Zircaloy irradiated at about 570 K. *Journal of Nuclear Materials*, 137(3), pp.185–189.

Jostsons, A., Kelly, P.M. & G, B.R., 1977. The Nature of Dislocation Loops in Neutron Irradiated Zirconium. *Journal of Nuclear Materials*, 66, pp.236–256.

Kulikov, D. & Hou, M., 2005. Vacancy dislocation loops in zirconium and their interaction with self-interstitial atoms. *Journal of Nuclear Materials*, 342, pp.131–140.

Kuwae, R. et al., 1983. Mechanism of Zircaloy nodular corrosion. *Journal of Nuclear Materials*, 119, pp.229–239.

Markley, F.L., 1988. Attitude determination using vector observations and the singular value decomposition. *Journal of the Astronautical Sciences*, 36, pp.245–258.

Meng, X. & Northwood, D., 1989. Second phases in Zircaloy-2. *Journal of Nuclear Materials*, 168, pp.125–136.

Motta, A.T., 1997. Amorphization of intermetallic compounds under irradiation — A review. *Journal of Nuclear Materials*, 244, pp.227–250.

Motta, A.T., Howe, L.M. & Okamoto, P.R., 1993. Amorphization kinetics of Zr3Fe under electron irradiation. *Journal of Nuclear Materials*, 205, pp.258–266.

Motta, A.T. & Lemaignan, C., 1992. A ballistic mixing model for the amorphization of precipitates in Zircaloy under neutron irradiation. *Journal of Nuclear Materials*, 195, pp.277–285.

Okamoto, H., 2006. Fe-Zr (iron-zirconium). *Journal of Phase Equilibria & Diffusion*, 27(5), pp.543–544.

Okamoto, H., 2010. Sn-Zr (Tin-zirconium). *Journal of Phase Equilibria and Diffusion*, 31(4), pp.411–412.

Perez, R.A., Nakajima, H. & Dyment, F., 2003. Diffusion in alpha-Ti and Zr. *Materials Transactions*, 44(1), pp.2–13.

Sawabe, T. et al., 2013. Analysis of atomic distribution in as-fabricated Zircaloy-2 claddings by atom probe tomography under high-energy pulsed laser. *Journal of Nuclear Materials*, 442, pp.168–174.

Shishov, V.N. et al., 1996. Influence of Neutron Irradiation on Dislocation Structure and Phase Composition of Zr-Base Alloys. *Zirconium in the Nuclear Industry: Eleventh International Symposium, ASTM STP 1295*, pp.603–622.

Shishov, V.N. et al., 2005. Influence of structure-phase state of Nb containing Zr alloys on irradiation-induced growth. *Zirconium in the Nuclear Industry: 14th Symposium*, 2(8), pp.666–685.

Stein, F., Sauthoff, G. & Palm, M., 2002. Experimental determination of intermetallic phases, phase equilibria, and invariant reaction temperatures in the Fe-Zr system. *Journal of Phase Equilibria*, 23(6), pp.480–494.

Stoller, R.E. et al., 2013. On the use of SRIM for computing radiation damage exposure. *Nuclear Instruments and Methods in Physics Research B*, 310, pp.75–80.

Stupel, M.M., Bamberger, M. & WEiss, B.Z., 1985. Determination of Fe solubility in αZr by Mössbauer spectroscopy. *Scripta Metallurgica*, 19, pp.739–740.

Sundell, G. et al., Redistribution of alloying elements in Zircaloy-2 after in-reactor exposure. *Journal of Nuclear Materials*.

Tournadre, L. et al., 2012. Experimental study of the nucleation and growth of c-component loops under charged particle irradiations of recrystallized Zircaloy-4. *Journal of Nuclear Materials*, 425(1-3), pp.76–82.

Valizadeh, S. et al., 2014. Effects of Secondary Phase Particle Dissolution on the In-Reactor Performance of BWR Cladding. *Journal of ASTM International*, 8(2), pp.729–753.

Varvenne, C., Mackain, O. & Clouet, E., 2014. Vacancy clustering in zirconium: An atomic-scale study. *Acta Materialia*, 78, pp.65–77.

Wahba, G., 1965. A least squares estimate of satellite attitude. *SIAM Review*, 7(3), p.409.

Was, G.S., 2007. Fundamentals of Radiation Materials Science. In *Fundamentals of Radiation Materials Science*. Springer Berlin Heidelberg New York, p. 83.

Williams, D.B. & Carter, C.B., 2009. Thickness determination. In *Transmission Electron Microscopy: A Textbook for Materials Science*. Springer Science+Business Media, LLC, 223 Spring Street, New York, NY, 10013, USA, pp. 352–354.

Woo, O.T. & Carpenter, G.J.C., 1988. Radiation-induced precipitation in Zircaloy-2. *Journal of Nuclear Materials*, 159, pp.397–404.

Yang, W.J.S., 1988. Precipitate stability in neutron-irradiated Zircaloy-4. *Journal of Nuclear Materials*, 158, pp.71–80.

Yang, W.J.S., Tucker, R.P. & Adamson, R.B., 1986. Precipitates in Zircaloy: Identification and the Effects of Irradiation and Thermal Treatment. *Journal of Nuclear Materials*, 138, pp.185–195.

Zou, H. et al., 1994. Solute distribution in annealed Zircaloy-2 and Zr-2.5Nb. *Journal of Nuclear Materials*, 208, pp.159–165.

Zou, H. et al., 1995. The solid solubility of Ni and Co in α-Zr: a secondary ion mass spectrometry study. *Journal of Nuclear Materials*, 223, pp.186–188.

5 CONCLUSIONS AND FUTURE WORK

The broad aim of this work was to assess the influence of proton irradiation on the microstructural and microchemical evolution in Zircaloy-2. Further, the effects of proton irradiation was compared to that of neutron irradiation. Proton irradiation experiments were performed at the Michigan Ion Beam laboratory, from which transmission samples were prepared for comparison to samples from the cladding and channel material of a BWR at various neutron fluences. The thesis presented here contains three manuscripts that detail the compositional changes that occur within second phase particles (SPPs) that release solute into the matrix [*Manuscript 1*], the effect that this has on dislocation structures [*Manuscript 2*], and the new structures that form as a result of matrix supersaturation [*Manuscript 3*]. Such analyses were made possible by the use of the aberration-corrected S/TEM FEI Titan ChemiSTEM™ microscope at The University of Manchester and through collaboration with The University of Oxford in the application of atom probe tomography (APT) to the study of irradiation-induced precipitation. The following is a summary of the key findings of this work and their significance in the field of irradiation damage in Zr alloys. The manuscripts describe the complete microstructural evolution of Zircaloy-2 under irradiation to a level of detail previously unprecedented; especially in regard to SPP dissolution, the resulting dispersion of alloying elements in the matrix in the form of clustering and nano-precipitation and, importantly, the effect of this on irradiation-induced dislocation evolution, which is traditionally considered most relevant to macroscopic phenomena. The key findings of each manuscript will now be described, followed by a section detailing the work's overall significance for the problem of irradiation-induced growth and, finally, future work.

5.1 MANUSCRIPT OUTPUTS

5.1.1 MANUSCRIPT 1: A COMPARISON OF PROTON AND NEUTRON IRRADIATION-INDUCED MICROCHEMICAL EVOLUTION IN ZIRCALOY-2

This manuscript concerned the evolution of SPPs under irradiation and demonstrated similarities between proton- and neutron-irradiated material, especially in the Fe-depletion of both $Zr(Fe,Cr)_2$ and $Zr_2(Fe,Ni)$ -type SPPs. The change in SPP composition was shown to agree well between the proton-irradiated material and neutron-irradiated data, both from the literature and within the present work. The heterogeneity of Fe-Cr SPPs before irradiation was shown to increase during irradiation, whereas the Fe-Ni SPP remained homogeneous throughout. This was proposed as evidence of better internal diffusion within the latter and may suggest why the Fe-Ni SPP is resistant to amorphisation at intermediate neutron irradiation temperatures but the Fe-Cr SPP is not. Further, the better irradiation resistance of the Fe-Ni SPP is evident from its delay in dissolution kinetics. In both proton and neutron-irradiated Zircaloy-2, grain boundary depletion in Fe and Ni was correlated with an increase in Sn content at the boundary, suggesting an inverse Kirkendall type mechanism. As a result of both SPP and grain boundary solute dispersion, the matrix is supersaturated in small transition elements. The effect of this dispersion is the subject of *Manuscript 2* and *3*.

5.1.2 MANUSCRIPT 2: A COMPARISON OF PROTON AND NEUTRON IRRADIATION-INDUCED DISLOCATION LOOP EVOLUTION AND ASSOCIATED MICROCHEMICAL CHANGES IN ZIRCALOY-2

The objective of this manuscript was to quantify the dislocation evolution in proton and neutron-irradiated Ziorcaloy-2 and to relate dislocation evolution to chemical changes in the matrix. The use of bright-field STEM allowed clear dislocation structures to be observed from normal to their habit plane, demonstrating that a-loops in proton-irradiated Zircaloy-2 have the same habit plane as those in neutron-irradiated material, and demonstrating for the first time

the large size of c-loops when projected from the <0001> matrix orientation. The a- and c-loop densities are in good agreement with the literature but the a-loop density show a general increasing tend with irradiation dose, which is unexpected from conventional wisdom regarding a-loop saturation (Griffiths et al. 1996). Such a discrepancy may be due to the clear imaging techniques used in the present work, or due to the high proton dose rate and irradiation temperature that may induce a lower initial dislocation density at the low dose range. Conversely, the (vacancy) c-loop densities agree much better with power reactor studies, suggesting that the proton irradiation parameters affect interstitial-type (a-loop) defects more than vacancy-type defects. This is likely, as the diffusivity of Zr self-interstitials is known to be greater than that of vacancies (Christensen et al. 2015), and so a higher irradiation temperature and dose rate may be expected to affect SIAs more than vacancies.

The interaction between point defects and the solute redistributed into the matrix by SPP and grain boundary depletion is discussed in this manuscript. Fe, Ni and Cr is observed to segregate to a-loops that align on the basal plane. Further, Sn is segregated in between dislocation positions and may be responsible for the alignment of a-loops due to opposing strain fields and the tendency of Sn to trap vacancies (Hood 1977; Hood 1988) and repel interstitials (Christensen et al. 2014). The nucleation of c-loops is then directly related to this segregation and resulting alignment, as we present for the first time direct evidence towards the nucleation of c-loop by a-loops. This observation explains the delay in c-loop nucleation and the decrease in a-loop density as c-loops nucleate, a phenomenon observed here and in the literature (Griffiths et al. 1987) to which explanations have remained elusive thus far.

5.1.3 MANUSCRIPT 3: NANOPRECIPITATION IN PROTON-IRRADIATED ZIRCALOY-2

The aim of this final manuscript was to better characterise the segregation observed to dislocation positions in *Manuscript 2*. In the previous manuscript, the sizes of the matrix clusters/precipitates were larger at the lowest proton dose of

2.3 dpa, and so this is where we began. Both STEM-EDS and APT were utilised to corroborate the findings from the one another and to provide complimentary information. Good agreement was found between the two characterisation techniques in terms of nano-rod morphology, dimensions and composition. The APT provided accurate compositional data in agreement with estimations from STEM-EDS, such that small nano-rods have composition $Zr_4(Fe_{0.67}Cr_{0.33})$, tending towards $Zr_3(Fe_{0.69}Cr_{0.31})$ as the rod volume increases to > ~400 nm^3, in agreement with reports of Zr_3Fe nucleation after neutron irradiation (Garzarolli et al. 1996; Goll & Ray 2002; Shishov et al. 1996).

The number density of rods was determined as higher than the a-loop density in *Manuscript 2* by a factor of ~3, which is likely to have a significant effect on mechanical properties such as hardness, which is conventionally attributed to a-loops alone. Further, its effect on irradiation-induced growth may be significant considering the alignment of nano-rods in the basal plane. In *Manuscript* 2, nano-clustering is widespread throughout the matrix at higher proton irradiation doses and is also demonstrated close to a partially dissolved Fe-Cr SPP in the neutron-irradiated material. As such, the proton and neutron-irradiated material are thought to be similar in regards to irradiation-induced precipitation.

5.2 SIGNIFICANCE TO THE PROBLEM OF IRRADIATION-INDUCED GROWTH

New alloy development in the nuclear industry is slow. After the initial fabrication process, the optimisation of processing parameters is conducted, the mechanical and corrosion performance is tested and finally the influence of neutron irradiation is considered. These are all necessary steps and may take years to inform one another (Sabol 2005). The final stage, neutron irradiation testing, is predominantly conducted in neutron test reactors. These experiments are not only time consuming, costly and hazardous, but they are only accessible by very few research groups, frequently commercial. The use of proton irradiation experiments to emulate neutrons allows the wider academic community to engage with developments in nuclear materials. As such, the problems that the industry faces

are shared globally and new insights are inevitable. Further, their timely nature allows a high throughput pre-testing phase to be introduced to the material selection process.

Irradiation-induced growth has been a significant topic of study since Buckley's proposed explanations of the problem (Buckley 1961). The present work provides evidence that proton irradiation is well suited to the emulation of the microstructural and microchemical changes that are observed after neutron irradiation. Direct, quantitative comparisons have been made, and while there are some slight differences between the effects of the different irradiative species, the stress states that are induced are likely similar. Further, due to the systematic approach of proton irradiation experiments and the inherent control of experimental variables, a mechanistic understanding of irradiation processes may be investigated. In the present work, the relationship between defect structures and microchemical evolution is central. The stabilisation of defect structures by chemical segregation and the effect that this has in the onset of c-loop nucleation, which is correlated to increased growth strains (Holt & Gilbert 1986), is significant. As such, STEM-EDS with high detection efficiency is invaluable for the study of such systems and in the design of the new.

5.3 SUGGESTION OF FUTURE WORK

As a direct progression from the present work, there are several specific studies that should take place. First, the characterisation of nano-precipitation as a function of proton and neutron irradiation dose is essential. The parallel use of STEM-EDS and APT has proven to work well in this regard. A structural analysis of the nano-rod or -clusters is also desirable. Second, further study is required of different SPP types and why some are more resistant to irradiation than others, as this affects matrix chemistry and, ultimately, dislocation structure. A more quantitative approach to the problem could be taken by particle extraction. However, it should be noted that the interaction between the SPP and the matrix is paramount in its dissolution, and so SPPs should always be studied within the

matrix in the first instance. The simulation of defective SPP systems and self-diffusion under dynamic ballistic processes is an inevitable avenue of investigation. While this has begun in the literature (Moura et al. 2001; Chen et al. 2005), it is uncommon, and bonding in such systems, both before and after irradiation, is an essential component to the understanding of their behaviour. Third, the effect of temperature is of interest to all of the microstructural and microchemical aspects described in this work. The temperature profile within a BWR can give rise to a range of environments at 280-330 °C (Azevedo 2011)). This, combined with the effect of a neutron flux profile, creates a large test matrix for many more proton irradiation experiments. As the use of neutron test reactors is a necessary step in alloy performance tests, direct comparisons between test reactor and proton-irradiated material would be a significant step in assessing the extent to which proton irradiation may be used as a method of materials selection for neutron irradiation experiments.

The work presented here in Zircaloy-2 demonstrates the detail with which irradiated material may be studied. There are therefore many similar investigations that are required for other alloys systems. For instance, Fe is thought to reduce the solubility of Nb and improve irradiation-induced growth resistance (Shishov et al. 2005). The effect of solid solution Nb in modern alloys such as ZIRLO™, how Nb interacts with Fe and the result that this has on defect structures is therefore essential. Further, the effect of this Nb-Fe interaction on Sn in the alloy, if any, would provide clues as to the relationship between Fe and Sn in regards to dislocation ordering. Zr alloy M5™ contains Nb but no Sn and so microstructural investigations in this system would be interesting in regards to dislocation loop alignment or lack thereof. There are many such details in various alloy systems that need addressing, and advanced characterisation techniques now available make this possible.

Stepping away from commercial alloys, the irradiation of binary Zr-Sn, Zr-Nb and Zr-X (X = Fe, Cr or Ni) test alloys will allow a reduction in the relative complexity of commercial systems. Building on the independent evolution of binary systems,

ternary alloys could then be studied to determine how the defect evolution differs and, hence, how alloying elements interact with one another. Such a systematic approach to the problem of irradiation-induced microstructural evolution is severely lacking in the literature and is necessary if a true mechanistic understanding is desired.

Lastly, irradiation-induced growth experiments on a proton irradiation beamline is the ultimate goal. In situ proton irradiation creep experiments have been performed in graphite and developed at the Michigan Ion Beam Laboratory (Campbell & Was 2013; Campbell & Was 2014). The instalment of The University of Manchester's Dalton Cumbria Facility beamline will allow the advancement of such in situ proton irradiation experiments. The work presented here suggests that proton irradiation induces similar defect structures to that of neutron irradiation of Zircaloy-2. As such, in situ growth experiments may be expected to yield similar macroscopic phenomena to those in power reactors.

5.4 REFERENCES

Azevedo, C.R.F., 2011. Selection of fuel cladding material for nuclear fission reactors. *Engineering Failure Analysis*, 18(8), pp.1943–1962.

Buckley, S.N., 1961. Properties of Reactor Materials and the Effects of Irradiation Damage. In London: Butterworths, p. 443.

Campbell, A. a. & Was, G.S., 2013. In situ proton irradiation-induced creep at very high temperature. *Journal of Nuclear Materials*, 433(1-3), pp.86–94.

Campbell, A.A. & Was, G.S., 2014. Proton irradiation-induced creep of ultra-fine grain graphite. *Carbon*, 77, pp.993–1010.

Chen, X.-Q. et al., 2005. Ab initio study of ground-state properties of the Laves phase compounds TiCr2, ZrCr2, and HfCr2. *Physical Review B*, 71(174101), pp.1–11.

Christensen, M. et al., 2015. Diffusion of point defects , nucleation of dislocation loops , and effect of hydrogen in hcp-Zr : Ab initio and classical simulations. *Journal of Nuclear Materials*, 460, pp.82–96.

Christensen, M. et al., 2014. Effect of alloying elements on the properties of Zr and

the Zr–H system. *Journal of Nuclear Materials*, 445(1-3), pp.241–250.

Garzarolli, F. et al., 1996. Effect of In-PWR Irradiation on Size , Structure , and Composition of Intermetallic Precipitates of Zr Alloys. *Zirconium in the Nuclear Industry: Eleventh International Symposium, ASTM STP 1295*, pp.541–556.

Goll, W. & Ray, I., 2002. The Behavior of Intermetallic Precipitates in Highly Irradiated BWR LTP Cladding. *Zirconium in the Nuclear Industry: Thirteenth International Symposium, ASTM STP 1423*, pp.80–95.

Griffiths, M. et al., 1987. Neutron damage in zirconium alloys irradiated at 644 to 710 K. *Journal of Nuclear Materials*, 150(2), pp.159–168.

Griffiths, M., Mecke, J.F. & Winegar, J.E., 1996. Evolution of Microstructure in Zirconium Alloys During Irradiation. *Zirconium in the Nuclear Industry: Eleventh International Symposium, ASTM STP 1295*, pp.580–602.

Holt, R. a. & Gilbert, R.W., 1986. c-component dislocations in annealed Zircaloy irradiated at about 570 K. *Journal of Nuclear Materials*, 137(3), pp.185–189.

Hood, G.M., 1988. Point defect diffusion in a-Zr. *Journal of Nuclear Materials*, 159, pp.149–175.

Hood, G.M., 1977. *Point defect properties of α-Zr and their influence on irradiation behaviour of Zr alloys*, Chalk River National Laboratories, Chalk River, Ontario, Canada.

Moura, C.S. et al., 2001. Point defect energetics in the ZrNi and Zr2Ni intermetallics. *Nuclear Instruments and Methods in Physics Research B*, 175(177), pp.526–531.

Sabol, G.P., 2005. ZIRLO – An alloy development success. *Zirconium in the Nuclear Industry: 14th Symposium*, 2(2), pp.3–24.

Shishov, V.N. et al., 1996. Influence of Neutron Irradiation on Dislocation Structure and Phase Composition of Zr-Base Alloys. *Zirconium in the Nuclear Industry: Eleventh International Symposium, ASTM STP 1295*, pp.603–622.

Shishov, V.N. et al., 2005. Influence of structure-phase state of Nb containing Zr alloys on irradiation-induced growth. *Zirconium in the Nuclear Industry: 14th Symposium*, 2(8), pp.666–685.

6 APPENDIX I: A GUIDE TO SRIM

6.1 RUNNING SRIM

Figure I-1 shows a screenshot of the input parameters for a Full Damage Cascades calculation. The elemental composition, density and displacement energies are selected by the user, as are the irradiative species and its properties. The Quick Kinchin-Pease calculation (another common choice) requires the same input parameters but simply requires selection of a different option for the calculation selection. The material composition and its properties are input in addition to the irradiative species'.

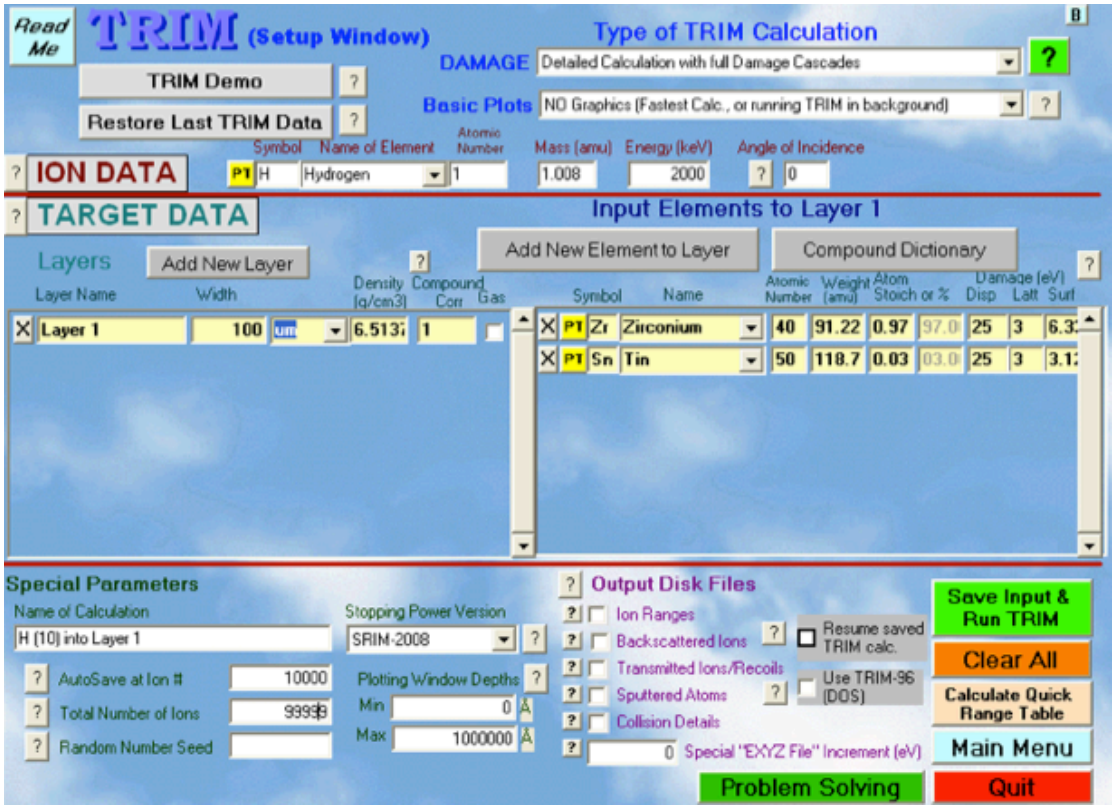

Figure I-1 The input window for the SRIM-2008 calculation.

6.2 RESULTS FROM SRIM

There are many output files for a single SRIM calculation, the most useful of which for our purposes are the vacancy and energy files. The latter is recommended by Stoller (Stoller et al., 2013) for use in damage calculation, but the former can also be used and the differences for the Quick Kinchin-Pease calculation between using the two types of file are minimal. The vacancy output file is much easier to use and so will be the focus of the remaining analysis.

6.3 COMPUTATIONAL PARAMETERS

The irradiative species, its energy and incidence angle were selected. The conversion from wt%, C, to at%, C', was necessary for the input parameters and so is demonstrated in Equation 1 for a binary alloy of components *i* and *j*. The mean density, ρ_{av}, in g cm^{-3}, the mean molar mass, M_{av}, in g mol^{-1} and the mean density, ρ'_{av}, in atoms cm^{-3} are given in Equations 2, 3 and 4, respectively, for the binary *i-j* - alloy.

(1) $$C'_i = 100\left[\frac{C_i M_j}{(C_i M_j)+(C_j M_i)}\right]$$

(2) $$\rho_{av} = 100\left[\frac{C_i}{\rho_i}+\frac{C_j}{\rho_j}\right]^{-1};$$

(3) $$M_{av} = 100\left[\frac{C_i}{M_i}+\frac{C_j}{M_j}\right]^{-1}$$

(4) $$\rho'_{av} = \frac{N_A \cdot \rho_{av}}{M_{av}}.$$

6.4 DPA CALCULATION

6.4.1 NUMBER OF COUNTS NEEDED PER DPA FOR THE TARGET

The number of counts needed to irradiate the target of a given area to one displacement per atom (dpa), C_{dpa}, at a particular penetration depth is given by Equation 5:

(5) $$C_{T\arg et} = \frac{Q \cdot x_1}{x_2} \cdot \frac{\rho \cdot A_a}{R_D},$$

where Q is the charge of the ion, a constant for protons at 1.602 x10^{-19} C ion^{-1}, x_1 a constant describing the number of counts per coulomb as 1 x10^{6} counts C^{-1}, x_2 simply the conversion between angstroms and centimetres as 1 x10^{8} Ang cm^{-1}, ρ the target density, adjusted for alloying composition, in atoms cm^{-3}, A_a the area of the aperture used in cm^2 and R_D the damage rate at a specific penetration depth, obtained from the SRIM calculation.

6.4.2 DIMENSIONAL PROOF

In the first part of Equation (5), the units of the constants simplify as:

(6) $$\frac{Q \cdot x_1}{x_2} \rightarrow \frac{C}{ion} \cdot \frac{counts}{C} \cdot \frac{cm}{angst} = \frac{counts \cdot cm}{ion \cdot angst}$$

In the second part of Equation 5, the units of the constants simplify as:

(7) $$\frac{\rho \cdot A_a}{R_D} \rightarrow \frac{atoms}{cm^3} \cdot cm^2 \cdot \frac{ion \cdot angst}{displ.} = \frac{atoms \cdot ion \cdot angst}{cm \cdot displ.}$$

Multiplying the first and second parts together simplifies the units to:

$$(8)\quad \frac{Q \cdot x_1}{x_2} \cdot \frac{\rho \cdot A_a}{R_D} \rightarrow \frac{counts \cdot cm}{ion \cdot angst} \cdot \frac{atoms \cdot ion \cdot angst}{cm \cdot displ.} = counts \cdot \frac{atoms}{displ} = \frac{counts}{dpa}$$

6.4.3 TOTAL NUMBER OF COUNTS NEEDED PER DPA

The total number of counts needed per dpa is equal to the number of counts given by Equation 5 plus the number of counts due to leakage per dpa, $C_{Leakage}$, a parameter tested prior to irradiation.

$$(9)\quad C_{Total} = C_{Target} + C_{Leakage},$$

where

$$(10)\quad C_{Leakage} = counts_{Leakage} \cdot \frac{hrs}{dpa}$$

and where the number of hours required for 1 dpa is given by Equation (11).

6.4.4 CALCULATION OF TIME REQUIRED FOR 1 DPA

The number of hours per dpa is calculated by dividing C_{Total} by the number of counts per hour, C_{hour}, a value measured by the stage detector prior to irradiation. The stage current at which this value is calculated should be used in the irradiation.

$$(11)\quad \frac{hrs}{dpa} = \frac{C_{Total}}{C_{hour}}$$

- As $C_{Leakage}$ both contributes to and depends on the calculation of the time required for 1 dpa of damage, the value of Equation 11 must be solved iteratively for a specific value on R_D and hence a specific penetration depth.

- Experimentally, the value of $C_{Leakage}$ was commonly 3% of C_{Target}.

6.4.5 CALCULATION OF DAMAGE VARIATION WITH RESPECT TO PENETRATION DEPTH

The time required per dpa was calculated for each alloy. As one of each alloy was to be irradiated on the same stage simultaneously, the longest calculated time for 1 dpa, *t*, was used experimentally to define the time at which all alloys will have undergone at least 1 dpa of damage.

SRIM output gives damage rate, R_D, as a function of penetration depth. The values of R_D are used in the calculation of hrs/dpa by use of Equation 11, and a graph is plotted of damage, *D*, variation with respect to penetration depth where:

$$D = nt\left(\frac{hrs}{dpa}\right)^{-1} \tag{12}$$

This gives a graph of dpa variation with respect to penetration depth for a specific alloy irradiated for a specific amount of time, *t*.

Plotting dpa with respect to penetration depth gives the damage at a penetration depth of 60% of the Bragg peak of approximately *n•dpa*, where *n* is the required damage. Increasing *n* has the effect of reducing the penetration depth range at which dpa = 1 ±0.1.

For example, when calculating the damage profile for 3 dpa the irradiation time is 3*t* and the Bragg peak lies at a penetration depth X. At 0.6X, the damage in the target is approximately equal to 3 dpa. Thus, calculations must be performed for each alloy at each dpa level required of that alloy. As it is difficult to perform analysis on a sample at a specific depth, a range is given such that the damage is 3 ±0.1 dpa.

6.5 EXPERIMENTAL PARAMETERS

Proton-irradiation was carried out in a 1.7 MV tandem particle accelerator at 2 MeV and an incidence angle of 0°. Temperature was maintained at 350 ±9° and the vacuum at < $\sim 10^{-8}$ torr.

6.6 REFERENCES

Stoller, R. E., Toloczko, M. B., Was, G. S., Certain, A. G., Dwaraknath, S., & Garner, F. a. (2013). On the use of SRIM for computing radiation damage exposure. *Nucl. Insturm. Meth. B*, *310*, 75–80. doi:10.1016/j.nimb.2013.05.008